Quality Assessment of Composite Materials using Ultrasonic Non-Destructive Testing Methods

by

Piotr Wiciak

A thesis
presented to the University of Waterloo
in fulfillment of the
thesis requirement for the degree of
Doctor of Philosophy
in
Civil Engineering

Waterloo, Ontario, Canada, 2020

Examining Committee Membership

The following served on the Examining Committee for this thesis. The decision of the Examining Committee is by majority vote.

External Examiner	DR. JOHN S. POPOVICS Professor
Supervisor(s)	DR. MARIANNA POLAK Professor DR. GIOVANNI CASCANTE Professor
Internal Member	DR. MAHESH PANDEY Professor
Internal Member	DR. SRIRAM NARASIMHAN Professor
Internal-external Member	DR. CAROLYN HANSSON Professor

Author's Declaration

This thesis consists of material, all of which I authored or co-authored: see Statement of Contributions included in the thesis. This is a true copy of the thesis, including any required final revisions, as accepted by my examiners.

I understand that my thesis may be made electronically available to the public.

Statement of Contributions

Chapter 5 of this thesis consists of a paper (Wiciak, Piotr, Giovanni Cascante, and Maria Anna Polak. 2020. "Frequency and Geometry Effects on Ultrasonic Pulse Velocity Measurements of Concrete Specimens." *ACI Materials Journal* 117 (2): 205-216. DOI:10.14359/51722399) that was co-authored by myself (P. Wiciak), my co-supervisor, Dr. Giovanni Cascante (G. Cascante), and my co-supervisor, Dr. Maria Anna Polak (M.A. Polak). The contributions of each co-author are the following:

- Conception and design of the study: P. Wiciak, G. Cascante, and M.A. Polak
- Acquisition of data: P. Wiciak
- Software (Matlab procedures): P. Wiciak
- Analysis and/or interpretation of data: P. Wiciak, G. Cascante
- Drafting the manuscript: P. Wiciak
- Revising the manuscript critically for important intellectual content: P. Wiciak, G. Cascante and M.A. Polak
- Approval of the version of the manuscript to be published: P. Wiciak, G. Cascante, and M.A. Polak

The contents of Chapter 6 have been incorporated within a paper that has been submitted for publication. P. Wiciak, G. Cascante, and M. A. Polak, “Novel application of wavelet synchrosqueezed transform (WSST) for condition assessment of cementitious materials.” Submitted to the NDT & E International journal. Submission date Aug 20, 2020. The contributions of each co-author (the author of this thesis and his two co-supervisors) follow the provided earlier list.

Abstract

Non-destructive ultrasonic evaluation (NDE) is commonly used for assessment of civil infrastructure and characterization of construction materials. It is an efficient technique that could save millions of dollars with respect to traditional intrusive tests. However, limitations regarding the use of NDE techniques are still present.

The conventional non-destructive testing (NDT) methods (impact echo, ultrasonic pulse velocity [UPV]) are focused on velocity; therefore, neither the frequency content of the response nor the frequency characteristics of the transmitter signal to a tested material is usually utilized. However, it has been shown that this can lead to misinterpretation of ultrasonic data. Even for the fairly simple method like UPV (where the method is based on the concept of measuring the time of flight for the first arriving ultrasonic wave from one side of the specimen to another), it has been shown that the UPV results may be affected by many factors, such as water-cement ratio, aggregate size, or distribution of moisture. Additionally, traditional wave velocity-based methods are not sufficient for early damage detection (which is an active research field in the non-destructive testing of civil infrastructure) as they use only one data point of information, neglecting the frequency content of ultrasonic signals. Finally, the long-term durability of glass-FRP (GFRP) in concrete remains an unresolved issue. The necessity of reliable NDE techniques for GFRP bars is even more important for in-situ testing of concrete members with GFRP reinforcement because the bars embedded in concrete show no visual deterioration and cannot be cut out of a structure to test in a traditional way.

The main objective of this research is to enhance the understanding of the frequency effects on ultrasonic measurements and establish a comprehensive methodology for early damage detection of composite materials (based on wave velocity, attenuation, and dispersion). This research consists of four studies.

First, a characterization procedure is developed, using a state-of-the-art laser Doppler vibrometer, to understand the frequency content transmitted by ultrasonic transducers typically used in civil engineering applications.

Second, a group of concrete specimens of different diameter and length is tested with a traditional ultrasonic pulse velocity method (using ultrasonic transducers with different resonant frequencies and the laser vibrometer) to evaluate how the frequency content of the recorded ultrasonic measurements changes with different resonant frequency transducers and how it depends on specimen dimensions.

Third, a new methodology, based on wavelet synchrosqueezed transform (WSST) and both velocity and attenuation approaches, is developed to address an issue of early damage detection in cementitious materials (i.e. concrete elements and cemented sand specimen). The proposed framework is verified with synthetic signals and two real, lab-scale applications.

Finally, the functionality of the newly developed ultrasonic procedure (i.e. based on characterized ultrasonic transducers, the WSST, and velocity and attenuation approach) is investigated on progressive damage of glass fibre reinforced polymer specimens. The ultrasonic evaluation is verified with the traditional destructive test (i.e. shear test) and numerical simulations.

The characterization procedure, developed for ultrasonic transducers typically used in civil engineering applications, reveals that frequency content, transmitted by the transducers to the tested medium, consists of more than just transducer resonant frequency. The importance of using well-characterized ultrasonic transducers (i.e. including the full frequency content in the NDT evaluation) is demonstrated on the ultrasonic evaluation of concrete elements, cemented sand specimen, and GFRP reinforcing bars. The study of frequency effects is continued with concrete cylinders of different dimensions. Therefore, practical recommendations regarding the minimum specimen length, effects of increasing length and diameter, and limitations regarding the use of high frequencies in the ultrasonic evaluation of concrete elements are given. Next, a framework based on wave velocity and attenuation (including a demonstration of the advantages of applying the wavelet synchrosqueezed transform [WSST]) is proposed for the evaluation of distributed damage (i.e. early damage induced by freeze and thaw cycles in concrete elements) and localized damage (i.e. cemented sand specimen with a subsurface void). The results indicate that the WSST technique has the potential to improve both the detection of distributed damage by up to 52% and localized damage detection by up to 36%. Finally, a progressive deterioration of GFRP reinforcing bars is studied using the developed ultrasonic procedure. The comparison of ultrasonic evaluation based on wave amplitude, destructive shear test, and numerical simulations shows that ultrasonic techniques can successfully predict the degradation of shear strength (and ultimately tensile strength) of GFRP bars (with the maximum error of 7%). The findings presented in this thesis provide practical recommendations and frameworks that can successfully increase the reliability of non-destructive ultrasonic evaluation of composite materials used in civil engineering applications.

Acknowledgements

First and foremost, I want to acknowledge the advice, support, and guidance of my supervisors Dr. Maria Anna Polak and Dr. Giovanni Cascante. I am thankful for the opportunity to study in the Ph.D. program at the University of Waterloo, and the time spent together on various aspects of an academic career and their friendship. I would also like to thank the members of the examining committee, Dr. Carolyn Hansson, Dr. Mahesh Pandey, and Dr. Sriram Narasimhan, for reviewing this thesis and providing invaluable feedback. Special thanks to the external member, Dr. John S. Popovics, who agreed to be the external examiner.

I want to acknowledge the financial support from the Natural Sciences and Engineering Council of Canada (NSERC) and OPG/UNENE through the NSERC-CRD program.

I also want to thank my unofficial, third co-supervisor, Ed Ginzel, for sharing his years of NDT expertise with me.

I am thankful for the opportunity to work with Dr. Stanislav Potapenko as his teaching assistant numerous times and our unique relationship.

I want to acknowledge the help from the laboratory technicians Anne Allen, Richard Morrison, Douglas Hirst, and Peter Volcic.

I am particularly thankful for my colleagues from the NDT group and Polak Army, especially Dr. Maria Jose Rodriguez-Roblero, Cristobal Lara, Dr. Fredy Diaz-Duran, Graeme Milligan, Ryan Barrage, and Nader Sleiman. I am grateful for your assistance throughout all stages of this research.

There are no words to express my gratitude to Kim and Rob Broberg for their friendship, support and accepting my wife, me, and our daughter as a part of their family.

Finally, I wish to thank my wife, Paula Wiciak, for her love and extraordinary effort during our time in Waterloo. Last but not least, I would like to thank my grandparents (Wladyslawa and Tadeusz, and Teresa and Walerian), parents (Margareta and Jerzy), and sister (Magdalena) for their continued support and encouragement and for helping me become who I am today.

Dedication

To my parents, Margareta and Jerzy,

a loving wife, Paula,

and my little angel Melania.

Table of Contents

List of Figures

List of Tables

Chapter 1
Introduction

Chapter 1 presents the research problem definition, the objectives and the expected contributions from the research project. The terms NDE and NDT are used interchangeably.

1.1 Problem statement

Composite materials have been used for the construction of structural elements for centuries. One of the oldest composites is concrete. It consists of aggregates and cement mortar. First known lime mortar was used in ancient Greece about 2000 B.C. Romans discovered that adding fine sandy volcanic ash to lime mortar creates strong mortar. They used it for the construction of concrete structures, including viaducts, the Colosseum and Parthenon. Subsequently, the art of producing hydraulic mortars and concrete seems to have disappeared for centuries. The first reinforced concrete building in the United States was built in 1875, which started the use of concrete in construction on a large scale. Concrete is traditionally reinforced in tension zones by steel rebars. However, due to corrosion and electromagnetic issues of steel, relatively recently, a new type of reinforcing bars has been introduced, namely fibre reinforced polymer (FRP) composites bars, as reinforcement for concrete. The use of FRP composite materials for construction in structural engineering increased significantly over the past 40 years (Erki & Rizkalla, 1993). FRP bars consist of fibres (glass, basalt, or carbon) and the resin (polyester, vinylester) holding the fibres together.

Non-destructive ultrasonic evaluation (NDE) is commonly used for the assessment of civil infrastructure and characterization of construction materials. It is an efficient technique that could save millions of dollars with respect to traditional intrusive tests. However, limitations regarding the use of NDE techniques are still present. First, the conventional non-destructive testing (NDT) methods (impact echo, ultrasonic pulse velocity [UPV]) are focused on velocity; therefore, neither the frequency content of the response nor the frequency characteristics of the transmitter signal to a tested material is usually utilized. However, it has been shown that this can lead to misinterpretation of ultrasonic data (Wiciak et al., 2020). To overcome the fact that the wave velocity methods are not sensitive in early damage detection (when damage is relatively small) (Stauffer et al., 2005), the latest trends in NDT evaluations focus more on the attenuation of a wavefront for both a longitudinal wave (P-wave) and a surface wave (Chaix et al., 2006; Kirlangic et al., 2015; 2016; Philippidis & Aggelis, 2005). Another approach includes more sensitive methods for detecting small changes in the velocity, such as coda

wave interferometry (Dai et al., 2013; Planès & Larose, 2013; Snieder, 2006). Often, attenuation-based techniques need proper identification of a frequency content transferred to a tested material. Moreover, the efficiency of the detection and the proper localization of a defect in the tested medium, based on traditional methods, is affected by the insufficient knowledge of the incident ultrasonic beam characteristics (Moss & Scruby, 1988). Therefore, the characterization procedure for transducers used in the condition assessment plays a key role in the non-destructive evaluation process.

Even for the fairly simple method like UPV (where the method is based on the concept of measuring the time of flight for the first arriving ultrasonic wave from one side of the specimen to another), it has been shown that the UPV results may be affected by many factors. Abo-Quadais (2005) studied the effect of concrete mix (i.e. water-cement ratio, aggregate size) on the P-wave velocity. The water content was also studied by Ohdaira and Masuzawa (2000). Popovics (2005) noted that the distribution of moisture in concrete and a degree of crack water filling has an influence on P-wave velocity. However, there has been little research studying the effects of specimen dimensions and frequencies used in a test on the UPV in concrete. Therefore, verification of the assumptions of ASTM C597-16 standard, which defines the UPV method (ASTM International, 2016a), and identifying the relationship between UPV results and ultrasonic transducers used (i.e. resonant frequency of the transducer), a coupling quality, and specimen dimensions (i.e. a length and a diameter of a concrete cylinder), with a special focus on the effect of frequency and attenuation is needed.

Early damage detection is of interest in the non-destructive testing of civil infrastructure. Traditional wave velocity-based methods are not sufficient as they use only one data point of information, neglecting the frequency content of ultrasonic signals. In practical/field applications, access to a structure is often limited to one side only (i.e. concrete slabs, vacuum building walls). Thus, surface wave analysis is a natural solution. Additionally, non-destructive evaluation can be improved through novel signal processing techniques that include more than one data-point of information. Velocity based methods analyze signals only in the time domain (UPV) or frequency domain (impact-echo) using basic fast Fourier transform algorithms. On the other hand, time-frequency (TF) methods allow for simultaneous analysis in time and frequency domains. Therefore, a new framework that includes wave velocity and attenuation and applies the benefits of TF methods (e.g. wavelet synchrosqueezed transform) for the condition assessment of cementitious materials evaluated from the surface is needed.

Finally, glass-FRP (GFRP) reinforcement is of increasing popularity in structural engineering due to the low cost in comparison to Carbon-FRP (CFRP). However, the long-term durability of GFRP in concrete remains an unresolved issue. It is also the main reason why the widespread application of GFRP cannot be readily accepted (Nkurunziza et al., 2005). Deterioration of GFRP material is mainly related to the following environmental factors: temperature, UV rays exposure, water/moisture, alkalinity, and load (Mukherjee & Arwikar, 2005a). When GFRP reinforcing bars are considered, the alkalinity of concrete pore water becomes the most critical issue. The necessity of reliable NDT techniques for GFRP bars is even more important for in-situ testing of concrete members with GFRP reinforcement. The bars embedded in concrete show no visual deterioration and cannot be cut out of a structure to test in a traditional way. Additionally, GFRP bars are nonmagnetic; therefore, the NDT solutions used for the evaluation of concrete elements with steel reinforcement cannot be applied. Thus, a new NDT approach to address the problem of condition assessment of GFRP reinforcing bars embedded in concrete elements is needed.

1.2 Research objectives

The main objectives of this research are to enhance the understanding of the frequency effects on ultrasonic measurements and establish a comprehensive methodology for early damage detection of composite materials (based on wave velocity, attenuation, and dispersion). To achieve the major objective, the following specific objectives are defined.

1. To understand the frequency content transmitted by ultrasonic transducers typically used in civil engineering applications. This objective is achieved with a characterization procedure using a state-of-the-art laser Doppler vibrometer. The measurements are taken through the air and solid medium (i.e. glass specimen).

2. To evaluate how the frequency content of the recorded ultrasonic measurements changes with different resonant frequency transducers and how it depends on specimen dimensions. To accomplish this goal, a group of concrete specimens of different diameter and length is tested with a traditional ultrasonic pulse velocity method (using ultrasonic transducers with different resonant frequencies and the laser vibrometer).

3. To investigate the applicability of novel signal processing techniques (i.e. wavelet synchrosqueezed transform, WSST) to attenuation based, early damage detection approach for cementitious materials. The objective is accomplished by verifying the WSST method using

synthetic signals and two real, lab-scale applications (i.e. concrete beams and cemented sand layer).

4. To investigate the functionality of the newly developed ultrasonic procedure (i.e. based on characterized ultrasonic transducers, WSST enhanced velocity and attenuation approach) to progressive damage of glass fibre reinforced polymer specimens. The ultrasonic evaluation is verified with the traditional destructive test (i.e. shear test).

1.3 General methodology and thesis organization

This thesis is divided into eight chapters, with four of them offering the novel research published/submitted/to be submitted to journal articles. Chapter 1 discusses the motivation, research objectives, and thesis organization.

Chapter 2 presents the literature review of engineering composites (i.e. concrete and fibre reinforced polymers) and the currently used non-destructive testing methods for concrete and glass fibre reinforced polymers.

Chapter 3 offers a theoretical background to the operations done in this study. First, the theory of elastic waves and wave attenuation is described. Next, the normal vibration of ultrasonic transducers is discussed with the thin plate theory. Then, a signal processing technique called wavelet synchrosqueezed transformed is shown. Next, two normalization approaches are introduced. Finally, the damage indicators used in this thesis are discussed.

In Chapter 4, the characterization of ultrasonic transducers in the kHz range is shown. The proposed characterization procedure is done in three phases, including laser vibrometer scans performed: (i) through the air, (ii) through the glass block, and (iii) on top of the glass block. Finally, two applications of characterized transducers are shown.

Chapter 5 reviews how specimen dimension and frequency affect the ultrasonic pulse velocity method. The laboratory experiments (i.e. calibration of ultrasonic equipment, ultrasonic evaluation, and laser vibrometer scans) are accompanied by the numerical simulation verifying the natural frequencies of the tested specimen.

Chapter 6 presents the novel application of the wavelet synchrosqueezed transform (WSST) for condition assessment of cementitious materials (i.e. concrete beams and cemented sand layer). The chapter discusses the capabilities and limitations of the WSST method in the ultrasonic range of

frequency. Two applications of the proposed WSST based attenuation method are shown (damage detection of (i) distributed damage and (ii) localized damage).

Chapter 7 investigates the deterioration of glass fibre reinforced polymers (GFRP) induced with the accelerated ageing test (conditioning of the bars in alkaline solution in elevated temperature). A comparison of ultrasonic evaluation (performed with characterized transducer and based on wave velocity and attenuation approaches), destructive shear test, and numerical simulation is offered. Finally, the correlation between ultrasonic features and shear strength is discussed.

Chapter 8 offers conclusions for all four studies and gives recommendations for possible future studies.

1.4 Significance of the research

This research offers contributions to the understanding and improvement of the state-of-practice in NDT of concrete and GFRP. The main contributions include:

- The characterization procedure reveals that the transmitted frequency content consists of resonances of the piezo-crystal and the wearing-surface plate. Plate vibration is significant. This is important for the methodology developed in this study, which is based on surface wave analyses. Additionally, when the high-frequency transducers (i.e. resonant frequency higher than 150 kHz) are used in civil applications, the central zone of the transducer wearing plate should be used for coupling

- The review of the UPV method offers practical recommendations regarding the minimum specimen length, which should be extended to 4 effective wavelengths to ensure a 5% relative error of the UPV test. When the diameter and wavelength ratio smaller or close to the unity, the P-wave velocity correction factor, based on the Poisson's ratio, must be included.

- The developed methodology based on wave attenuation can be used for the early detection of damage, and laser technology is a promising tool to reduce coupling effects in the field. Receiver selection is performed based on the laser-vibrometer characterization procedure of the ultrasonic transmitter used. The results indicate that the WSST technique has the potential to improve both the detection of distributed damage by up to 52% and localized damage detection by up to 36%.

- The pilot study on GFRP bars shows that the developed ultrasonic procedure can successfully identify bar degradation and offers a promising correlation with shear strength reduction (and ultimately tensile strength). The maximum error of expected values of 7% was observed, which means that attenuation can be used as an estimate of strength, which is a large strain property.

Chapter 2
Literature review

This chapter presents a literature review on engineering composites (i.e. concrete, FRP) and discusses currently used NDT methods.

2.1 Engineering composites

In modern engineering materials, the term composite refers to a material made of two or more components (i.e. reinforcement, filler, and binder) different in composition and retaining their own identities (Mahajan & Aher, 2012). Composites are designed to improve combinations of mechanical properties (e.g. stiffness, toughness). In the engineering field, the typical composite materials include (Callister Jr. & Rethwisch, 2014):

- particle-reinforced composites (e.g. large-particle, dispersion-strengthened),
- fibre-reinforced composites (e.g. continuous, discontinues),
- structural composites (e.g. laminates, sandwich panels)
- nanocomposites.

In this Ph.D. research, large-particle-reinforced (i.e. concrete) and fibre-reinforced composites (i.e. glass-fibre reinforced polymer) will be investigated.

2.1.1 Concrete

Concrete is the most utilized structural material in civil engineering applications (Mehta, 2001). It is a composite material that consists of aggregate particles (sand, gravel), which are bound as a solid body by binding medium (cement paste). In that composite, cement paste creates the matrix, whereas sand and gravel are the particulates. The particles should be evenly distributed within the matrix. The aggregates are used as a filler material and help to decrease the price (as they are cheaper materials). The mix of fine sand particles and cement produces mortar. Concrete is a brittle material, strong in compression but weak in tension. In order to address that issue, reinforcing bars (rebar, typically made from steel) are placed in concrete to produce reinforced concrete (RC). Therefore, tension forces (after the concrete cracks) are developed in the bars (MacGregor & Wight, 2005). Exposure to external conditions such as rain, salty environment (marine industry, road salt solution), varying service

temperatures leads to deterioration of RC. Corrosion of steel rebar is a common issue and eventually results in cracking and increased failure risk of an RC member (Wootton et al., 2003). Wootton et al. (2003) presented thirteen different surface protection options and their influence on resistance to accelerated corrosion. In the report (Sanjurjo et al., 1993), different metallic coatings for steel rebar are tested in order to increase the corrosion resistance of the rebar. These attempts increase the service life of the RC structure. In highly salty environmental applications, other non-corrosive materials like stainless steel or fibre-reinforced polymers (FRP) are used.

2.1.1.1 Reinforced concrete defects

Amongst the common types of defects in RC spalling/delamination, cracks, and voids/honeycombing can be indicated. These defects are usually due to environmental (e.g. physical, chemical, or mechanical) or internal factors (e.g. alkali-aggregate reaction and volume change) and may compromise the durability and service life of a structure (Maierhofer et al., 2010; Son & Yuen, 1993; Tesfamariam & Martin-Perez, 2010).

- Spalling/Delamination

ACI (American Concrete Institute, 2018) defines spalling as a flake-shape piece of material that is detached from a larger concrete element. Delamination refers to the separation of material due to the formation of crack parallel to the surface of the concrete. Both of these types of defects are usually caused by corrosion of the reinforcement (Son & Yuen, 1993).

- Cracks

Son and Yuen (1993) describe three main types of cracks: (i) plastic shrinkage cracks, when the freshly places large surface elements are subjected to rapid loss of moisture, (ii) settlement cracks, when the plastic concrete, during hardening, is locally restrained by reinforcing bars, and (iii) cracks of hardened concrete that can be caused by drying shrinkage, thermal stresses, and various physical aggression factors like freeze-thaw cycling, fatigue, reinforcing bar corrosion or service load.

- Voids and honeycombing

These defects are a result of incomplete fill of the voids between coarse aggregate particles by a mortar during construction (Son & Yuen, 1993). Honeycombing is usually a result of improper concrete mix design or poor casting practice. Honeycombing repairs include surface patching or complete replacement of the affected member.

2.1.2 Fibre-reinforced polymer

Fibre-reinforced polymer (FRP) is the composite made of resin (most resins used in composites are the thermosetting type, which means that once they are formed, they cannot be reformed) and fibres (most commonly used in structural engineering applications are: glass or carbon). The main function of resins it to protect the fibres from environmental factors, while fibres provide load-bearing properties (Gowayed, 2013). FRP composites are considered as an interesting structural material because they provide lighter and more durable structures, in the sense of being free of the deterioration caused by the corrosion of steel (Erki & Rizkalla, 1993). In Table 2-1, selected parameters of steel, stainless steel and GFRP (Fiberline Composites, 2017) are compared. The main advantages of FRP composites include (Erki & Rizkalla, 1993):

- high ratio of strength to mass density (as shown in Table 2-1),
- corrosion and magnetic resistance,
- low axial thermal expansion.

Table 2-1. Reinforcing materials - comparison of properties (Fiberline Composites, 2017)

property	steel rebar	stainless steel rebar	Fiberline ComBAR®
ultimate tensile strength (MPa)	> 500[1)]	655	> 1,000
ultimate elongation (‰)	> 25[1)]	50	> 16.7
elastic modulus E (GPa)	200	190	> 60
bond strength (MPa)	13.7	13.7	12.2[2)]
min. required concrete cover (mm)	40 (exposed) 30 (unexposed)	< 30	d_b + 10 mm
density (g/cm3)	7.85	7.92	2.2
thermal conductivity (W/mK)	60	16	< 0.5
coefficient of thermal expansion (1/K)	0.8 to 1.2 x 10^{-5}	1.73 x 10^{-5}	0.6 x 10^{-5} (axial) 2.2 x 10^{-5} (radial)
specific resistance (μΩcm)	1 – 2 x 10^{-5}	7.2 x 10^{-5}	> 10^{12}
magnetism	yes	slightly	no

[1)] for grade 400R steel rebar
[2)] values for 16 mm ComBAR® bars (certification of compliance with ISIS specifications/CSA S807, University of Toronto)
Sources for material values of steel and stainless steel on request.

As for any material, FRP has some disadvantages (Erki & Rizkalla, 1993):

- The high cost (in comparison to traditional steel, however it still remains a good alternative to stainless steel),
- Low elastic modulus.

- Low failure strain.
- Higher (than steel) radial thermal expansion.
- Deterioration due to the ultra-violet (UV) radiation.

Glass-FRP (GFRP) reinforcement is a material of increasing popularity in structural engineering due to the low cost in comparison to Carbon-FRP (CFRP). In addition to the foregoing drawbacks, the durability of GFRP in concrete remains an unresolved issue. It is also the main reason why the extended application of GFRP cannot be easily accepted (Nkurunziza et al., 2005).

2.1.2.1 Fibres

The main function of fibres in FRP composites is to provide the strength and stiffness to the composite. One of the popular fibre types is aramid fibres (AFRP), which provide high modulus and strength in the axial direction of the fibres (Gowayed, 2013). The major drawback of AFRP is its degradation due to UV in the presence of oxygen. Therefore, the application of AFRP in civil engineering is limited.

In structural engineering, the most commonly used FRP composites are CFRP and GFRP. Carbon fibres can be manufactured using different hydrocarbon precursor materials: rayon, polyacrylonitrile (PAN), or pitch. Among these three precursors, Rayon is used in less than 1% of the production of carbon fibres (Gowayed, 2013). CFRP has the highest tensile modulus of elasticity among FRP composites, which makes CFRP an excellent structural reinforcing material (Erki & Rizkalla, 1993).

GFRP is the least expensive FRP reinforcement (Erki & Rizkalla, 1993). There are several types of glass fibres used in for the manufacturing of GFRP: E-glass (E stands for electrical), C-glass (C for corrosion), S-glass (Strength). The tensile modulus of elasticity varies from 69 to 87 GPa (Gowayed 2013), which is significantly lower than the modulus of elasticity of conventional reinforcing steel (200 GPa; Table 1).

2.1.2.2 Resin (matrix)

The fibres are mixed with a resin material (matrix), which provides protection to the fibres and also transfer stresses between them (Kemp & Blowes, 2011). There are two commonly used types of polymeric matrices used for FRP composites: thermosetting and thermoplastic. Thermosetting resin has good thermal stability, chemical resistance, and low creep and relaxation behaviour. Because of these properties, thermosetting resins are the preferred matrix type for civil engineering. Popular thermosetting resins include epoxy, polyester, and vinyl ester, which vary in properties (Kemp &

Blowes, 2011). The use of a particular resin type depends on the application. In the structural engineering applications, a vinyl ester is usually used due to better corrosion resistance and thermal properties. It also provides better impact resistance and fatigue properties (Fiberline Composites, 2017).

2.1.2.3 Additives

The last components that are added in the manufacturing process are the additives. Depending on the function, fillers can be divided into three groups (Fiberline Composites, 2017):

- Price-reduction

These additives are usually called fillers. They are used to reduce the price of the final product.

- Function-related

Function-related additives can be described as materials added to achieve a certain function. One example is adding pigments to help against UV deterioration.

- Process-related

The final group includes the additives added by the manufacturer in order to ease or speed up the manufacturing process.

2.1.2.4 Manufacturing

In the process of FRP composites manufacturing, different techniques can be involved. The techniques include the pre-impregnation production process, filament winding, and pultrusion (Callister Jr. & Rethwisch, 2014). The latter method will be review in more detail as the GFRP bars used in this research are manufactured with the pultrusion method. The scheme of the pultrusion process is presented in Figure 2-1. The process is used for the manufacture of profiles with a constant cross-section. First, the fibres are precisely placed in the desired position with respect to the profile cross-section and are impregnated with the resin. Next, the combination of the two materials is heated and cured until the final shape is achieved. The last step is to cut the profile into final lengths.

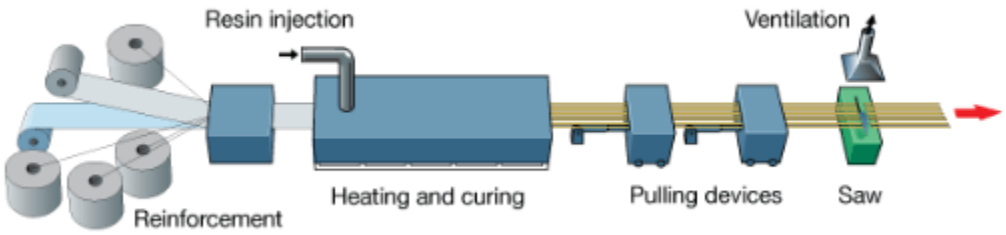

Figure 2-1. Pultrusion process scheme (Fiberline Composites, 2017)

The pultrusion is a process that can easily be automated with the control of the individual steps, which results in consistent quality (Fiberline Composites, 2017).

2.2 Current NDT methods

2.2.1 Concrete

The condition of concrete may be affected by the quality of design, manufacturing, loads applied to a structure, character of the loads, environmental deterioration, or ageing. The integrity of concrete is essential for the safety of a structure. Micro-defects are also present in concrete before the loads are applied. One example of such are voids in the mortar matrix. The micro-defects may be a result of shrinkage, creep, bleeding, settlement of coarse aggregates etc. (Kim et al., 2005). In order to assess the condition of concrete/mortar, NDE methods may be applied. Two major groups of NDT techniques are electromagnetic and acoustic. In the first group, the most popular are ground penetration radar (GPR), thermal imaging, electrical resistance testing, and radiography. Among the acoustic methods, the impact echo, ultrasonic pulse velocity (UPV), and surface wave analysis can be distinguished (McCann & Forde, 2001; Popovics, J. S., 2003; Tesfamariam & Martin-Perez, 2010). The latest trends focus more on the attenuation of the wavefront (Aggelis et al., 2005; Kirlangic et al., 2015) and more sensitive methods for detecting small changes in velocity (e.g. coda wave interferometry (Dai et al., 2013; Planès & Larose, 2013; Snieder, 2006)). Ultrasonic non-linear methods, such as non-linear elastic wave spectroscopy or non-linear impact resonance acoustic spectroscopy, have been shown to be very sensitive to microstructural changes (Bittner & Popovics, 2019; Eiras et al., 2014; Eiras et al., 2016; Eiras et al., 2018).

2.2.1.1 Impact echo

In the impact echo (IE) technique, a hammer strike is usually used as the source of the wave. The receiving transducer is placed on the same surface, which is used with the hammer. The recorded time signal is the echo from the boundary or the internal anomaly. Often times, the frequency representation of measured time is used (Popovics, J. S., 2003). The major benefit of the IE method is that only one access surface is needed. The technique was successfully applied to the detection of large voids, extensive cracking and thickness evaluation. However, the IE method cannot be applied to small voids and vertical cracks (Abraham & Popovics, 2010; Popovics, J. S., 2003). The thickness or the distance to an internal reflector can be calculated as:

$$th = \beta \frac{\mathrm{V_P}}{2f}, \tag{2-1}$$

where th is the thickness or the depth, β is the factor related to section shape, $\mathrm{V_P}$ is the P-wave velocity, and f is the fundamental IE frequency (the lowest value frequency of a significant peak). More recent studies show that β can be related to the frequency of the zero group velocity of the first symmetric Lamb mode of a plate structure (Abraham & Popovics, 2010; Gibson & Popovics, 2005)

2.2.1.2 Ultrasonic pulse velocity

Wave velocity depends on the medium properties; therefore, the UPV method is a very popular technique used in NDE in civil engineering (Popovics, J. S., 2003). Propagation velocity of the longitudinal (P-wave) through the material (V_P) can be calculated as:

$$\mathrm{V_P} = \sqrt{\frac{\mathrm{E}(1-\nu)}{\rho(1+\nu)(1-2\nu)}} \tag{2-2}$$

where E is the Young's modulus, ν is the Poisson's ratio, and ρ is the density. The major benefit of the UPV is its simplicity. The method is based on the concept of measuring the time of the first arrival of the ultrasonic wave from one side of the specimen to another. Moreover, UPV is an ASTM standard test method for concrete specimens (ASTM International, 2016a). The standard specifies the applications of UPV as an assessment of the relative quality of concrete and the presence of imperfections (i.e. voids, cracks, and the effectiveness of its repairs). UPV can also be applied to monitoring changes in the condition of a specimen (ASTM International, 2016a). In spite of the easiness of the method, the results obtained depend highly on the transducers used, the coupling quality, and the specimen dimensions. In the UPV method, an ultrasonic transmitter-receiver configuration is used.

Transducers are placed on the opposite faces of the tested specimen. The velocity of the P-wave through the specimens is calculated by dividing the time of the first arrival by the length of the specimen.

2.2.1.3 Surface wave analysis

Another approach assumes the use of Rayleigh surface waves. The depth of penetration is associated with the wavelength (Ensminger & Bond, 2011), so it can be controlled by changing the frequency used in the tests. In the Surface Wave Analysis group, two methods can be distinguished: Spectral Analysis of Surface Waves (SASW) and Multi-channel Analysis of Surface Waves (MASW). Both methods are well-established techniques used in soil properties determination and are being successfully adapted to the evolution of structural materials. When the SASW method is applied to a concrete slab, the medium is impacted at several frequencies, so the vibrations created by Rayleigh wave penetrating different depths can be observed (Zerwer et al., 2002). In the MASW, responses from a multichannel system are used. The MASW test gives additional information about the velocity or attenuation of surface waves (Kirlangic et al., 2015).

2.2.2 GFRP in civil engineering

Within NDT methods used for the evaluation of composite materials, three major categories can be distinguished: chemical, electromagnetic, and physical. The common purpose of each method is to detect the smallest possible damage Composites are popular materials in the aerospace industry. Therefore, many NDE solutions can be found in that field, namely: thermography, ultrasonic waves (P and S-waves applied to laminate composites), acoustic microscopy, ultrasonic guided waves, fibre optics-based strain measurements, laser shearography, eddy current, or microwaves (Halabe, 2013; Karbhari, 2013). However, the void content in the aircraft laminates is significantly lower than what can be accepted in civil infrastructure applications (Mouritz, 2000).

Among methods applied to civil engineering thermography, GPR, digital tap hammer, microwaves, acoustic emission (AE), and ultrasonic waves can be found in the literature (Karbhari, 2013). The first group of research activities focuses on the analysis of the bond between an FRP layer and the other base material. Halabe (2013) showed that with infrared thermography, it possible to identify an artificially introduced debonded area in the GFRP reinforced bridge decks. The same technique was applied to GFRP and CFRP wrapped concrete cylinders with pre-inserted debonded areas between the wrapping layer and concrete. Another successful application included GPR (Halabe, 2013), when the authors were able to identify the simulated air- and water-filled voids between the GFRP bridge deck

and wearing surface. The same areas were detected with a digital tap hammer. Feng et al. (2002) used electromagnetic imaging (microwaves) for the detection of debonded areas between the concrete column and the GFRP jacket. Chiachio et al. (2017) presented a Bayesian method modelling for ultrasonic measurements (performed with high frequencies: 5 MHz, with the sample immersed in a water tank) of CFRP laminate with post-fatigue delamination.

The second group includes GFRP bars, for which the orientation of fibres follows the length of the bar (in contrast to aerospace industry applications). Ghaib et al. (2018) analyzed how AE signals change during the tensile test. They showed significant slope changes in AE results, while the stress-strain relationship remained linear. Park et al. (2015) tested concrete beams with GFRP reinforcement subjected to saline solution. The AE test results showed a good correlation with the mechanical responses. Finally, the GFRP bars were extracted from the beams and tested in tension with the presence of AE sensors. Ultrasonic methods were also successfully used. Castro and Carino (1998) compared Young's modulus obtained from the tensile test and ultrasonic pulse velocity method (54 kHz), showing good agreement between the two approaches. Xu et al. (2018) used PZT (lead zirconate titanate) transducers to monitor bond-slip between a GFRP bar and a concrete specimen. One PZT sensor was embedded in concrete while a PZT patch was attached to the bar, enabling continuous monitoring during a pull-out test.

The applications based on wave amplitude analysis are also reported in the literature. Mouritz (2000) investigated the influence of void content in GFRP laminates on ultrasonic wave velocity and attenuation. He used 500 kHz and 1 MHz transducer in his study. Mahmoud et al. (2011) tested concrete specimens with the CFRP layer in accelerated ageing conditions using surface waves excited at 110 kHz. Amongst ultrasonic features, wave velocity and peak amplitude were used.

Chapter 3
Theoretical background

3.1 Elastic waves

3.1.1 Derivation of the governing wave equation – elastic isotropic solid

The derivation of the governing wave equation will be conducted based on a differential element presented in Figure 3-1 and looking at the x-axis (Rose, 1999).

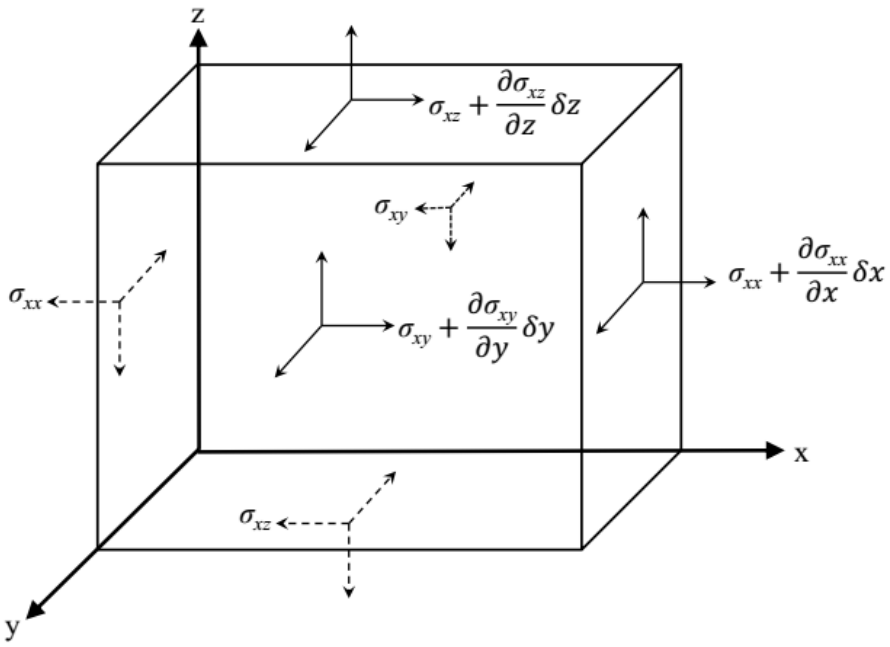

Figure 3-1. Stresses act on a differential cubic solid element (Kirlangic, 2013)

Based on Newton's second law sum of the stresses equal to *ma*, and equilibrium equation (in the x-direction) can be written as:

$$\left(\sigma_{xx} + \frac{\partial \sigma_{xx}}{\partial x}\delta x - \sigma_{xx}\right)\delta y \delta z + \left(\sigma_{xy} + \frac{\partial \sigma_{xy}}{\partial y}\delta y - \sigma_{xy}\right)\delta x \delta z + \left(\sigma_{xz} + \frac{\partial \sigma_{xz}}{\partial z}\delta z - \sigma_{xz}\right)\delta x \delta y = f_x. \tag{3-1}$$

This can be simplified as:

$$\left(\frac{\partial \sigma_{xx}}{\partial x}+\frac{\partial \sigma_{xy}}{\partial y}+\frac{\partial \sigma_{xz}}{\partial z}\right)\delta x\delta y\delta z=f_x. \tag{3-2}$$

Applying: $f_x=\rho\delta V\ddot{u}_x$, where ρ is a density, and u_x is the displacement in the x-direction, and $\ddot{u}_x$ means double differentiation with respect to time, one can finally write that:

$$\frac{\partial \sigma_{xx}}{\partial x}+\frac{\partial \sigma_{xy}}{\partial y}+\frac{\partial \sigma_{xz}}{\partial z}=\rho\ddot{u}_x. \tag{3-3}$$

The same process can be repeated with respect to y, and z axes and results respectively with:

$$\begin{aligned}\frac{\partial \sigma_{yx}}{\partial x}+\frac{\partial \sigma_{yy}}{\partial y}+\frac{\partial \sigma_{yz}}{\partial z}&=\rho\ddot{u}_y\\ \frac{\partial \sigma_{zx}}{\partial x}+\frac{\partial \sigma_{zy}}{\partial y}+\frac{\partial \sigma_{zz}}{\partial z}&=\rho\ddot{u}_z,\end{aligned} \tag{3-4}$$

where u_y and u_z are the displacements in y and z axes, respectively.

The stress-strain relationships are:

$$\begin{aligned}\sigma_{xx}&=\lambda_L\epsilon_V+2\mu_L\epsilon_{xx}\\ \sigma_{yy}&=\lambda_L\epsilon_V+2\mu_L\epsilon_{yy}\\ \sigma_{zz}&=\lambda_L\epsilon_V+2\mu_L\epsilon_{zz}\\ \sigma_{xy}&=2\mu_L\epsilon_{xy}\\ \sigma_{xz}&=2\mu_L\epsilon_{xz}\\ \sigma_{yz}&=2\mu_L\epsilon_{yz},\end{aligned} \tag{3-5}$$

where ϵ_V is a volumetric strain equal to: $\epsilon_V=\epsilon_{xx}+\epsilon_{yy}+\epsilon_{zz}$; λ_L, and μ_L are Lamé's constants. The elastic constants can be transformed into the engineering constants (Young's modulus: E, and the shear modulus):

$$\begin{aligned}\lambda_L&=\frac{vE}{(1+v)(1-2v)}\\ \mu_L=G&=\frac{E}{2(1+v)},\end{aligned} \tag{3-6}$$

where v is the Poisson's ratio.

Now, combining stress-strain elastic relations (Equation 3-5) into Equation 3-3, one will get Navier's governing equation:

$$\frac{\partial}{\partial x}(\lambda_L \epsilon_V + 2\mu_L \epsilon_{xx}) + \frac{\partial}{\partial y} 2\mu_L \epsilon_{xy} + \frac{\partial}{\partial z} 2\mu_L \epsilon_{xz} = \rho \ddot{u}_x, \tag{3-7}$$

where strain tensors are defined as:

$$\epsilon_{xx} = \frac{\partial u_x}{\partial x};\ \epsilon_{xy} = \frac{1}{2}\left(\frac{\partial u_x}{\partial y} + \frac{\partial u_y}{\partial x}\right);\ \epsilon_{xz} = \frac{1}{2}\left(\frac{\partial u_x}{\partial z} + \frac{\partial u_z}{\partial x}\right). \tag{3-8}$$

Equation 3-7 can be rewritten:

$$(\lambda_L + \mu_L)\frac{\partial \epsilon_V}{\partial x} + \mu_L \nabla^2 u_x = \rho \ddot{u}_x, \tag{3-9}$$

where ∇^2 is the Laplacian operator $\left(\nabla^2 = \frac{\partial^2}{\partial x^2} + \frac{\partial^2}{\partial y^2} + \frac{\partial^2}{\partial z^2}\right)$. A similar process can be repeated for *y*, and *z* axes, which results with:

$$\begin{aligned}(\lambda_L + \mu_L)\frac{\partial \epsilon_V}{\partial y} + \mu_L \nabla^2 u_y &= \rho \ddot{u}_y \\ (\lambda_L + \mu_L)\frac{\partial \epsilon_V}{\partial z} + \mu_L \nabla^2 u_z &= \rho \ddot{u}_z.\end{aligned} \tag{3-10}$$

3.1.2 Longitudinal and transverse waves

In order to solve for equations of motion, divergence and curl operators need to be involved. Detailed solutions can be found in (Rose, 1999). Two solutions can be found. The first one is due to the propagation volume change. The second solution describes the propagation due to the rotation. The velocities of propagation of these waves can be read from wave equations and are given as:

1. P-wave (longitudinal or compressional wave)

$$V_P = \sqrt{\frac{\lambda_L + 2\mu_L}{\rho}} = \sqrt{\frac{E(1-v)}{\rho(1+v)(1-2v)}}. \tag{3-11}$$

2. S-wave (transverse or shear wave)

$$V_S = \sqrt{\frac{\mu_L}{\rho}} = \sqrt{\frac{E}{2\rho(1+v)}}. \tag{3-12}$$

3.1.3 Surface (Rayleigh) wave

The existence of the surface waves was predicted by Lord Rayleigh in the XIX century. Later on, they were observed as a result of earthquakes on the surface of the earth. The derivation of the Rayleigh wave velocity equation follows (Rose, 1999) and is conducted for isotropic, homogeneous, linear elastic semi-space. For the two-dimensional plane case, displacements can be defined with the potential functions:

$$\begin{aligned} u_x &= \frac{\partial \phi}{\partial x} + \frac{\partial \psi}{\partial z} \\ u_z &= \frac{\partial \phi}{\partial z} - \frac{\partial \psi}{\partial x}, \end{aligned} \tag{3-13}$$

where ϕ and ψ are potential functions associated with dilatation and rotation, respectively. Next, the dilatation ϵ_V and the rotation in the *x*-*z* plane ($\bar{\omega}_y$) can be written as:

$$\begin{aligned} \bar{\varepsilon}_{xz} &= \frac{\partial u_x}{\partial x} + \frac{\partial u_z}{\partial z} = \frac{\partial}{\partial x}\left(\frac{\partial \phi}{\partial x} + \frac{\partial \psi}{\partial z}\right) + \frac{\partial}{\partial z}\left(\frac{\partial \phi}{\partial z} - \frac{\partial \psi}{\partial x}\right) = \nabla^2 \phi \\ 2\bar{\omega}_y &= \frac{\partial u_x}{\partial z} - \frac{\partial u_z}{\partial x} = \frac{\partial}{\partial z}\left(\frac{\partial \phi}{\partial x} + \frac{\partial \psi}{\partial z}\right) - \frac{\partial}{\partial x}\left(\frac{\partial \phi}{\partial z} - \frac{\partial \psi}{\partial x}\right) = \nabla^2 \psi. \end{aligned} \tag{3-14}$$

Next, Equations 3-13 and 3-14 can be substituted into wave equations (Equations 3-9 and 3-10):

$$\begin{aligned} (\lambda_L + 2\mu_L)\frac{\partial}{\partial x}(\nabla^2 \phi) + \mu \frac{\partial}{\partial z}\nabla^2 \psi &= \rho \frac{\partial}{\partial x}\left(\frac{\partial^2 \phi}{\partial t^2}\right) + \rho \frac{\partial}{\partial z}\left(\frac{\partial^2 \psi}{\partial t^2}\right) \\ (\lambda_L + 2\mu_L)\frac{\partial}{\partial z}(\nabla^2 \phi) - \mu \frac{\partial}{\partial x}\nabla^2 \psi &= \rho \frac{\partial}{\partial z}\left(\frac{\partial^2 \phi}{\partial t^2}\right) - \rho \frac{\partial}{\partial x}\left(\frac{\partial^2 \psi}{\partial t^2}\right). \end{aligned} \tag{3-15}$$

Equations 3-15 can be added together, resulting in:

$$\frac{\partial^2 \phi}{\partial t^2} = \frac{\lambda_L + 2\mu_L}{\rho}\nabla^2 \phi = V_P^2 \nabla^2 \phi, \tag{3-16}$$

and subtracted from each other, giving:

$$\frac{\partial^2 \psi}{\partial t^2} = \frac{\mu_L}{\rho}\nabla^2 \psi = V_S^2 \nabla^2 \psi. \tag{3-17}$$

In order to solve Equations 3-16 and 3-17, the harmonic solution of waves travelling in the direction of the *x*-axis is assumed as:

$$\phi = F(z)e^{i(\kappa x-\omega t)}$$
$$\psi = G(z)e^{i(\kappa x-\omega t)} \tag{3-18}$$

In Equation 3-18, F and G are the functions of amplitudes varying with a position in the z-axis, ω is the angular frequency, and κ represents the wave number (where: $c = {}^{\omega}/_{\kappa}$, with c being the velocity). Substituting Equation 3-18 into (3-16) and (3-17) respectively, and rearranging:

$$\frac{d^2F(z)}{dz^2} - \left[\kappa^2 - \left(\frac{\omega}{V_P}\right)^2\right]F(z) = 0$$
$$\frac{d^2G(z)}{dz^2} - \left[\kappa^2 - \left(\frac{\omega}{V_S}\right)^2\right]G(z) = 0. \tag{3-19}$$

Solutions of Equations 3-19 have a form:

$$F(z) = A_1 e^{-\alpha z} + A_2 e^{\alpha z}$$
$$G(z) = B_1 e^{-\beta z} + B_2 e^{\beta z} \tag{3-20}$$

where $= \sqrt{\kappa^2 - \frac{\omega^2}{V_P^2}}$, $\beta = \sqrt{\kappa^2 - \frac{\omega^2}{V_S^2}}$, and A_1, A_2, B_1, B_2 are arbitrary constants. Discarding the second terms of solutions (3-20), which do not attenuate, the potential functions for an increase with depth can be written as (the amplitude indexes are dropped for the convenience of further calculations):

$$\phi = A_1 e^{-\alpha z} e^{i(\kappa x-\omega t)}$$
$$\psi = B_1 e^{-\beta z} e^{i(\kappa x-\omega t)} \tag{3-21}$$

Rewriting the equations for stresses in terms of potential functions:

$$\sigma_{xx} = \lambda_L \bar{\varepsilon}_{xz} + 2\mu_L \epsilon_{zz} = \lambda_L\left(\frac{\partial u_x}{\partial x} + \frac{\partial u_z}{\partial z}\right) + 2\mu_L \frac{\partial u_z}{\partial z}$$
$$= (\lambda_L + 2\mu_L)\frac{\partial^2 \phi}{\partial z^2} + \lambda_L \frac{\partial^2 \phi}{\partial x^2} - 2\frac{\partial^2 \psi}{\partial x \partial z} \tag{3-22}$$
$$\sigma_{xz} = 2\mu_L \epsilon_{xz} = 2\mu_L \frac{1}{2}\left(\frac{\partial u_x}{\partial z} + \frac{\partial u_z}{\partial x}\right) = \mu_L\left(2\frac{\partial^2 \phi}{\partial x \partial z} - \frac{\partial^2 \psi}{\partial x^2} + \frac{\partial^2 \psi}{\partial z^2}\right).$$

The boundary conditions at the surface ($z = 0$) must be satisfied, implying that: $\sigma_{zz} = 0$ and $\sigma_{zx} = 0$. Including potential functions (3-21) into (3-22):

$$A_1[(\lambda_L + 2\mu_L)\alpha^2 - \lambda_L \kappa^2] - 2B_1 \beta \mu i \kappa = 0 \tag{3-23}$$

$$2A_1 i\alpha\kappa + (\beta^2 + \kappa^2)B_1 = 0.$$

As: A_1,B_1 are arbitrary values; they can be eliminated by taking the ratio of Equations 3-23, which leads to:

$$-4\beta\mu\kappa^2\alpha = (\beta^2 + \kappa^2)[(\lambda_L + 2\mu_L)\alpha^2 - \lambda_L\kappa]. \tag{3-24}$$

Next, Equation 3-24 can be squared on both sides; one can recall that: $\alpha = \sqrt{\kappa^2 - \frac{\omega^2}{V_P^2}}$, $\beta = \sqrt{\kappa^2 - \frac{\omega^2}{V_S^2}}$, and finally divide by the common factor $(\mu_L^2\kappa^8)$:

$$16\left(1 - \frac{\omega^2}{V_P^2}\frac{1}{\kappa^2}\right)\left(1 - \frac{\omega^2}{V_S^2}\frac{1}{\kappa^2}\right) = \left[2 - \left(\frac{\lambda_L + 2\mu_L}{\mu_L}\right)\frac{\omega^2}{V_P^2}\frac{1}{\kappa^2}\right]^2\left(2 - \frac{\omega^2}{V_S^2}\frac{1}{\kappa^2}\right)^2. \tag{3-25}$$

From Equations 3-11 and 3-12: $\left(\frac{\lambda_L+2\mu_L}{\mu_L}\right) = \left(\frac{V_P}{V_S}\right)^2$, and let denote Rayleigh wave velocity: $c = {}^{\omega}/_{\kappa} = V_R$. Those manipulations lead to:

$$16\left(1 - \frac{V_R^2}{V_P^2}\right)\left(1 - \frac{V_R^2}{V_S^2}\right) = \left(2 - \frac{V_R^2}{V_S^2}\right)^4. \tag{3-26}$$

There are different approximate solutions present in the literature:

$$\frac{V_R}{V_S} \cong \frac{0.87+1.12\nu}{1+\nu}$$
$$\frac{V_R}{V_S} \cong 0.874027 + 0.195608\nu - 0.0425231\nu^2 - 0.0569549\nu^3 \tag{3-27}$$

(Rose, 1999; Vinh & Malischewsky, 2006)

The solution does not depend on frequency. Therefore, it can be stated that Rayleigh waves are non-dispersive in a homogenous medium. However, if the condition is not satisfied, the surface wave behaviour can be dispersive. Popovics and Abraham (2010) recommended that in such a situation, it is better to call the propagating waves as surface-guided waves.

The displacements of a Rayleigh wave can be obtained by substituting the potential functions (3-21) into Equations 3-13. Calculating partial differentiations gives:

$$u_x = A_1 i\kappa e^{-\alpha z}e^{i(\kappa x - \omega t)} - B_1\beta e^{-\beta z}e^{i(\kappa x - \omega t)}$$
$$u_z = -\alpha A_1 e^{-\alpha z}e^{i(\kappa x - \omega t)} - B_1 i\kappa e^{-\beta z}e^{i(\kappa x - \omega t)}. \tag{3-28}$$

Finally, B_1 can be calculated from (3-23) so:

$$u_x = A_1 i\kappa\left[e^{-\alpha z} - \frac{2\alpha\beta}{\beta^2+\kappa^2}e^{-\beta z}\right]e^{i(\kappa x-\omega t)}$$
$$u_z = \alpha A_1 \kappa\left[-\frac{e^{-\alpha z}}{\kappa} - \frac{2}{\beta^2+\kappa^2}e^{-\beta z}\right]e^{i(\kappa x-\omega t)} \quad (3\text{-}29)$$

In Equations 3-29, the expressions in brackets are responsible for attenuation with the depth of the medium. It is usually assumed that the effective depth of penetration of Rayleigh waves is one wavelength (Ensminger & Bond, 2011).

3.2 Attenuation and material damping

Wave attenuation is an important parameter that measures the decrease of wave intensity as the wave propagates in a medium. The change in wave amplitude can happen due to many factors such as geometrical spreading (i.e. beam spreading), scattering (the effect due to not truly homogeneous material including crystal discontinuities, grain boundaries, particles, and voids), absorption (when elastic motion converts energy into heat), and mode conversion (Ensminger & Bond, 2011).

Depending on the ratio between average grain size and wavelength, three scattering regimes are usually defined (Ensminger & Bond, 2011):

Table 3-1. Scattering of Ultrasonic Waves (Ensminger & Bond, 2011)

Regime	Grain-wavelength	Attenuation
long-wavelength	$\lambda > D$	$\alpha = \frac{A_1^* D^3 c^4}{\lambda^4}$
mid-frequencies	$\lambda \approx D$	$\alpha = \frac{A_2^* D c^2}{\lambda^2}$
short-wavelength	$\lambda < D$	$\alpha = A_3^* D$

Where A_1^*, A_2^*, A_3^* are the coefficients, dependent on elastic moduli; c is the velocity of wave propagation (Ensminger & Bond, 2011). Based on the (Ensminger & Bond, 2011) and (ASTM International, 2016a), it can be seen that the attenuation has smaller values for long wavelengths (low frequencies) and will increase with decreasing wavelength. Therefore, ASTM recommends the use of low frequencies (20-100 kHz) in the ultrasonic evaluation (ASTM International, 2016a).

Total attenuation, i.e. a combined effect of geometrical spreading and material damping) can be expressed as (Zerwer et al., 2002):

$$\frac{A_1}{A_2} = \left(\frac{x_1}{x_2}\right)^{\beta^*} e^{\alpha_x(x_1 - x_2)} \tag{3-30}$$

where A_1 and A_2 are the amplitudes measured at the distances x_1 and x_2 from the source, β^* is is the geometric attenuation constant ($\beta^* = 0$ for plane waves and –0.5 for surface waves (cylindrical wavefront)), and α_x is the attenuation coefficient (caused by material damping). The total attenuation expression can be rearranged:

$$\alpha_x = \frac{1}{x_2 - x_1}\left[\ln\left(\frac{A_2}{A_1}\right) - \beta^* \ln\left(\frac{x_2}{x_1}\right)\right] \tag{3-31}$$

Often, the damping ratio is calculated using the attenuation coefficient. For small values of damping ratios (i.e. less than 10%), the damping ratio can be calculated as (Clough & Penzien, 1993):

$$\zeta = \frac{\lambda}{2\pi}\alpha_x \tag{3-32}$$

where λ is the wavelength of the ultrasonic wavelength and can be related to ultrasonic wave velocity (V) and frequency (f) as $\lambda = \frac{V}{f}$. In this thesis, attenuation and damping words are used interchangeably and refer to a reduction in amplitude of wave motion.

3.3 Normal vibration of ultrasonic transducers (thin plates theory)

Normal vibration of ultrasonic transducers can be expressed as a solution of the fourth-order partial differential equation of an all-clamped thin plate (Eriksson et al., 2015; Feeney, Kang, Rowlands et al., 2019; Leissa, 1969):

$$D^* \nabla^4 w(x,t) + \rho \frac{\partial^2 w(x,t)}{\partial t^2} = 0 \tag{3-33}$$

where $w(x,t)$ is a time and position-dependent normal displacement of the plate, ρ is the volume density, and D^* is the rigidity defined as:

$$D^* = {Eh^3}/{12(1-\nu^2)} \tag{3-34}$$

The rigidity depends on the following properties: Young's modulus (E), plate thickness (h), and Poisson's ratio (ν).

For square plates, Leissa (1969) gives the following form for the mode shapes ($W(x,y)$):

$$W(x,y) = \sum_{m=1}^{p}\sum_{n=1}^{q} A_{m,n}\left[\cosh {\epsilon_m x}/{a^*} - \cos {\epsilon_m x}/{a a^*} - \alpha_m\left(\sinh {\epsilon_m x}/{a^*} - \sin {\epsilon_m x}/{a a^*}\right)\right]\left[\cosh {\epsilon_n y}/{a^*} - \cos {\epsilon_n y}/{a^*} - \alpha_n\left(\sinh {\epsilon_n y}/{a^*} - \sin {\epsilon_n y}/{a^*}\right)\right], \quad (3\text{-}35)$$

where a^* is the plate side length, m and n are modal coordinates, $A_{m,n}$ is a mode-dependent amplitude and $\epsilon_m, \epsilon_n, \alpha_m,$ and α_n are the eigenfunction parameters. For the case of an all clamped plate, the values of the parameters can be found in Leissa (1969).

3.4 Wavelet synchrosqueezed transform (WSST)

In this thesis, the recorded signals are analyzed in time and frequency domains separately. Additionally, a time-frequency (TF) method called the wavelet synchrosqueezed transform (WSST) is used, which is an improved version of the continuous wavelet transform (CWI) that eliminates smearing observed around the frequency values on time-frequency graphs. It is assumed that multi-component acoustic signals can be represented as a linear combination of amplitude and phase-modulated components called intrinsic mode functions (IMF) (Daubechies et al., 2017):

$$x(t) = \sum_{k=1}^{K} x_k(t) + \eta(t) \quad (3\text{-}36)$$

where $\eta(t)$ represents the error of modelling. Each IMF is defined as:

$$x_k(t) = A_k(t)\cos\left(\phi_k(t)\right) \quad (3\text{-}37)$$

where $A_k(t)$ and $\phi_k(t)$ are instantaneous amplitude and phase. The instantaneous frequency can be calculated as: $f_k(t) = {d\phi_k(t)}/{2\pi dt}$. In the first step of the WSST, wavelet coefficients are calculated $W_x(a,b)$, where a is the scale parameter (responsible for stretching of the wavelet), b is the time offset, and ψ^* denotes a complex conjugate of the selected mother wavelet.

$$W_\psi x(a,b) = \frac{1}{\sqrt{a}}\int x(t)\psi^*\left(\frac{t-b}{a}\right)dt \quad (3\text{-}38)$$

The common choice of wavelet for acoustic applications is the Morlet wavelet defined as (Büssow, 2007; Daubechies, 1992; Torrence & Campo, 1998):

$$\psi(t) = \pi^{-1/4} e^{i2\pi f_0 t} e^{-t^2/2} \quad (3\text{-}39)$$

where t represents nondimensional time and f_0 is the nondimensional centre frequency of the mother wavelet. The centre frequency is often selected, so the ratio between the highest and the second-highest peaks of ψ is $1/2$. In the literature, approximate values of $f_0 = 5/2\pi$ (Daubechies, 1992) and $f_0 = 6/2\pi$ (Torrence & Campo, 1998) can be found. The Morlet wavelet embedded in the wavelet toolbox in Matlab uses the first value. To overcome the smearing effects happening on the frequency axis, the reassignment along this axis is done. For each point (a, b) an instantaneous frequency $\omega_x(a, b)$ is computed by

$$\omega_x(a,b) = -i\big(W_x(a,b)\big)^{-1} \frac{\partial}{\partial b} W_x(a,b). \tag{3-40}$$

Then, the time-scale plane is mapped $[(b,a) \rightarrow (b, \omega_x(a,b))]$ to the time-frequency with an operation called synchrosqueezing. The synchrosqueezing transform $T_x(\omega_l, b)$ is given by

$$T_x(\omega_l, b) = (\Delta\omega)^{-1} \sum_{a_k : |\omega(a_k,b) - \omega_l| \le \Delta\omega/2} W_x(a_k, b)\, {a_k}^{-3/2} (\Delta a)_k \tag{3-41}$$

where a_k are discrete values of the scale, $(\Delta a)_k = a_k - a_{k-1}$, frequencies ω_l are centres of the bins $[\omega_l - \frac{1}{2}\Delta\omega, \omega_l + \frac{1}{2}\Delta\omega]$ and $\Delta\omega = \omega_l - \omega_{l-1}$.

For the multi-component signals, the signal components are well separated in the time-frequency domain if the following inequality is satisfied (Daubechies et al., 2011):

$$|\omega_k - \omega_{k-1}| \ge d[\omega_k + \omega_{k-1}], \tag{3-42}$$

where ω is the instantaneous frequency of two consecutive components ($k-1$ and k), and d is a positive separation constant. For the Morlet wavelet, the value of $d = 0.2$ can be used. If the individual components are well-separated, they can be estimated by inverting the synchrosqueezing transform:

$$x_i(t) = \Re e\left(C_\psi^{-1} \sum_l T_x(\omega_l, b) \right) \tag{3-43}$$

where $\Re e(.)$ defines the real part of the function and the C_ψ is the normalization constant.

The experimental signals are time series of a finite length; therefore, the discontinuities at the endpoints of the signals exist and affect the transform. The wavelets, when translated over the endpoints, extend outside the boundary. The cone of influence (COI) describes a region in which the effect is significant, and amplitude cannot be represented reliably (Nobach et al., 2007). The COI can be estimated as (Torrence & Campo, 1998):

$$COI = \sqrt{2} \cdot a = \sqrt{2} \cdot {}^{f_0}/_{f} \tag{3-44}$$

where f_0 is a wavelet's centre frequency, f is a frequency, and the angular frequency and frequency are related as $\omega = 2\pi f$. In this study, the WSST methodology implemented in the synchrosqueezing toolbox in Matlab is used (with Morlet wavelet). More explanation of the WSST technique can be found in Daubechies et al. (2011) and Thakur et al. (2013).

3.4.1 WSST and other TF techniques

There are many approaches for the analysis of non-stationary signals. These methods include the short-time Fourier transform (STFT), the continuous wavelet transform (CWT), the Wigner-Ville distribution (WVD, and other quadratic distributions), or Hilbert-Huang transform (HHT) (Bouchikhi et al., 2011). The STFT divides the signal into time segments and then computes the spectrum of each segment. The length of the selected window determines the resolution in time and frequency of the representation. The selected resolution is constant over the whole TF-plane. In the CWT, the analyzed signal is convoluted with shifted and scaled versions of the selected mother wavelet. Therefore, the time-frequency resolution varies over the TF-plane. Both techniques are linear and fall short for the analysis of non-linear signals (e.g. quadratic chirp). A possible improvement of the TF representation can be obtained with the WVD, which offers high-resolution representation in both time and frequency for non-stationary signals (Pachori & Nishad, 2016). However, the WVD is quadratic and generates cross-terms (if analyzed signal consists of more than one mono-component or in case of nonlinear frequency modulation), which can lead to incorrect analysis of the results (Ghofrani & McLernnon, 2008; Pachori & Nishad, 2016). Another non-linear technique is the HHT, which is based on the signal decomposition into a sum of amplitude and frequency modulated sine waves and extraction of instantaneous amplitudes and frequencies using the demodulation technique (such as Hilbert transform). The results of the HHT are displayed for each sine wave instead of the TF-plane (Bouchikhi et al., 2011).

Improvements in TF resolution can also be obtained through synchro-squeezing of transforms (squeezed-STFT, WSST (Daubechies et al., 2011)). The synchrosqueezeing of the existing transform is performed based on the examination of local oscillations with respect to time and re-allocation of each value of the original transform to a new frequency on the TF plane (Mihalec et al., 2016). The benefit of WSST is offered through the combination of the advantages of CWT (improved resolution over STFT) and sharpening provided by synchrosqueezing. Figure 3-2 presents a comparison of WVD, CWT, and WSST results for the signal composed of a 200 Hz sinusoid (sampled at 1kHz for 1.5

seconds) and a chirp whose frequency varies sinusoidally between 250 and 450 Hz. For CWT and WSST, the Bump wavelet implemented in Matlab is used.

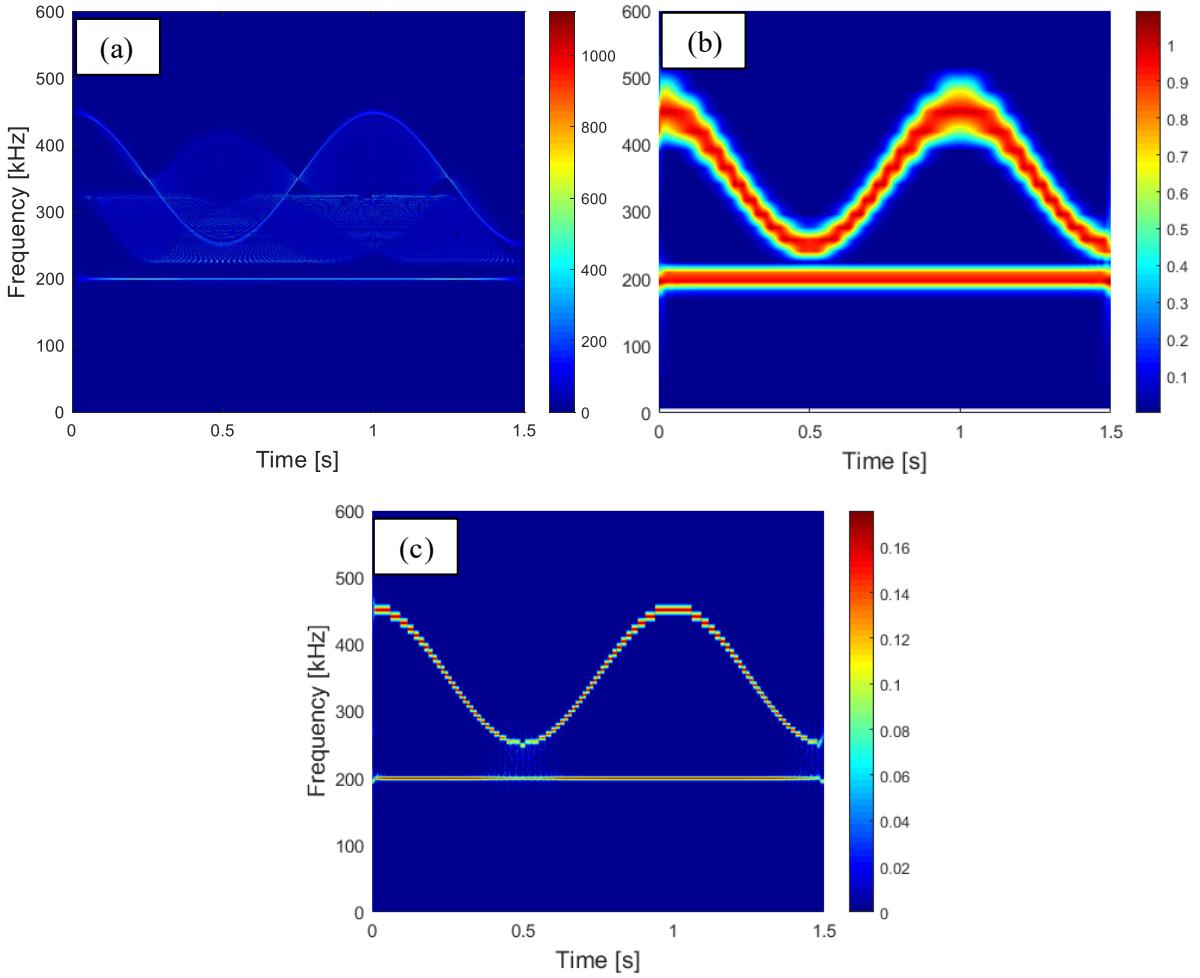

Figure 3-2. Comparison of different TF techniques: (a) Wigner-Ville distribution, (b) continuous wavelet transform, and (c) wavelet synchrosqueezed transform

It can be concluded that the resolution of the WVD graph is the highest; however, the artifacts present around the chirp signal make an interpretation of the results difficult. When WSST and CWT results are compared, the benefit of synchrosqueezed is evident.

In this thesis, the extraction of modes is done by the selection of ridges on the TF-plane obtained with the WSST. However, if the modes are separated well-enough, the extraction is also possible from

the traditional CWT and selection of the ridge (Ghofrani & McLernnon, 2008). Therefore, the conclusions of the work presented in the thesis are not so much dependent on the use of WSST.

3.5 Normalization

The results presented herein are normalized using two normalization approaches. The measurements taken for a group of points (e.g. a scan of a transducer diameter) can be stacked in an array M. In the global normalization, the maximum value for the whole matrix (Figure 3-3-a) is found, and the signals are normalized with respect to that value. The global normalization shows the overall behaviour of the signals. The vectors in the array M can also be normalized with respect to the maximum values of each vector (Figure 3-3-b). In such a situation, a term self-normalization is used. This approach allows analyzing all of the local effects in the matrix at the same time.

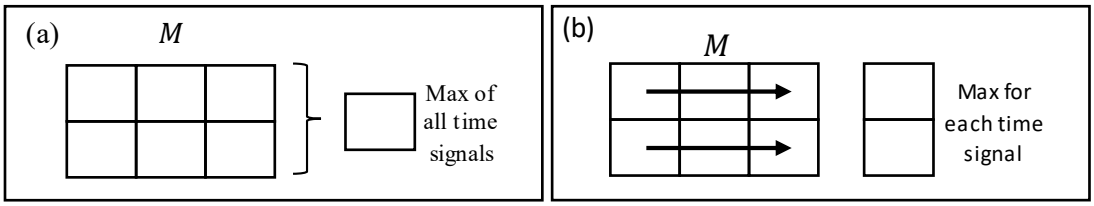

Figure 3-3. Maximum value of an array calculation: (a) global normalization and (b) self-normalization.

3.6 Damage indicators

In the application sections of this thesis, specimens in different conditions are compared. Therefore, damage assessment indices, giving a quantitate meaning are needed. For a comparison of time signals, a residual signal (x_R) is defined as a difference between the reference signal (x_{ref}) and the signal of interest (x): $x_R = x_{ref} - x$. Assuming specimens in different conditions, three additional indices are used. First, spectral areas are compared for each condition individually, and relative energy (RE) is defined as:

$$RE = 100 * {}^{E_i}/_{E_{INT-MAX}} \tag{3-45}$$

where E_i is the spectral energy for the i-th location (considered separately for both condition), and $E_{INT-MAX}$ is the spectral energy calculated for the intact condition at the location in the array that gives the maximum value, and each time the spectral energy (E_{f1f2}) is calculated as:

$$E_{f1f2} = \sum_{f1}^{f2} |X(k)|^2 \tag{3-46}$$

where $|X(k)|$ is the modulus of the FFT of the discrete time-signal x. The spectral energy is defined in the bandwidth from $f1$ to 2 , defined as a frequency in kHz. The bandwidth is selected based on individual test needs. For comparison purposes, bandwidth must consist of an equal number of samples.

The RE indicator measures how the total spectral energy changes along the beam, for each condition separately, with respect to the maximum value of the intact beam.

Additionally, the relative attenuation index (RAI) is introduced. It measures a percentage difference of the total energies measured for two different material conditions with respect to the initial condition. The relative attenuation at each location is calculated as such:

$$RAI = 100 * {(E_{INT} - E_{DAM})}/{E_{INT}} \tag{3-47}$$

where E_{INT} and E_{DAM} are total signal energies computed for the initial and damaged conditions based on frequency spectra for each individual location.

Finally, for the dispersion curves analysis, relative dispersion index (RDI) is used:

$$RDI = 100 * {\left|\sum {V_{PH-INT}}^2(f) - \sum {V_{PH-DAM}}^2(f)\right|}/{\sum {V_{PH-INT}}^2(f)} \tag{3-48}$$

where V_{PH-INT} and V_{PH-DAM} are phase velocities, and f denotes a frequency range of interest.

Chapter 4
Characterization of ultrasonic transducers using laser Doppler interferometer in kHz-range for civil engineering applications

4.1 Introduction

The condition of structural materials in civil engineering applications is critical for the safety of structures. The most popular ultrasonic non-destructive techniques (NDT) used for the evaluation of the material's condition are based on wave velocity and use piezoelectric transducers for both emission and reception of ultrasonic waves (ASTM International, 2020). A piezoelectric element in a transducer converts electrical energy into mechanical energy (motion) and vice-versa. Thus, transducers can be operated both as transmitters and receivers of ultrasonic waves (Schmerr, Lester W. & Song, 2007). The conventional NDT methods are focused on velocity; therefore, neither the frequency content of the response nor the frequency characteristics of the transmitter signal to a tested material is usually utilized. However, it has been shown that this can lead to misinterpretation of ultrasonic data (Wiciak et al., 2020).

To overcome the fact that the wave velocity methods are not sensitive in early damage detection (when damage is relatively small) (Stauffer et al., 2005), the latest trends in NDT evaluations focus more on the attenuation of a wavefront for both a longitudinal wave (P-wave) and a surface wave (Chaix et al., 2006; Kirlangic et al., 2015; 2016; Philippidis & Aggelis, 2005). Another approach includes more sensitive methods for detecting small changes in the velocity, such as coda wave interferometry (Dai et al., 2013; Planès & Larose, 2013; Snieder, 2006). Ultrasonic non-linear methods, such as non-linear elastic wave spectroscopy or non-linear impact resonance acoustic spectroscopy, have been shown to be very sensitive to microstructural changes (Bittner & Popovics, 2019; Eiras et al., 2014; Eiras et al., 2016; Eiras et al., 2018). Often, attenuation-based techniques need proper identification of a frequency content transferred to a tested material. Moreover, the efficiency of the detection and the proper localization of a defect in the tested medium, based on traditional methods, is affected by the insufficient knowledge of the ultrasonic beam characteristics (Moss & Scruby, 1988). Therefore, the characterization procedure for transducers used in the condition assessment plays a key role in the non-destructive evaluation process.

A need for characterization of ultrasonic transducers has been acknowledged in the past and a variety of application fields. The American Institute of Ultrasound in Medicine (AIUM) expressed a need for

characterization of pulse-echo transducers in 1977 (Erikson, 1979a). The AIUM identified the special need for the ways of describing parameters, including frequency response, sensitivity, and characteristics of a beam profile and the reflected waveform. Erikson (1979b) proposed a calibration procedure based on a tone-burst test in which a transducer is submerged in water and operates in a pulse-echo mode. The generated pulse (in a range of 1-4 MHz) was reflected from stainless steel, and a relative sensitivity was obtained (the amplitudes are measured as voltage). Papadakis (1979) stated that the centre frequency of an ultrasonic transducer was usually lower than the resonance frequency of the piezoelectric element. He also summarized experimental methods (used for transducers with a centre frequency of 10 – 15 MHz) used for characterization of the spatial distribution of pressure amplitude (including optical methods; e.g. photoelastic method) and the transducer surface motion (evaluated with a scanning electron microscope). Miller and Eitzen (1979) presented characterization methods developed at the National Bureau of Standards for ultrasonic transducers used typically in medical applications (with central frequency in the range from 0.5 to 30 MHz). The procedures considered a probe in a water tank (to simulate the nature of human tissue), and the authors concluded that the methods did not satisfy the full characterization need for pulse-echo ultrasonic transducers. Chivers (1986) used hydrophones for the characterization of an ultrasonic transmitter (a 7.5 MHz-transducer placed in a distilled water-filled tank) and a time-delay spectrometry method. In the method, the excitation frequency of the transmitter was swept linearly in time. Additionally, the central frequency of the filter applied to the measured signal was modified adequately. It was assumed that the hydrophone operated in a linear range (as the hydrophone was not calibrated in absolute terms). Moss and Scruby (1988) investigated ultrasonic transducers using a laser interferometer. Typical ultrasonic transducers (2.25, 4, and 10 MHz transducers were placed on wedges of 30, 45 and 60°) used for metallic surfaces were coupled to aluminum test blocks. This approach had a benefit of transducers experiencing real-life coupling conditions. The response beam was measured on the opposite side of the test-block. The authors stated that the main strength of the laser calibration was due to the non-contact nature of measurements and the very localized reception area (i.e. a point). In 1985, efforts of Erikson, Papadakis, Miller, and others were put together by the ASTM in the form of standard practice for evaluating characteristics of ultrasonic transducers (ASTM International, 2014b), which was based on tests performed in a water-filled tank on high-frequency transducers (0.5 MHz and higher centre frequencies). Wang et al. (1992) proposed an automated characterization station with a motorized transducer holder. Signal processing techniques, including neural network and pattern recognition techniques, were also applied for the characterization of ultrasonic transducers for one-dimensional

signals such as impulse responses of transducers (Obaidat & Abu-Saymeh, 1992; 1998). More recent research is focusing on modelling and determining the key components (such as electrical impedance, sensitivity, acoustic radiation impedance, etc.) of ultrasonic transducers on an overall response (Canney et al., 2008; Fei et al., 2019; Schmerr, L. W. et al., 2006; Wolf et al., 2008).

However, not much work has been done for the characterization practices for low-frequency transducers (with the resonant frequency lower than 500 kHz), which are typically used in the evaluation of structural materials. Tallavo et al. (2011) estimated frequency response function (FRF) for ultrasonic transducers with the nominal resonant frequency of 50 kHz and compared responses measured with accelerometers and ultrasonic transducer of the same type. The most recent characterization attempts that can be applied to civil applications are based on the use of laser vibrometers. Kirlangic et al. (2017) used a laser vibrometer for the estimation of FRFs of accelerometers used beyond the nominal frequency range. Mahbaz et al. (2019) compared responses of 1 MHz transducers measured with face-to-face configuration and laser vibrometer scans and computed frequency response function. Then, experimental results were reproduced in numerical simulation. Feeney et al. (Feeney et al., 2019; Feeney, Kang, Somerset et al., 2019) compared responses of flexural ultrasonic transducer (focusing on maximum displacement observed in the wear plate) measured with laser vibrometer with solutions of the differential equation for a thin plate, which represents vibration observed in a transducer membrane.

Existing research described above is beneficial for the characterization of low-frequency transducers; however, it does not focus on the frequency content that is generated and transferred to a tested material. This is fundamental information from the highly attenuative structural material standpoint, as different frequency components will be affected differently by the material flaws and the internal structure of tested material. An important gap in knowledge is related to the transducer's wearing plate, which is a plate at the front surface of a transducer. The plate is designed to provide matching acoustic impedance with the tested material (Brisken & Smith, 1980). The wear plate should: (i) assure maximum transmission of ultrasound and do not change the shape of the wave-form pulse and (ii) prevent damage to the piezo crystal. Previous work does not address if the whole wear surface contributes equally to the overall frequency content and the effect of a solid medium (and coupling condition) on the response of the transmitter.

This research bridges the described gap and is focused on identifying the key sectors of a contact surface of P-wave ultrasonic transducers used typically in the evaluation of structural materials (with

the resonant frequencies of 54, 150, and 250 kHz) and associating the effect of these sectors on overall frequency response. The effect of the coupling with tested material is also investigated. Finally, the applicability of a glass-block sample for the characterization of ultrasonic transducers in the reception mode is investigated.

The methodology includes characterization performed with the state-of-the-art laser Doppler vibrometer. First, the response of the transmitter is measured through the air and compared with the analytical solution of a thin vibrating plate. Next, the critical sectors along the transducer diameter are defined, and the effect of location within the transducer surface on the frequency content is discussed. The test is repeated for the 250-kHz transducer when coupled with a glass-block. The characterization with a piece of glass offers similar acoustic parameters to concrete with an advantage of transparency, which allows for the investigation with the laser vibrometer. Finally, the response is measured at the top of the glass block. The received beam pattern is compared with the beam generated by the transmitter, and the boundary effects are examined. The applicability and limitations of the setup are discussed regarding the characterization of ultrasonic receivers. Finally, the findings of this study are put to the test in two civil engineering NDT applications. In the first application, the authors show how the knowledge of characterized transducers improves the analysis of frequency content in the ultrasonic evaluation of concrete specimens, and how the frequency content is affected in this highly attenuative material. In the second application, the authors use the information about the frequency content sent to the tested concrete beams in two conditions to select the most sensitive ultrasonic features. This allows for a 24% relative improvement in the accuracy of the proposed methodology.

4.2 Theoretical background

Two methods are used for a comparison of time signals. Firstly, a residual signal (x_R) is defined as a difference between the reference signal (x_{ref}) and the signal of interest (x): $x_R = x_{ref} - x$. Additionally, a correlation coefficient (*CC*) between the two signals is calculated as:

$$CC(x_1,x_2) = \frac{1}{N-1}\sum_{i=1}^{N}\left(\frac{x_1-\mu_1}{\sigma_1}\right)\left(\frac{x_2-\mu_2}{\sigma_2}\right), \tag{4-1}$$

where $\mu_{1,2}$ and $\sigma_{1,2}$ are the mean and standard deviation of signals x_1 and x_2.

4.3 Characterization procedure and setup

The following section provides details on the proposed characterization methodology, tested ultrasonic transducers and describes the laboratory setups. Details of the signal processing techniques are also given.

4.3.1 Methodology

A transducer characterization procedure designed in this study focuses on answering the three fundamental questions: (i) what signal a transmitter sends, in the sense of the frequency content, (ii) how a solid medium affects the transmitted signal (i.e. how the vibration of the wear face of the transmitter is affected), and (iii) what is the characteristic of the signal arriving at a reception point (i.e. what a receiver measures). Table 4-1 presents each activity of the proposed methodology, refers to sections with the individual results, shows a flow chart of the procedure used, and gives the main conclusions.

Table 4-1. Methodology and flow chart of data processing. Tx denotes a transmitter.

Activity	Flow chart	Main conclusions
What is sent: through-the-air setup (Section 4.4.1)	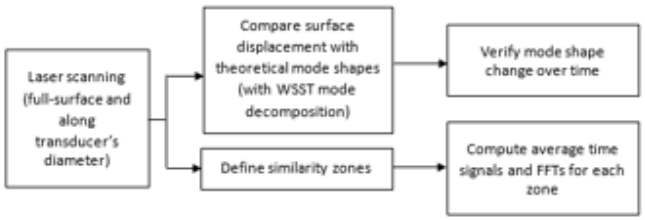	• The surface responses consist of resonances of piezo-crystal and wearing-plate itself • Different sections of wear-face contribute differently to the overall response • It is critical to ensure constant coupling area and quality
Effect of interference between a transmitter and the tested medium (Tx = 250 kHz) (Section 4.4.2)	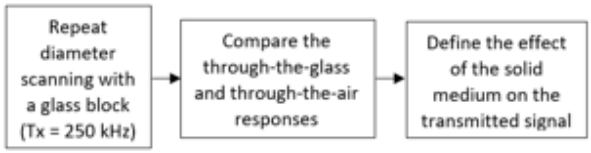	• Glass block does not affect the nominal frequency frequency-wise • Frequency content is modified in the below 100 kHz range – important for applications in concrete
Top of the glass-block vibration: what a receiver senses (Section 4.4.3)	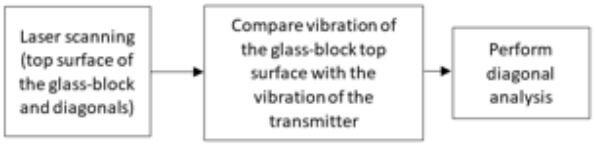	• Top glass surface vibration is quickly affected by the boundary effects • Precise windowing is required for the future characterization of receivers
Application 1: Improvement in a proper interpretation of ultrasonic data (Section 4.5.1)	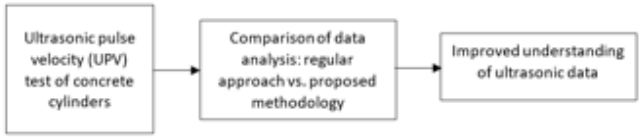	• Characterization enables for the identification of the frequency content of responses • If the characterization and frequency analysis is not followed, interpretation of ultrasonic data might be inaccurate
Application 2: Condition assessment of concrete: early damage detection (Section 4.5.2)	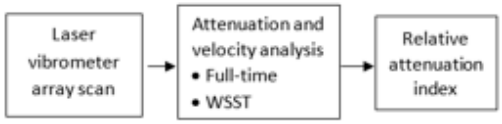	• Characterization provides a rationale for mode decomposition and analysis of waves in individual wavelengths • Up to 24% of improvement due to the application of the characterization based approach

To answer the first question, wear surfaces of three ultrasonic transducers (54, 150, and 250 kHz P-wave transducers from Proceq) are scanned with the laser Doppler vibrometer (Figure 4-1-a). The measured surface displacement is verified with the theoretical mode shapes observed in thin plates (Equation 3-35). A complex response, occurring for the first oscillation, is studied with the WSST technique. Next, the vibration for different points along the transducer diameter is compared, and the

similarity zones are defined. The zone analysis allows us to find out how the frequency content of the multi-component response signal is affected depending on the position on the wear-face. This is a critical consideration for the practical aspect of how a transducer should be coupled.

The second problem is addressed with the application of the glass-block and 250 kHz transducer (Figure 4-1-b). The application of the transparent material allows for the laser scanning and reveals how the vibration of the wear-face is affected by the coupling with the solid medium, which is usually impossible to measure with non-transparent construction materials like concrete. The wear surface is scanned anew and is compared with the previous scan obtained with the through-air configuration. The differences observed in both setups are presented in time and frequency domains. Moreover, the WSST is used to show how each frequency component behaves over time for both setups.

The top surface of the glass block is examined to answer the third question. The section of the top surface, laying directly on top of the transmitter, is compared with the vibration of the wear-surface. The boundary-related patterns are additionally studied with the analysis of the vibration along the top surface diagonals (Figure 4-1-c). The measured responses suggest that the signals that would normally be measured with a receiver are very quickly affected by the boundary effects, which implies that the portion of the signal used for the characterization of an ultrasonic receiver should be very limited.

Finally, the benefits of the proposed characterization procedure are given in section 4.5, based on two lab-scale applications. In the first application, ultrasonic pulse velocity results of concrete cylinders of different lengths are analyzed. An evaluation is first performed using the wave velocity approach (only the nominal frequency is assumed in the transmitted signal), and next, it is enriched with the proposed characterization procedure. Conclusions coming from both approaches are given and compared.

The second application considers a condition assessment problem. Concrete beams in two conditions (intact and damaged through the freeze-thaw cycles) are tested from the surface with the laser vibrometer. The frequency content of the measured responses is explained with the matching transducer profile obtained with the characterization procedure. The characterization provides a strong justification for the application of the mode decomposition technique (i.e. WSST) and analysis of individual components. The proposed approach is compared with the evaluation without prior knowledge of the transmitted signal.

4.3.2 Ultrasonic transducers and laboratory setup

Three ultrasonic transducers in the transmission mode are examined in this study. This study focuses on the transducers typically used in the evaluation of civil engineering materials. Therefore, 54-kHz transducer (Proceq, P-wave transducer; which belongs to the recommended range of resonant frequencies, i.e. 20-100kHz, by the ASTM for the evaluation of concrete (ASTM International, 2016a)). Additionally, transducers with nominal frequencies of 150 and 250 kHz (Proceq, P-wave transducers) are tested. These frequencies correspond to shorter wavelengths and allow for the detection of smaller defects. The characterization is performed with the state-of-the-art Doppler laser vibrometer. The signals are read with a laser sensor head (LSH, Polytec OFV-534), which is connected to the vibration controller (OFV-2570), and finally stored in a computer. The laser vibrometer in the displacement mode can measure vibration amplitudes in a frequency range of 30 kHz – 24 MHz (bandwidth) and pulse amplitudes up to 150 nm (peak to peak). The measurement range is 50 nm/V

The laser technology has the benefit of being contactless (therefore, all coupling effects are eliminated), and has a flat frequency response in the frequency range used in this study. The resolution is less than $50\,{}^{fm}\!/_{\sqrt{Hz}}$, where *fm* corresponds to femtometre ($1x10^{-15}$ m), the recorded signals are sampled at the rate of 25 MHz.

In section 4.4.1, the responses for all transducers are measured through the air using setup 1 – configuration 1 (shown in Figure 4-1-a). A function generator (HP33120A) is used to provide a different input signal (54, 150, and 250 kHz square pulses) to the transmitter. Grids of measurement points are presented in Figure 4-2. For the 54-kHz transducer (50 mm diameter), responses are measured at 45 positions distributed evenly (with a 1mm spacing) along its diameter (shown in Figure 4-2-a). The smaller diameter (25 mm) of 150 and 250-kHz transducers implied a modification in the scanning grid. Thus, the modified spacing of 0.5 mm is used for the scan along the diameter, resulting in 40 measuring points. Moreover, the full surface scans are performed for all of the transducers and the sample grid used for scanning of 150 and 250 kHz transducers is shown in Figure 4-2-b (a set of 12 concentric circles with a minimum radius of 1 mm and increasing with 1 mm interval. A total of 24 points are recorded per circle).

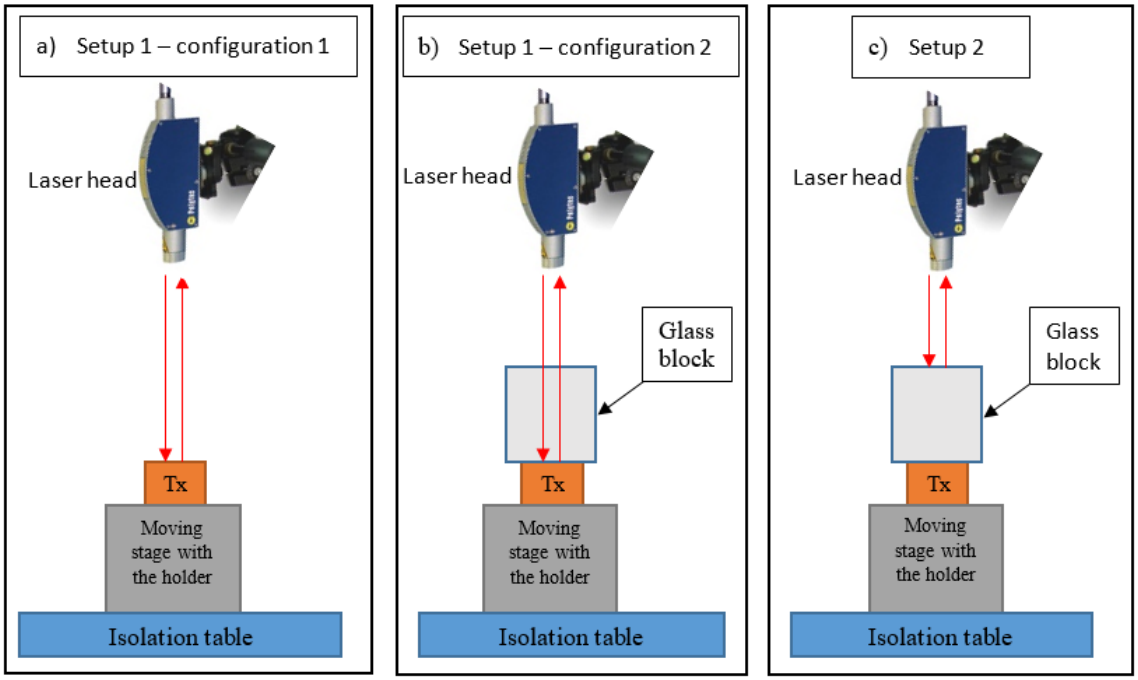

Figure 4-1. Transducer characterization setups: (a) through-the-air setup used for the evaluation of wear surface, (b) wear surface evaluation with the addition of the glass block, (c) setup for the evaluation of the displacement of the top of the glass block.

Next, a glass block is added to setup 1, resulting in setup 1-configuration 2 shown in Figure 4-1-b. In this configuration, the glass block (K9/BK7) with an 80 mm square cross-section and a height of 130 mm is used. The glass is transparent and allows the laser beam to penetrate through it and measure the response of the transmitter in contact with the medium. The acoustical impedance of glass is similar to concrete ($Z_{K9} = 14.2\text{x}10^5$, $Z_{CONCRETE} = 10.4\text{x}10^5$ $[g/cm^2 s]$). Therefore, the behaviour observed in the test is expected to be similar when the transducer is used in applications with concrete specimens. Due to the expected wavelengths (assuming a P-wave velocity of 5100 $\frac{m}{s}$ and nominal frequencies for the transducers, one can calculate the wavelengths: $\lambda_{54} = 92, \lambda_{150} = 33, \text{and } \lambda_{250} = 20\ mm$) and physical dimensions of the glass, only the 250 kHz transducer gives a ratio of more than four wavelengths per length. Therefore, the effect of contact between transducer and medium is only studied based on 250 kHz transducer. In the through-the-glass configuration, the responses are measured along transducer diameter.

Additionally, the applicability of a glass-block sample for the characterization of ultrasonic receivers is investigated by the surface scan covering the same area as the transducer wear face top of the glass

block (setup 2, Figure 4-1-c). Finally, responses are also measured on top of the glass block along the two diagonal lines (111 points are recorded with 1 mm spacing, Figure 4-2-c).

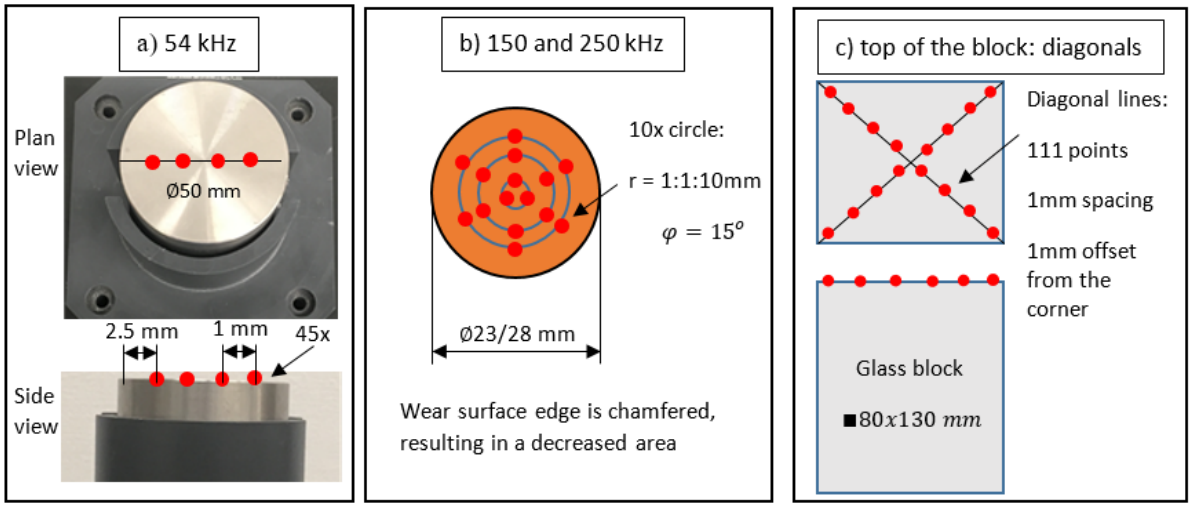

Figure 4-2. Measurement grids used for laser data acquisition: (a) linear grid used for 54 kHz transducer, (b) polar grid used for 150 and 250 kHz transducers, and (c) diagonal lines used for the response of the top of the glass block.

4.4 Characterization results

4.4.1 What is sent: through-the-air setup

In the first group of tests, responses of ultrasonic transducers are measured through the air to investigate what a transducer sends. The readings are taken using two types of measurement grids: (a) along a diameter of the transmitter and (b) using a circular grid (presented in Figure 4-2), enabling a scan of a whole wear surface. Responses measured with the laser vibrometer are compared with the first six theoretical mode shapes of thin all-fixed square plates (calculated based on Equation 3-35). It is assumed that 10% of the plate side length is used as fixed support. Next, the frequency content dependency with a position of the measurement point is investigated.

4.4.1.1 Comparison to analytical mode shapes

A typical response measured at the centre of the 54 kHz transducer, along with the excitation pulse, is shown in Figure 4-3. The time steps associated with the first three peaks observed in the response signal are selected for the comparison between the diameter's displacement shape and the theoretical mode

shapes. The first peak occurs during the active phase of the excitation pulse (forced vibration), while the two other peaks are present through the passive phase (damped response).

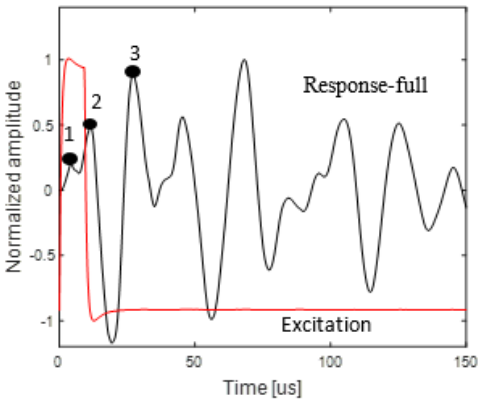

Figure 4-3. Time signal measured at the centre of 54 kHz transducer: the excitation pulse (red line) and the response (black). Black dots highlight three displacement peaks picked for detailed analysis: (a) t1 = 4.3 µs, (b) t2 = 11.52 µs, and (c) t3 = 27.15 µs.

Figure 4-4 presents a comparison between the displacements measured along transducer diameter (for three selected time-steps) and best matching theoretical mode shapes. The shape observed for the first peak (Figure 4-4-a) has a complex form and is a combination of mode shapes found in thin plates. However, once the excitation pulse turns into the passive phase, the damped response goes through the mode 5 (Figure 4-4-b) and finally vibrates with mode 1 (Figure 4-4-c).

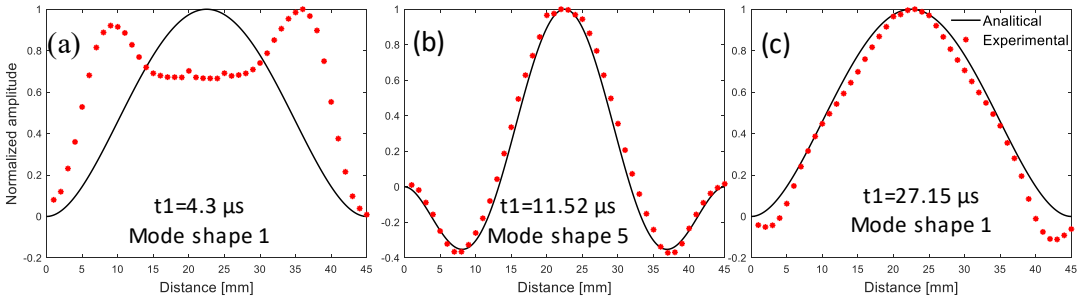

Figure 4-4. Comparison of analytical mode shapes and measured surface displacement along 54 kHz transducer diameter: (a) t1 = 4.3 µs, (b) t2 = 11.52 µs, and (c) t3 = 27.15 µs.

The surface displacement presented in Figure 4-4-a is further studied with the WSST technique, which enables the decomposition of a complex signal into its components and then analyzes the individual components separately. Instantaneous frequencies are calculated for each measuring location, and a sample time-frequency representation for the centre of the 54-kHz transducer is

presented in Figure 4-5-a. Based on the strongest frequency ridges observed in the time-frequency plots, two modes are selected. The first mode (mode 30) represents the ridge seen around 30 kHz. The second ridge corresponds to the driving frequency of 54 kHz (mode 50).

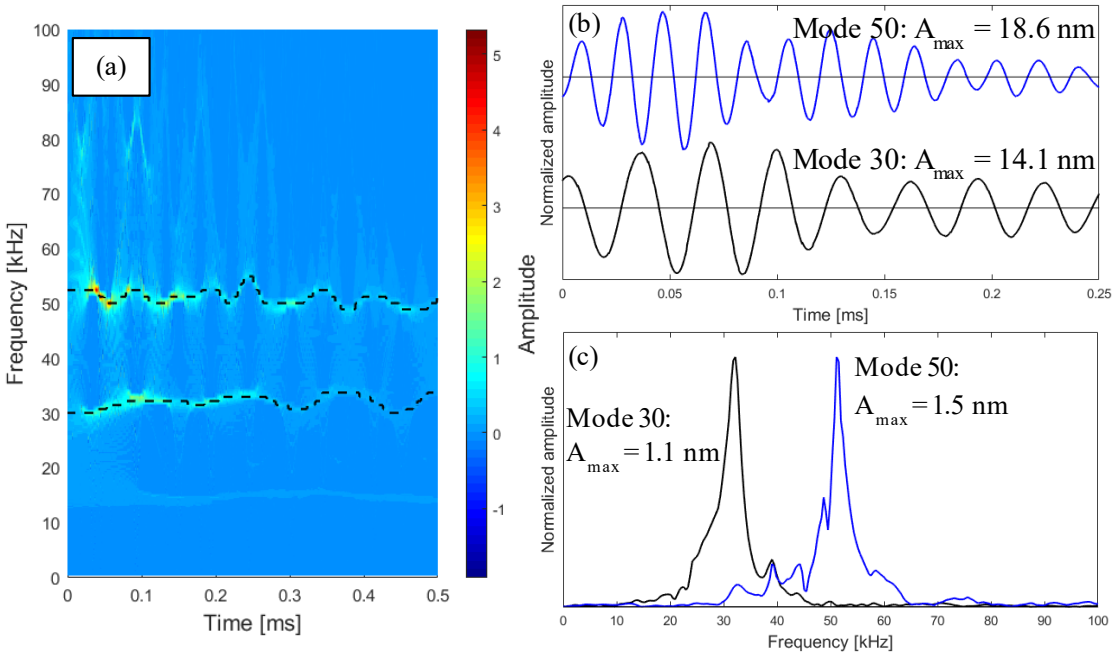

Figure 4-5. WSST analysis of the signal recorded at the centre of the 54 kHz transducer: (a) instantaneous frequencies estimated with WSST; Black-dashed lines highlight the frequencies selected for signal reconstruction, and the reconstructed signals (b) time signals: mode 30-kHz (black) and mode 50-kHz (blue), and (c) corresponding Fourier spectra. Amplitudes are self-normalized for all signals in (b) and (c).

The sample reconstructed signals are presented in the time (Figure 4-5-b) and frequency (Figure 4-5-c) domains. The two main frequencies seen in Figure 4-5-a are now well represented in two separate signals and can be analyzed individually. This separation is critical from an ultrasonic test standpoint, as the individual mode represents a unique wavelength that penetrates a material. Therefore, the mode signals will consist of different information about the tested material due to different propagation depths, attenuation effects, or the ratio between wavelengths and specimen dimensions and aggregates/defects (which has been shown to play a significant role in the interpretation of ultrasonic

data, (Wiciak et al., 2020)). The reconstruction process is performed for all points along the diameter of the transmitter.

The mode decomposition with the WSST (Figure 4-6) enables the identification that the overall surface displacement presented in Figure 4-4-a is generated not only by the resonance of piezoelectric crystal (i.e. mode 50, mode shape 4) but also by the resonance of the surface-wearing plate of the transducer itself (i.e. mode 30, mode shape 1). The contribution of the surface displacement due to the plate vibration is significant, and the maximum displacement ratio between mode 50 and mode 30 is 0.75. This leads to the conclusion that (i) the construction of the sensor should be revisited by the manufacturer and modified, so the resonant frequency of the piezo element matches the resonance of the plate, and (ii) from the point of view of the transducer user, the plate resonant frequency has to be taken into account in the NDT evaluation. The provided analysis also gives a physical meaning to the modes extracted with the WSST.

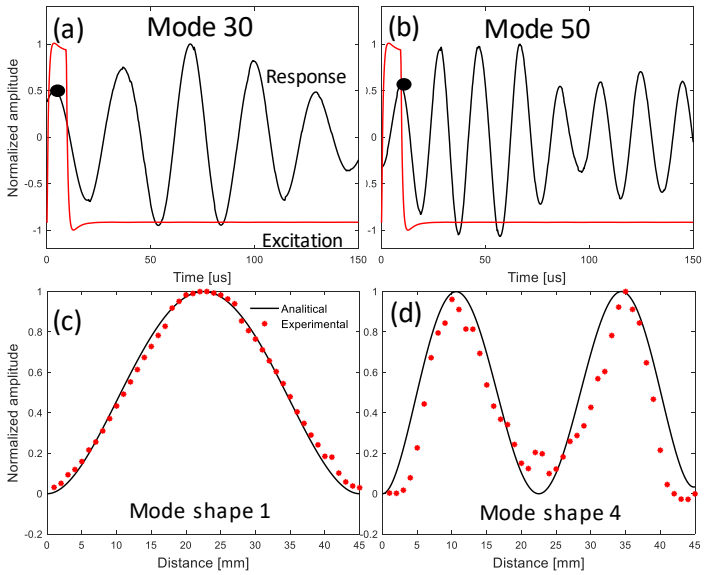

Figure 4-6. Reconstructed time signal of (a) mode 30 and (b) mode 50 measured at the centre of the 54-kHz transducer and the comparison of analytical mode shapes and measured surface displacements along transducer diameter for (c) mode 30 and (d) mode 50, observed for the first maximum displacement.

The same process is repeated for 150 and 250-kHz transducers. Figure 4-7 shows a measured displacement at the centre of the 150-kHz transducer. The first maximum displacement occurs after the excitation signal turns off. However, an additional time step, at the moment of active excitation, is also considered.

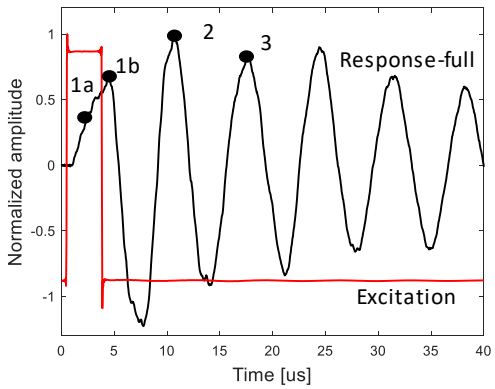

Figure 4-7. Time signal measured at the centre of 150 kHz transducer: the excitation pulse (red), and the response (black). Black dots highlight four time steps picked for detailed analysis: (a) t = 2.89 µs, (b) t = 4.45 µs, (c) t = 10.7 µs, and (d) t = 17.62 µs.

Surface displacement along the diameter, at four time-steps selected based on Figure 4-7, is shown in Figure 4-8. During the active excitation phase, the effect of mode superposition is not as significant as in 54-kHz transducer. The subsequent displacement peaks follow the mode 1 mode shape. Therefore, the 150-kHz transducer presents a simpler response character that does not go through different mode shapes and is considered as much better design than the 54-kHz transducer.

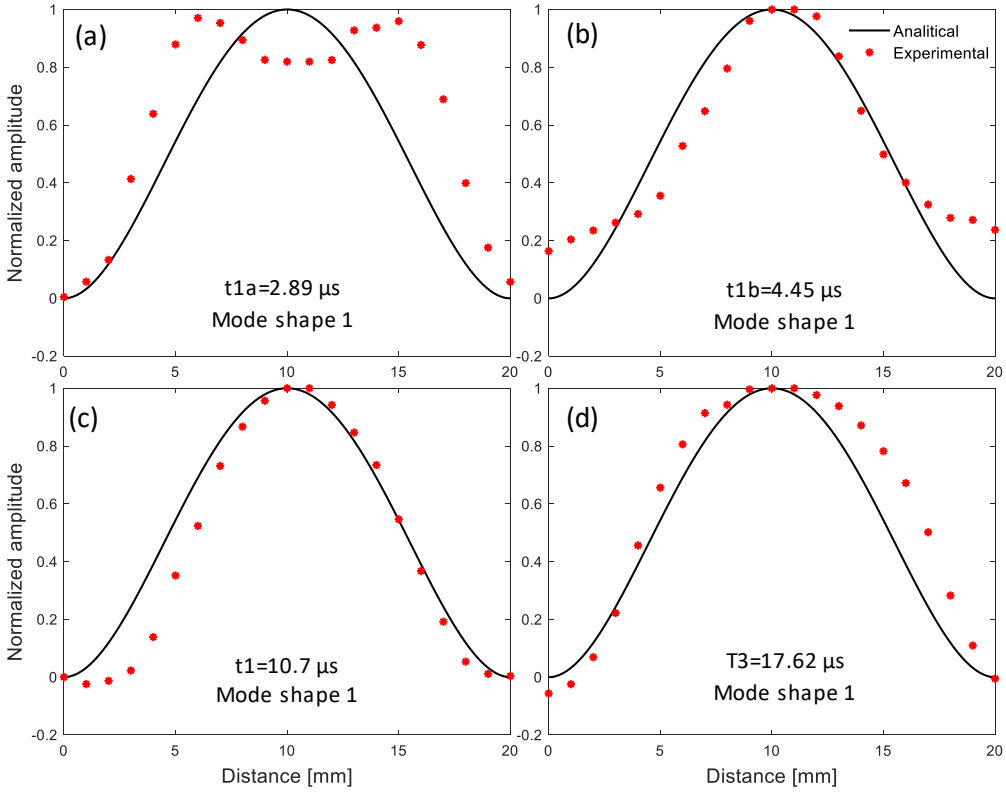

Figure 4-8. Comparison of analytical mode shapes and measured surface displacement along 150 kHz transducer diameter: (a) t = 2.89 µs, (b) t = 4.45 µs, (c) t = 10.7 µs, and (d) t = 17.62 µs.

A different vibration character is seen for the 250-kHz transducer. The time signal measured at the centre of the 250-kHz transducer is presented in Figure 4-9, and similarly to the 150-kHz transducer, the first maximum displacement occurs during the off-phase of the excitation signal. The time-steps to analyze are selected in the same way as for the 150-kHz transducer and are shown in Figure 4-10.

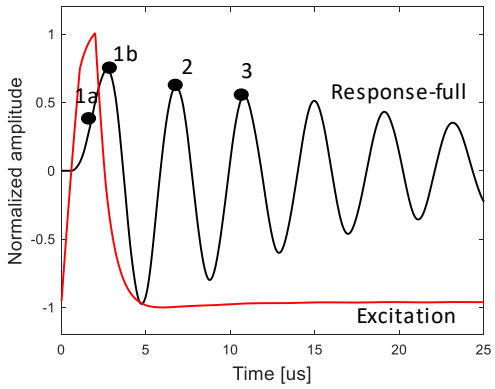

Figure 4-9. Time signal measured at the centre of 250 kHz transducer: the excitation pulse (red), and the response (black). Black dots highlight four time steps picked for detailed analysis: (a) t = 1.74 µs, (b) t = 2.7 µs, (c) t = 6.76 µs, and (d) t = 10.82 µs.

During the active excitation phase, the effect of mode superposition is present; however, it is again not as prominent as for the 54-kHz transducer. The surface displacement for the time-step of the first maximum centre displacement has a similar form as mode 1 but also includes elements of the fifth mode and, overall, can be seen as a transition state between the modes. However, the surface displacement observed from the second peak onwards follows only the 5th mode shape.

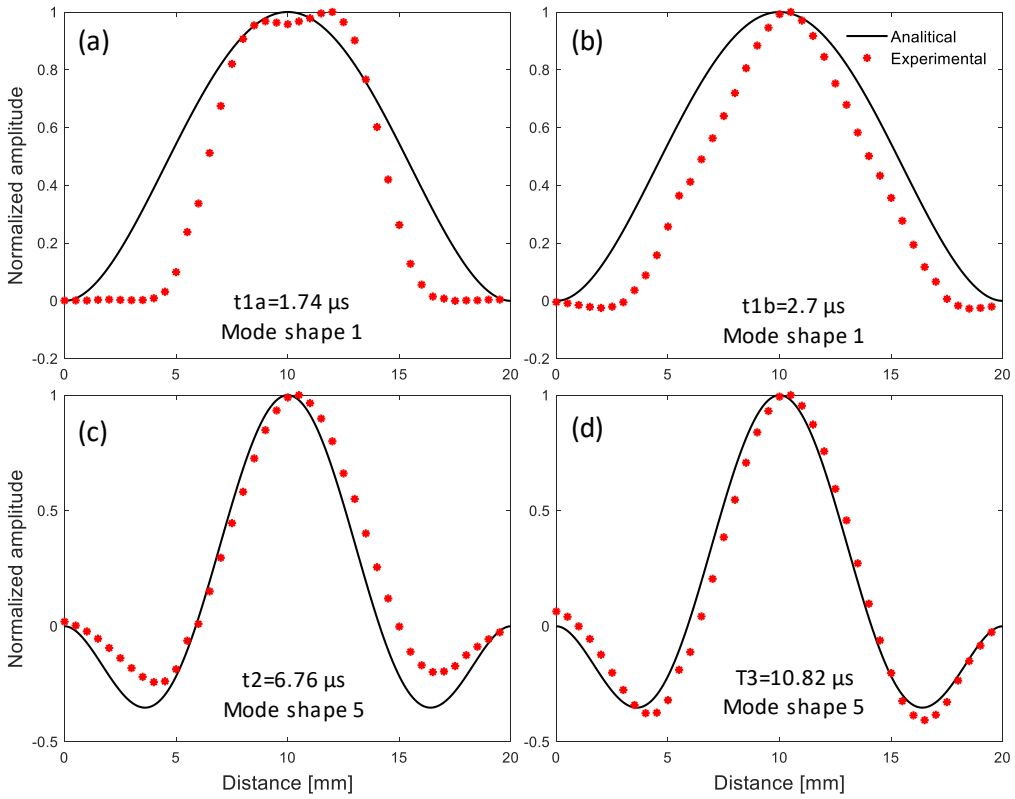

Figure 4-10. Comparison of analytical mode shapes and measured surface displacement along 250 kHz transducer diameter: (a) t = 1.74 µs, (b) t = 2.7 µs, (c) t = 6.76 µs, and (d) t = 10.82 µs.

The analysis of three types of P-wave transducer shows that they do not respond to the excitation in the same way. For all transducers, the surface displacement during the active phase of the excitation pulse has a complex form and consists of resonances of the piezo crystal and wear-surface plate. The surface behaviour changes during the passive phase of the excitation, when the observed vibration matches analytical mode shapes.

4.4.1.2 Wear face section effect on the frequency content

Next, the impact of different sections of the wear surface on frequency content is studied. Typical time signals recorded along the diameter of the 54-kHz transmitter are presented in Figure 4-11.

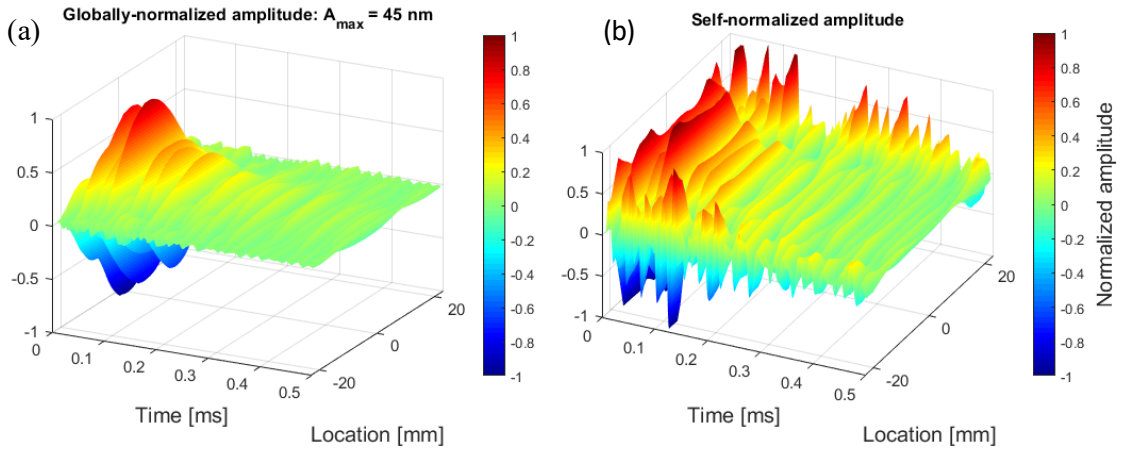

Figure 4-11. Time signals recorded along the diameter of the 54-kHz transmitter. The responses are (a) normalized globally, and (b) self-normalized.

The main energy is localized at the centre (Figure 4-12, Z1: centre) of the transmitter. Therefore, an average of signals localized at the centre is a potentially reasonable candidate for frequency analysis. However, the self-normalized time signals (Figure 4-11-b) show that the edges represent a different pattern, resulting in additional average signals to be analyzed (Figure 4-12, Z3: edge). Finally, an additional transition zone (Figure 4-12, Z2: middle) should be defined. A conceptual definition of the zones is shown in Figure 4-12.

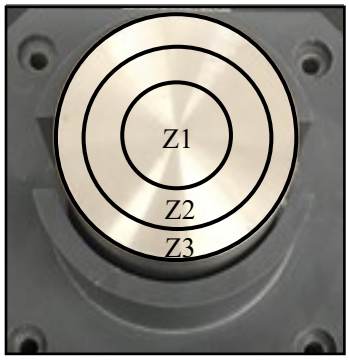

Figure 4-12. Conceptual sketch of the three zones of unique vibration character: Z1 (centre), Z2 (mid), and Z3 (edge).

In order to find ranges that should be used for the calculation of average signals, residual signals (between a reference position, coming either from the centre, edge, or middle sections and the consecutive positions along the diameter) are calculated. Finally, a correlation coefficient (Equation 4-

1) is calculated between the reference position and the arbitrary position. Figure 4-13 presents the similarity analysis with respect to the vibration pattern present at the centre.

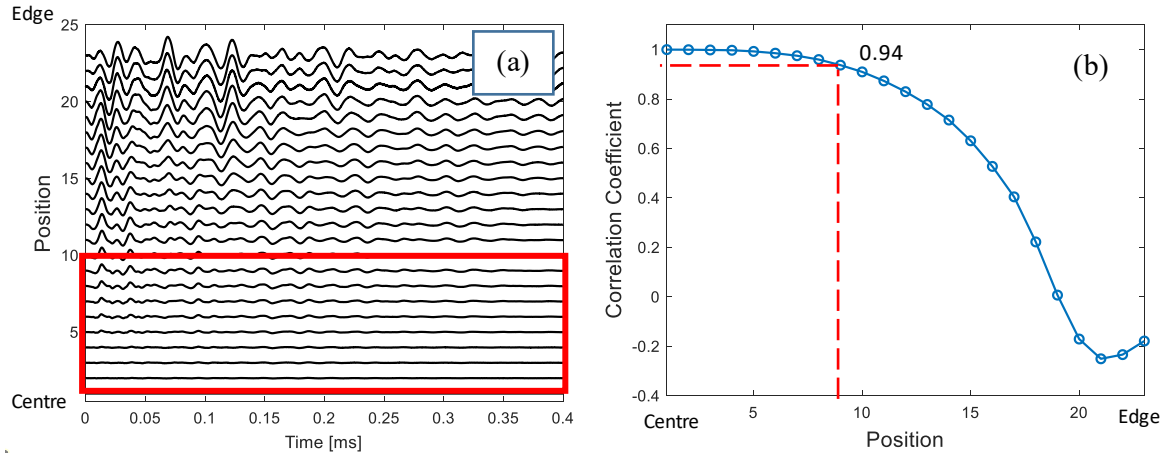

Figure 4-13. The similarity of time signals along the diameter: (a) residual signals with respect to the centre and (b) the correlation coefficient values.

The centre of the transducer is represented by a position number 1, while the edge of the transducer is defined as position number 23. A decrease in similarity is observed as the selected point moves away from the reference point located at the centre of the transmitter. The threshold value of the correlation coefficient is set to 94%, and nine points (i.e. positions 1 – 9) are selected to generate the averaged signal. Next, the reference point is set in the middle section (as per Figure 4-12) between the centre and the edge (position number 15). To extend the number of points taken for averaging, the correlation coefficient threshold is lowered to 82%. As a result, positions 10-18 are included in the calculation.

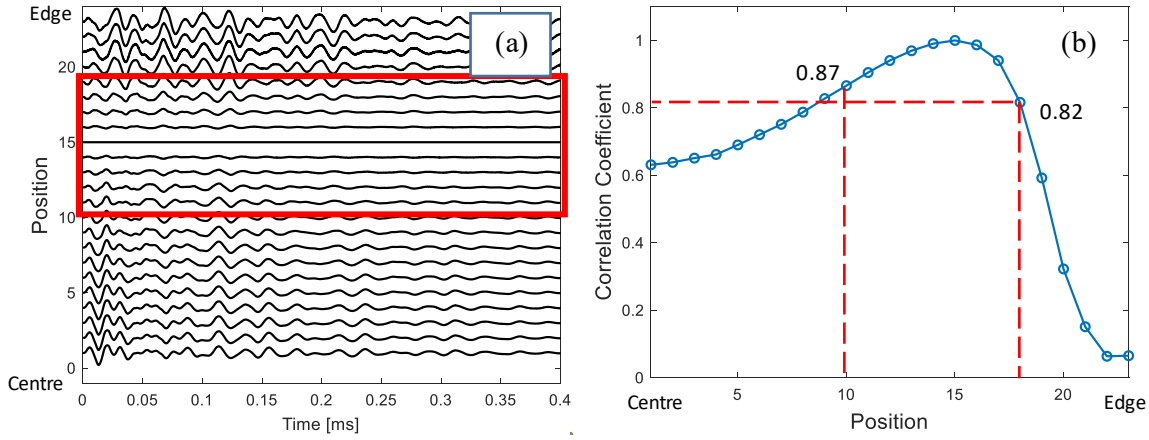

Figure 4-14. The similarity of time signals along the diameter: (a) residual signals with respect to the mid-section and (b) the correlation coefficient values.

Finally, the reference position is selected close to the edge (6 mm from the edge; position number 21 in Figure 4-15). The threshold is selected as 86%, resulting in the first five points (measured from the edge) taken for the average signal (Figure 4-15).

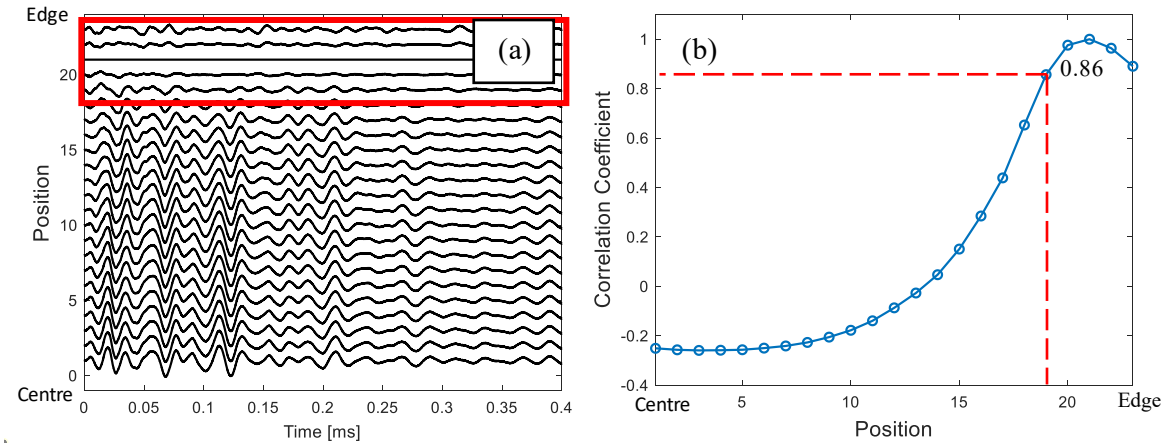

Figure 4-15. The similarity of time signals along the diameter: (a) residual signals with respect to the edge and (b) the correlation coefficient values.

Figure 4-16 presents the averaged signals for the three distinct regions and their corresponding spectra. The signals are normalized to the maximum amplitude of the central section. A significant vibration amplitude decrease is observed. However, more important differences arise in the frequency domain. First of all, the central signal (representing the majority of energy) additionally to the nominal resonant frequency includes a second significant peak (32 kHz). Less prominent peaks can also be

distinguished (16 and 39 kHz). These frequencies would normally be disregarded. However, when the middle section is taken into account, the importance of the 39-kHz component rises. For the averaged signal representing the edge vibration, the frequency character is completely different, with the most prominent frequency of 39 kHz. Moreover, the higher than nominal frequencies (62 and 75 kHz) become significant peaks. The information about edge vibration is an important piece of information that might be helpful in explaining the presence of frequencies in ultrasonic evaluation.

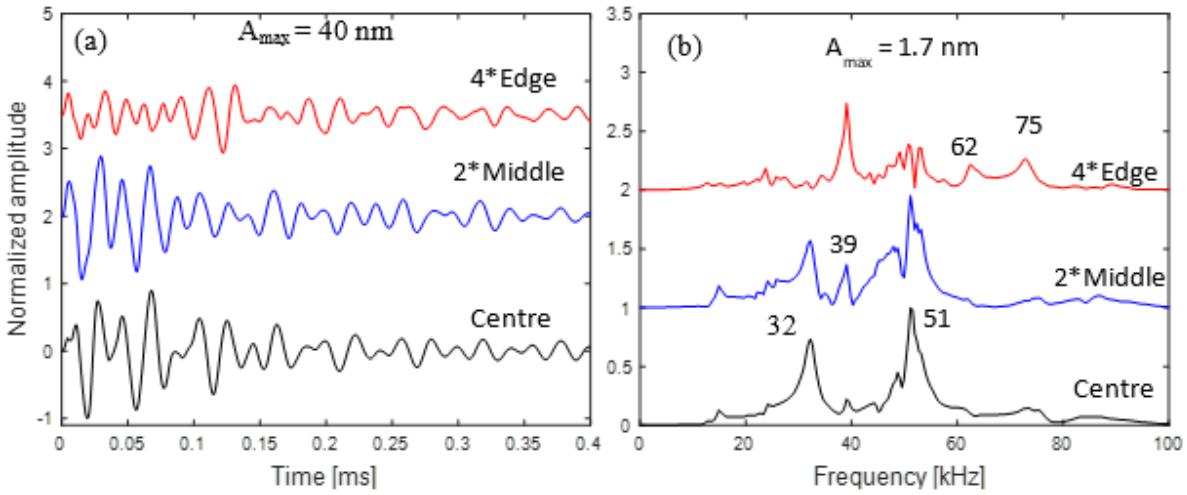

Figure 4-16. The average section signals: (a) time signals calculated based on the points selected in Figure 4-13 - Figure 4-15 and (b) their corresponding spectra. The amplitudes are normalized with respect to the maximum absolute amplitude for the centre signal.

The same procedure was applied to the 150 and 250-kHz transducers. Analogically, the three regions were defined as the centre, middle, and edge sections, and the average signals are presented in time and frequency domain in Figure 4-17.

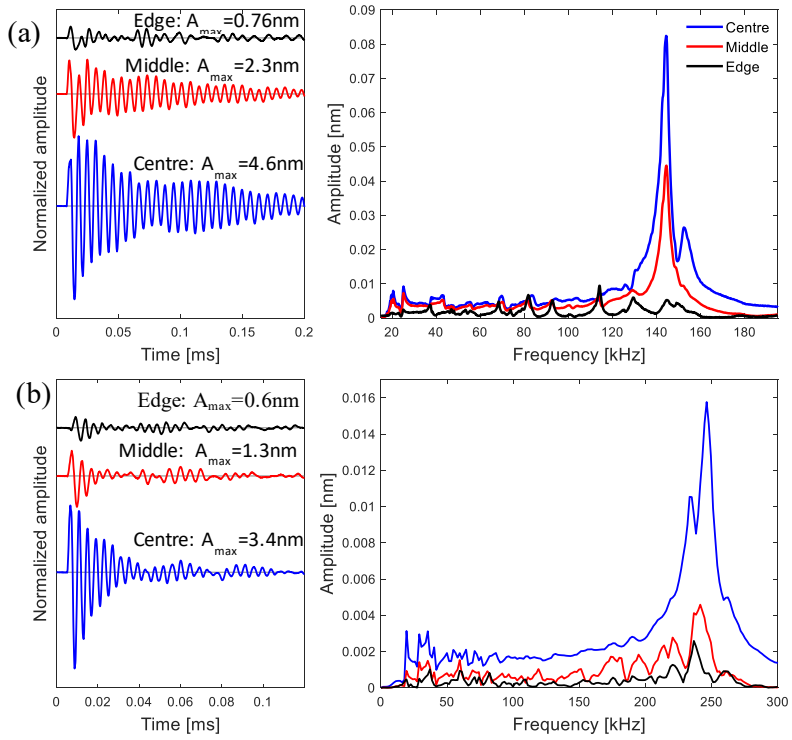

Figure 4-17. The spectra of the average signals calculated for (a) 150 and (b) 250 kHz transmitters and time signals for the central and edge sections of these transducers.

For the 150-kHz transducer, the central and mid-section regions show similar frequency behaviour with the dominating resonant frequency at 144 kHz (which is within 5% of the nominal value). In contrast, the peak with the highest amplitude of the edge signal does not occur at the nominal frequency. Furthermore, the lower frequency peaks become more significant. The effect is even more important for the 250-kHz, in which the vibration character observed at the centre (the frequency peak matches the nominal resonant frequency) is lost even for the middle section. The below 50-kHz frequencies are significant components for every section considered for the 250-kHz transducer. Consequently, when the higher frequency transducers are used in civil applications, it becomes important to keep track of what is being sent to the tested medium.

The results of the wear surface section analysis show that it is crucial to maintain consistency in coupling throughout the whole testing procedure. If in either different tests or with the dismounting of transducers, different areas of the transducer are coupled, it will lead to different frequency content being transferred to the tested medium. As a result, waves with different wavelengths will be propagating, and inconsistencies related to wavelength to specimen dimension or defect ratios will skew

the evaluation. To limit the frequency content being transferred, it might be beneficial to provide coupling for just the central section of the transducer.

4.4.2 Effect of interference between a transmitter and the tested medium

In the next phase of characterization, an effect of interference between a transmitter and the tested medium is studied. It is intended to imitate the acoustic parameters of concrete specimens. Therefore, a glass specimen (K9 glass) with a similar acoustical impedance to concrete is used. In this phase, only the 250-kHz transducer is considered due to the limitation related to wavelengths generated by the probe and the dimension of the glass block. The 250-kHz transducer is glued into a glass block. The responses measured on the wear face of the transmitter through-the-air (using the setup presented in Figure 4-1-a) are compared with the responses acquired with the glass-block (through-the-glass setup shown in Figure 4-1-b). An example of the wear-surface vibration measured along the transducer diameter for the through-the-air and through-the-glass configurations is presented in Figure 4-18.

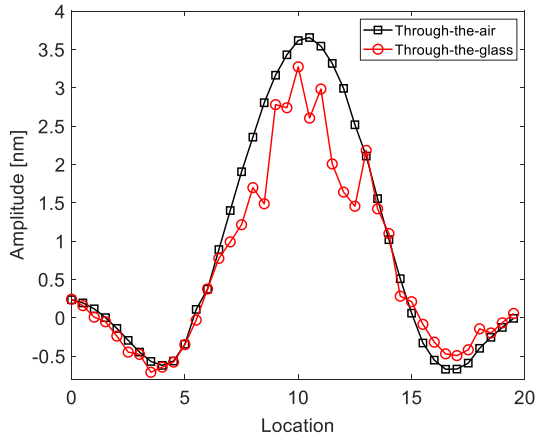

Figure 4-18. Comparison of vibration measured for the 250-kHz transducer along the diameter for the through the air (black line) and through the glass block (red line) testing setups.

The vibration shape observed in Figure 4-18 does not change with the presence of a medium. Although, some amplitude reduction is present, and the signal-to-noise ratio is worse when the laser beam goes through the glass-block. The detailed analysis of the vibration is presented in Figure 4-19 for the signals measured for the central section of the transducer (as per Figure 4-12).

The main difference observed in time signals is the change in amplitude. A similar effect is present in the frequency domain for the nominal frequency, where the maximum amplitude is reduced by 35%.

A more important difference is observed for the low frequencies. The below 50 kHz frequency components are significantly reduced, and the peaks around 55-kHz are more prominent.

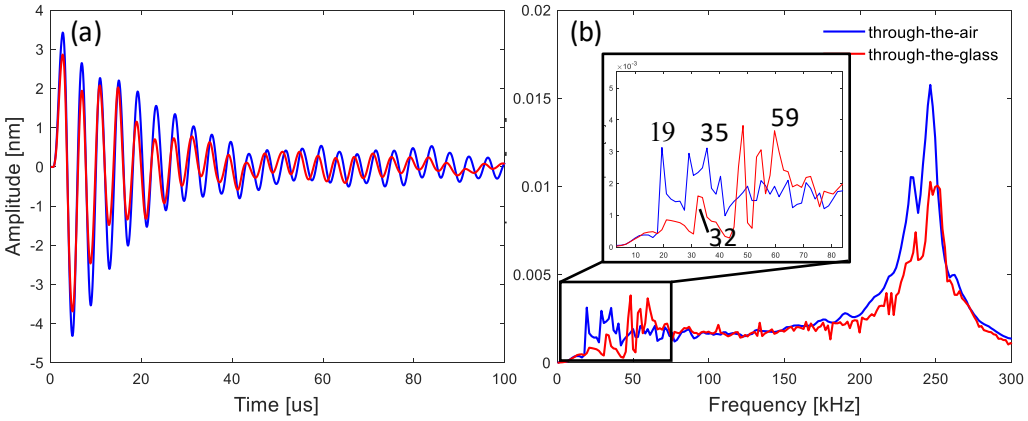

Figure 4-19. Analysis of signals measured at the centre of the 250-kHz transducer for the through the air (blue line) and through the glass block (red line) testing setups: (a) time signals and (b) frequency spectra. The main differences in the low-frequency range are marked.

WSST technique is used to study how the frequency content changes with time for both setups. The instantaneous frequencies estimated with WSST are shown in Figure 4-20. Colormaps are oversaturated (amplitude-colour-wise, the same level of oversaturation) to show the effects also on lower-than-nominal frequencies. It can be seen that the energy of the nominal frequency component attenuates much faster when the response of the transducer is read through the glass-block (the dark red colour is present only during the first 40 us in the glass test, whilst it is present practically throughout the whole presented time for the air readings). Moreover, more substantial participation of 50 kHz component is observed when the response is read through the glass.

Based on the scans acquired with the two setups, it can be concluded that the presence of the glass block does not affect the nominal frequency significantly (only the amplitude reduction effect is present). At the same time, the frequency content is modified in the below 100 kHz range. Although the amplitude in that range is low, relative to the nominal frequency, it might play a significant role for the applications in concrete, where the non-homogenous nature of the material significantly attenuates ultrasonic waves.

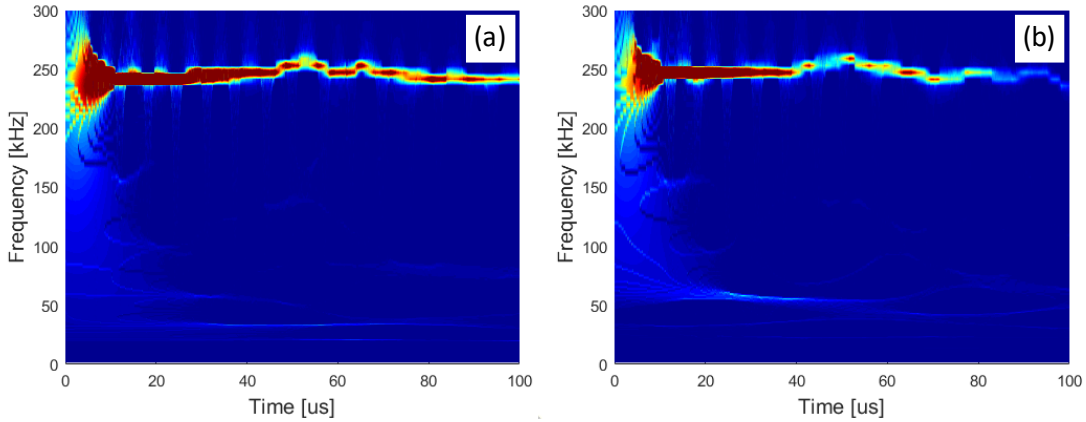

Figure 4-20. Instantaneous frequencies estimated with WSST for (a) the through-the-air and (b) through-the-glass setups.

4.4.3 Top of the glass-block vibration

The next phase of characterization includes scans of the top surface of the glass block measured along the two diagonal lines and directly on top of the transmitter. It is an initial step for the future characterization of receivers. Firstly, the area located directly on the opposite side of the transmitter is measured. It can be interpreted as the mechanical excitation that would be experienced by a receiver. The surface scan is compared with the vibration of the wear surface of the transmitter measured in the through-the-air configuration (Figure 4-21). The difference in amplitude scale is because of the additional amplifier used in setup 2.

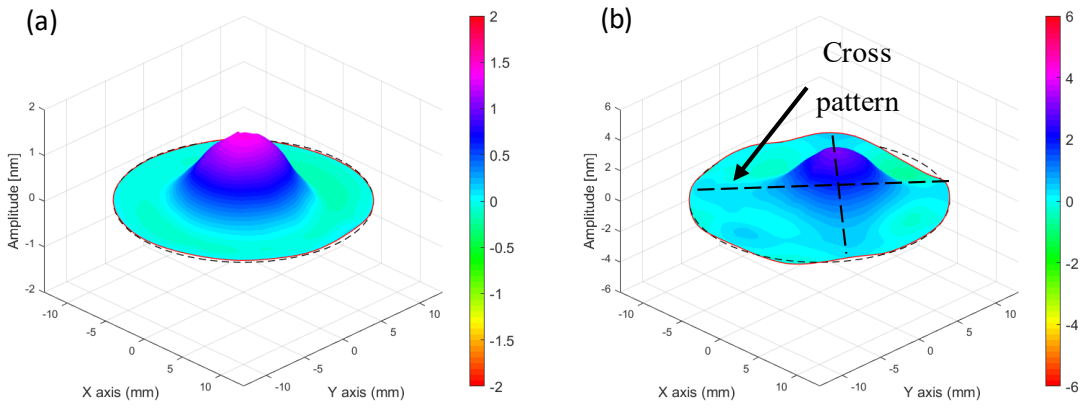

Figure 4-21. Surface movement plots: (a) the vibration of the wear surface of the transmitter measured in the through-the-air configuration, and (b) the response measured on the top of the glass

block directly on top of the transmitter. The units of colour bar scale are nm. The difference in amplitude scale is because of the additional amplifier used in setup 2.

The maximum vibration observed on the top of the glass block appears at the centre and matches the maximum vibration of the wear surface. However, a cross pattern (along diagonals of the block) is also present. In order to explain the pattern, the scanning surface is complemented by the scans along the two diagonals. Figure 4-22 presents snapshots from the animation created based on measured responses. At first, the arrival of the P-wave is observed (Figure 4-22-a), which is followed by the creation and progression of the surface wave travelling from the corners into the centre of the block (Figure 4-22-b and c).

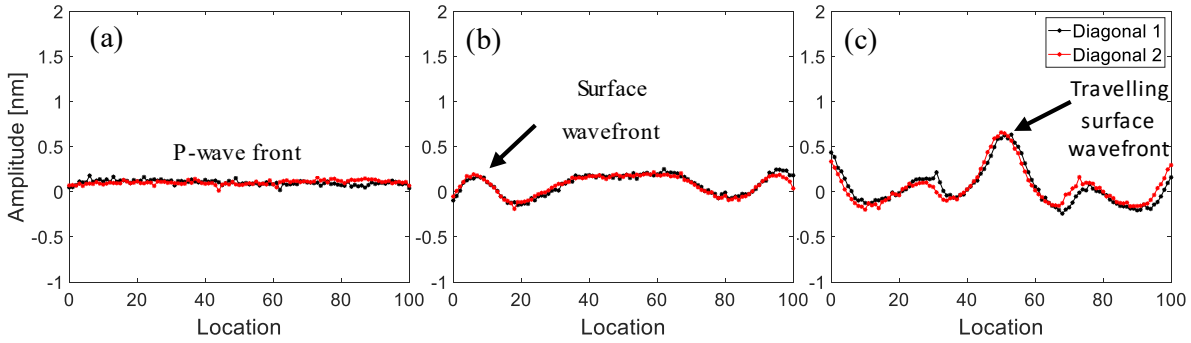

Figure 4-22. The response measured at the top of the glass block along two diagonal lines (black and red colours): (a) the arrival of the P-wave, (b) early stage in the progression of the surface wave, and (c) surface wave arrival at the centre of the block.

This observation means that the top surface, and eventually, the wear surface of the receiver, vibrates differently depending on the boundary conditions, and the response of the ultrasonic receiver is a unique signal. Effectively, the characterization of a receiver can only be performed when the first arriving oscillation is isolated, and a precise windowing (eliminating the boundary conditions effects) is needed.

4.5 Application of characterized transducers

In the following section, the advantage of using characterized transducers in ultrasonic tests is presented based on two experimental applications.

Firstly, a typical wave velocity test (ultrasonic pulse velocity) is considered. Observations obtained from the regular examination are compared with the additional analysis that takes into account the frequency content of signals. It is shown that the identification of frequency components of received

signals is only possible through the characterization of the ultrasonic transducer. A new set of conclusions based on improved interpretation of ultrasonic measurements is offered.

In the second application, an early damage detection problem in concrete specimens is considered. It is demonstrated that a typical velocity-based approach is not sensitive to early damage evaluation. The characterization is used to describe the frequency content of measured surface waves. The well-described transducer profile provides a strong rationale for the mode decomposition technique (WSST) and analysis of individual modes (which represent individual wavelengths). This has a critical importance for surface wave analysis, meaning that each mode offers different penetration depth. Based on a selection of the most sensitive mode, a 24% improvement in early damage indicator (RAI) can be obtained.

4.5.1 Improved understanding of ultrasonic signals measured in concrete specimens of different length

The first application of transducer characterization aims in a proper interpretation of ultrasonic data. A typical ultrasonic pulse velocity (UPV) test is performed on a set of concrete specimens in a direct configuration. The UPV method the ASTM standard test method for concrete (ASTM International, 2016a). This technique is based on the concept of measuring the time of flight for the first arriving ultrasonic wave from one side of the specimen to another. At the same time, wave velocity depends on the elastic properties of the medium. Therefore, it is possible to track the evolution of a specimen condition by observing changes in the wave velocity. In the investigation, tested specimens have a cylindrical shape with a constant diameter (D = 10 cm) and ten length variations (L = 5 cm to 50 cm long, with a 5 cm length increment between specimens). All specimens were cast at the same time from an industrial concrete batch (standard air-entrained mix of 30 MPa, with the air content of 7.5 %; Fine aggregates meet the grading requirements of ASTM C33 (ASTM International, 2018b), fineness modulus is in a range of 2.3 and 3.1; the nominal maximum size of the coarse aggregate: 19mm; slump test of 90 mm). The specimens are tested with the 250-kHz characterized transducers (symbols Tx and Rx are used to denote a transmitter and receiver). The experimental setup is shown in Figure 4-23-a (the details of the setup can be found in Chapter 5). HP33120A function generator is used to provide an input signal (250 kHz square pulse, which is amplified to the amplitude of ± 125V) to the transmitter. Each specimen is supported on the holder, and the sensors are placed on each face of the cylinder. The readings (a time signal represents an average of 16 measurements) are taken and stored by Keysight DSO-X 3032T oscilloscope (all specimens are tested at the same age – 56 days).

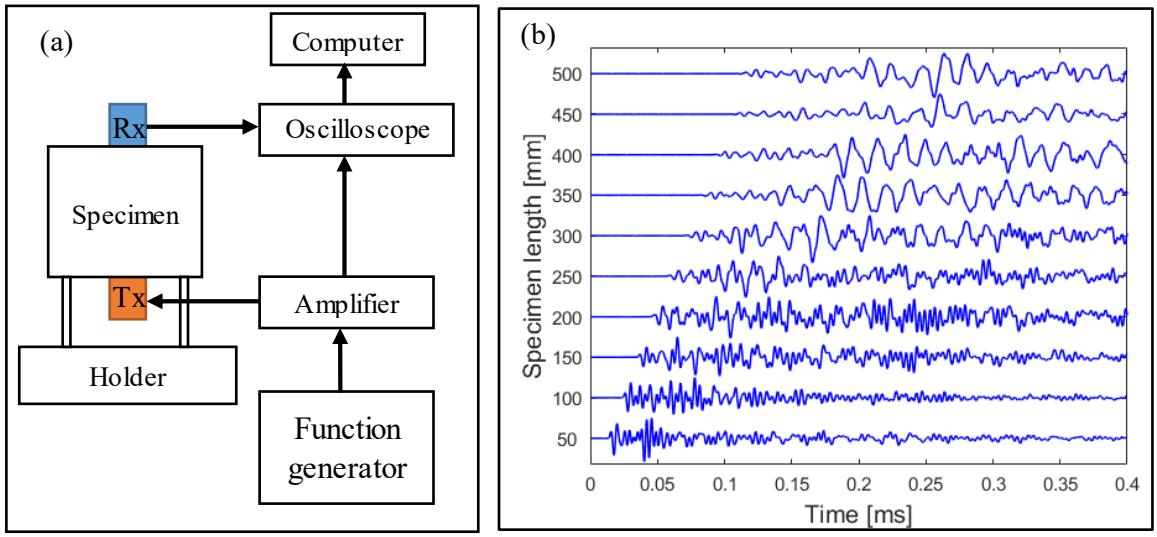

Figure 4-23. Ultrasonic pulse velocity test: (a) experimental setup and (b) measured time signals for specimens with D = 10cm and different lengths (L), tested under Tx = 250 kHz inputs. Amplitudes are self-normalized to highlight the first arrival and change in their character.

Figure 4-22-b shows measured signals during the UPV test for all specimens (amplitudes are self-normalized to highlight the first arrival and change in their character; only the first 0.4 ms is presented). The UPV takes into account only the first arrival time, and the detection of it can be performed automatically without recording of longer wave-forms. In the presented data, the first arrival is distinct for all specimens, and the P-wave velocity can be calculated. However, it is evident that this measure is insensitive to detect a change in the vibration character that is present as the specimen length increases. If the long wave-form is not recorded, that change would not even be detected. In such a situation, one could calculate the wavelength for the P-wave based on the nominal frequency of the transmitter (250 kHz) and measured velocity (average of 4915 m/s), which gives a wavelength of 20 mm that gives an ability to detect small defect within the material. That is where the UPV method ends.

On the other hand, the change in the vibration characteristics of the full-time signals can be studied in the frequency domain. Recorded time signals (with the removed DC value) are transformed into the frequency domain with the fast-Fourier transform algorithm implemented in the signal processing toolbox in Matlab.

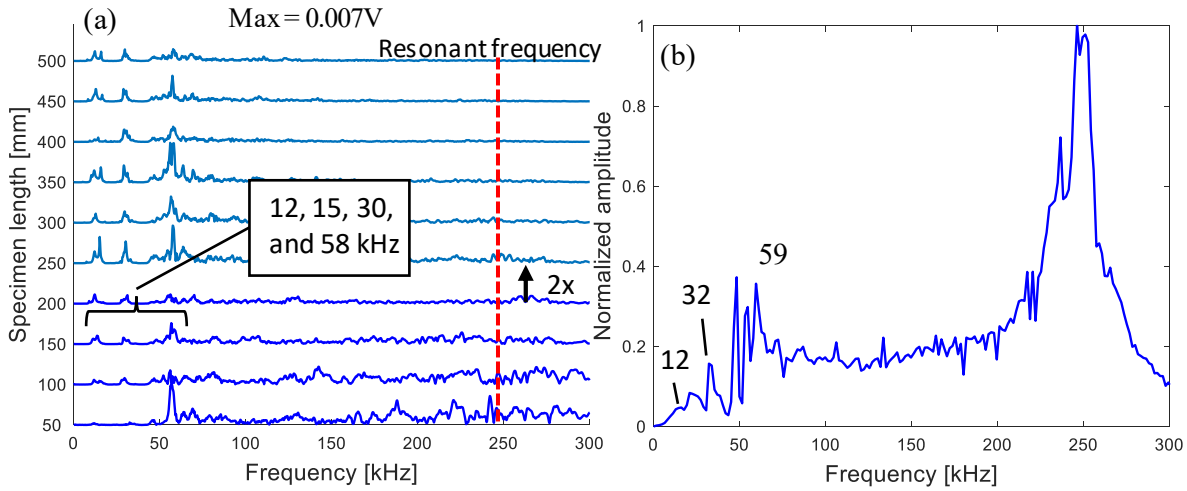

Figure 4-24. Frequency analysis: (a) amplitude spectra calculated for the UPV signals and (b) transducer characterization spectrum for the central section. The UPV spectra are normalized to the maximum value for the shortest specimen. The amplitudes for the specimens longer and including 250 mm are multiplied by 2 (highlighted with a light-blue colour). The red dashed line shown the resonant frequency of the transducer. The transducer characterization spectrum is self-normalized.

Figure 4-24-a presents the frequency representation of the recorded signals for all ten length combinations. The frequency associated with the resonant frequency is not present for most of the signals (besides the shortest specimens), and the main frequency peak for all specimens is located around 58 kHz. The reduction in the main frequency and amplitude reduction is expected in concrete due to the non-homogenous composition. However, the explanation of the lower frequencies shown in the box in Figure 4-24-a is not clear at this stage of analysis, and one would need to proceed with time-consuming analysis verifying if the origin of these frequencies is related to the natural frequencies of the specimens. For simple geometries, analytical salutations exist, or it is possible to model the specimens using any finite element analysis software (given that the modal analysis module is available).

Alternatively, the rationale of the low frequencies presence can be found through the characterization procedure. These frequencies do not change with specimen length, which means that they are geometry-independent. Figure 4-24-b shows the characterization spectra obtained with the glass block (and presented earlier in Figure 4-19-b). Based on the characterization, it is known that the low frequencies were sent by the transmitter. Therefore, the question if a certain frequency is the natural frequency of the tested specimen can be eliminated.

Moreover, the measured responses consist only of the frequencies much lower than the nominal transmitter frequency, which means that one deals with much longer wavelengths. Therefore, identification of small defects might not be possible. For the wavelength associated with the P-wave arrival, one can use an approach presented by Wiciak et al. (2020), in which the width of the first pulse is used for the calculation of the actual arriving frequency. Wiciak et al. (2020) reported a change in wavelength from 30 mm for the shortest specimen to 46 mm for the longest specimen, which means that the first arriving wave can have a wavelength of up to 2.3 times longer than the wavelength calculated based on the nominal resonant frequency of the transmitter. Based on the characterization, the experimental setup can be then optimized in the iterative process, so the resonant frequency of the receiver matches the maximum frequency peak observed in the first iteration for the received signals.

4.5.2 Selection of ultrasonic features based on the characterization of the transmitter for damage assessment of concrete

The second application presents a distributed damage assessment problem in concrete beams. The transducer characterization results (i.e. the frequency content transmitted to a tested medium) provides a strong rationale for the selection of frequency ranges for analysis. The ultrasonic evaluation is verified with the destructive compression test.

Two rectangular concrete beams (41 cm x 8 cm x 10 cm; 12.5mm nominal aggregate size, measured concrete strength at 28 days is 35 MPa) in intact and damaged conditions are tested with the characterized 54-kHz transducer and the state-of-the-art Doppler laser vibrometer. The responses are measured at the top surface of the specimen. One specimen is left in as-cast condition and is used as a reference, while the second specimen is subjected to eight weeks of freeze-thaw cycles. Each cycle lasts 24 hours and consists of a gradual temperature increase from -25 C° to +25 C° with ±2 C° (details of the experiment can be found in (Fartosy, 2018)).

The experimental setup is shown in Figure 4-25-a. A function generator (HP33120A) is used to provide an input signal (54 kHz square pulse, which is amplified to the amplitude of ± 125V) to the transmitter (located at the left end of the beam), and the response is read with a laser sensor head (LSH, Polytec OFV-534), which is connected to the vibration controller (OFV-2570). A total of 200 points are recorded on the surface of the beam for each condition (the first measuring point is located 100 mm away from the source on the top surface of the beam, and the spacing between the points is 1 mm). Each recorded time signal represents an average of 500 measurements.

The analysis starts with a visual inspection, which shows no difference between the beams. Then, a reference UPV test is carried out, which shows a negligible difference between beams. When a high amplitude resolution was assured (manual zoom-in, exposing the first arriving oscillation in time signals), P-wave velocity recorded for the intact and damaged conditions were: 4610 and 4411 m/s, which gives a relative difference of 4%. However, a typical test would not pay such high attention to identifying the true first arrival. If the first peak is considered as the first arrival, then the relative difference drops to 1%. These values would be considered as within the error level. Therefore, a more sensitive approach is needed, and a surface wave test with the laser vibrometer focusing on changes in signal amplitude is performed. The signals are analyzed with the WSST technique (Equation 3-41). Figure 4-25-c presents a typical instantaneous frequency plot estimated with the WSST for the measured response. The two frequencies observed in the response match the characteristic profile of the transmitter used in the test (presented in Figure 4-16). A presence of the additional frequency component (other than the driving frequency) is well explained. Therefore, the two modes (called mode 30 and mode 50, which are centred around 30 and 50 kHz) can be reconstructed with the WSST algorithm and used in the next phase of the analysis. Analysis of individual components of the response offers a benefit of unique wavelength analysis. Assuming wave velocity of 2364 m/s (calculated based on data shown in Figure 4-25-b) and frequencies for the modes of 32 kHz and 51 kHz, the following wavelengths (λ) can be calculated $\lambda_{30} = 74\ mm$ and $\lambda_{50} = 46\ mm$. It is typically assumed that surface waves penetrate the material up to one wavelength, which means that the modes will provide different information about the material profile. As mode 30 penetrate deeper into the beam, the analysis of that mode is considered as a more promising candidate for material evaluation.

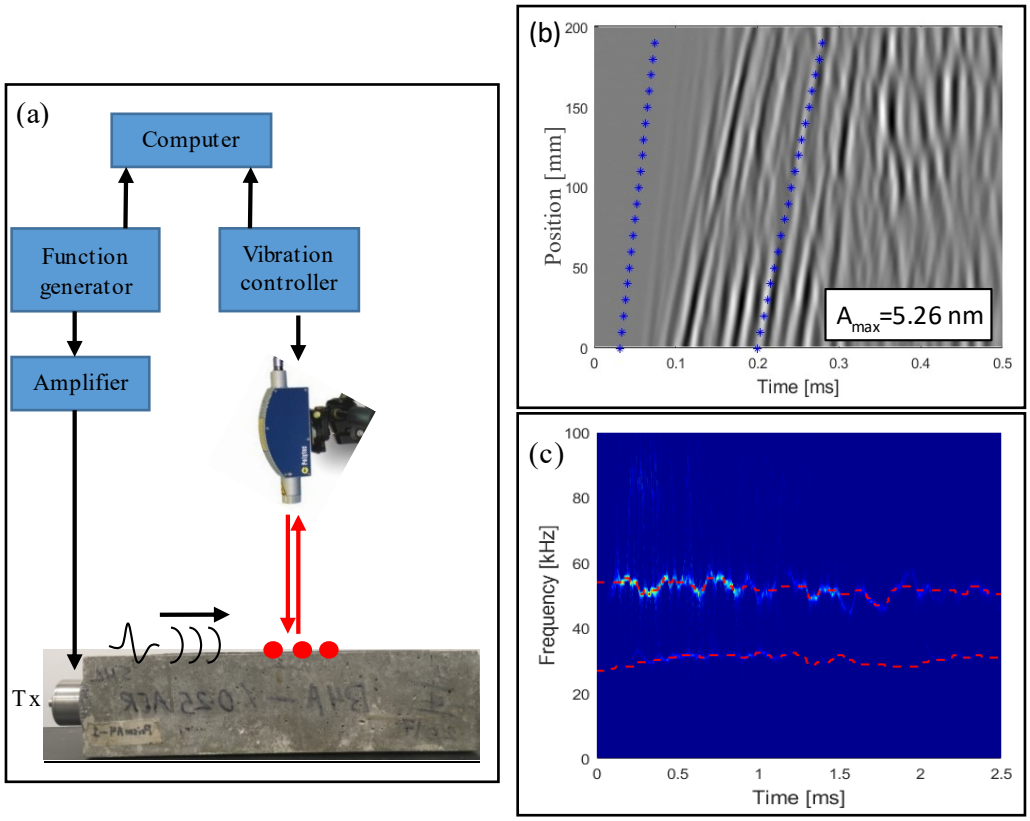

Figure 4-25. (a) Experimental setup, (b) sample time signals measured for the beam in intact condition; blue stars highlight the window used in this study, and (c) instantaneous frequencies estimated with WSST for the typical response measured with the laser vibrometer.

Next, both the full-time signals and the reconstructed mode signals are windowed with a sharp Tukey window (cosine fraction of 0.1) and a duration of 0.2 ms (the window is presented in the Figure 4-25-b with blue stars). The window ensures that the responses do not include reflection from the end side of the beam. The back-propagating wave is seen from 0.35ms for the farthest locations. Fast Fourier transform is used to analyze the windowed signals in the frequency domain. For each location, total spectral energies are calculated based on the frequency range from 1 to 100 kHz (according to equation 3-46). The first damage indicator calculated is the relative energy (RE, Equation 3-45), and it is presented in Figure 4-26 for full-time and reconstructed mode signals.

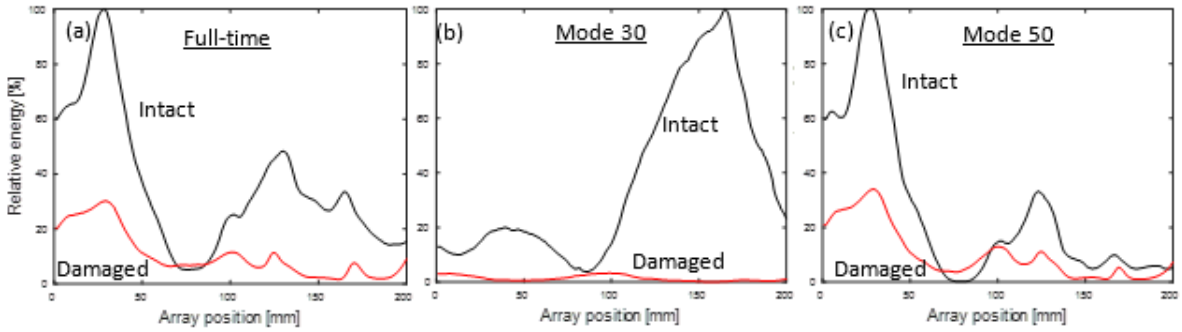

Figure 4-26. Relative energy (for each graph, signals are normalized to the maximum value for the intact beam): (a) full-time signals, (b) mode 30, and (c) mode 50.

The RE graph shows the total spectral energy trend for each condition with respect to the maximum value for the intact beam. A difference in material condition can be detected with the RE graphs in a situation when the two lines stay apart, and when the line for the damaged specimen has much lower values than the intact one. For the full-time signals, the separation between the two conditions is high for the first 70 locations and modest in the second half of the measured distance. A drop observed between positions 50 and 100 can be associated with a small size of the beams and some local boundary effects. Mode 30 offers strong separation in the second half of the measurement array. Additionally, the values for the damaged line are much lower than for the intact line, and the overall separation obtained with mode 30 is improved than the one obtained for the full-time signals. The similar character as in the full-time signals is preserved in the mode 50. However, the area when the intact values are higher than the ones observed for the damaged specimen is reduced. Therefore, mode 50 offers worse condition separation quality.

The total spectral energies are also compared point by point between two conditions, and the relative attenuation index (RAI) values are calculated (Equation 3-47). Table 4-2 presents the mean RAI values (calculated over the whole measurement array). A Higher RAI value means that the two conditions are farther away from each other. The RAI confirms the results obtained with the RE.

Table 4-2. Summary of relative attenuation indices calculated for the beams

Signal type	Mean relative attenuation index [%]
Full-time signals	71.1
WSST - Mode 30	88.3
WSST - Mode 50	61.3

Finally, a verification compression test has been performed on the beam slices (cross-sectional cuts of 40 mm thickness).

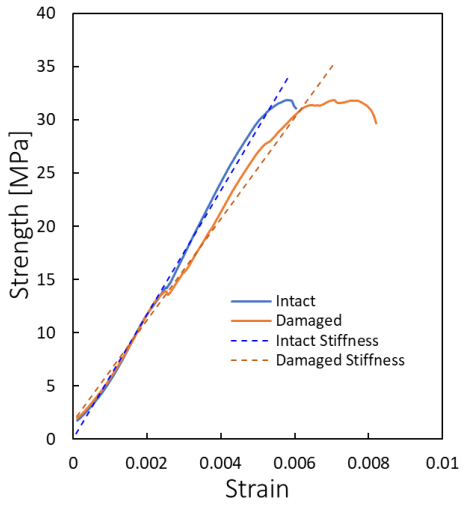

Figure 4-27. Example stress-strain curve obtained from the compression test of beams in intact (blue) and damaged (orange) conditions

The freeze and thaw test aimed to induce early damage; therefore (after 56 cycles), no significant reduction in compressive strength is reported (2% reduction). However, concrete elements have been deformed more in the damage condition, resulting in a 20% strain increase. The results follow the findings of Marzouk and Jiang (1995), who reported no significant changes in dynamic elastic properties for up to 200 cycles of freeze and thaw.

4.6 Conclusions

This study presents the characterization of three P-wave ultrasonic transmitters that are frequently used in the evaluation of civil engineering materials. The wear surface displacement has been measured with

the state-of-the-art laser vibrometer. The following main conclusions can be given, and the detailed conclusions are presented in Chapter 8.

1. The wear surface responses of ultrasonic transducers tested in the study (i.e. with nominal resonant frequencies of 54, 150, and 250 kHz) consist of resonances of the piezo-crystal and wearing-plate itself. The quarter-wave matching wear plate is designed to increase energy output by constructive wave interference; however, it does so at the expense of frequency bandwidth.

2. Different sections of the wear-face (i.e. central, middle, and edge sections) contribute differently to the overall response. Therefore, it is critical to ensure constant coupling area and quality of coupling throughout the whole duration of the test or series of tests if condition monitoring is considered.

3. Characterization of 250 kHz transducer with the addition of a solid medium (i.e. glass block) shows that the glass block does not affect the nominal frequency. However, the frequency content is modified in the range below 100 kHz, which is important for applications in concrete elements.

4. The vibration of the top surface of the glass block was also examined, investigating the possible application for the characterization of receivers. It has been shown that the top glass surface vibration is quickly affected by the boundary effects, and precise windowing is required for the future characterization of ultrasonic receivers.

5. The study of concrete elements shows that the characterization enables the identification of the frequency content of measured ultrasonic responses. Additionally, if the characterization and frequency analysis are not followed, the interpretation of ultrasonic data might be inaccurate, which can result in a 20% error of P-wave velocity estimation.

6. Characterization provides a rationale for mode decomposition (i.e. it has been demonstrated that the frequency content of the transducer response comes from the resonances of the piezo-element and the wear plate itself) and analysis of waves in individual wavelengths.

Chapter 5
Frequency and geometry effects on ultrasonic pulse velocity measurements of concrete specimens

5.1 Introduction

Concrete is the most consumed structural material in civil engineering applications (Mehta, 2001). The condition of concrete plays a key role in load carrying capacity and, thus, the safety of structures. The assessment of civil infrastructure and characterization of construction materials is commonly performed with ultrasonic nondestructive evaluation (NDE) techniques. Among the acoustic methods, impact echo, ultrasonic pulse velocity (UPV), and surface wave analysis can be distinguished (McCann & Forde, 2001; Popovics, J. S., 2003). The latest trends focus more on the attenuation of a wavefront for both a longitudinal wave (P-wave) and a surface wave (Aggelis et al., 2005; Chaix et al., 2006; Kirlangic et al., 2015; 2016) and more sensitive methods for detecting small changes in the velocity (e.g. coda wave interferometry (Dai et al., 2013; Planès & Larose, 2013; Snieder, 2006); these changes are related to the microstructure of concrete and can be analyzed using experimental techniques such as X-ray diffraction, scanning electron microscope, or mercury intrusion porosimetry (Huo et al., 2016)). The ultrasonic pulse velocity (UPV) method, the ASTM standard test method for concrete (ASTM International, 2016a), is studied and analyzed in this work. The major benefit of the UPV is its simplicity. The method is based on the concept of measuring the time of flight for the first arriving ultrasonic wave from one side of the specimen to another. It has been shown that the UPV results may be affected by many factors. Abo-Quadais (2005) studied the effect of concrete mix (i.e. water-cement ratio, aggregate size) on the P-wave velocity. The water content was also studied by Ohdaira and Masuzawa (2000). Popovics (2005) noted that the distribution of moisture in concrete and a degree of crack water filling has an influence on P-wave velocity.

However, there has been little research studying the effects of specimen dimensions and ultrasonic frequencies used in a test on the UPV in concrete. In the 40s and 60s of the twentieth century, Jones (Jones, 1949; Jones, 1957; Jones & Facaoaru, 1968; Jones & Facaoaru, 1969) investigated the effects of path length, the shape of the specimen, and the natural frequency of transducers on the UPV. Jones and Facaoaru (1969) set a minimum specimen length recommendation as 100 mm when the maximum aggregate is less than 30 mm, and 150 mm when the aggregate is less than 45 mm. The measuring path should also be adjusted based on a resonate frequency of an ultrasonic transducer. The path should be

from 100 to 700 mm for the transducers with a natural frequency higher than 60 kHz (the highest considered frequency is 200 kHz), from 200 to 700 mm for the transducers with the natural frequency higher than 40 kHz, and finally, longer than 1500 mm for the probes with the natural frequency higher than 20 kHz. Additionally, minimal transverse specimen dimensions are proposed as 70, 150, and 300 mm (for the transducers with a natural frequency higher than 60, 40, 20 kHz). However, the justification of these numbers is not given, and no test results are presented. It is suggested that the given recommendations may need to be modified with the improvement in the state of knowledge. The ASTM C597-16 (ASTM International, 2016a) indicates that the pulse velocity does not depend on the tested object dimensions as long as reflections from boundaries do not impede the specification of the arrival time. The only limitation stated by ASTM C597-16 (ASTM International, 2016a) is that the least dimension of the tested specimen has to be larger than the wavelength of ultrasonic waves. Some ideas, in terms of expressing the specimen dimension with respect to nominal frequencies of ultrasonic transducers, can be found in ASTM D2845-08 ($D \geq 5\lambda \geq 15d$, where D is the minimum lateral dimension, and d is the average grain size (ASTM International, 2008)) with the exception that the dimension restrictions are developed for rock materials, in which aggregate sizes are smaller than in concrete, and in a different frequency range than the one typically used for concrete.

This research is focused on verifying the assumptions of ASTM C597-16 (ASTM International, 2016a) and identifying the relationship between UPV results and ultrasonic transducers used (i.e. resonant frequency of the transducer), a coupling quality (i.e. the effect of contact sensors on the UPV results), and specimen dimensions (i.e. a length and a diameter of a concrete cylinder), with a special focus on the effect of frequency and attenuation. In this study, the authors discuss those factors by using three types of ultrasonic transducers. A low frequency (i.e. 54 kHz), the UPV typical transducer, and two higher resonant frequency transducers (i.e. 150 kHz and 250 kHz) are used. A group of thirty specimens (three groups with a different diameter with ten different lengths in each group) gives a comprehensive range of dimension-to-wavelength ratios.

Firstly, this study ensures that the resonant frequencies of the specimens are not masking ultrasonic frequency features by a simple numerical modal analysis. The authors also show the real responses of the ultrasonic transducer, measured with the state-of-the-art laser vibrometer. A difference that is introduced by a transducer frequency response function (FRF) is discussed. The Doppler laser vibrometer is also used to show that a vibration mode present in the high-frequency tests (i.e. 250 kHz) is dominated by low frequencies, which leads to an attenuation analysis. This study shows that the

minimum length-to-wavelength ratio should be greater than four to keep the error of the UPV test within 5%. The study also discusses the specimen diameter to wavelength ratio and indicates that when the ratio is smaller than 3, the observed wave velocity is lower than the P-wave velocity and approaches longitudinal bar velocity. Finally, the material damping ratio is calculated for concrete cylinders in the ultrasonic frequency range of 54 kHz to 250 kHz

5.2 Theoretical background

The P-wave velocity can be calculated as distance over time, but it also depends on the medium properties (Equation 3-11). If the specimen radius is small in comparison to the wavelength (i.e. $D/\lambda \leq 1$, where D is a specimen diameter, and λ is a wavelength), P-wave velocity approaches the bar longitudinal-velocity (Jones & Facaoaru, 1969; Khan, Zahid et al., 2010):

$$V_{BarL} = \sqrt{\frac{E}{\rho}} \tag{5-1}$$

For any finite length specimen, the longitudinal, bending, and torsional natural vibration modes can be excited. The frequencies for the natural vibration modes for beams with cylindrical cross-sections can be calculated as (ASTM International, 2014a; Verástegui-Flores et al., 2015):

$$f_{axial} = \frac{V_{BarL}}{2L} \tag{5-2}$$

$$f_{bending} = \sqrt{\frac{3.1699}{T}} * \frac{D}{2L^2} * V_{BarL} \tag{5-3}$$

$$f_{torsional} = \frac{V_S}{2L} \tag{5-4}$$

where: D is a specimen's diameter, T is a dimension and Poisson's ratio-dependent correction factor (ASTM International, 2014a), and V_S is S-wave velocity.

A variation of damping ratio with the specimen length is used in this paper based on the first arriving wave. The geometric attenuation term in Equation 3-31 can be dropped (as $\beta = 0$ for plane waves) and a concept of an effective wavelength (λ_P, which is the wavelength calculated based on the width of the first arriving pulse) normalized with the specimen length is introduced. Therefore the damping ratio presented in Equation 3-32 can be rewritten as:

$$\zeta = \frac{1}{2\pi}\frac{\lambda_P}{L}\ln\left({}^{A_0}/_{A_L}\right) \tag{5-5}$$

where A_0 is the reference amplitude (i.e. the first peak amplitude of the shortest specimen tested with 54 kHz transducer) and A_L is the first peak amplitude measured for a specimen with an arbitrary length (L). The literature on the material damping ratio of concrete is very limited. Kuhl and Kaiser (1952) tested concrete samples in the sonic frequency range. They reported values of the damping ratio of $3.9 - 4.6x10^{-3}$. However, it has to be noted that the specimens were tested up to 10 kHz; therefore, the reported values cannot be compared with the values presented in this study.

In this chapter, the recorded signals are analyzed in time and frequency domains separately. Moreover, the short-time Fourier transform (STFT) is used, which transforms a time signal $x(t)$ into the time-frequency domain. The spectrogram is defined as the squared amplitude of the STFT:

$$|\mathrm{X(t,f)}|^2 = \left| \int_0^t x(t) w(t-\tau)\, e^{-i2\pi f t} dt \right|^2 \tag{5-6}$$

where $w(t)$ is the analysis window function, and the position of the window is given as τ. The STFT is beneficial over the conventional Fourier transform as it provides temporal information along with the frequency.

Finally, two concepts of a wavelength are considered in this study. First, a wavelength in a traditional sense is called a nominal wavelength ($\lambda_{nominal}$) and is calculated based on P-wave velocity and a nominal resonant frequency of each transducer. Moreover, a wavelength associated with the first arriving wave peak is used and denoted as: λ_P, which is calculated based on P-wave velocity and a frequency calculated based on a width of the first arriving pulse (or time between the two consecutive zero-crossing points on a response plot). The λ_P can also be treated as the effective wavelength.

5.3 Experimental methodology

The investigation is performed in two phases. Firstly, a Doppler laser vibrometer is used to characterize ultrasonic transducers used in the study, to identify vibration modes observed in the tests, and to compare typical laser and ultrasonic measurements. Secondly, a traditional UPV evaluation is performed using a transmitter/receiver configuration to evaluate the influence of specimen dimensions on UPV results. In the presented experiments, 30 concrete specimens are tested. Assuming the worst standard deviation value presented by Yaman et al. (2001), i.e. $\sigma = 76\frac{m}{s}$ and the mean velocity of $4500\frac{m}{s}$, the sample size of 30 specimens gives the acceptable difference between the true average and the sample average equal to 1% (ASTM International, 2017a). The specimens are tested with three

types of ultrasonic P-wave transducers: 54, 150, and 250 kHz. In the following sections, the preparation of specimens and laboratory setups used in the test are described. Table 5-1 gives details of each activity of the methodology, refers to the corresponding results section, and presents the main conclusions.

Table 5-1. Methodology and flow chart of data processing

Activity	Flow chart	Main conclusions
Calibration of ultrasonic equipment (sections 5.4.1-5.4.3)	Time delay calibration • Face to face • Calibration rods • Specimens → Time delays for each specimen diameter Response of piezo-drive to different excitation frequency (i.e. 54, 150, and 250 kHz) → Frequency dependent response Characterization of ultrasonic transducers with laser vibrometer → Compute FFT for different position along diameter	• Perform time-delay calibration directly on test specimens along with face-to-face calibration • Ultrasonic results are affected by frequency-dependent amplifier effects • The response of ultrasonic transducers includes multiple resonances
Numerical simulation (section 5.4.4)	Modal analysis of concrete specimens → Resonant frequency of specimens (i.e. axial, bending, and torsional)	• Resonant frequencies of specimens do not mask ultrasonic results
UPV tests (sections 5.4.5-5.4.8)	UPV tests • Ultrasonic transducer/receiver • Ultrasonic transducer/laser vibrometer → • Diameter effect • Length effect • Evaluation of damping	• Minimum specimen length should be extended to at least four effective wavelengths • Lower velocity is observed until the specimen diameter is larger than three times the effective wavelength

5.3.1 Specimens

In this study, two groups of concrete specimens are tested. The first group consists of 10 standard cylindrical specimens of size 100 x 200 mm used for evaluation of concrete strength (ACI Committee 318, 2014; ASTM International, 2014a). The second group of 30 specimens was used for ultrasonic evaluation. The ultrasonic evaluation specimens were produced in three different diameters (D = 100, 150, and 200 mm) and ten length variations (L = 50 to 500 mm long, with a 50 mm length increment between specimens). Therefore, when the specimen D10L15 is analyzed, it is the specimen with a diameter of 100 mm and a length of 150 mm. All specimens were cast from an industrial concrete batch

(standard air-entrained mix of 30 MPa, water/cement ratio of 0.55, with the air content of 7.5 %; Fine aggregates meet the grading requirements of ASTM C33 (ASTM International, 2018b), fineness modulus is in a range of 2.3 and 3.1; the nominal maximum size of the coarse aggregate: 19mm; slump test of 90 mm) mixed in a concrete mixing vehicle. All concrete specimens were cast at the same time, wetted for five days, after which the moulds were removed. Compressive strength test specimens were stored in a humidity room, while ultrasonic evaluation specimens were stored in a laboratory environment until performing the ultrasonic evaluation due to the space limitation in the humidity chamber. At the age of 28 days, five cylinders were tested for compressive strength, according to ASTM: C39 (ASTM International, 2018a) (the average compressive strength was 34.86±1.67 MPa). At the age of 56 days, the additional test for static Young's modulus and Poisson's ratio (ASTM International, 2012) was performed, and the compression test was repeated (both tests were done with the remaining five specimens). Material properties obtained in the second test are listed in Table 5-2.

Table 5-2. Material properties at 56 days

	56 days
Compressive strength [MPa]	35.45±2.64
Static Young's modules (E) [GPa]	26.3
Poisson's ratio (ν)	0.19

5.3.2 Laboratory setup

A schematic diagram of the test setups is shown in Figure 5-1-a and Figure 5-1-b. ASTM recommends transducers with a resonant frequency in the range of 20-100 kHz in the UPV test (ASTM International, 2016a). Therefore, in the first setup (Figure 5-1-a), ultrasonic transducers with the resonant frequency: fc=54 kHz are used. The 54 kHz transducer is the older generation than the probe presented in Chapter 4; therefore, the characterization of that probe needs to be performed.

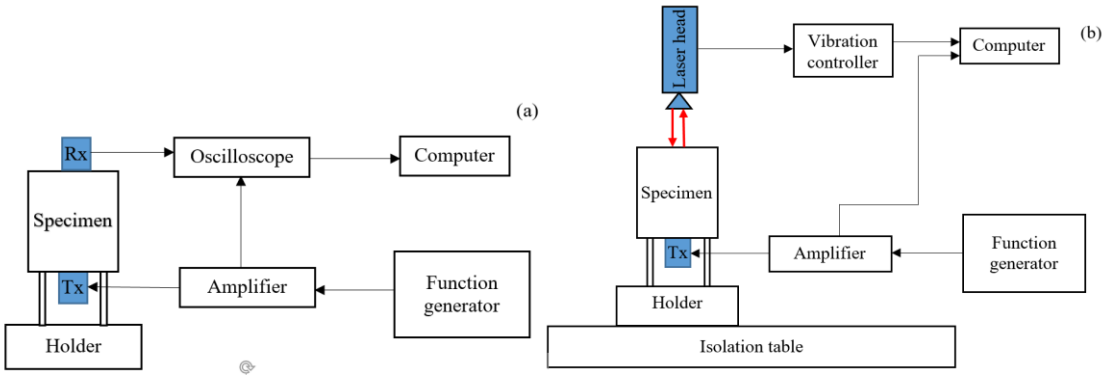

Figure 5-1. Laboratory setups used for: (a) ultrasonic transmitter (Tx)/receiver (Rx) setup, and (b) ultrasonic transmitter/laser vibrometer configurations.

On the other hand, the use of higher frequencies is required for the detection of smaller imperfections. Thus, ultrasonic transducers of fc=150 kHz and fc=250 kHz are also used in this work. HP33120A function generator is used to provide a different input signal (54, 150, and 250 kHz square pulses, which are amplified to the amplitude of ± 125V) to the transmitter. Each specimen is supported on the holder, and the sensors are placed on each face of the cylinder. The readings are taken and stored by Keysight DSO-X 3032T oscilloscope.

The setup with a laser vibrometer is shown in Figure 5-1-b. The use of the laser vibrometer helps to eliminate the effect of the receiver frequency response on the output reading. The laser vibrometer has a flat frequency response in the ultrasonic range (i.e. 24 MHz bandwidth) and measures vibrations in physically interpretable vibration units, e.g. displacement [nm], or velocity [nm/s]. The laser system is used in the displacement decoder mode enabling measurement of vibration displacement up to ±75nm. The input section of the laser vibrometer experimental setup remains unchanged as in the transmitter-receiver test. The response is read with a laser sensor head (LSH, Polytec OFV-534), which is connected to the vibration controller (OFV-2570). The laser system is triggered by the input signal, which is also recorded. The response is measured over the 4 cm wide circular area of a top surface of the cylinder (a total of 24 radial positions at five different radii are used).

5.3.3 Calibration of ultrasonic equipment

An important step in the measurements is the calibration of ultrasonic equipment (Khan, Zahid et al., 2010) to evaluate a time delay introduced by the instrumentation itself and the coupling between the transducer and the medium. In this study, the calibration is performed and compared using steel rods

(length of 51, 101, 150, and 201 mm), PVC rods (length: of 49, 100, 158, and 199 mm), and the concrete specimens themselves. The latest accounts for the actual coupling for the specimens tested. Moreover, a face-to-face calibration of ultrasonic transducers is performed.

5.3.4 Ultrasonic transmitter/receiver measurements

The first group of tests is the standard UPV configuration (i.e. using the ultrasonic transmitter-receiver configuration shown in Figure 5-1). The P-wave velocity of concrete specimens is calculated as distance over time. The time of flight is manually selected from the recorded data. Each recorded signal represents an average of sixteen measurements. The maximum measured variance between a single measurement and the average is 4%. The main wavelengths corresponding to the nominal resonant frequencies for each transducer are presented in Table 5-3.

Table 5-3. Ultrasonic transducers and corresponding main nominal wavelength (V_P = 4500 m/s).

Transducer	Wavelength [mm]
Low frequency (f_c = 54 kHz)	83.3
Medium frequency (f_c= 150 kHz)	30
High frequency (f_c= 250 kHz)	18

5.3.5 Ultrasonic transmitter/laser vibrometer measurements

For the laser vibrometer measurements, the input signals are generated with ultrasonic transducers. Laser vibrometer tests follow the same procedures described for the ultrasonic transmitter-receiver tests. However, because the signal to noise ratio is smaller than for UPV measurements, each signal represents an average of 150 measurements.

5.4 Experimental results and discussion

5.4.1 Time delay calibration

The first calibration was performed on the calibrating rods. The time delay is evaluated from the time of flight-length plots obtained from calibration rods. The delay is calculated from a linear regression intercept of the measured time of flight data points. However, the obtained delays do not provide consistent UPV results when used in concrete specimens. The time delays calculated based on PVC and steel rods do not account for the attenuation introduced by aggregates in concrete, nor the actual time delay due to the response of the electronic system (which can be affected by different coupling

between transducers and two different calibration rod materials). Therefore, a face-to-face calibration (when wear surfaces of transmitter and receiver are coupled) for all transducers is performed. Delays obtained from this test can be treated as the delay that is present in the system for a zero specimen length. However, this approach does not account for the actual coupling between the tested material and the transducers. To account for that, the calibration was performed based on the UPV data. First, the first arrival times are plotted against the specimen length, and the linear interpolation is performed. Based on the interpolation line equation, a delay is evaluated, so the y-intercept matches the face to face calibration time (Table 5-4).

Table 5-4. Time delays [us] of the ultrasonic systems used in the study.

		Transducer nominal frequency		
Procedure		54 kHz	150 kHz	250 kHz
Face to face		3.06	0.76	0.8
Rod calibration (averaged)		3.99	1.35	1.22
Concrete specimens	D10	1.07	-0.14	0.13
	D15	-0.42	0.28	2.99
	D20	0.66	0.87	0.18

Next, all of the time-signals are corrected with respect to the individual delay. The procedure has to be applied for each specimen set as the delay might be affected differently depending on the coupling and an aggregate-wavelength interaction. Therefore, it is recommended to perform the calibration on the actual material, including the information about transducers face-to-face calibration.

5.4.2 Input pulse frequency components

First, an electric input pulse analysis is performed. Amplified time traces for square pulses used in the study (54, 150, and 250 kHz) with corresponding frequency spectra are shown in Figure 5-2.

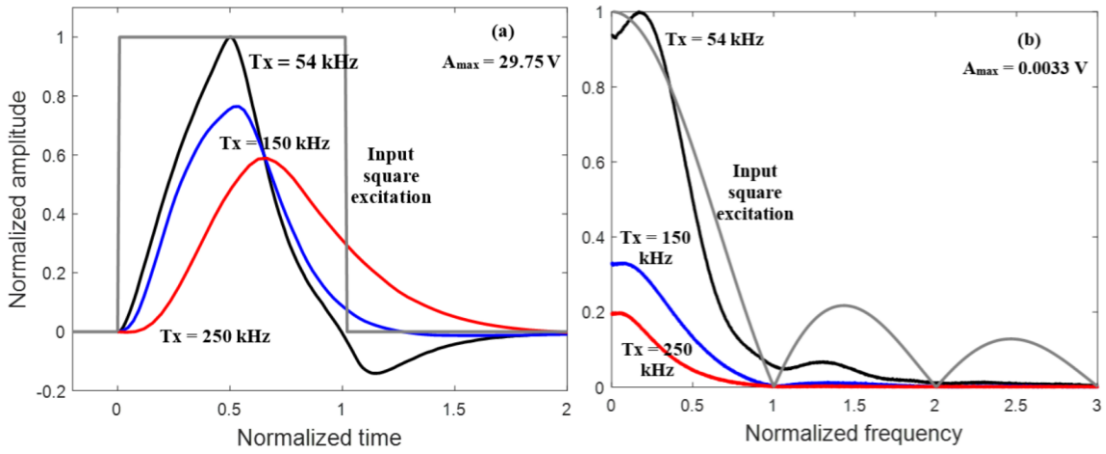

Figure 5-2. (a) Amplified electric square pulses used as excitation for different transducers; maximum amplitude (A_{max} = 29.75 V), and (b) corresponding spectra; A_{max} = 0.0033 V.

Despite the constant square excitation function, a significant amplitude change in the time signals can be distinguished due to the limitation of the electronic circuit of the amplifier. The response of the amplifier is frequency-dependent and can lead to up to 40% amplitude reduction for the input pulse. Moreover, it introduces a slight frequency shift. The frequency of the pulse can differ by up to 7% of the nominal value. The observed values are device-dependent and should be considered when building a test setup.

5.4.3 Ultrasonic transmitter output

An ultrasonic signal measured by a receiver should be treated as a convolution of the input signal sent to the specimen, coupling between the transmitter and the specimen, specimen characteristics, coupling between the receiver and the specimen, and finally, the receiver characteristic. The measured signal can be expressed in the frequency domain as:

$$Y(\omega) = X(\omega)H_{C1}(\omega)H_O(\omega)H_{C2}(\omega)H_{Rx}(\omega) \tag{5-7}$$

where $H_O(\omega)$ is the frequency response function (FRF) of a tested element, $X(\omega)$ and $Y(\omega)$ are the measured input and output signals, $H_{C1}(\omega)$ *and* $H_{C2}(\omega)$ are the FRFs of the coupling, and H_{Rx} is the FRF of the receiver. Therefore, it is critical to know the properties of the input signal and the receiver (i.e. perform a transducer characterization process). It can be assumed that the coupling effect is accounted for with the calibration of the transducers.

Ultrasonic transducers used in the study are scanned with the laser vibrometer to characterize the input signals for the UPV test. The setup follows the one shown in Figure 5-1-b. The laser has a limitation of maximum measured displacement. Therefore, the amplifier cannot be used, and a 10V square pulse is used as the input. The readings (27 for the 54 kHz and 17 equally spaced points for the 150 and 250 kHz transducers are used) are taken along a diameter of the transducers at the wear face. Then, the readings are grouped into three segments responsible for the edge, mid-section, and central response of the transducer. The averaged response of each group is evaluated and shown in the frequency domain in Figure 5-3. A slight shift in the nominal resonant frequencies is seen. The areas further away from the center contribute less to the maximum frequency. Those areas introduce other, lower than nominal frequencies. In the extreme case of 250 kHz transducer, one can observe strong amplitudes within 15-38 kHz range, and the edges of the transducer present very little energy within the nominal frequency bandwidth.

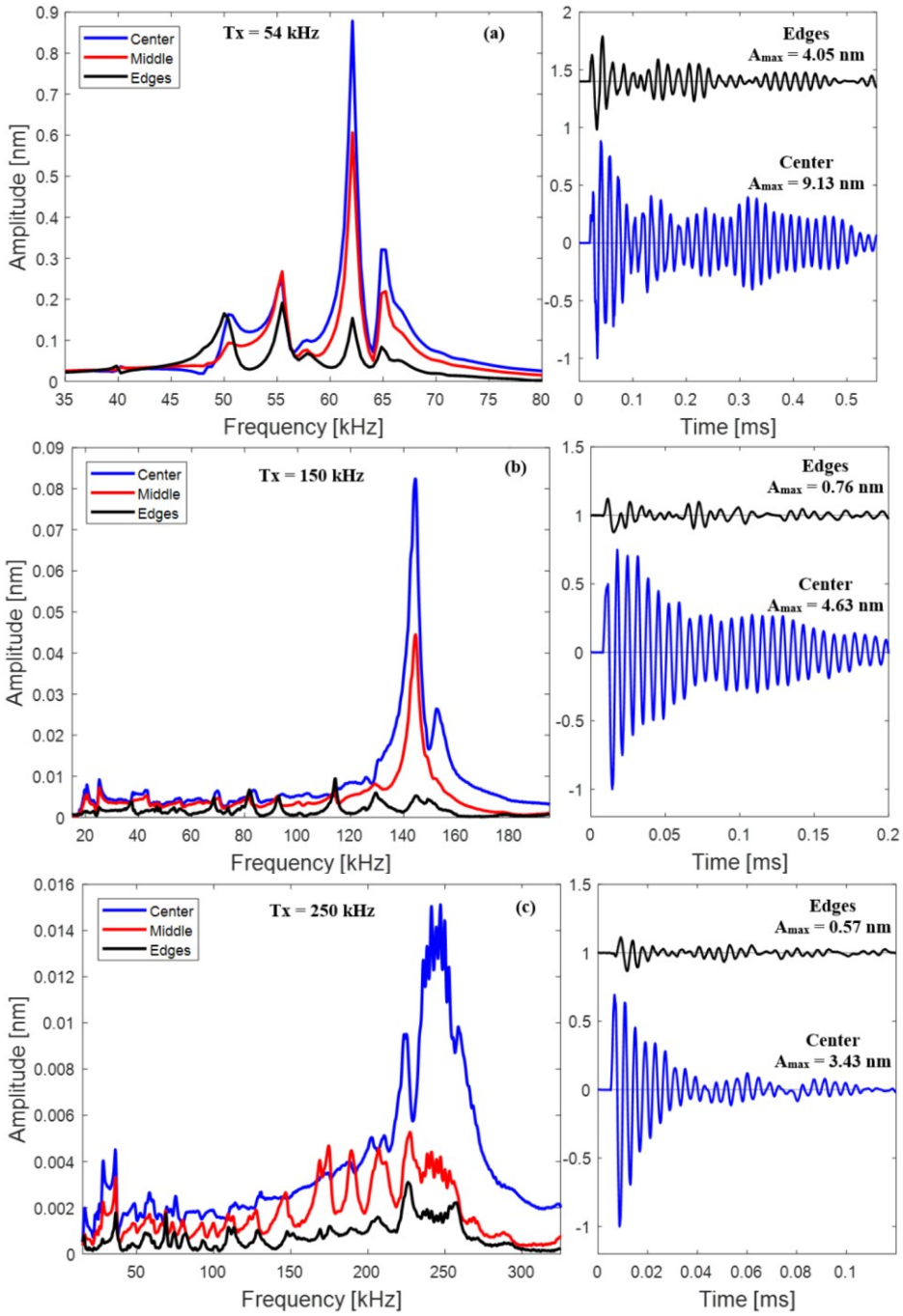

Figure 5-3. Frequency response of ultrasonic transducers measured with a laser vibrometer. Nominal frequencies: (a) Tx = 54 kHz, (b) Tx = 150 kHz, and (c) Tx = 250 kHz. Transducer wear face is divided into three regions, which contribute differently in overall frequency response. To emphasize the difference between time signals, only centre and edge time signals are shown.

5.4.4 The natural frequency FEA analysis

A numerical modal analysis is performed to characterize the tested specimens and verify that the resonant frequencies of the specimens are not masking ultrasonic results. The D10 specimen group was modelled as a solid, homogenous medium in Abaqus using the following material properties: assumed concrete density: 2.407 $\frac{g}{cm^3}$; Young's modulus: 47.133 GPa (which is a dynamic property, calculated based on the UPV data, taken as an average in the D10 specimen group); and the Poisson's ratio: 0.18678. The simulation uses a free-free boundary condition, and it aims to find the frequencies of the longitudinal, bending, and torsional vibration modes. The whole geometry is meshed with linear wedge elements of 6-node linear triangular prism type (C3D6 (Dassault Systemes Simulia Corp, 2012)). The simulation uses a linear perturbation procedure in a frequency mode. The procedure extracts eigenvalues to calculate the natural frequencies and the corresponding mode shapes (Dassault Systemes Simulia Corp, 2012). Table 5-5 shows a range of the natural frequencies obtained using the numerical simulation with the theoretical values for cylindrical shapes.

Table 5-5. Range of theoretical and numerical natural frequencies of specimen group D10 based on specimens D10L5 and D10L50.

	Frequency [kHz]		
	Axial	Bending	Torsional
Theory	4.41-36.61	1.63-112.38	2.86-23.76
ABAQUS	4.59-37.86	1.51-115.50	2.79-23.06
Relative Difference [%]	3.41-4.01	2.77-7.32	2.72-2.97

The range of results is given by specimens D10L5 and D10L50. The model shows a good correlation with the theoretical values. For short specimens, the natural frequencies are within the ultrasonic range of frequencies used in the study. However, the natural frequencies are dimension dependent and can be easily tracked when Fourier amplitude spectra are analyzed for different specimen length. Therefore, the natural frequencies are either not masking ultrasonic readings or can be easily identified.

5.4.5 Laser vibrometer analysis

In the laser vibrometer test, the specimens are scanned using the setup shown in Figure 5-1-b. The main goal is to identify the main vibration mode that governs the displacement of the receiving surface under the 250 kHz excitation frequency, which is beyond the frequency range by ASTM (ASTM International, 2016a). Readings are taken at 121 locations at the top surface of a specimen. The main benefit of the test is that the reading is not affected by the receiver's FRF. Through Figure 5-4 to Figure 5-6, the laser vibrometer readings taken at the center of specimens D10L5, D10L15, and D10L35 are compared with the ultrasonic receiver readings (both in the time and frequency domains).

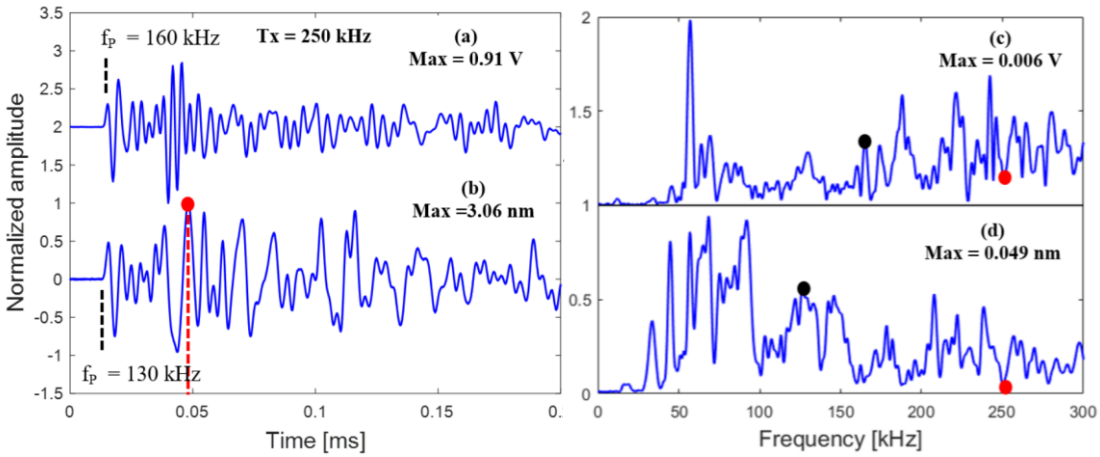

Figure 5-4. Comparison of ultrasonic and laser vibrometer readings under 250 kHz input excitation for specimens D = 10cm, L = 5cm; (a) time signal measured with the ultrasonic receiver (b) time signal measured with the laser vibrometer; the red line corresponds to the time step presented in Fig. 5-8 while the black dashed lines highlight the first pulse; (c, d) corresponding amplitude Fourier spectra; f_P = frequency from the first arriving pulse; the red dots correspond to the nominal resonant frequency of the transmitter while the black dots correspond to the frequency of the first pulse.

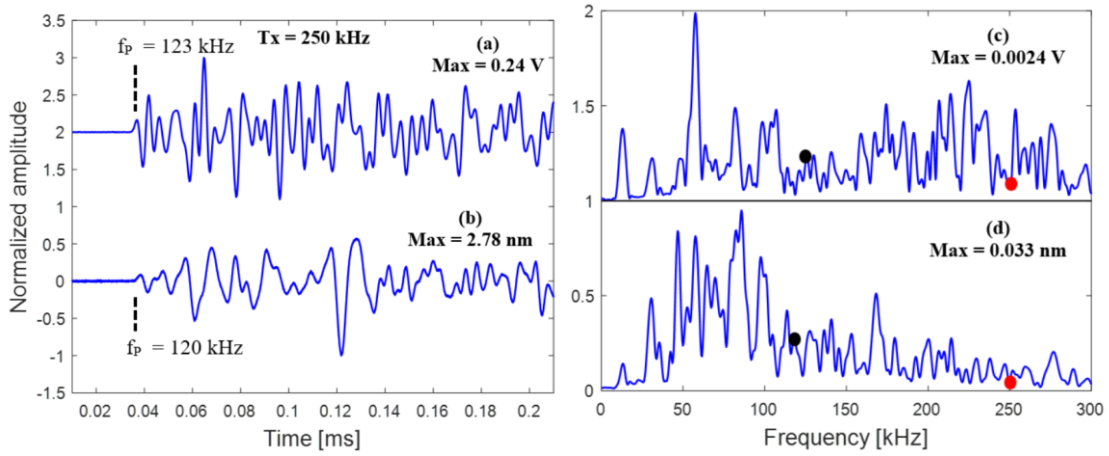

Figure 5-5. Comparison of ultrasonic and laser vibrometer readings under 250 kHz input excitation for specimens D = 10cm, L = 15cm; (a) time signal measured with the ultrasonic receiver (b) time signal measured with the laser vibrometer; the black dashed lines highlight the first pulse; (c, d) corresponding amplitude Fourier spectra; f_P = frequency from the first arriving pulse; the red dots correspond to the nominal resonant frequency of the transmitter while the black dots correspond to the frequency of the first pulse.

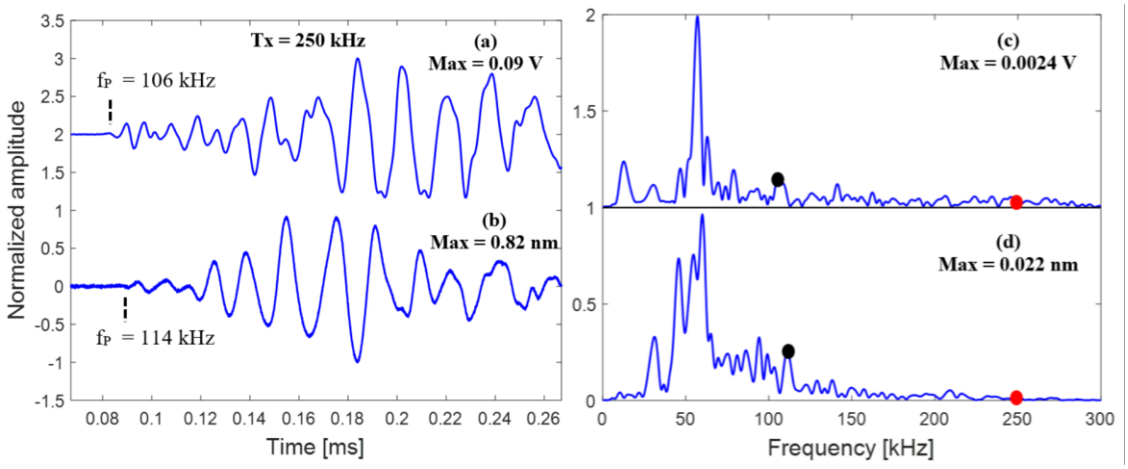

Figure 5-6. Comparison of ultrasonic and laser vibrometer readings under 250 kHz input excitation for specimens D = 10cm, L = 35cm; (a) time signal measured with the ultrasonic receiver (b) time signal measured with the laser vibrometer; the black dashed lines highlight the first pulse; (c, d) corresponding amplitude Fourier spectra; f_P = frequency from the first arriving pulse; the red dots correspond to the nominal resonant frequency of the transmitter while the black dots correspond to the frequency of the first pulse.

For the time signals, the first couple of oscillations are present (duration of 0.2 ms of the signals, including pre-arrival, is presented). For the calculation of Fourier spectra, a rectangular window with a duration of 0.4 ms is applied to the signals. A noticeable amplitude reduction can be observed. In the case of laser reading for D10L35 (Figure 5-6-b), 150 averages give still a relatively noisy signal and a barely noticeable first arrival. When the frequency of the first pulse is analyzed (highlighted at each time trace; the frequencies are also represented on Fourier spectra with black dots), a decrease is observed. It is important to note that even for the shortest specimen (i.e. 5 cm), the first pulse frequency is much lower than the expected input frequency. In the 250 kHz test, the size of aggregates plays a key role. The ratio of aggregate size ($\phi_{aggreg} = 20\ mm$) to a nominal wavelength ($\lambda_{nominal} = 18\ mm$; Table 5-3) is: $\phi_{aggreg} / \lambda_{nominal} = 1.11$. In the frequency domain, two effects can be observed. Firstly, for both the ultrasonic and the laser vibrometer readings, the attenuation of high frequencies can be seen. A progression of the attenuation of high frequencies with specimen length can be seen in Figure 5-4 to Figure 5-6. The analysis is also continued in the time-frequency domain. Figure 5-7 presents the STFT spectrograms calculated for specimens D10L5 (Figure 5-7-a) and D10L50 (Figure 5-7-b). For the calculation of spectrograms, a 0.16ms Gaussian window with a 50% overlap is used.

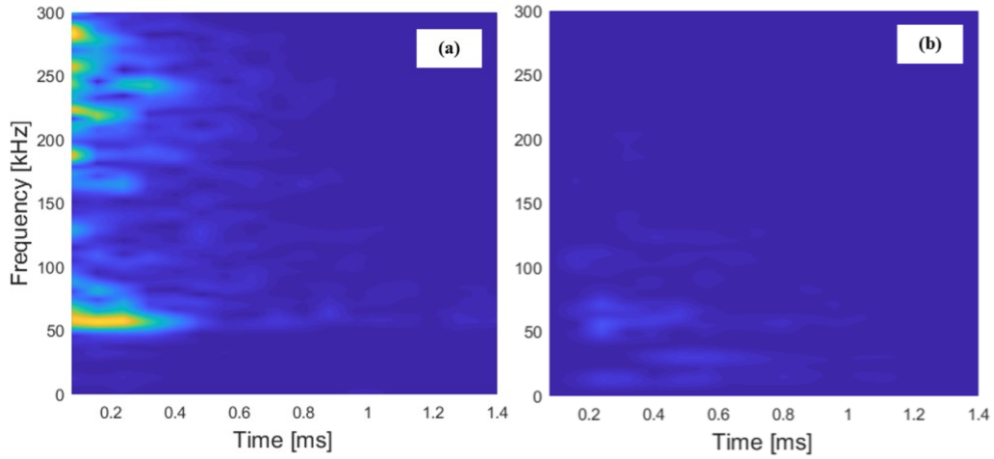

Figure 5-7. STFT time-frequency representation of the ultrasonic signals measured under 250 kHz input excitation for specimens of D= 10cm (a) L = 5cm, (b) L = 50cm. The amplitude limit is the same for both figures. The meaning of colour is yellow=high and blue=low values.

The amplitude attenuation is observed both with time and increasing specimen length. Even for the shortest specimen (L = 5cm), the effect is significant, and the high frequencies attenuate much faster than the 50 kHz component. When the specimen gets longer, the frequencies above 150 kHz are

attenuated completely, and the frequencies lower than 50 kHz become more dominant. Secondly, the ultrasonic data show a single dominating frequency peak (57 kHz) while a couple of dominating frequencies are present in the case of the laser vibrometer measurements. The difference comes from the convolution of the real response with the receiver FRF. Therefore, it would be beneficial to deal with a calibrated transducer to have a non-biased response. Finally, a typical surface scan (measured for the specimen D10L5) is presented in a graphical form, so the mode of surface vibration is visible (Figure 5-8). A low-pass FIR filter with a 300 kHz stop-band frequency is applied to the signals, so the main vibration mode, along with the high frequencies, can be observed.

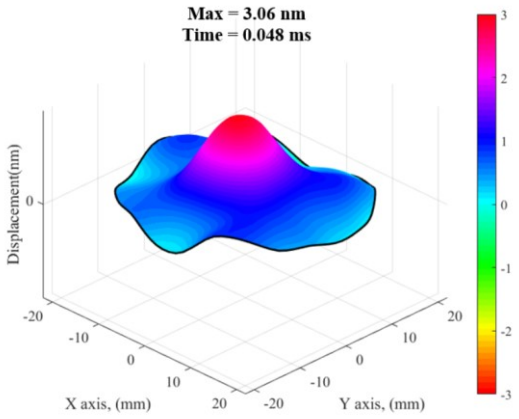

Figure 5-8. Maximum displacements measured with the laser vibrometer in the specimen D10L5 (D = 10cm, L = 5cm) under 250 kHz excitation. Maximum displacement for specimens D10L15: Max = 2.78 nm and D10L35: Max = 0.82 nm.

In terms of observed displacements, once again, the amplitude attenuation is distinguishable. When specimens D10L5 and D10L35 are compared, the relative difference between the first arriving peaks (P_{peak}) is 95%, while the maximum vibration is reduced by 75%.

Moreover, in the D10L5 specimen, the energy is more concentrated in the center of the scanned surface with the strong influence of high-frequency vibration seen near the edges, while for the D10L35, the edge vibration is reduced, and the main energy is distributed over the larger surface area. As a result, the wear face of the receiver will be affected differently, causing a different behaviour of the receiver. Additionally, the main vibration mode is related to low frequencies present in the responses, and it becomes more evident as the specimen length increases, and high frequencies attenuate completely.

5.4.6 Diameter effects

In the first set of the UPV results, diameter effects are studied. The diameter effects are not included in the ASTM standard (ASTM International, 2016a). For each tested specimen, velocity for the first arrival is calculated (times are corrected with the time delays given in Table 5-4). The effective wavelength (λ_P) is calculated based on maximum velocity for each diameter and a frequency calculated based on a width of the first arriving pulse. Next, the velocities are plotted against corresponding specimen length normalized to the effective wavelength. Table 5-6 summarizes a ratio between specimen diameter and both nominal and effective wavelengths.

Table 5-6. Diameter-wavelength ratio for all the tested configurations

Tx	D/λ ratio	D10	D15	D20
54kHz	$D/\lambda_{nominal}$	1.22	1.80	2.42
	D/λ_P	0.46 – 1.11	1.17 – 1.62	1.79 – 2.05
150kHz	$D/\lambda_{nominal}$	3.35	4.92	6.61
	D/λ_P	1.60 – 2.74	2.19 – 3.28	2.94 – 4.40
250kHz	$D/\lambda_{nominal}$	5.50	8.27	10.70
	D/λ_P	1.78 – 3.96	2.51 – 4.41	3.16 – 7.74

The width of the first arriving pulse changes with specimen length. Therefore, for effective wavelength comparison, a length-dependent range of the ratios observed for all diameter groups is presented. Figure 5-9 presents a variation of the P-wave velocity for specimens of different diameters tested with the 54 kHz transducer setup.

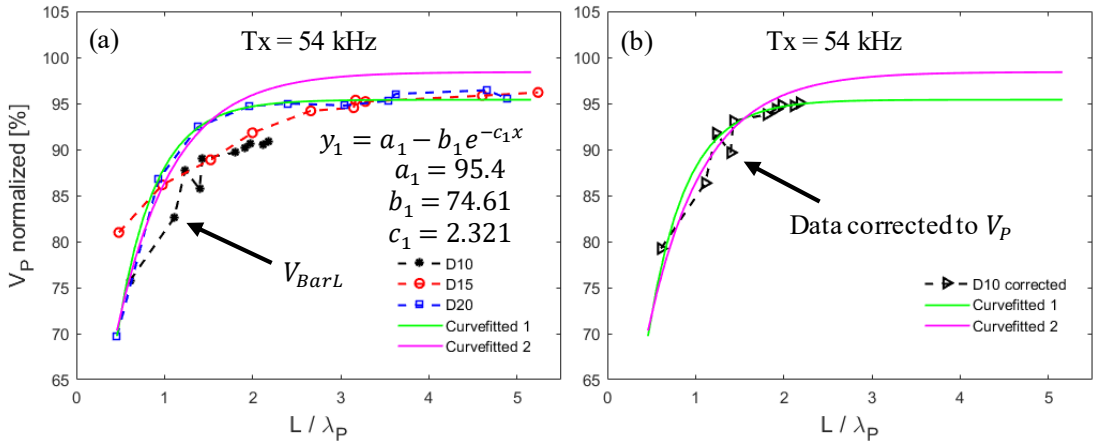

Figure 5-9. Variation of the wave velocity with the specimen length (Tx = 54 kHz) normalized to Vp = 4673m/s; black, red, and blue colours correspond to different specimen diameters; the green fitted line is fitted based on D20 while the "curvefitted 2" line is fitted based on Fig. 5-10-c; (a) For the specimen group with D = 10cm velocities deviate from the expected P-wave velocity values (b) corrected velocity values for the D = 10cm specimen group.

An exponential curve (curve fitted line 1) given as $y = a - be^{-cx}$, where a, b, and c are fitted line parameters, is fitted to the results of the D20 group tested with 54 kHz transducer. It can be seen that the specimen group D10 has a significantly lower value of velocity in comparison with the other two sets and the fitted curve (Figure 5-9-a). This phenomenon can be explained, taking into consideration the diameter to effective wavelength ratio. When the ratio is lower than the unity (in the case of the tested group D10, it can be as low as 0.43) the V_P formula (Equation 3-11) is not valid as the medium is restricted by its boundary from the effective wavelength point of view. In such a situation, a velocity of the first arriving wave is given as the V_L (Equation 5-1) Therefore, if the V_L has to compared to other V_P results, it needs to be corrected by a ratio of: $^{1-\nu}/_{(1+\nu)(1-2\nu)}$, where ν is a Poisson's ratio. The corrected V_P results for D10 specimens are presented in Figure 5-9-b. The correction shifts the results, so they match with the curve fitted line 1. However, the results still have lower values than the curve fitted line 2 (fitted based on Figure 5-10-c). For the specimens tested with 54 kHz transducer $D/\lambda_P \leq 2$ (Table 5-6) and the P-wave velocity is still affected by the bar vibration effect. If the error has to be kept within 5%, the ratio has to be increased to: $D/\lambda_P \geq 3$. Moreover, it is important to note that if the high frequency (e.g. 250 kHz) have to be used in the UPV test, the relative difference between $D/\lambda_{nominal}$ and D/λ_P can reach up to 70% (Table 5-6).

5.4.7 Length effects

Regarding the specimen length, the ASTM recommends using specimens that are at least one wavelength long (ASTM International, 2016a)[11]. The effects of an increasing length are not defined. In this part of the study, each diameter group is tested with a set of three transducers. The P-wave velocity is then presented against specimen length normalized to the effective wavelength (shown in Figure 5-10).

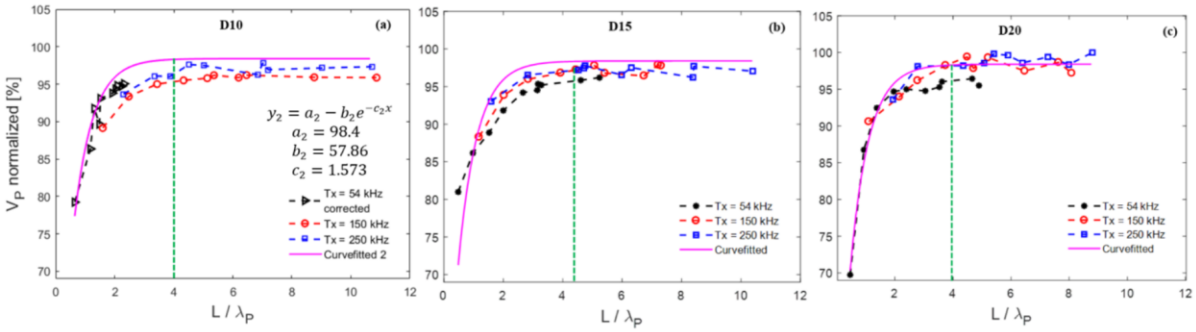

Figure 5-10. Variation of the wave velocity with the specimen length, normalized to Vp = 4673m/s; a) specimens D = 10cm with L = 5cm to L = 50cm, (b) specimens D = 15cm with L = 5cm to L = 50cm, and (c) specimens D = 20cm with L = 5cm to L = 50cm; the curve fitting is performed based on results presented in (c). The green vertical dashed lines show the minimal normalized length values so that the error between measured P-wave values and the fitted line is within 5%.

An exponential curve is fitted based on the D20 UPV results and added for each diameter group. A small diameter effect is still observed. P-wave velocity values that are observed for groups D10 and D15 presented in Figure 5-10-a and Figure 5-10-b, are slightly lower (up to 5%) than for the group D20 Figure 5-10-c. Therefore, consistency in specimen sample size is critical for the correctness of UPV results. When ASTM's 1-wavelength criterion (ASTM International, 2016a) is used, the difference between the lowest and the highest value observed in the tests can reach up to 20%. If the criterion is not fulfilled, the error increases rapidly to up to 30%. To keep the error of the UPV method within a 5% margin, a minimum length should be increased to 4 wavelengths (highlighted with the green vertical lines in Figure 5-10). Therefore, the near field effect can be omitted. An important note can be made for the high frequencies used in the test. One might select short wavelengths to detect smaller defects. However, the first arriving pulse can have a much longer width (i.e. a lower frequency), and the effective wavelength can be different than the anticipated one. Table 5-7 shows the comparison of the

effective wavelength (minimum and maximum values from all the specimen lengths are presented) to the nominal wavelength ($\lambda_P/\lambda_{nominal}$).

Table 5-7. The minimum and maximum values of effective to nominal wavelength ratios

	$\frac{\lambda_P}{\lambda_{nominal}}$		
Specimen	54 kHz	150 kHz	250 kHz
D10	1.05-1.57	1.04-1.56	1.35-3.00
D15	1.11-1.54	1.54-2.31	1.86-3.27
D20	1.18-1.35	1.51-2.27	1.44-3.52

In terms of high frequencies (i.e. 250 kHz), one might end up with the three times longer effective wavelength than the nominal wavelength (the worst-case scenario in the study gives 64mm instead of 18mm). Effectively, one would end up with a wavelength that would be produced by a 70 kHz transducer. Therefore, a small imperfection would still be difficult to detect using the velocity approach. Sample frequency spectra (an amplitude for each spectrum is normalized with respect to the highest observed value; amplitudes for the specimens longer than 250mm are multiplied by a factor of two) of tested specimens (D10 all lengths) are presented in Figure 5-11.

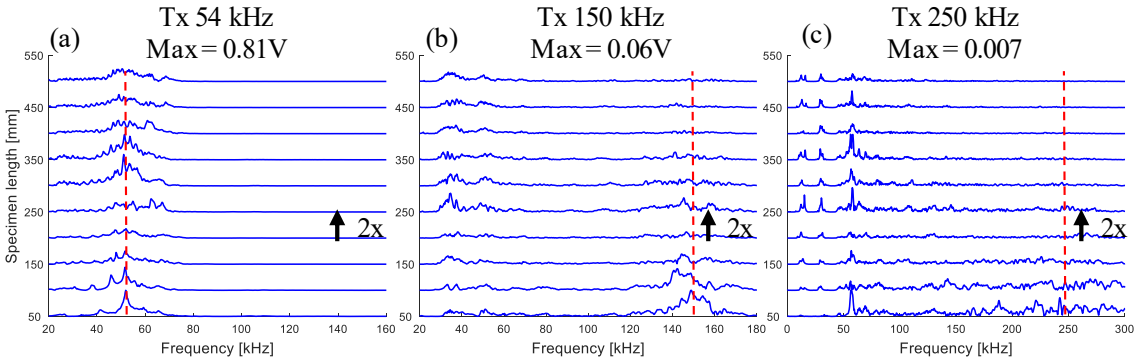

Figure 5-11. Variation of amplitude Fourier spectra for specimen D = 10cm and different lengths tested under (a) Tx = 54 kHz, (b) Tx = 150 kHz, and (c) Tx = 250 kHz inputs with the declared resonant frequency values of ultrasonic transducers (red vertical dashed lines). For each graph, amplitudes are normalized to the highest observed value. The amplitudes for specimens of $L \geq 250mm$ are multiplied by a factor of 2.

The frequencies below 100 kHz observed in Figure 5-11-b and Figure 5-11-c have constant values (i.e. do not depend on a specimen length. Therefore, the natural frequencies do not affect the UPV results). These frequencies are the characteristic frequency features presented in Figure 5-3-c, and their correct identification would not be possible without the proper characterization of the transducer. The effective wavelength effect is the most observable in the case of 250 kHz transducers. The nominal frequency is practically fully attenuated, starting from 25 cm of specimen length.

5.4.8 Amplitude analysis – attenuation

For the analysis of damping ratio based on P_{peak} amplitudes, the simplified damping ratio equation (Equation 5-5) is used. For each diameter group, the logarithmic decrement ($\ln(A_0/A_L)$) is presented against normalized length in Figure 5-12.

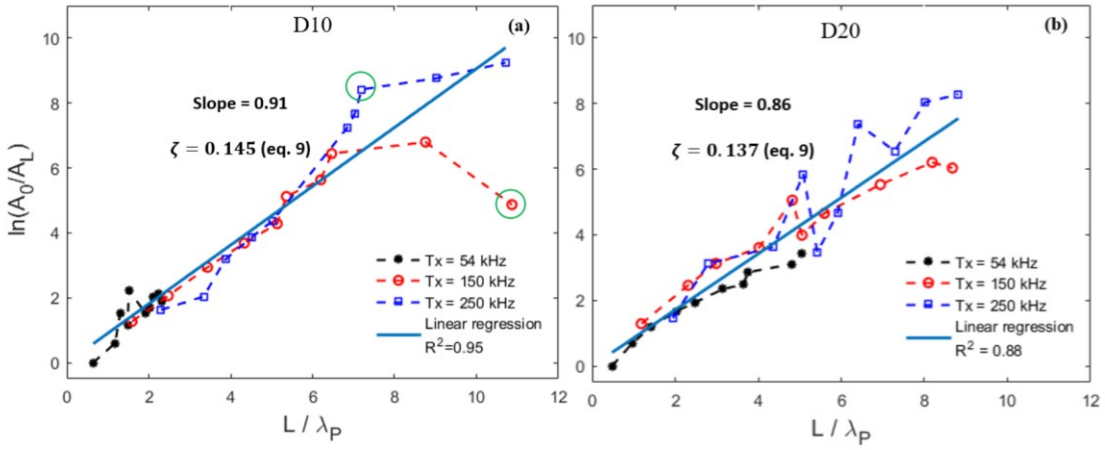

Figure 5-12. Variation of the logarithmic amplitude decrement with the normalized specimen length; a) specimens D = 10cm with L = 5cm to L = 50cm, the green circles highlight values removed from the linear regression (b) specimens D = 20cm with L = 5cm to L = 50cm; the damping ratio is calculated based on the slope of the regression line for each graph.

For the reference amplitude, A_0, the amplitude measured with 54 kHz transducer for the shortest specimen (L = 5cm) is used. Next, a linear regression model is used for the relationship between the logarithmic decrement and the normalized specimen length. Finally, the damping ratio is calculated as the slope of the regression line divide by 2π (rearranged Equation 5-5), and the mean damping ratio is $\zeta = 0.14$. For specimen group D15, higher variability was observed. However, the slope obtained with the linear regression showed the same value for the damping ratio. No clear relationship between the

damping ratio and frequency is observed in the frequency range used in the test (54-250 kHz). However, the variability of measured amplitude increases as the higher frequencies are used, and specimens get longer. The presented damping ratio analysis was performed in the ultrasonic range of 54-250 kHz, and it cannot be compared with reported values in the literature for the audio-frequency range.

5.5 Conclusions

UPV is a common method for the assessment of a relative concrete condition. In the presented study, several tests and specimen aspects are investigated, and the following main conclusions ensuring the increase in the UPV method reliability can be offered. The detailed conclusions are presented in Chapter 8.

1. It is recommended to perform the time delay calibration process directly on test specimens (a couple of different spacing distances between the transmitter and receiver have to be measured) along with the face-to-face calibration (to include the baseline delay of the ultrasonic system).
2. The current ASTM (ASTM International, 2016a) requirement (i.e. minimum specimen length of a single wavelength) causes the error of the UPV method up to 20%. The requirement should be extended to 4 effective wavelengths to ensure a 5% relative error.
3. It is found that at a certain specimen length level, recorded time signals have completely modified character. In practice, the arriving wave has a longer wavelength than the one sent from the transmitter. Therefore, the use of high frequencies (i.e. above 150 kHz) is limited and might be misleading because of the mismatch between the anticipated and arriving wavelengths. In such a situation, an effective wavelength should be used.
4. For the specimen diameter and wavelength ratio smaller or close to the unity, the longitudinal velocity is present, which is lower than the P-wave velocity. The effect is observed until $D/\lambda_P \geq 3$, and when is present, the P-wave velocity correction factor, based on the Poisson's ratio, has to be included.

Chapter 6
Novel application of wavelet synchrosqueezed transform (WSST) for condition assessment of cementitious materials

6.1 Introduction

The condition of structural materials in civil engineering applications is critical for the safety of structures. Therefore, the material's current strength is the most desired outcome of the non-destructive evaluation (NDE). Unfortunately, traditional ultrasonic non-destructive testing (NDT) methods for concrete, such as impact echo or ultrasonic pulse velocity (UPV), can only evaluate the elastic properties (McCann & Forde, 2001; Popovics, J. S., 2003). Some attempts have been made to find the relationship between concrete stiffness (evaluated in the low strain ultrasonic test) and strength (obtained in the large strain compressive test); however, due to the non-homogeneous character of concrete, the universal formula relating the two parameters do not exist.

A promising approach, based on the Griffin-Irwin criterion, has been demonstrated in the field of fracture mechanics. The criterion relates fracture stress and fracture toughness (which is a function of Young's modulus and strain energy release rate). Fracture propagation is a dynamic process, which means that the criterion relates large and low strain properties. In the studies on maraging steel and titanium alloy, Vary (1979; 1980) defined an empirical relationship in which the fracture strength depends on fracture toughness, wave velocity and the attenuation factor (a derivative of attenuation coefficient with respect to frequency). A similar observation has been made by Wang and Adler (1984) in their experimental study on graphite. They found that the attenuation coefficient is proportional to the porosity of graphite and expressed the fracture strength as a function of Young's modulus and attenuation coefficient. Based on these observations, the development of micro-cracks can be tracked with the attenuation analysis and offers a promising approach for application in concrete.

To overcome the low sensitivity of wave velocity-based methods in early damage detection (Stauffer et al., 2005), the latest trends focus more on the attenuation of a wavefront for both a longitudinal wave (P-wave) and a surface wave (Chaix et al., 2006; Kirlangic et al., 2015; 2016; Philippidis & Aggelis, 2005). Ultrasonic non-linear methods, such as non-linear elastic wave spectroscopy or non-linear impact resonance acoustic spectroscopy, have been shown to be very sensitive to microstructural changes (Bittner & Popovics, 2019; Eiras et al., 2014; Eiras et al., 2016; Eiras et al., 2018). Another approach focuses on the frequency-dependent scatter/attenuation for monitoring of concrete, which

allows to detect and locate the areal position of distributed sub-wavelength cracks in concrete (Song & Popovics, 2019a; Song & Popovics, 2019b).

In practical/field applications, access to a structure is often limited to one side only (i.e. concrete slabs, vacuum building walls). Thus, surface wave analysis is a natural solution. So far, the surface wave-based methods have been successfully applied for the characterization of the surface crack depth and quality of repair (Aggelis et al., 2009; Aggelis & Shiotani, 2007). Krstulovic-Opara et al. (1996) showed that based on the surface wave dispersion, it is possible to determine stiffness profiles within structural elements and monitor the curing of concrete with respect to depth. The change in signal amplitude of more than 95% was reported by Aggelis et al. (2011) when cracked specimens were compared with sound ones. In et al. (2009) used surface waves (the responses were measured with ultrasonic transducers and microphones) for the characterization in asphaltic concrete. Finally, non-contact sensing techniques were also applied for the reception of surface waves. Ham et al. (2017) and Song et al. (2019a) used a silicon-based MEMS acoustic array located at a few millimetres from concrete cover. However, the detailed frequency content that is transferred to the tested medium has been disregarded. Additionally, responses are usually measured with ultrasonic transducers, which do not have a flat frequency response.

Another limitation of the traditional ultrasonic NDT methods is related to sensing devices. ASTM recommends piezoelectric transducers with resonant frequency in the rage of 20-100 kHz (ASTM International, 2016a). However, the actual frequency content that is generated by the transducers is not known. In the wave velocity applications, it typically is not considered an issue; however, Wiciak et al. (2020) showed that additionally to the driving frequency, other frequency components might be excited, and the arriving wavelength might be different than anticipated. However, if the change of signal amplitude due to defects is analyzed, proper frequency characterization is a necessity. Additionally, the signal's amplitude depends highly on a coupling quality. The effect of coupling can be eliminated by using non-contact devices such as non-contact piezoceramic transducers (Abraham et al., 2012) or lasers (Mori et al., 2002; Owino & Jacobs, 1999). Alternatively, mixed setups consisting of a contact transmitter and non-contact receiver (Abraham et al., 2012; Zhu & Popovics, 2005) or non-contact transmitter and coupled receivers (Choi et al., 2018) have also been developed.

Finally, non-destructive evaluation is being improved through novel signal processing techniques that include more than one data-point of information. Velocity based methods analyze signals only in the time domain (UPV) or frequency domain (impact-echo) using basic fast Fourier transform

algorithms. On the other hand, time-frequency (TF) methods allow for simultaneous analysis in time and frequency domains. Popular TF techniques include short-time Fourier transform (STFT) and wavelet transform (WT). The typical civil engineering applications focus on a system identification problem (i.e. estimation of natural frequency, damping ratio, and mode shapes: (Kijewski & Kareem, 2003; Xiang & Liang, 2012; Yang et al., 2011)). TF methods were also applied for the evaluation of seismic attenuation (Reine et al. 2009). Recently, squeezed versions of some TF methods have been developed, such as squeezed-STFT (SFT, (Thakur & Wu, 2011)), or wavelet synchrosqueezed transform (WSST, (Daubechies et al., 2011)). Those transforms offer reduced smearing observed around the frequency values on time-frequency graphs and allow for decomposition of multi-component signals into individual components with the exclusion of noise. The original TF applications included analysis of electrocardiographs (Daubechies et al., 2011; Thakur & Wu, 2011) and speech signals (Daubechies et al., 2017). Later on, the TF methods have been adopted for fault detection of highly non-stationary vibration signals (e.g. gearboxes, (Hazra et al., 2017)), and successful applications of the WSST to seismic measurements have also been reported (Herrera et al., 2013; Wang, P. et al., 2014). The analysis of extracted components allows observing how individual frequencies, and wavelengths, are affected while a wave propagates in a medium.

This research offers the novel application of the WSST to include the wave attenuation approach for condition assessment of cementitious materials evaluated from the surface. Firstly, the capabilities and limitations of the method are examined on three synthetic models. Next, the characterization of the ultrasonic transducer is performed with the laser Doppler vibrometer. The responses are measured along the transducer diameter, and the resonant frequencies are defined from amplitude spectra. The most sensitive vibration modes are extracted from the recorded signal with the WSST. This allows for the analysis of individual wavelengths.

The WSST is also applied to two experimental evaluations. The first application focuses on the distributed damage detection issue by examining concrete beams in two material conditions (the damage is induced by freeze and thaw cycles). The responses are measured using four different sensors (i.e. accelerometer, ultrasonic probe, laser Doppler vibrometer, and hydrophone). Two sensors are full-contact receivers; the laser is a non-contact receiver (i.e. no coupling effects); whereas the hydrophone is placed in a plastic tube with a rubber membrane and offers a novel application of surface measurements using fluid interphase that is considered as a semi-contact receiver. The responses of all sensors are analyzed with the WSST, and the selection of the most sensitive transducer is discussed. In

the second application, a localized damage detection problem is considered based on a cemented sand specimen with an embedded subsurface void.

In the proposed methodology, full-time signals and modes extracted from WSST are analyzed and compared. The relative attenuation index is introduced and calculated based on the spectra of recorded signals. Additionally, phase velocity dispersion curves are analyzed, and the relative dispersion index is used for quantitative comparison.

6.2 Experimental procedure and setup

6.2.1 Methodology

The proposed methodology is divided into four sections: (i) a synthetic data example, presenting capabilities and limitation of the WSST technique, focusing on the ultrasonic frequency range, (ii) characterization of ultrasonic transmitter and extraction of vibration modes with the WSST, and applications of the WSST-based velocity and attenuation analysis technique for the evaluation of (iii) distributed damage, and (iv) localized damage. Table 6-1 gives details of each activity of the methodology, refers to the corresponding results section, and presents the main conclusions.

In the synthetic data example section, the first two models are used to verify how the COI affects signals in the ultrasonic frequency range and the quality of the reconstructed signal with the WSST. Next, a multi-component model is considered to identify the limits when the reconstruction is possible from the engineering point of view (some errors added to the COI effect are acceptable).

The ultrasonic transducer characterization is critical because it reveals the frequency content that is sent to the tested specimen. It enhances a selection of the receiving sensors and helps to predict the frequency content seen by the receivers.

In the distributed damage evaluation application, concrete beams in intact and damaged (subjected to freeze and thaw cycles to induce micro-cracks) conditions are tested. The responses are measured at the top surface of the specimen with four different sensors: hydrophone, accelerometers, ultrasonic transducer, and the state-of-the-art laser Doppler vibrometer. Attenuation and velocity analyses are performed based on the full-time signals and the modes extracted with the WSST technique. For the discrete frequency bands, relative energy and relative attenuation indices are proposed and used for the condition assessment.

The localized damage evaluation application presents a cemented sand specimen with a subsurface void examined with the laser vibrometer. The same processing techniques are used, with an additional analysis of phase velocity dispersion. As a result, a relative dispersion index is utilized to prove the presence of the void further.

Table 6-1. Methodology and flow chart of data processing

Activity	Flow chart	Main conclusions
WSST-synthetic data example (Section 6.3.1)	Cone of influence effects (COI) → • Discontinuous sine • Continuous decaying sine → Reconstruction quality Reconstruction limitations → Multi-component signal → Define the minimum distance between components	• COI effect increases exponentially with frequency. • WSST mode separation possible for components with the frequency ratio up to 0.67
Ultrasonic transducer characterization with a laser vibrometer (Section 6.3.2)	Measure surface displacement along diameter → Select representative point → Compute FFT and WSST	• WSST mode decomposition offers enhancement in the fundamental understanding of transmitter signals. • Extracted modes enable individual wavelength analysis.
Application 1: distributed damage evaluation (Section 6.3.3)	4 different senor array scans: accelerometer, laser vibrometer, UTx, and hydrophone. → Attenuation and velocity analysis • Full-time • WSST → Attenuation analysis in discrete frequency bands → Relative attenuation index	• WSST-based RAI offers 52% improvement in the damage detection; • The laser provides the best non-contact evaluation
Application 2: localized damage evaluation (Section 6.3.4)	Laser vibrometer array scan → Attenuation and velocity analysis • Full-time • WSST → Phase velocity analysis → Relative dispersion index Attenuation analysis in discrete frequency bands → Relative attenuation index	• WSST-based RAI offers 36% improvement in the damage detection; • The void presence is further proved with high RDI values.

6.2.2 Specimens

In this study, two groups of specimens are tested. In the application of distributed damage evaluation, concrete beams are examined. Two rectangular concrete beams (41 cm x 8 cm x 10 cm; 12.5mm

nominal aggregate size, measured concrete strength at 28 days is 35 MPa) are tested with the characterized 54-kHz P-wave ultrasonic transmitter (Proceq) and four different receivers (i.e. accelerometers (Acc.; Dytran 3055B3), ultrasonic transducer (UTx; 54-kHz P-wave Proceq), hydrophone (hyd.; Teledyne TC4013), and the state-of-the-art laser Doppler vibrometer (laser)). The accelerometer used in the study has a sensitivity of 500 mV/g and bandwidth in the range from 1 Hz to 10 kHz. However, in the ultrasonic application, it is used beyond its flat rage. Therefore, it operates as a resonant transducer (the nominal resonant frequency of 35 kHz), as proposed by Kirlangic et al. (2017). As a result, the measured signal cannot be converted to the units of acceleration. The hydrophone offers a usable frequency bandwidth range from 1 Hz to 170 kHz and the receiving sensitivity of 1V/µPa. One of the beams is left in an as-cast condition and is used as a reference. The second specimen is subjected to eight weeks of freeze-thaw cycles. Each cycle lasts 24 hours and consists of a gradual temperature increase from -25 C° to +25 C° with ±2 C°.

In the localized damage evaluation application, a cemented sand specimen (sandbox, made of silica sand [Barco #71] mixed with about 10% by weight gypsum cement) is tested. The particle size distribution of the sand is given as D10 = 0.12 mm, D50 =0.18 mm, Cu = 1.8, and Cc = 1.04. The details of the properties can be found in Khan et al. (2006). The cemented sand has a depth of 300 mm and lateral dimensions of 1060x870 mm. The cemented sand lies on top of dry sand (450 mm thick) and is bounded by the chipboard box (with 60 mm-thick styrofoam inner-isolation). Considering the nominal frequency used in the test (54 kHz) and observed wave velocity (1183 m/s), the medium is considered as homogeneous. During the preparation of the specimen, a void has been embedded at the central section of the box (a balloon with a diameter of 80mm was placed, so the distance from the top surface to the top of the balloon is 80mm).

6.2.3 Test configuration

Firstly, the setup used for the characterization of the 54-kHz P-wave ultrasonic transducer (Proceq) is discussed (Figure 6-1-a). The characterization presented herein repeats the procedure performed for the 54 kHz transducer in Chapter 4. However, only the central section of the transducer will be used. The characterization is performed with the state-of-the-art Doppler laser vibrometer. The signals are read with a laser sensor head (LSH, Polytec OFV-534), which is connected to the vibration controller (OFV-2570), and finally stored at a computer. The laser technology has the benefit of being contactless (therefore, all coupling effects are eliminated), and has a flat frequency response in the frequency range used in this study. The responses of the transmitter are measured through air. A function generator

(HP33120A) is used to provide an input signal (54 kHz square pulses and the amplitude of ±5V) to the transmitter. A grid showing measurement points is presented in Figure 6-1-b. Responses are measured at 45 positions distributed evenly (with a 1mm spacing) along its diameter (50 mm), and a 2.5 mm offset from the transducer edge is used.

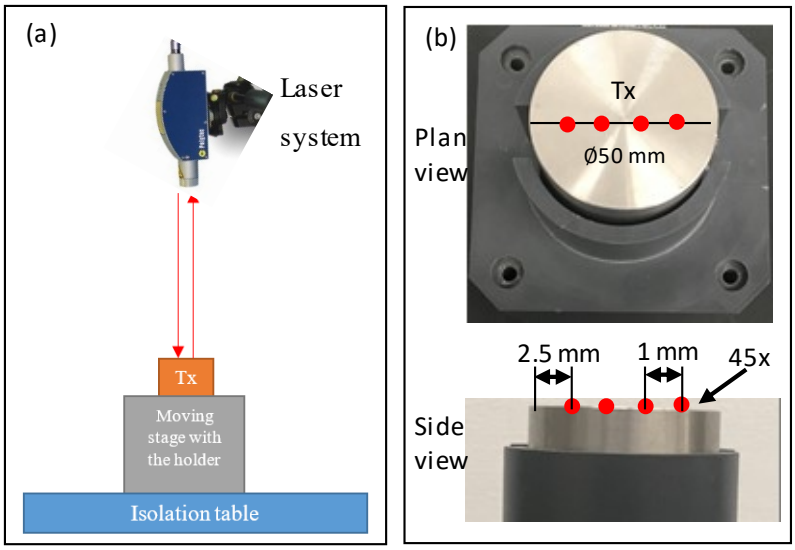

Figure 6-1. Laboratory setups used in this study: (a) Transducer characterization setup and (b) measurement grid used for the laser measurements

The experimental setup used for the laser vibrometer test of concrete beams in application one is shown in Figure 6-2-a. HP33120A function generator is used to provide an input signal (54 kHz square pulse, which is amplified to the amplitude of ± 125V) to the transmitter (located at the side of the beam). The response is read with a laser sensor head (LSH, Polytec OFV-534), which is connected to the vibration controller (OFV-2570). A total of 200 points are recorded for each condition (the first measuring point is located 100 mm away from the source on the top surface of the beam, and the spacing between the points is 1 mm). Each recorded time signal represents an average of 500 measurements. The challenge of attenuation measurements is disruption from variations in physical transducer coupling. The laser vibrometer test offers non-contact sensing and is considered as a baseline for other contact or semi-contact sensors studied in this chapter. The repetitiveness test for the laser consists of three measurements of the first location in the array and comparison of the amplitudes of the first peak and the cumulative energy in the frequency range from 25 to 35 kHz. The following coefficients of variations of the measurement error have been calculated: 4% (P-Peak) and 6% (frequency range).

For the remaining sensing techniques used in application one, the excitation part presented in Figure 6-2-a is unchanged. The responses recorded with the hydrophone, accelerometers, and ultrasonic transducer are measured at 10 locations (the first location is 100 mm from the source, and the spacing used is 20 mm). The issue of repetitiveness for the contact or semi-contact sensors is addressed with the following practice: vibration is measured at the first response, and then the sensor is moved to consecutive locations. Therefore, the error in repetitiveness is not greater than the overall attenuation trend observed along with the whole sensing array. The attenuation trend for contact and semi-contact sensors is then verified against the non-contact results obtained with the laser vibrometer. The responses measured with accelerometers (ICP power supply: Dytran 4121) are recorded and stored (16 time-averages are used) with a digital oscilloscope (Agilent DSO-X 3014A). The responses in the ultrasonic setup are also stored with the oscilloscope (16 measurements are used for averaging). For the responses measured with the hydrophone, a digital filter-amplifier (Kronh-Hite 3384) is used. An eight-pole Butterworth band-pass filter is applied (2-200 kHz), and the response is amplified by 20 dB. Signals are recorded with the oscilloscope, and each recorded hydrophone signal is an average o 128 measurements. The hydrophone is placed in a water-filled square tube with a rubber membrane at the bottom of the tube. The hydrophone is secured and does not touch the tube walls. The tube with the hydrophone is placed on the concrete beam, so only the membrane is with contact with the specimen (the tube does not touch the specimen). This solution offers a novel application of the hydrophone for surface measurements using fluid interphase and is considered as a semi-contact receiver.

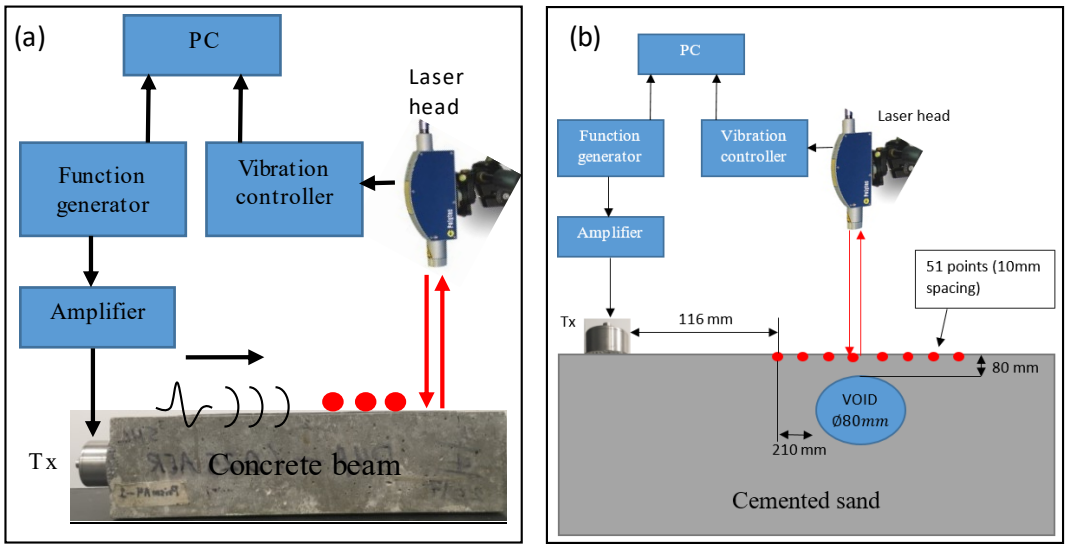

Figure 6-2. Laboratory setups used in this study: (a) setup used for concrete beams and (b) cemented sand data collection setup

In the setup used in application two, for the evaluation of the sandbox, the ultrasonic transmitter (54-kHz P-wave transducer made by Proceq) is placed on the surface of the cemented sand 50 mm away from the edge (along the mid-section, Figure 6-2-b). The function generator (HP33120A) provides an input signal (5V, 54 kHz square pulse), which is amplified to the amplitude ±125V. The responses are read with a laser sensor head (LSH, Polytec OFV-534), which is connected to the vibration controller (OFV-2570), similarly to the characterization setup. Two measurement lines are used. The intact line goes 80 mm to the side of the void edge, and the void line goes directly through the void. The response is measured at 51 locations (with 10 mm spacing) for both lines, and the first response is measured 116 mm away from the transmitter. Therefore, the void is located 210 mm away from the first reception position.

6.3 Results and discussion

In this section, the main characteristics of the WSST technique are demonstrated on a synthetic data example (ultrasonic frequency range of 5 to 100 kHz). Next, to demonstrate the use of the WSST method in non-destructive testing applications, three studies are presented: a) characterization of an ultrasonic transmitter, b) evaluation of distributed damage on lab-scale concrete beams, and c) evaluation of localized damage on a cemented sand layer. In the distributed damage study, beams in two different conditions (intact and damaged) are examined. The damaged condition is induced by

applying freeze and thaw cycles to introduce micro-cracks in the specimen. The surface responses are recorded with four different sensors, including the novel use of hydrophones for surface wave reception and a state-of-the-art laser Doppler vibrometer. In the last study, a cemented sand specimen with localized damage (i.e. subsurface void in a section of the specimen) is analyzed with the laser vibrometer.

6.3.1 WSST-synthetic data example

Three simple synthetic models are considered to verify the applicability of the WSST technique for the analysis of ultrasonic signals and identify the practical features of the method. The first step in the WSST algorithm is to compute the wavelet coefficients. Therefore, computational issues typically occurring for continuous wavelet transform, like the cone of influence (COI) effect, will be present. The COI effect is not observed for cyclic signals. Therefore, the first model consists of the discontinuous signal $x(t) = 100\sin(2\pi f t)$ defined for $8T < t < 16T$, where $f = 5\ kHz$, t is a time vector, and T is the period associated with the frequency f. Figure 6-3 shows the instantaneous frequencies estimated with the WSST (Figure 6-3-a), the original and reconstructed time signals (Figure 6-3-b), and the residual signal calculated between them (Figure 6-3-c).

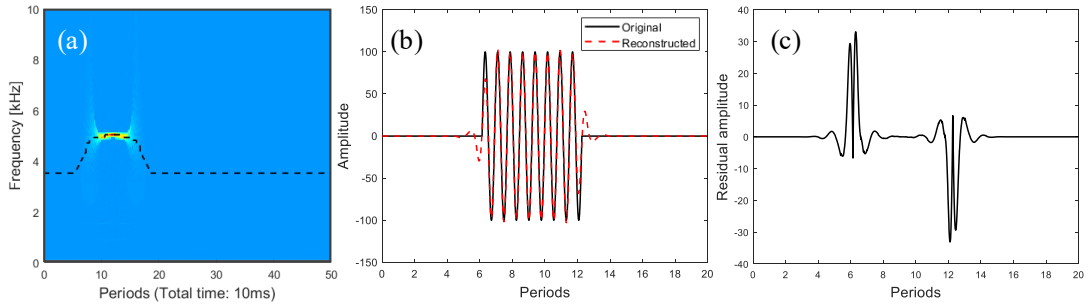

Figure 6-3. Synthetic sinusoidal signal of finite duration. (a) Instantaneous frequency estimated with WSST, (b) original [black line] and reconstructed time signal [red-dashed line], and (c) residual [error] signal

The first model shows that when there is no signal at the beginning of the vector, the COI effect does not occur. Instead, the effect shifts to the beginning and end of the active signal (i.e. to the regions when the cyclic signal is discontinuous). The observed error between the original and reconstructed signals has the same amplitude but opposite phase. If the signal starts immediately, then the COI effect is observed at the beginning, and it leaks to the end of the total signal. Next, a set of exponentially decaying sinusoidal signals is considered:

$$x_i(t) = A\sin(\omega_D t)e^{-\omega\zeta t} \tag{6-1}$$

where ζ is the damping ratio, ω_D and ω are damped and undamped angular natural frequencies (the relationship between them is $\omega_D = \omega\sqrt{1-\zeta^2}$, and $\omega = 2\pi f$, where f is frequency), and t is time. A frequency set (f_i) is given from 5 to 100 kHz with an increment of 1 kHz, and ζ is taken as 2%. The total simulation time is 10 ms, and the signals are sampled, ensuring a constant rate of 100 points per period. Figure 6-4-a presents the sample WSST results calculated for 5 kHz signal and highlights the COI at the beginning of the signal (the analogical region is present at the end of the signal).

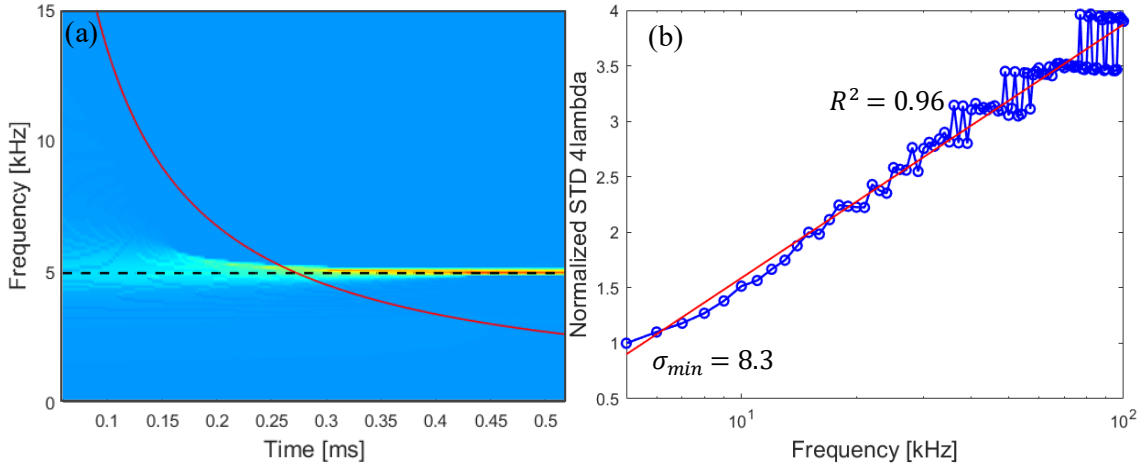

Figure 6-4. Results of model 2: (a) Sample instantaneous frequency estimated with WSST for 5 kHz signal. The red line highlights the COI calculated based on Equation 3-44. (b) Standard deviation of the error (residual) signal, calculated based on two first periods of signals.

The frequency of the reconstructed signals is reproduced perfectly. However, within the COI presence (which can be extended to two periods of signal), the signal amplitude is not reconstructed correctly. The smaller-scale effect is observed at the end of the signal. The signal reconstruction procedure has been performed for all signals, and the energy ratio between reconstructed and original signals based on two periods of the signal has been calculated. Additionally, the standard deviation of the error (residual) signal has also been calculated, based on two periods. The energy ratio decreases exponentially, and the variation of the standard deviation of the residual signal with the frequency is presented in Figure 6-4-b. When the frequency is expressed on a logarithmic scale, the trend is linear ($R^2 = 0.96$). Both statistical features are changing exponentially with frequency. It can be concluded that the representation of the reconstructed signal amplitude (within two periods) is progressively worse

as the signal frequency increases. This observation is critical for multi-component signals that are recorded in the NDT tests.

Finally, an effect of the multi-component signal is studied to define the practical frequency range between the components where the reconstruction with WSST is possible. A synthetic model of a response of a 2-DOF system is considered as

$$x(t) = x_1 + x_2 = \sum_{i=1}^{2} 100\cos(\omega_{D_i} t)e^{-\omega_i \zeta_i t} + n(t) \tag{6-2}$$

where x_1 and x_2 are two vibration modes, ω_D and ω are damped and undamped angular natural frequencies, ζ is the damping ratio, and $n(t)$ is the added noise. The purpose of the model is to examine and extract the vibration modes of the response, and to investigate the effect of the frequency spacing on the extracted modes; therefore, the damping ratio for each DOF is equal ($\zeta_1 = \zeta_2 = 2\%$), and the narrow-band noise ($n(t)$) with 50% of initial amplitude is used (white noise is filtered with a minimum-order band-pass (10-100 kHz) filter with a 60-dB stopband attenuation). Signal x_1 is defined with a frequency set (f_1), given from 5 to 100 kHz with an increment of 1 kHz, while the signals x_2 has a constant frequency: $f_2 = 30\ kHz$.

For each iteration of the loop, the frequency f_1 is selected anew, and the overall system response is computed accordingly to Equation 6-2. Next, instantaneous frequencies are computed, and the mode signals are reconstructed based on the frequency ridge calculated within ±1.5 kHz of each frequency component. In order to investigate only the effect of the frequency distribution of modes in a multi-component signal on the reconstruction quality, the first two periods of the signals are disregarded (therefore, the COI effect is minimal). The energy ratio between the original (x) and reconstructed ($\tilde{x}$) components is used and calculated as: $E_{ratio} = \sum \tilde{x}^2 / \sum x^2$. Next, an average and standard deviation of both reconstructed components are computed. The distribution of the averaged energy ratio with respect to the frequency ratio calculated based on Equation 3-42 is shown in Figure 6-5.

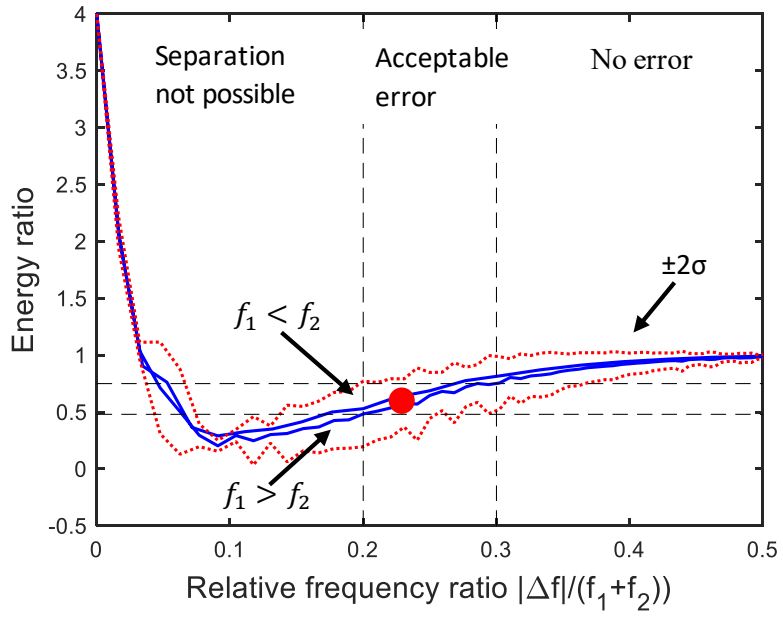

Figure 6-5. Energy ratio averaged for two modes, between reconstructed and original time signals (first two periods are disregarded to omit excessive COI effect). The red dotted lines show the distribution of the standard deviation between energy ratios of the individual modes. The red point highlights the frequency ratio for an ultrasonic transducer used in this study (presented in section 6.3.2).

Three frequency regions can be defined. The no-error region (region 1) is defined as long as the energy ratio stays above 0.7, which corresponds to the relative frequency ratio ($|\Delta f|/(f_1 + f_2)$) greater than 0.3. Equation 3-42 defines that the separation is possible for the frequency ratio greater than 0.2; therefore, an acceptable reconstruction error zone (region 2) is defined as $0.2 > |\Delta f|/(f_1 + f_2) > 0.3$. The lower end of that zone corresponds to the energy ratio of 0.48. Finally, when the frequency ratio is below 0.2, the reconstruction is not possible (region 3). In the extreme case (the frequency ratio lower than 0.05), the two components are reconstructed as one, and the standard deviation is minimal. The red point in Figure 6-5 shows the frequency ratio for an ultrasonic transducer used in this study (presented in section 6.3.2). Figure 6-6 shows sample signals belonging to the acceptable error region (f_1 = 20 kHz and f_2 = 30 kHz, $|\Delta f|/(f_1 + f_2) = 0.2$), defined in Figure 6-5.

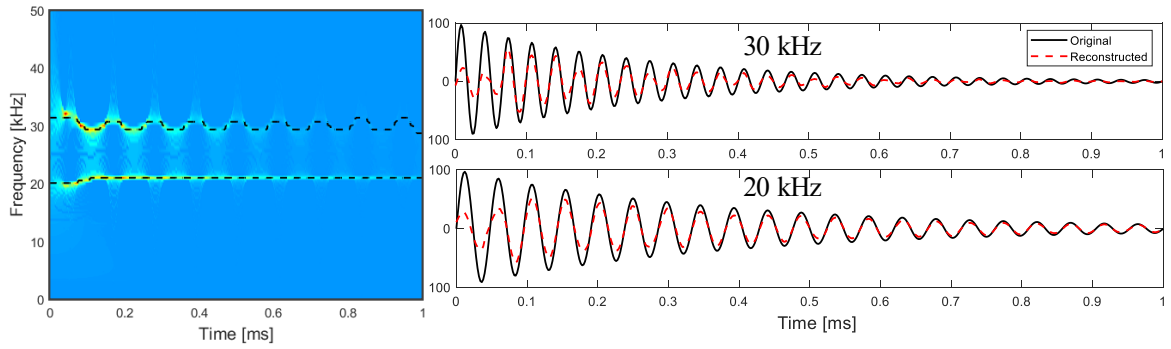

Figure 6-6. Sample instantaneous frequency plots, and original and reconstructed time signals from the acceptable error zone (f_1 = 20 kHz and f_2 = 30 kHz, $|\Delta f|/(f_1 + f_2) = 0.2$).

When the separation is not affected (region 1), the only observed amplitude error is associated with the COI effect. When a pair of modes is within region 2 (Figure 6-6), the separation is still possible, and reconstructed signals continue to possess the correct frequency content. However, the time duration when the amplitude is not represented reliably increases. Finally, when signal components are close to each other (region 3), the separation is not possible, and the reconstructed signals will have the frequency content of both modes.

6.3.2 Transducer characterization

The common assumption of a single resonant frequency is not true for ultrasonic transducers and affects the interpretation of NDT data. Therefore, a detailed characterization of a source signal is needed. It explains the complex character of the received signals and justifies mode decomposition analysis with the WSST. A wear surface of the 54-kHz transmitter is scanned with the laser vibrometer using the setup presented in Figure 6-1. Figure 6-7-a presents typical displacements (the amplitudes are normalized with respect to the maximum amplitude observed along the diameter) measured along the transducer diameter. Most of the energy (i.e. the largest displacement) is observed in the central section of the diameter. Therefore, displacement recorded at the centre of the wear face is shown in Figure 6-7-b, and is selected to represent the overall transmitted frequency content.

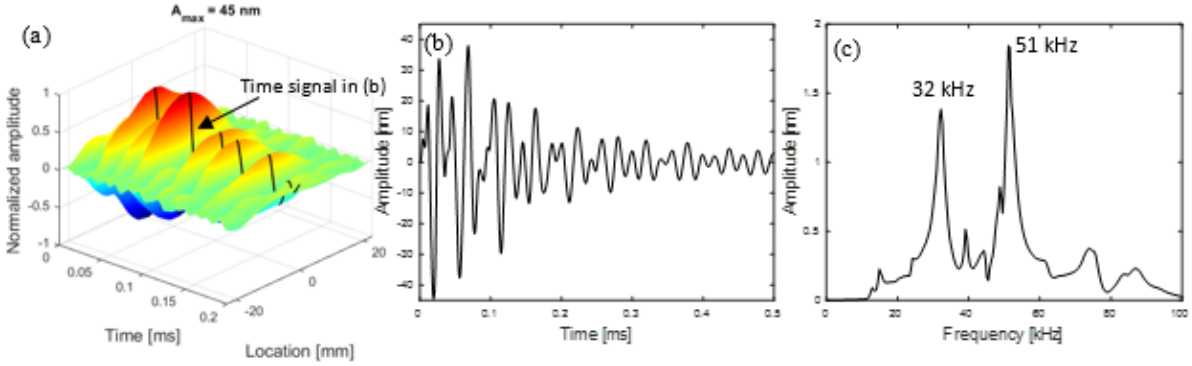

Figure 6-7. Typical transducer characterization: (a) Time signals recorded along the diameter of the 54-kHz transmitter. The responses are normalized globally, (b) time signal recorded at the centre of the wear face [also, highlighted in (a)], and (c) the spectra of the signal recorded at the centre.

Figure 6-7-c reveals that in addition to the nominal resonant frequency, there are other frequencies present in the signal. The second significant peak is present at 32 kHz. Less prominent peaks can also be distinguished (16 and 39 kHz). These frequencies would normally be disregarded. The frequency ratio between the main peaks is 0.62, yielding that the WSST separation is possible. Figure 6-8-a shows the instantaneous frequencies estimated with WSST; two main modes are selected for extraction.

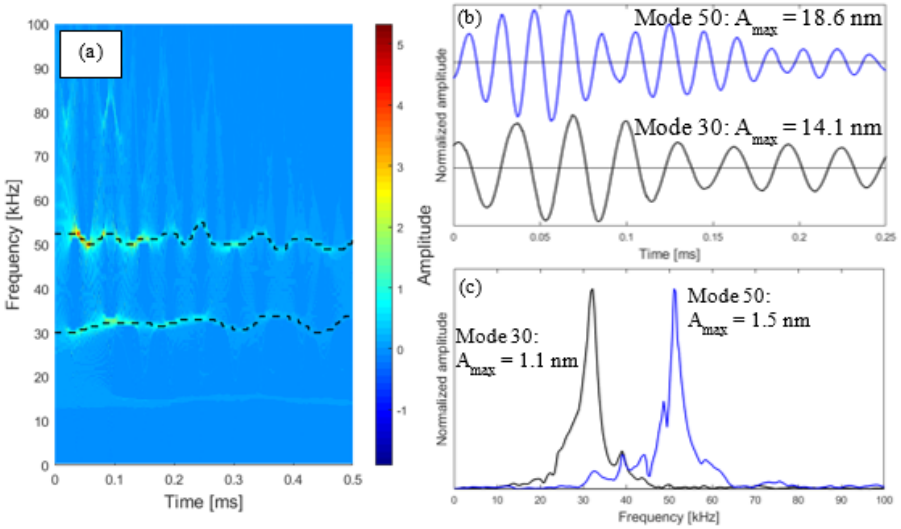

Figure 6-8. WSST analysis of the signal recorded at the centre of the wear surface: (a) instantaneous frequencies estimated with WSST and the reconstructed signals: (b) time signals and (c) Fourier spectra. Mode 30-kHz is represented in black colour, while mode 50-kHz is presented with blue colour. (Repeated Figure 4-5)

The extracted modes are presented in time and frequency domains in Figure 6-8-b and c. The analysis of the surface displacement for the mode signals shows that transmitted signals are generated not only by the resonance of piezoelectric crystal but also by the resonance of the surface-wearing plate of the transducer itself. The extracted modes can be used for the estimation of frequency response functions for individual mode. It is also important because, based on that information, the adequate receiver can be selected (i.e. the natural frequencies of receivers can be selected). It can also be expected that the received information will have a similar frequency content. It means that in the analysis of surface waves, the information about two different depths (primitive profiling information – based on a single sensor, driven at the single excitation frequency) will be obtained.

6.3.3 Application to distributed damage (concrete beams)

In the first application, concrete beams in two conditions are tested using four different sensors. The visual inspection of the beams shows no difference between them. The analysis starts with the reference test (UPV). The results show the negligible difference in P-wave arrival time between beams. When a high amplitude resolution was assured, P-wave velocity recorded for the intact and damaged conditions were: 4610 and 4411 m/s, which gives a relative difference of 4%. However, a typical test would not pay such high attention to identifying the true first arrival. If the first peak is considered as the first arrival, then the relative difference drops to 1%. These values would be considered as within the error level. Next, in the main surface wave test, two transducers are full-contact (i.e. accelerometers, ultrasonic transducers), one is considered as semi-contact (i.e. a hydrophone is submerged in a water-filled tube with a rubber membrane at the bottom the tube; therefore, only the membrane is in contact with the tested surface), and the laser Doppler vibrometer is the non-contact sensing solution. Assuming wave velocity of 2364 m/s (as observed for the first arriving wave in Figure 6-9) and frequencies for the modes of 32 kHz and 51 kHz, the following wavelengths can be calculated $\lambda_{30} = 74\ mm$ and $\lambda_{50} = 46\ mm$. The sample time and frequency representation of the recorded signals are presented in Figure 6-9. The signals are windowed up to 0.75 ms prior to the FFT calculation.

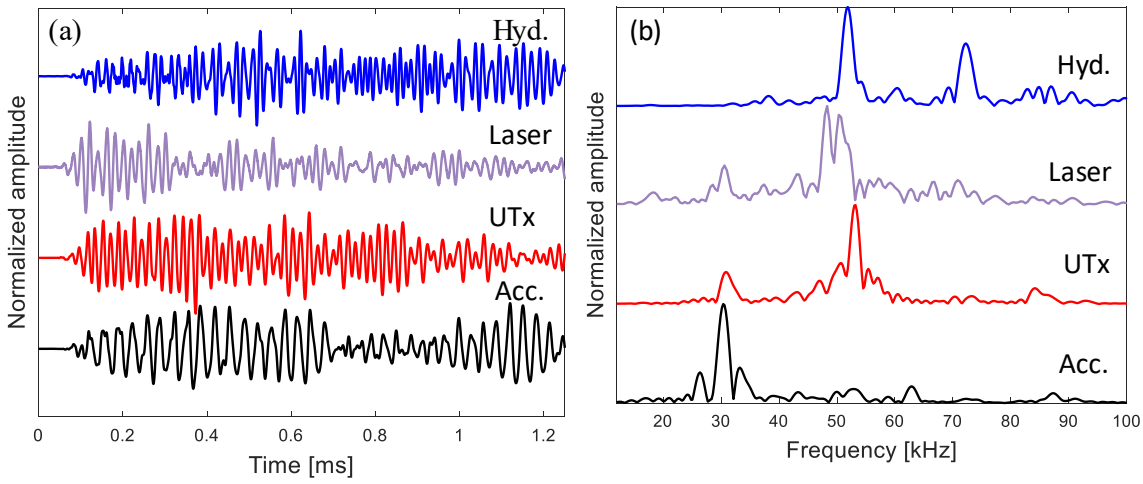

Figure 6-9. Sample signals recorded with a hydrophone (Hyd.), laser vibrometer (laser), ultrasonic transducer (UTx), and an accelerometer (Acc.): (a) time signals, and (b) frequency spectra.

The frequency spectra show that despite the same excitation used in all tests, the responses have different frequency content. The laser and ultrasonic results are the most similar, showing the frequency peaks around 30 and 50 kHz. The accelerometer provides only one peak centred at its resonant frequency. The accelerometer has been selected, so the resonant frequency matches one of the modes of the transmitter. It should be noted that only due to the characterization of the source, the procedure of the adequate selection of the receiver is possible. The hydrophone is not sensitive below 40 kHz, and the 30 kHz peak is not present in the spectrum. However, the 50 kHz peak is observed, and one additional significant peak is also present at 70 kHz. That frequency is present in the frequency content generated by the transmitter (Figure 6-7-c). Next, the instantaneous frequencies are estimated with WSST (Figure 6-10), and the appropriate modes corresponding to the main frequencies transmitted to the specimens (i.e. 30 and 50 kHz modes) are extracted.

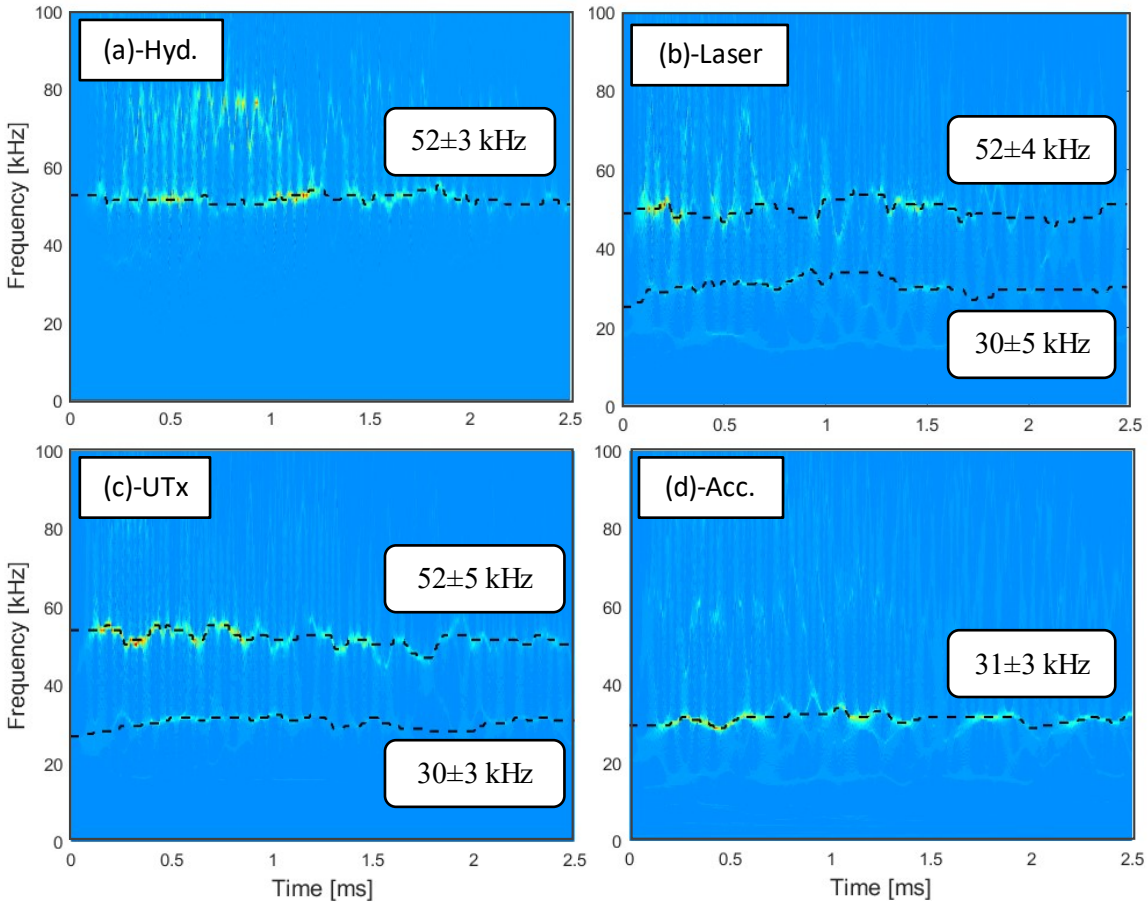

Figure 6-10. Instantaneous frequencies estimated with WSST for the signals recorded with: (a) hydrophone, (b) laser vibrometer, (c) UTx, and (d) accelerometer. The colour scale for all plots is practically the same, in a range of 0 (blue)-0.2 (red). The mean value and variation range for each frequency ridge are highlighted in a textbox

The reconstructed signals are presented in the time and frequency domains in Figure 6-11. The reconstruction of mode 30 for the hydrophone signals is not possible. The same is not possible for mode 50 and accelerometer signals. The reconstructed signals have similar frequency content centred at one of the transmitter modes. Therefore, the analysis of the modes provides an easier interpretation of the material condition.

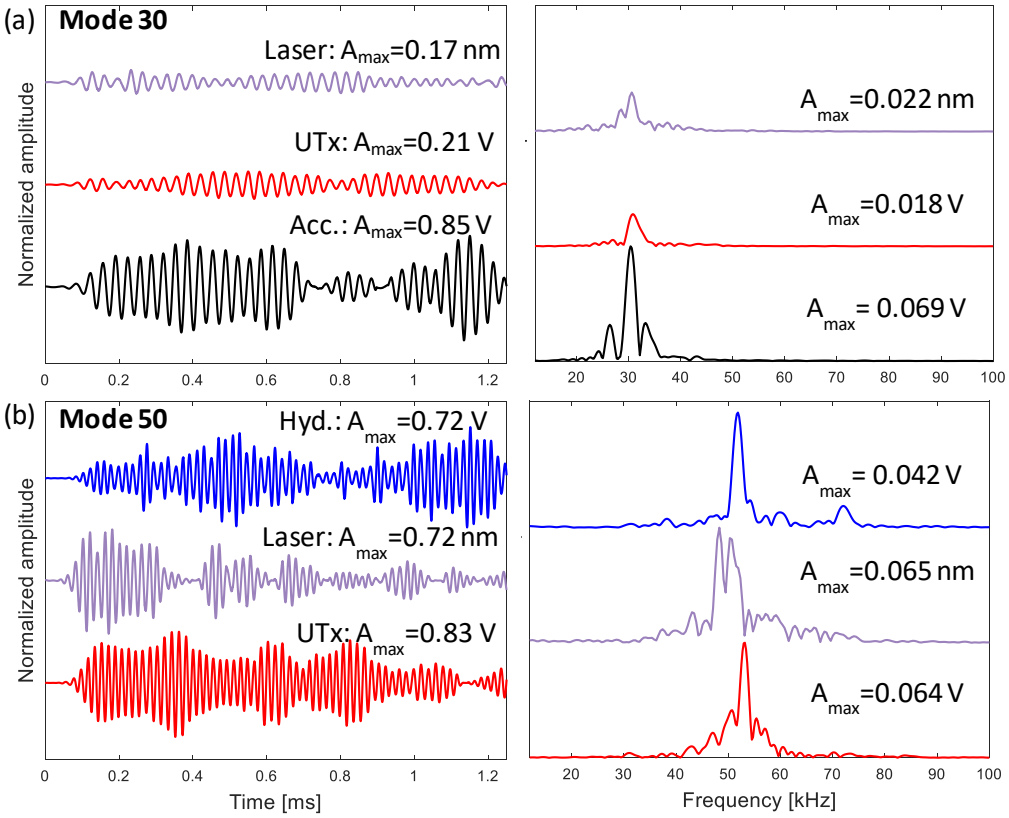

Figure 6-11. Mode signal reconstructed from the frequency ridges shown in Figure 6-10: (a) mode 30 and (b) mode 50. Both modes are presented in the time and frequency domains. Mode 30 was not available for the hydrophone, and the reconstruction of mode 50 was not possible for the accelerometer. Amplitudes for each sensor are normalized with respect to mode 50.

All sensing techniques are analyzed based on the raw time signals and the mode signals. The procedure and sample results are presented based on the laser vibrometer data.

6.3.3.1 Laser vibrometer: full-time signal analysis

The time signals recorded at 200 receiving points for both conditions are baseline-corrected with respect to the consent wave velocity of 2364 $^{m}/_{s}$. Next, three segments are considered, array positions (a) 1-31, (b) 90-121, and (c) 165-195. For each segment, an average signal is calculated, and the time signals normalized with respect to the maximum displacement value for both conditions are shown in Figure 6-12-a. The window with a duration of 0.2 ms has been applied before the analysis in the frequency domain (the window prevents the analyzed signals from the reflections coming from the other end of the beam). The normalized spectra for all segments are presented in Figure 6-12-b.

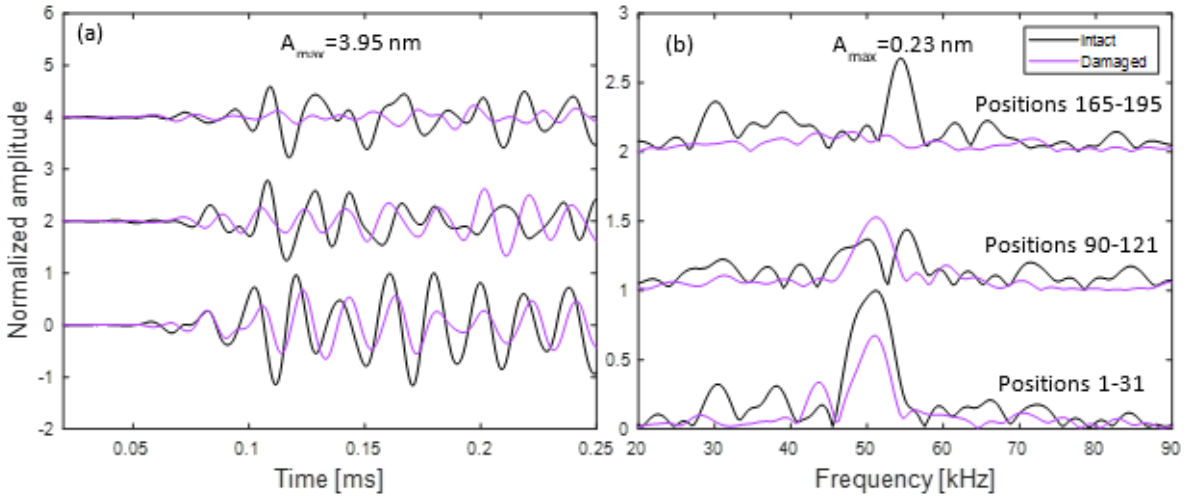

Figure 6-12. Average baseline-corrected signals recorded for concrete beams: (a) time signals for three segments: positions 1-31, 90-121, and 165-195, (b) corresponding spectra for both conditions (intact-black line, damaged-purple line).

The analysis of time signals recorded for both conditions shows that the relative difference of maximum values progresses from 32% for the first segment to 56% for the last segment. Change in the material condition is better observed based on the spectral area when the relative difference gives values between 43 and 54%. Two frequency bins are defined next. The bins are defined as ranges of 30 and 50 kHz ±10 kHz. The relative energy trend (Equation 3-45) for the range 30 is shown in Figure 6-13.

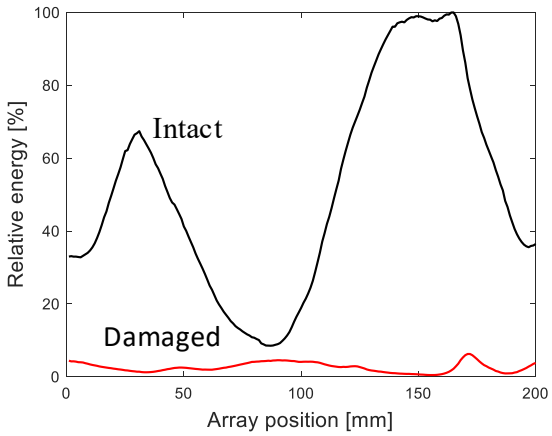

Figure 6-13. Relative energy trend for range 30 kHz. Maximum COV of the measurement error is 6%.

For range 30, the relative energies of both conditions are well separated with the mean relative attenuation index (RAI) along the tested beam length is 90%. The separation based on mode 50 is worse

in the second half of the tested length, which might be due to the attenuative nature of concrete. The positions where the relative attenuation drops below zero are excluded from the calculation of the mean attenuation value. The attenuation approach, even when it is applied to full-time signals, gives good separation between material conditions. The application of frequency bins improves the assessment, and the 30 kHz mode is more sensitive for distributed damage detection. Some boundary condition effects (related to the small size of the specimens) are seen in the attenuation curves; however, the correct assessment can be done.

6.3.3.2 Laser vibrometer: modes extracted with the WSST

Next, the reconstructed with the WSST mode 30 is selected for analysis. The baseline-corrected time signals of the mode for the three segments and the corresponding averaged frequency spectra are presented in Figure 6-14.

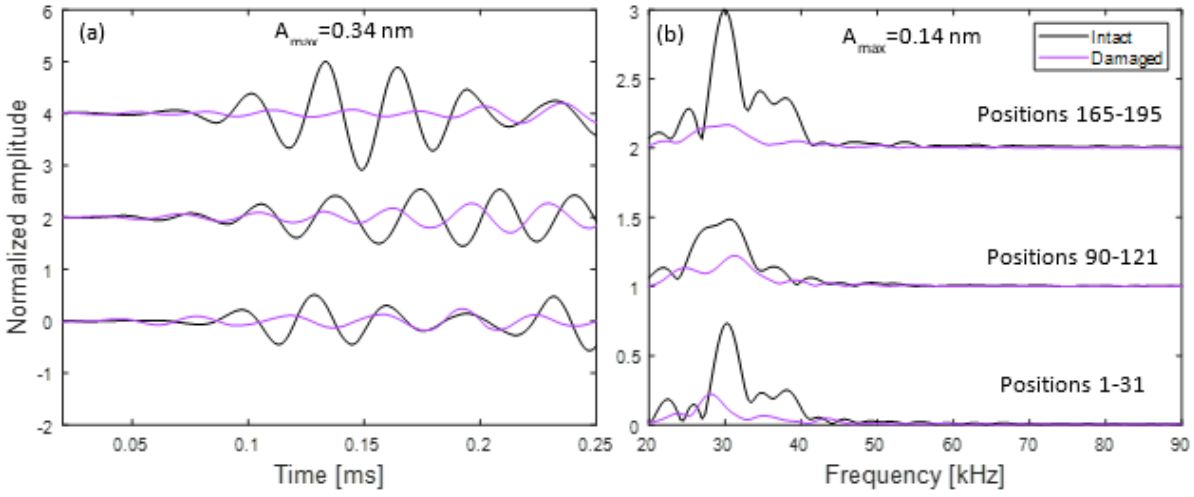

Figure 6-14. Average baseline-corrected mode 30 signals recorded for concrete beams: (a) time signals for three segments: positions 1-31, 90-121, and 165-195, (b) corresponding spectra for both conditions (intact-black line, damaged-purple line).

The relative difference between maximum amplitudes for mode 30 offers better separation between the two conditions (reduction of 63-64%). Moreover, in the windowed part of the signals, the amplitudes experience an increased attenuation, and the spectral areas are decreased by 54-76%.

The relative energy trend is shown in Figure 6-15. The two conditions are well separated. However, due to the increased destructive interference of waves in the middle of the tested length, the average relative amplitude is less than in the full-time signals (i.e. RAI = 88%). However, if the RAI values

lower than 49% (the lowest value of the range 30 in Figure 6-13) are eliminated, then the mean value reaches 90%.

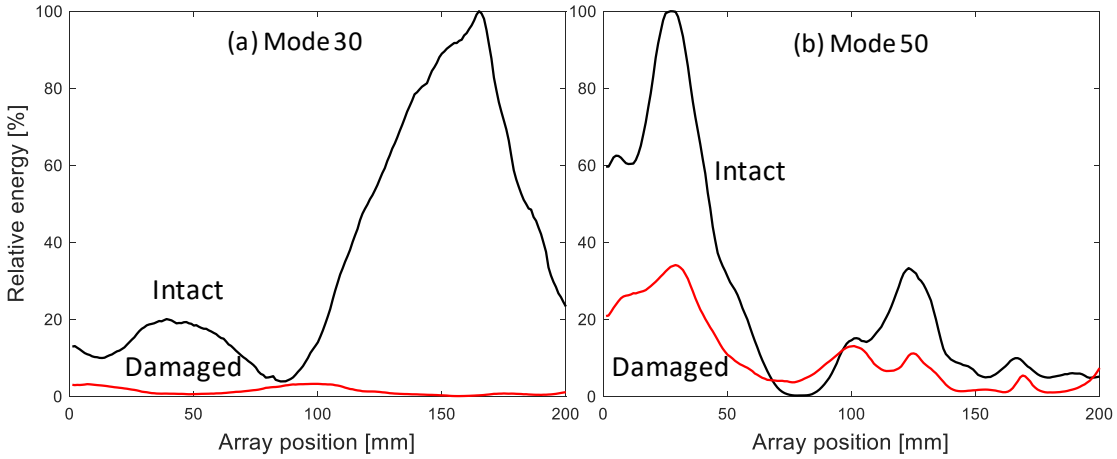

Figure 6-15. Relative energy calculated for (a) mode 30 and (b) mode 50. Maximum COV of the measurement error is 6%.

The procedure is repeated for mode 50. The analysis of mode 50 shows that the mode is less sensitive to damage detection. The relative difference between maximum amplitudes for both conditions drops to 34%. A lower value is also observed for the relative spectral area difference (49%) when compared to previous cases. The analysis of the relative energies (presented in Figure 6-15-b) shows that mode 50 offers only a modest separation between two conditions with an average RAI value of 60% (disregarding the negative RAI values).

6.3.3.3 Compression test verification

Finally, a verification compression test has been performed on the beam slices. The example stress-strain curve is presented in Figure 4-27. The freeze and thaw test aimed to induce early damage; therefore (after 56 cycles), no significant reduction in compressive strength is reported (2% reduction). However, concrete elements have been displaced more in the damage condition, resulting in a 20% increase in strain. The results follow the findings of Marzouk and Jiang (1995), who reported no significant dynamic elastic properties for up to 200 cycles of freeze and thaw.

6.3.3.4 Summary results: concrete beams

The methodology presented based on the laser vibrometer data has been applied to all sensing techniques, and the review is shown in Figure 6-16.

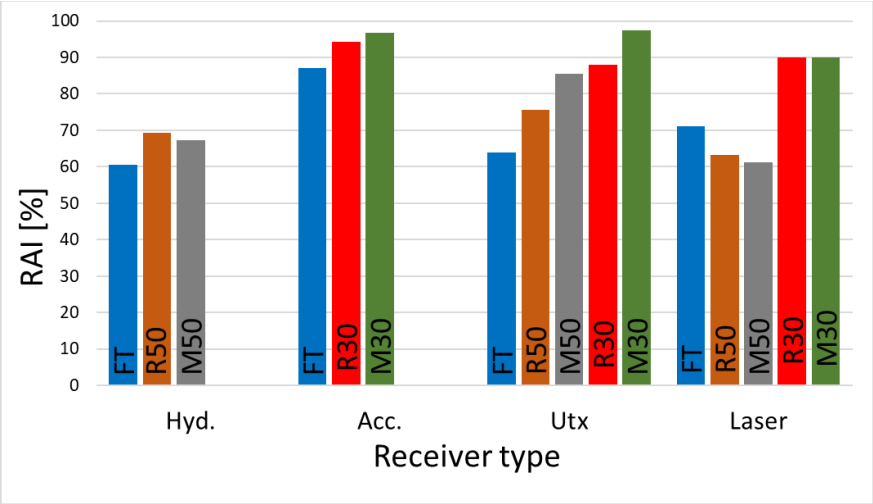

Figure 6-16. Summary of the relative attenuation index for concrete beams. For the analysis with a hydrophone, 30 kHz mode was not available, and for accelerometer, 50 kHz mode was not available. Maximum COV of the Laser measurement error is 6%.

When the full-time signals are analyzed, the best results were obtained for accelerometers with the RAI value of 87%. The successful separation between the two conditions was possible due to the prior knowledge of the transmitted signal coming from the characterization process and selecting the accelerometer with matching resonant frequency. The methodology can be improved by applying frequency ranges associated with the frequency peaks of the transmitted signal. The most sensitive frequency range is centred at 30 kHz. Therefore, similar RAI values were obtained for the sensors for which that frequency is available (i.e. accelerometers, UTx, and laser vibrometer). The lowest separation was obtained for the hydrophone, which is not sensitive in the low-frequency range. The frequency range centred at 50 kHz, which is related to the frequency of excitation, is less sensitive for the condition assessment of the tested beams. The WSST algorithm offers further improvements, and mode 30 gives the best RAI values. For all sensors, except the hydrophone, the RAI is above 90%, and the highest value was calculated for ultrasonic transducers (RAI = 97%; the receiving transducer is of the same type as the transmitter; therefore, the frequency parameters of the two probes match).

6.3.4 Application to localized damage (cemented sand)

The second application considers a cemented sand specimen (shown in Figure 6-2-b). Two series of measurements are taken, where the first line of measurements goes through the sound section of the specimen, and the other one goes on top of the subsurface void. The first group of analyses is performed

on the original time signals. Figure 6-17-a presents time signals for the reference line (intact condition), while Figure 6-17-b shows time signals for the line placed on top of the void. Blue marks show the window that is applied before the fast Fourier transform is calculated. The amplitude spectra of the windowed signals are presented in Figure 6-17-c (intact) and Figure 6-17-d (damaged). The traditional wave velocity-based approach is not sensitive for the localized damage detection, as no significant change is observed for the inclination of the first arrival line. However, a sharp drop of signal amplitude is observed when the measuring point lies on top of the void (locations 20-30 in Figure 6-17-b). A similar effect is observed in the frequency domain. Although the two lines have different frequency content (due to the boundary effects, present even in the windowed signals), a distinct drop in spectral amplitude is observed in the with-void line case. Moreover, the intact line keeps the frequency content constant over the whole measurement array, which is different for the with-void line (i.e. the frequency content is modified for the locations after the void).

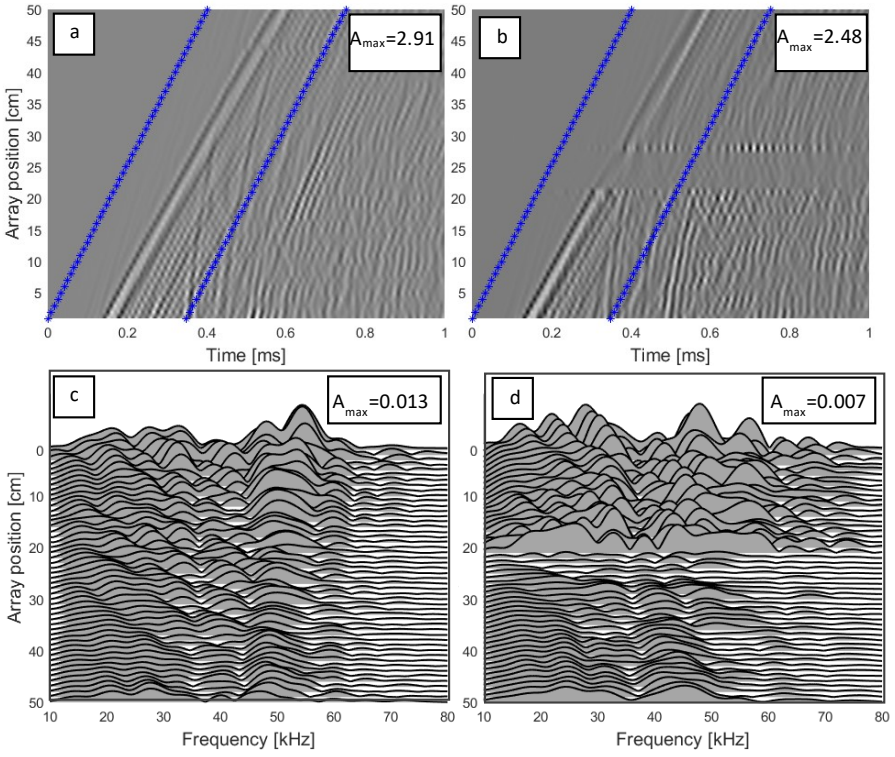

Figure 6-17. Original time signals and frequency spectra (calculated for the windowed signals) measured respectively for (a and c) intact line and (b and d) void-line. Blue marks show the window applied prior to the FFT. The ordinate scales in a and b are reversed in c and d.

The visual analysis identifies the presence of the void. However, a quantitative parameter is needed. For each location, the RE and RAI are calculated and presented in Figure 6-18. The indicators are calculated based on the whole spectral range, the frequency range of 30±10kHz, and the range 50±10kHz (the ranges are centred on the significant resonances presented in Figure 6-7-c). For the RE trend presented in Figure 6-18, three significant sections can be distinguished: before the void (before), on top of the void (on-void), and after the void (after). The 30-kHz frequency bin shows the least variability (the 30-kHz mode penetrates deeper into the material), and the conclusions will be presented based on this vibration mode. Before the void (locations 0-20), the relative energies for both lines decline at a similar rate, and the RAI values fluctuate around zero. When the wave reaches the void (locations 20-30, highlighted with the blue dashed vertical lines in Figure 6-18), the energy in the with-void line is distinctly lower, and the RAI reaches the mean value of 78%. Finally, after the void, the signal energy is less affected (mean RAI of 43%); however, it does not retrieve the values seen in the intact line.

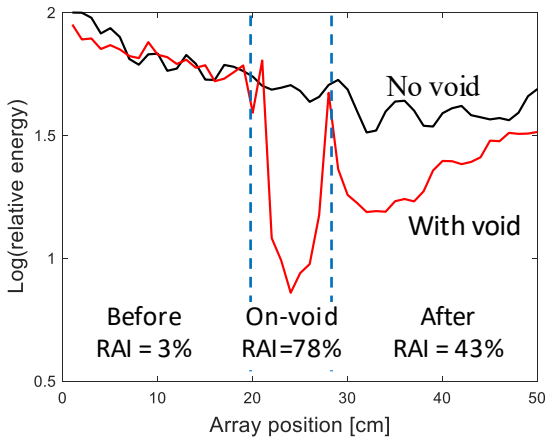

Figure 6-18. Relative energy for the 30 kHz range presented for two measurement lines. The amplitudes are normalized to the maximum value in the no void line. Vertical dashed lines define three locations: before, on, and after the void. The mean RAI values for the 30 kHz range are provided for each sector.

Additionally, frequency-wavenumber plots (FK plots) are computed with the two-dimensional Fourier transform, and phase velocity dispersion plots are calculated based on the FK peaks; only the significant peaks are selected. The dispersion curve plots for the full-time signals are presented in Figure 6-19. The relative dissimilarity index (RDI) is used to give more quantitative meaning to

dispersion plots shown in Figure 6-19. The RDI is calculated accordingly to Equation 3-48, taking a relative difference of summed phase velocities for each condition for a certain frequency range. The damage condition manifests itself with an additional anti-symmetric mode seen in the phase velocity plot. Therefore, when the RDI is calculated, it gives high values (100% and above) regardless of the selected frequency range. However, the best results are obtained when the range is defined between 10 and 20 kHz.

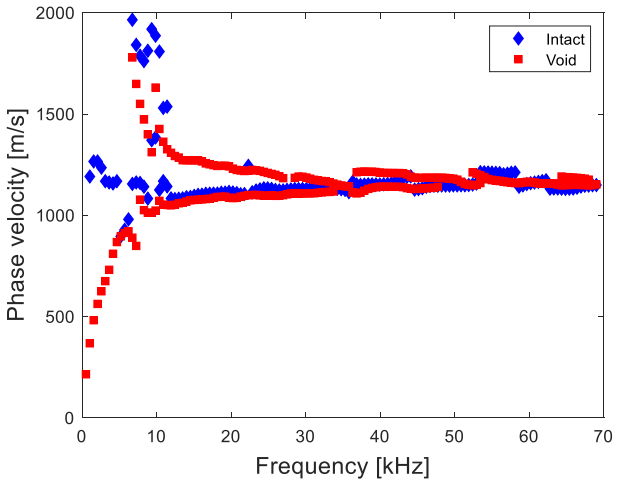

Figure 6-19. Phase velocity dispersion plot calculated for the full-time signals

6.3.4.1 Modes extracted with the WSST

In the next phase, the recorded responses are subjected to the wavelet synchro-squeezing transform. A typical instantaneous frequency plot is shown in Figure 6-20. The amplitude is oversaturated purposely, highlighting the spectral position of the ridges (solid red lines) that are used for the extraction of modes. Both modes are analyzed in the section.

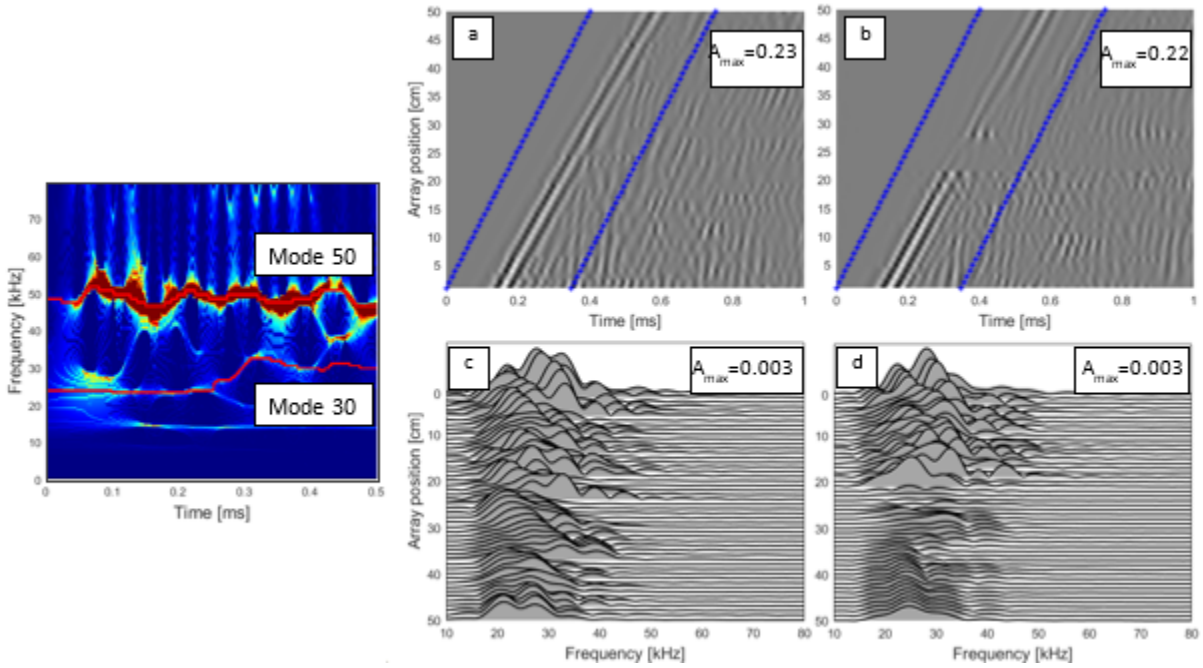

Figure 6-20. Typical instantaneous frequencies estimated with the WSST technique. Red solid lines represent the ridges that are used in the reconstruction of mode signals. Reconstructed mode-30 time signals and frequency spectra (windowed signals) measured for (a and c) the intact line and (b and d) void-line. Blue marks show the window applied prior to the FFT. The ordinate scales in a and b are reversed in c and d.

Figure 6-20 also presents mode 30 signals in both time and frequency domains. It can be seen that the main displacement is strongly associated with the arrival of the wave, and the reflections do not play a significant role as before. The same attenuation pattern in amplitudes is observed. Another benefit of using the mode is that the frequency is narrowed, and it is simpler to keep track of the changes that happen after the wave leaves the void. The relative energy plot is repeated for the mode 30 signals and is presented in Figure 6-21. A sharp drop (RAI up to 70 %) is seen for location 20-30, and finally, after the void, the relative attenuation is lower (RAI with the mean value of 39%).

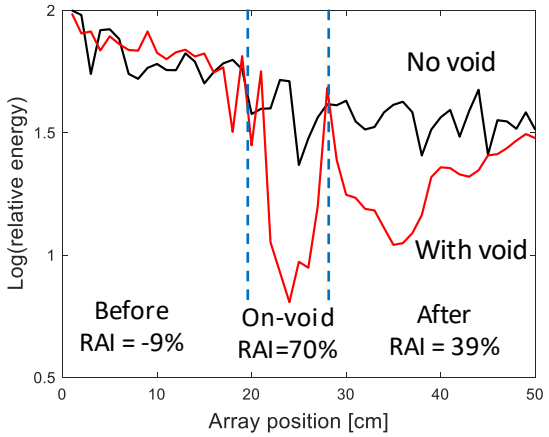

Figure 6-21. Mode 30 results: relative energy for mode 30 presented for two lines. The amplitudes are normalized to the maximum value in the no void line. Vertical dashed lines define three locations: before, on, and after the void. The mean RAI values for the 30 kHz mode are provided for each sector.

Mode 30 signals offer an improvement when the condition before and on void are compared. The difference between the mean RAI values for both locations reaches 79%, which improves the evaluation based on full-signal by 5%. Next, the dispersion curves are calculated and presented in Figure 6-22-a.

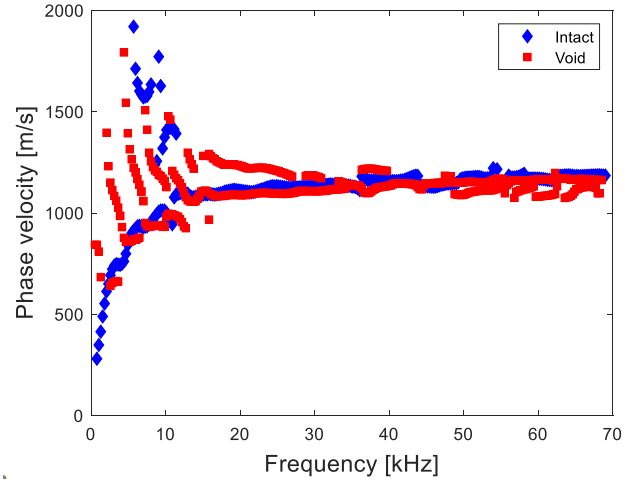

Figure 6-22. Phase velocity dispersion plot for mode 30 signals.

The maximum RDI value that can be obtained for mode 30 signals is lower than for the full-time signals. However, the frequency range that offers RDI of 120% is extended and includes ranges from 10-30 kHz and 20-30 kHz.

Finally, reconstructed signals for mode 50 are analyzed. The strongest displacement for mode 50 is observed later than the first arrival. The attenuation trend is preserved as before. For the intact line, the frequency content of the signals is unchanged throughout all measuring points. The presence of the void attenuates the signal amplitude and modifies the frequency content observed after the void. Mode 50 is less effective than mode 30, although the void can also be identified. The comparison of RAI before and on top of the void sections gives the lower value of their difference: 43%. Finally, the RDI is calculated based on the phase velocity dispersion curves of mode 50. Because of the frequency content of the mode, only the frequency ranges starting from 30 kHz give elevated values of RDI of 100%. Overall, mode 50 is less effective than previous approaches.

6.3.4.2 Summary results: cemented sand

The results of full-time, mode 30, and mode 50 approaches are compared. For each method, a difference between mean RAI values for the on void and before the void sections is calculated and presented in Figure 6-23. The approach based on the original time signals and whole spectral range is considered as a reference point for the modified method based on the WSST technique.

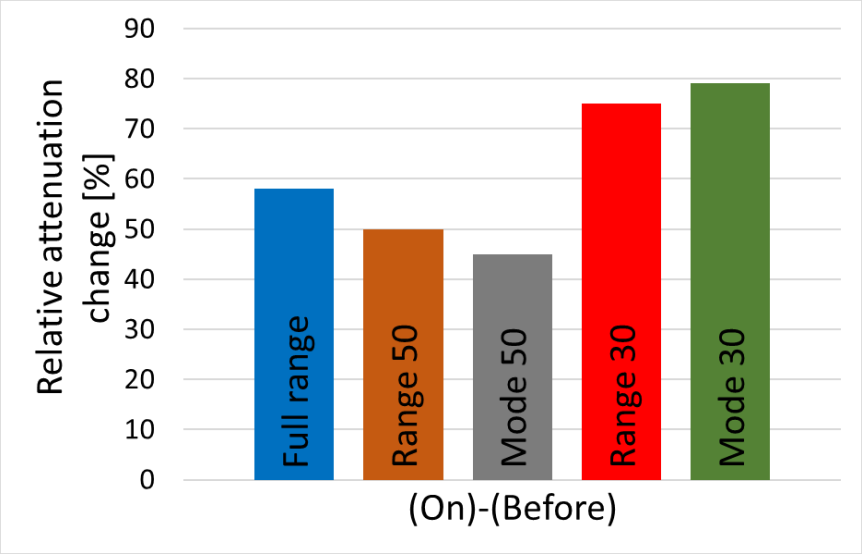

Figure 6-23. Attenuation differences between mean RAI values for the on top of the void (On) and before the void (Before) sections

It can be concluded that the separation between the before and on void conditions, obtained based on the full spectral range is not sufficient (58%). The results can be improved by narrowing the analyzed range of frequencies. However, one has to perform that carefully. Only range 30 provides the

improvement (75%) in the proper condition characterization (range 50 is less sensitive and is responsible for lower separation value for the approach based on the whole spectral range). The selection of frequency ranges can be made only based on the prior knowledge of the transmitted signal, which has to be obtained from the characterization procedure.

Further improvements can be obtained with the help of the WSST technique. Two modes are extracted (mode 30 and mode 50); however, only the 30-kHz mode increases the separation between two conditions to 79%. For all methods, when the measuring point is located after the void, the amplitude is slightly restored (by approximately 30%) than when directly on top of the void. An additional condition indicator that can be used is based on a difference between the before the void and after the void sections, which measures the permanent loss of energy.

6.4 Conclusions

In this study, the advantages of applying the WSST to include the wave attenuation approach for condition assessment of cementitious materials is demonstrated. The application of the WSST to ultrasonic signals is first demonstrated based on three numerical models. Next, the characterization of the ultrasonic transducer used in the study is performed. The WSST is used to extract the main modes that are transmitted to the specimens. Finally, two applications are considered: the method is applied to the detection of distributed damage (concrete beams subjected to freeze and thaw cycles) and localized damage (cemented sand specimen with the undersurface void). The following conclusions can be offered detailed conclusions regarding each section of this study are presented in Chapter 8.

1. COI effect increases exponentially with frequency, and the mode separation with WSST is possible for components with the frequency ratio up to 0.67.
2. WSST mode decomposition offers enhancement in the fundamental understanding of transmitter signals, and the extracted modes enable individual wavelength analysis.
3. It has been demonstrated that the ultrasonic evaluation based on WSST-based RAI offers improvement of up to 52% in distributed damage detection and up to 36% in localized damage detection.

Chapter 7
Ultrasonic evaluation and finite element analysis of damage in glass fibre reinforced polymer (GFRP) bars

7.1 Introduction

The use of fibre reinforced polymer (FRP) composite materials for construction in structural engineering increased significantly over the past 40 years (Erki & Rizkalla, 1993). FRP composites are used as alternative reinforcing material because of high strength-to-weight ratio, high stiffness-to-weight ratio, and corrosion resistance. Glass-FRP (GFRP) reinforcement is of increasing popularity in structural engineering due to the low cost in comparison to Carbon-FRP (CFRP). However, the long-term durability of GFRP in concrete remains an unresolved issue. It is also the main reason why the widespread application of GFRP cannot be readily accepted (Nkurunziza et al., 2005).

Deterioration of GFRP is mainly related to the following environmental factors: temperature, UV rays exposure, water/moisture, alkalinity, and load (Mukherjee & Arwikar, 2005a). When GFRP reinforcing bars are considered, the alkalinity of concrete pore water becomes the most critical issue. To address the unspecified long-term durability property of GFRP, accelerated ageing tests are being performed (Arczewska et al., 2017; ASTM International, 2019; Chen et al., 2007). Mukherjee and Arwikar (2005a; 2005b) showed how conditioning in elevated temperature affects structural scale test and the microstructure of the bar. Damage in both the matrix and fibres was observed in the outer layer of the bar.

Different testing protocols exist (e.g. tensile, flexure, and shear test) in the quality assurance applications of the GFRP bars (Genikomsou et al., 2018). Tensile properties are especially important for the reinforcing bars used in concrete. ASTM D7205 (ASTM International, 2016b) specifies details of the test method for tensile properties of FRP bars. The standard requires that the length of the tested specimens is not less than 40 times the diameter (and not shorter than 380 mm) plus two times the anchor length. The anchors and gripping system have to be designed specifically for FRP, as it has been found that the traditional gripping causes damage to FRP bars (Arczewska, 2017; ASTM International, 2016b). It also has been reported that GFRP reinforcement is characterized by significantly higher tensile strength than the traditional steel (Arczewska, 2017). Therefore, a larger bar requires substantial testing frame capacity.

Thereby, attention has been brought to other testing protocols. A similar degradation rate has been observed for shear and tensile properties (Arczewska, 2017). Therefore, to determine tensile strength degradation, the shear test might be performed. The shear test is more feasible as the specimen length does not depend on bar diameter, and the shear strength of GFRP bars is much lower when compared with tensile strength. However, shear testing requires a special device with cutting blades that are prepared uniquely for a specific bar diameter. When a variation in bar diameter during manufacturing or provided by different manufacturers is considered, this provides a logistical problem. A possible solution to testing GFRP bars can be offered with the non-destructive testing methods. The necessity of reliable NDT techniques for GFRP bars is even more important for in-situ testing of concrete members with GFRP reinforcement. The bars embedded in concrete show no visual deterioration and cannot be cut out of a structure to test in a traditional way. Additionally, GFRP bars are nonmagnetic; therefore, the NDT solutions used for the evaluation of concrete elements with steel reinforcement cannot be applied. Thus, a new NDT approach to address the problem of condition assessment of GFRP reinforcing bars embedded in concrete elements is needed.

The review of the current NDE methods used for GFRP is presented in Chapter 2.2.2. However, these advanced techniques (i.e. analysis of surface waves and wave attenuation) were not applied to GFRP bars. Additionally, a comparison between the shear test and ultrasonic evaluation for GFRP bars at different deterioration levels has not been reported in the literature. Moreover, the reviewed literature does not consider the effects of bar diameter and frequency on the ultrasonic features.

This chapter presents a pilot study of damage evaluation in bare GFRP bars. This is a prerequisite step before an evaluation of bars embedded in concrete members can be done (which is outside of this thesis's scope), which is a true challenge in field inspections. The bars are selected because of their simple geometry, which allows for predictable wave propagation and easies the lab handling. In this study, GFRP bars subjected to an accelerated ageing test (alkaline solution at the temperature of 60°C) are tested using both ultrasonic testing and destructive shear test. Ultrasonic evaluation is performed with the novel approach of using laser Doppler vibrometer for the characterization of P-wave transducers (54 and 150 kHz), and both wave velocity and attenuation approaches are applied. Wave propagation in GFRP bars is analyzed by comparing ultrasonic and laser vibrometer results, focusing on the effects of bar diameter and frequency used in the test. Additionally, the laboratory experiments are supplemented with a numerical simulation of wave propagation. The results show that the dispersion of ultrasonic waves plays a significant role, and evaluation results depend on bar diameter

and frequency of excitation. Deterioration of GFRP bars can be monitored using both wave velocity and attenuation approaches; however, the sensitivity of attenuation-based evaluation is superior. Numerical simulations show an opportunity to monitor wave dispersion with array scans taken along bar length.

7.2 Theoretical background

7.2.1 Wave propagation in a solid cylinder

Rose (2014) describes that for any laminar structures, which can be described by having one dimension smaller than the others, is naturally a waveguide. This applies to the GFRP bars analyzed in this chapter.

The wave propagation problem in a three-dimensional solid cylinder was studied independently by Pochhammer and Chree at the end of the 19th century. The Pochhammer-Chree theory describes the axially symmetric, torsional, and flexural wave propagation (a sinusoidal wave of frequency f) in an infinite homogeneous, isotropic cylinder of uniform cross-section, with traction free boundary conditions on the surface of the bar (Rigby et al., 2018). The Pochhammer's frequency equation for axially symmetric wave propagation, relating wavenumber (κ) and angular frequency (ω) is given as (Miklowitz, 1978):

$$\frac{2p}{r}(q^2+\kappa^2)J_1(pr)J_1(qr)-(q^2-\kappa^2)J_0(pr)J_1(qr)-4\kappa^2 pqJ_1(pr)J_0(qr)=0 \qquad (7\text{-}1)$$

where r is the radius of the cylinder, $p^2=\omega^2/V_L^2-\kappa^2$, $q^2=\omega^2/V_T^2-\kappa^2$, and V_L is the velocity of longitudinal waves and V_T is the velocity of transverse waves in an unbounded medium. J_0 and J_1 are Bessel functions of the first kind of order zero and one. Finally, $\kappa=\omega/V_{PH}$, where V_{PH} is the phase velocity.

The Pochhammer's frequency equation for non-axially symmetric wave propagation (of flexural waves) is defined as (Miklowitz, 1978):

$$J_1(\alpha)J_1^2(\beta)\left(g_1O_\beta^2+g_2O_\alpha O_\beta+\mathrm{g}O_\beta+g_4O_\alpha+g_5\right)=0 \qquad (7\text{-}2)$$

where $O_x=O_1(x)=x\,J_0(x)/J_1(x)$ is Onoe's function of the first kind of order one, and

$$
\begin{aligned}
g_1 &= 2\left(\beta^2 - \zeta^{*2}\right)^2 \\
g_2 &= 2\beta^2\left(5\zeta^{*2} + \beta^2\right) \\
g_3 &= \beta^6 - 10\beta^4 - 2\beta^4\zeta^{*2} + 2\beta^2\zeta^{*2} + \beta^2\zeta^{*4} - 4\zeta^{*4} \\
g_4 &= 2\beta^2\left(2\beta^2\zeta^{*2} - \beta^2 - 9\zeta^{*2}\right) \\
g_5 &= \beta^2(-\beta^4 + 8\beta^2 - 2\beta^2\zeta^{*2} + 8\zeta^{*2} - \zeta^{*4})
\end{aligned}
\tag{7-3}
$$

and $\alpha = pr$, $\beta = qr$, and $\zeta^* = \kappa r$.

A numerical solution of Equation 7-1 that implements the bisection as a root-finding algorithm developed by Puckett (2004) is used in this study. A solution of Equation 7-2 is not readily available in the literature. Therefore, a commercial software called Disperse (Pavlakovic et al., 2020) is used to find the anti-symmetric solution.

7.2.2 Alkaline solution penetration depth in GFRP bars

Katsuki and Uomoto (1995) studied the deterioration of GFRP rods due to alkali. They investigated the penetration depth of alkaline solution based on electron probe microscope analyzer (EPMA) pictures of the sections of conditioned rods and tensile test results. GFRP bars (with vinyl ester resin, 6 mm bar diameter) were conditioned for up to 120 days. The conditioning causes a degradation of bar tensile strength from 1690 MPa (unconditioned bars) to 480 MPa (at 120 days). As a result, they proposed that the failure strength can be obtained with the unaffected cross-sectional area of the GFRP bar. They also assumed that the tensile strength of the affected area is equal to zero. Katsuki and Uomoto proposed that the penetration depth (x) of alkaline solution into a GFRP bar can be calculated as:

$$
x^* = \sqrt{2D^{**}ct} \tag{7-4}
$$

where x^* is the penetration depth measured for the surface of the rod, D^{**} is the mass diffusion coefficient, c is the alkaline concentration, and t is the time. In this study, the values of D^{**} and c reported by Arczewska (2017) are used to estimate the ingress depth of the alkaline solution.

7.3 Experimental procedure and setup

7.3.1 Methodology

The proposed study consists of four activities: (i) bar conditioning (i.e. accelerated deterioration), (ii) ultrasonic tests, (iii) numerical verification, and (iv) reference intrusive test (i.e. shear test).

First, accelerated ageing of GFRP bars is achieved with the alkaline immersion test (the details of the test are given in Chapter 7.3.2). The testing procedure follows ASTM D7705 (ASTM International, 2019), and elevated temperature (60°C) is selected as the only accelerating factor. The total duration of the alkaline immersion test is six months. Each month, a set of bars is taken out from the conditioning chamber and tested using both NDT ultrasonic techniques (i.e. wave velocity and amplitude approaches are used) and a traditional intrusive method (i.e. shear test).

The ultrasonic tests start with the characterization of ultrasonic transducers used in experiments (this section is presented in Chapter 4). The responses in the tests are measured with different types of sensors (i.e. 54 and 150 kHz P-wave ultrasonic transducers, and the state-of-the-art laser vibrometer). Therefore, a dependency of frequency content with a transducer type is studied next with wavelet synchrosqueezed transform (WSST). Cross-sectional surface vibration of the bar, measured with the laser vibrometer for four bar-diameters tested under different frequencies, is also discussed. The main ultrasonic damage evaluation study is based on wave velocity and amplitude approaches. P-wave velocity is measured in two configurations (i.e. axial and transversal configurations, shown in Figure 7-1). Amplitude change is calculated based on the amplitude of the first arriving peak and based on discrete frequency bands.

In the next step, the analysis is complemented with numerical simulations. A wave propagation model is developed in Abaqus. In the section on the calibration of the model, theoretical dispersion curves for symmetric and antisymmetric bar vibration modes are used. Next, bar deterioration is simulated with a decreased bar diameter. Responses measured at a side of the bar and the top of the bar are analyzed and compared with the laboratory results.

Finally, the ultrasonic evaluation is verified with a reference intrusive test. Each month of conditioning in an alkaline solution, a set of bars is tested in shear accordingly to ASTM D7617 (ASTM International, 2017b). Strength reduction graphs are obtained and compared with the ultrasonic evaluation. The overall methodology and main conclusions are given in Table 7-1.

Table 7-1. Methodology summary. D13 means a bar with a 13 mm diameter.

Activity	Flow chart	Main conclusions
Fundamental understanding of waves in GFRP bars (section 7.4.2)	Ultrasonic tests with ultrasonic transducers (UTx) and laser vibrometer • 54 kHz • 150 kHz → Compare UTx and laser • Time • FFT • WSST Laser surface scanning → Analysis of surface displacement	• The frequency content of responses changes with bar diameter • Cross-sectional displacement patterns change with bar diameter

Ultrasonic evaluation (section 7.4.3)	Wave velocity tests
	• Axial configuration
	  • 54 and 150 kHz
	• Transverse configuration
	  • 150 kHz
	→ Wave velocity retention graph
	Wave attenuation tests (54 and 150 kHz)
	• P-Peak
	• Discrete frequency bands
	→ Wave velocity retention graph
		• Wave velocity successfully identified damage progression (the selectivity is low)
		• Attenuation approach offers increased sensitivity
		• No consistent conclusion regarding the effect of bar diameter on ultrasonic features

Numerical simulations (section 7.4.4)	Calibration of the model • Simulated Mexican Hat Wavelet (30, 54 and 150 kHz) • Real excitation (54 and 150 kHz) → Comparison of dispersion curves • Bar side readings • Theoretical dispersion curves Simulation of deterioration (reduced diameter) → Analysis of • Theoretical dispersion curves • Numerical simulations (side readings) • P-Peak (top of the bar)	• Change in wave velocity (axial readings) is insignificant • Analysis of wave dispersion (side of bar measurements) shows promising results • Ultrasonic transducers should be selected based on tested bar diameter
Shear test (section 7.4.5)	Shear test (conditions 0-6) • D13 • D16 • D20 • D25 → Shear strength retention graph	• Shear strength trends follow results found in the literature • Smaller bars are affected more • Good agreement with numerical results (diameter effects)

In the following sections, details on the preparation and conditioning of specimens, ultrasonic tests, numerical simulations, and the shear tests are given.

7.3.2 Specimens: preparation and conditioning

In this study, 1-meter long GFRP bars of diameters: $\phi 13, 16, 20, \text{and } 25$ mm are used (the following abbreviation is used in the rest of the chapter: D13, D16, D20, and D25). For each diameter, a total of 28 bars are used. The alkaline immersion test has been selected in order to induce progressive damage to the bars. The alkaline solution is designed in accordance to the ASTM D7705 standard (ASTM International, 2019) and comprises of 118.5 g of $Ca(OH)_2$, 0.9 g of NaOH, and 4.2 g of KOH per 1 L of deionized water. The alkaline environment is considered as an equivalent of the environment that bars would experience in concrete (pH of 12.6-13). The test is designed to have only the temperature as an accelerating factor, and the elevated temperature is set to 60°C. The ends of the bars are protected by a layer of epoxy.

A set of 4 bars, from each diameter, is not conditioned in the solution and is treated as a baseline condition (also called condition 0 in the following sections). The remaining part is kept in the solution for up to 6 months. Every month (i.e. 28 days), a set of 4 bars per diameter is taken out of the conditioning chamber and tested. The bars are washed, dried, and weighed. Next, bars are cut into 300 mm pieces (disposing 50 mm from each end). As a result, a set of 12 short specimens is obtained per diameter. Six specimens are tested with a shear test, and the remaining six bars are tested non-destructively.

7.3.3 Ultrasonic evaluation

The ultrasonic evaluation is performed using three setups. Transducers used are P-wave ultrasonic transducers (Proceq), with nominal frequencies of 54 and 150 kHz. A function generator (HP33120A) is used to provide an input signal (54 and 150 kHz square pulse, which is amplified to the amplitude of ± 125V) to the transmitter. Figure 7-1-a presents a typical ultrasonic pulse velocity (UPV) configuration (the UPV is described in Chapter 5, (ASTM International, 2016a)) is used in the first setup (axial setup). Ultrasonic transducers are placed on both ends of a bar. 3-D printed caps (printed out of PC-ABS) are used to ensure the concentric position of transducers and the bar. Additionally, 3-D printed holders (PC-ABS, with elastic bands) are used to provide equal coupling pressure during all tests. Therefore, not only the wave velocity analysis is used, but also the attenuation of the signal amplitude can be used.

Next, ribs on the side of a bar are removed (a 30mm length form each bar end is polished), and an aluminum square plates (25x25x2mm) are glued to a bar. This increases a coupling area of transducers (only 150-kHz transducers are used, due to their smaller wear-surface area) that are glued

perpendicularly with respect to the bar's length (transverse setup is shown in Figure 7-1-b). The transverse configuration can be used when the access to bar ends is not possible (which is the case in most field applications). Alternatively, new structures can be designed to have additional reinforcing bars for condition monitoring purposes (these bars would not play any structural role), enabling access to the bar ends. In axial and transverse configurations, responses are measured with matching ultrasonic transducer and recorded (16 time-averages are used) with a digital oscilloscope (Agilent DSO-X 3014A). In the third setup, the transmitter part is the same as presented in the axial setup, and the responses are measured with a laser Doppler vibrometer. A laser sensor head (LSH, Polytec OFV-534) is connected to the vibration controller (OFV-2570), and the measured responses are stored on a computer. The measuring grid consists of concentering circles (shown in Figure 7-1-d) with a radial step of 1.5 mm and 24 points per each circle. Each recorded time signal represents an average of 500 measurements. A total of 75 to 171 points are recorded, depending on a bar diameter.

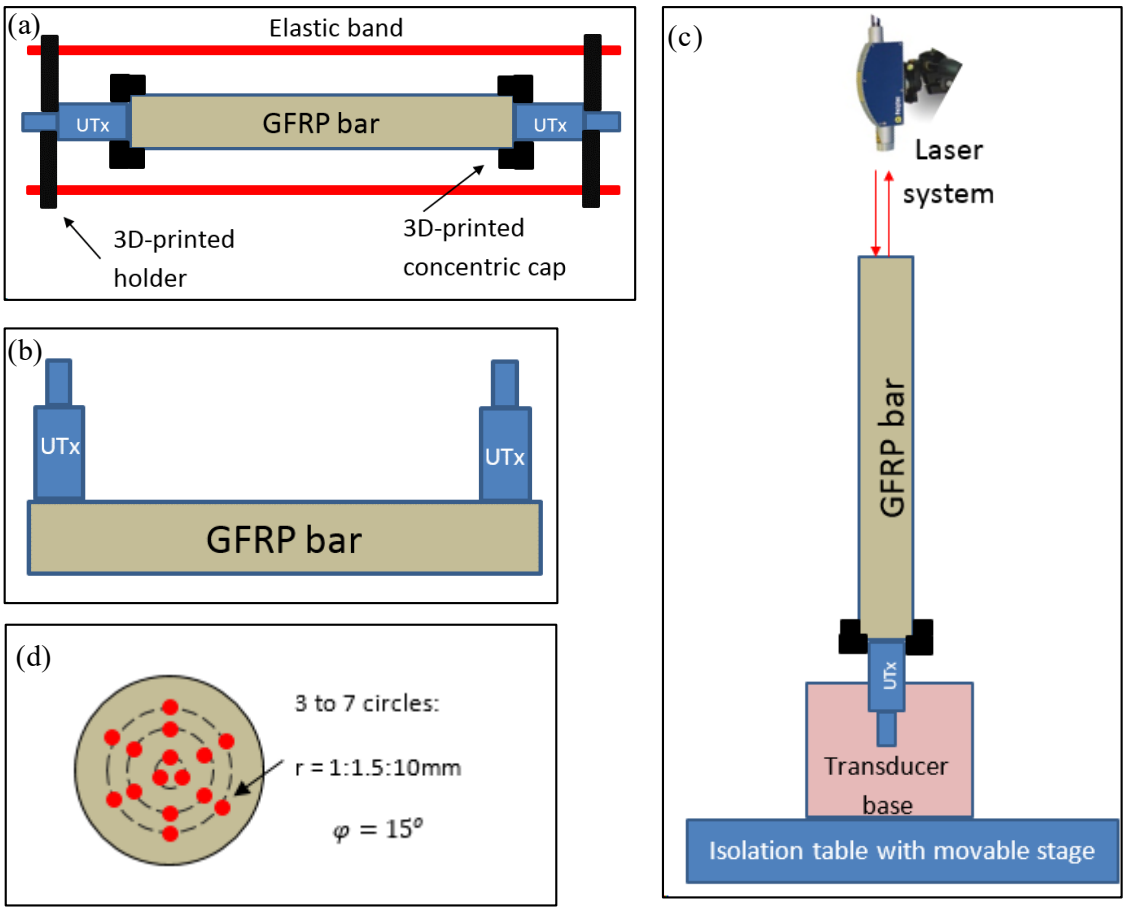

Figure 7-1. Laboratory setups used in this study: (a) axial setup, (b) transverse setup, (c) laser vibrometer setup, and (d) measuring grid used in the laser tests

7.3.4 Numerical model

A finite element model is designed in Abaqus to explore the wave propagation in a GFRP bar. The following sections discuss the requirements and details of the model.

7.3.4.1 Finite element mesh

Mesh element size plays an important role in the accuracy of numerical models. In wave propagation problems, the element size is selected based on the highest frequency (f_{MAX}) and the lowest velocity (V_{MIN}) of propagating wave. If the elements are too large, high frequencies will be filtered out, while too small elements might cause numerical instabilities (and can drastically increase the computational time of a simulation). An approximate element size (g) can be calculated as $g \leq \varsigma \lambda_{MIN} =$

$\varsigma V_{MIN}/f_{MAX}$. The constant ς is selected depending on mass matrices ($\varsigma = 0.25$ when the consistent mass approach is used, and $\varsigma = 0.2$ if the lumped mass approach is used (Zerwer et al., 2003)). Assuming consistent mass approach, the wave velocity of 3000m/s (the lowest velocity observed in the phase velocity dispersion graph presented in Figure 7-19), and frequency of 280 kHz (the upper frequency defining a bandwidth in Figure 7-14), the maximum allowed element size is 2.67 mm. Element size is investigated in the model calibration section, as smaller elements are needed to capture the diameter reduction due to the alkaline solution ingress in the GFRP bar deterioration simulations. The whole geometry is meshed with 8-node linear brick elements with reduced integration (C3D8R (Dassault Systemes Simulia Corp, 2012)). The simulations are run in the explicit mode.

7.3.4.2 Time increment

Simulation time increment (τ) can be calculated as $\tau \leq g/V_P$, where V_P is the P-wave velocity. Assuming the element size of 2.5 mm and the highest velocity observed in the laboratory tests (5171m/s), the maximum simulation time step becomes $\tau = 0.48\mu s$. The stable time increment calculated in Abaqus is $\tau = 0.047\mu s$, which allows the use of smaller element size.

7.3.4.3 Boundary conditions

To replicate the boundary conditions of the laboratory experiments, the side of the bar and the top surface have all-free boundary conditions applied. At the bottom surface of a modelled bar, an excitation is prescribed (defined in section 7.3.4.5) as a displacement in either axial or radial direction. Therefore, both axial and transversal vibration can be observed

7.3.4.4 Material properties

In the simulations, GFRP is simulated as a linear elastic material. Materials parameters are provided by the manufacturer E = 55GPa, $\rho = 2220\frac{kg}{m^3}$, and Poisson's ratio of 0.25 is assumed (as the wave propagation is in the longitudinal bar direction). Finally, material damping is simulated with a Rayleigh damping model available in Abaqus. The Rayleigh damping can be related to the experimental damping (Equation 3-32) as:

$$\zeta = \frac{\alpha^*}{2\omega} + \frac{\beta^{**}\omega}{2} \tag{7-5}$$

where ω is the angular frequency, α^* and β^{**} are mass and stiffness proportional damping coefficients. The coefficients can be calculated with the following formulas (Zerwer et al., 2002):

$$\alpha^* = \frac{2\zeta\omega_1\omega_N}{\omega_1+\omega_N}$$
$$\beta^{**} = \frac{2\zeta}{\omega_1\omega_N} \quad (7\text{-}6)$$

where ω_1 and ω_N are the first and the highest natural frequencies of the vibration modes with high contribution to the response. In this study, the frequency content of characterized transducers is used in the calculation of the damping coefficients.

7.3.4.5 Excitation function

The excitation used in the model is applied as uniform displacement on one of the cross-sectional areas of the GFRP bar (details how the excitation is applied can be found in Figure 7-15-b). Two types of loading functions are used: (i) simulated Mexican hat wavelet (MHW) and (ii) the real surface displacement measured in the ultrasonic characterization process (Chapter 4). The MHW is either centred at the main resonant frequencies of 54 kHz transducer (i.e. 30 and 54 kHz) or the resonant frequency of 150 kHz probe (i.e. 150 kHz).

7.3.5 Shear test

Arczewska (2017) showed that the strength degradation rate for GFRP bars is the same for tensile and shear tests. However, the shear test does not require extensive laboratory capabilities as the tensile test (which is essential for large diameter bars). Therefore, the shear test that follows the ASTM D7617 standard procedure (ASTM International, 2017b) is used in this study. In the shear test method, a shear test device is used (presented in Figure 7-2). The device consists of two bar seat metal blocks and two bottom blades (these elements hold GFRP bars), and guides (that create a space between the bottom blades). These parts are held together with two threaded rods. The upper blade is loose and placed on the bar before the test. The upper blade is then pushed down, producing double shear, by a testing machine.

Figure 7-2. Shear test device

The MTS C-64 machine is used in the load control mode (with the rate of 45 MPa/min, the rate is adjusted for each bar diameter). The load is applied until a second peak is observed (and the load drops to 70% of the observed peak force) on the load-displacement (of the machine head) curve. Finally, transverse shear strength (τ_u) is calculated as

$$\tau_u = \frac{P_S}{2A} \tag{7-7}$$

where P_S is the maximum failure force, and A is the cross-sectional area of the bar. In accordance with the ASTM standard, six bars are tested per each diameter and condition. The specimen length is selected as 300mm. During the test, a bar is placed centrally in the shear testing device.

7.4 Results and discussion

7.4.1 Transducer characterization

In this study, two P-wave transducers (Proceq) with the resonant frequencies of 54 and 150 kHz are used. The characterization procedure and the results are presented in Chapter 4. The GFRP bars have diameters that are smaller than the diameters of both probes (the only exception is 150 kHz prove and the 25mm bar when both objects have the same diameter). Therefore, only the central signals and their frequency content (presented in Figure 4-16 and Figure 4-17-a) are considered in the analysis of recorded signals of the GFRP bars and shown in Figure 7-3.

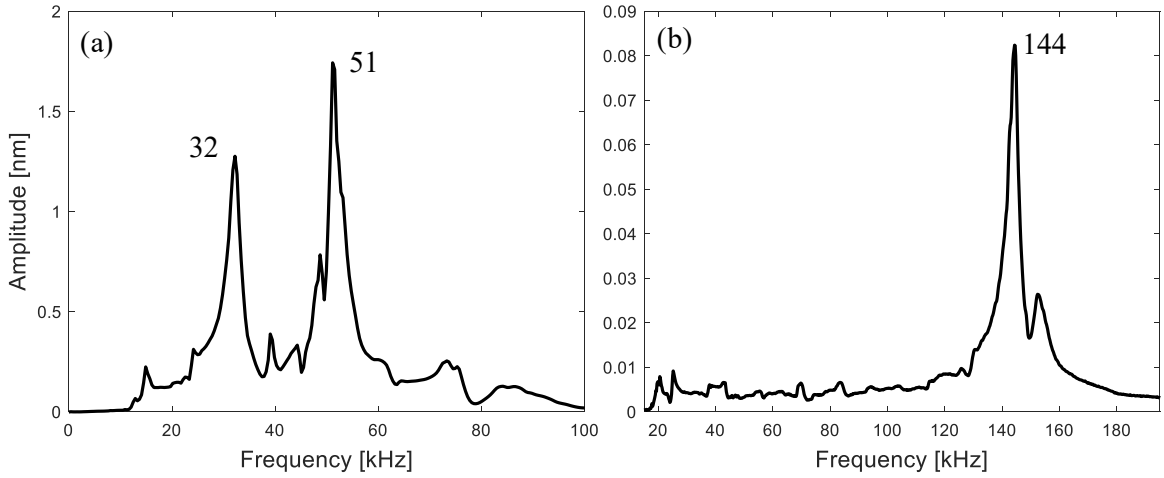

Figure 7-3. Characterization frequency results for (a) 54 and (b) 150 kHz transducers

The 54-kHz probe emits two major frequencies, 30 and 50 kHz, while the 150-kHz probe sends mainly the nominal resonant frequency. These frequencies, assuming wave velocity of 5171 m/s as observed in the 25mm GFRP bar, correspond to the following wavelengths: 172, 96, and 34 mm.

7.4.2 Fundamental understanding of waves in GFRP bars

Since wavelengths are longer than bar diameters in all test configurations (considering excitation frequency and bar diameters), GFRP bars should be treated as thin bars. The ultrasonic analysis starts with a fundamental understanding of waves in the tested specimens and discussion how frequency content and mode shapes change with the excitation frequency, receiver type, and bar diameter.

7.4.2.1 Frequency content analysis

Sample time signals, measured with both ultrasonic transducers and laser vibrometer, are analyzed first. Self-normalized responses, measured for unconditioned bars, are presented in Figure 7-4. Signals measured with 54-kHz transducer show the most similarity for all bar diameters. However, when laser vibrometer data is analyzed, the widening of the first arriving peak is observed. More diameter effects are visible when the bars are tested with 150-kHz probes (i.e. when the wavelengths used in the test are shorter). First arrivals for all diameter and sensor configurations are distinct, which means that the UPV method can be used for the evaluation of bar condition.

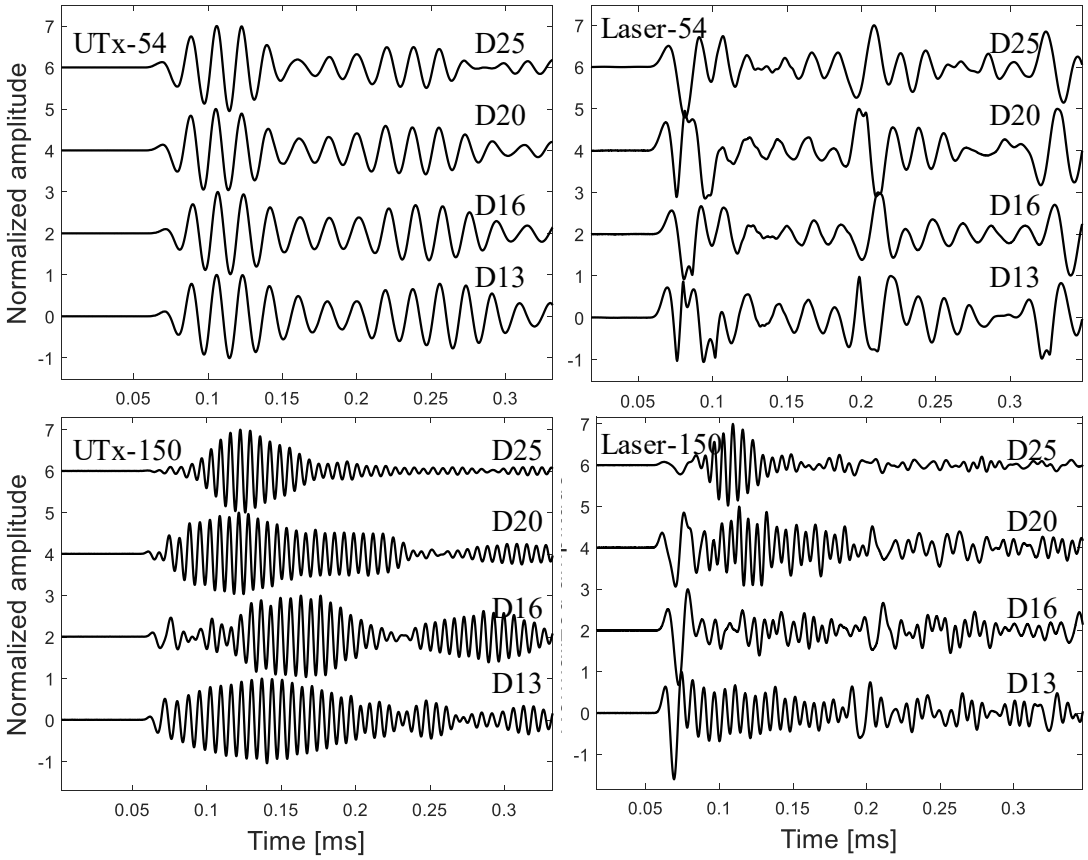

Figure 7-4. Sample self-normalized time signals measured for unconditioned bars. Ultrasonic results are presented in the left column, and the laser results are shown in the right column. Bars are tested with both 54 and 150 kHz frequency of excitation.

Due to the changing nature of the width of the pulses present in time signals, the WSST method is selected for the detailed analysis of the frequency content. Figure 7-5 presents instantaneous frequencies estimated with the WSST method for sample responses. The investigation is carried for bars with the smallest and largest diameters, i.e. 13mm and 25 mm, under 54 kHz excitation. The ultrasonic signals are measured with the axial setup (Figure 7-1-a). For the laser vibrometer responses (measured with the setup presented in Figure 7-1-c), only the signal for the central location of the bar cross-section is shown.

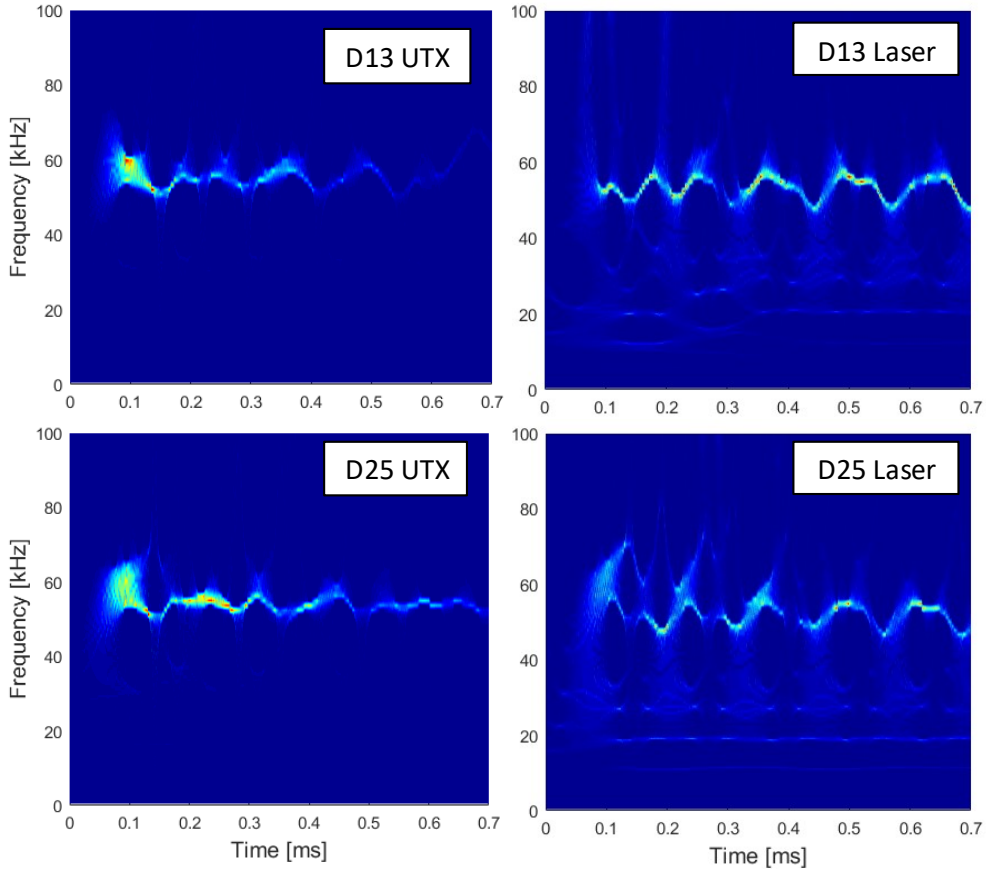

Figure 7-5. Sample WSST results for unconditioned bars, Tx = 54 kHz

Similar frequency content is seen when both diameters are compared. A significant difference is observed between the laser vibrometer and ultrasonic transducer responses. The laser vibrometer has a flat frequency response, which means that the measured response is not altered by the laser vibrometer characteristics. As a result, more frequency ridges are seen in the instantaneous graphs, and the frequencies can be explained with the characterization shown in Chapter 4. On the other hand, the ultrasonic transducer responses are concentrated on the resonant frequency of the ultrasonic transducer (i.e. 54 kHz), and the other frequencies are not clearly visible. Figure 7-6 presents a similar dataset; however, the bars are tested under 150 kHz excitation.

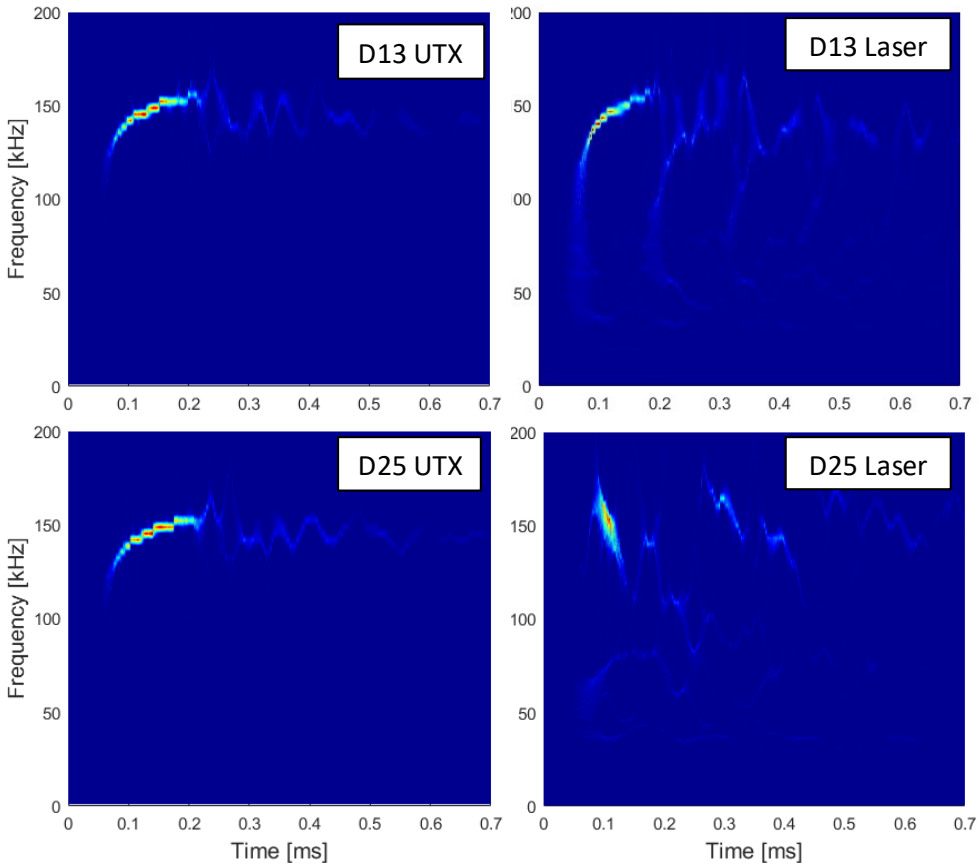

Figure 7-6. Sample WSST results for unconditioned bars, Tx = 150 kHz

Different frequency behaviour is observed when the specimens are tested under 150 kHz excitation. Strong non-linear character of the instantaneous frequencies is observed, with an extreme case recorded for the D25 bar with the laser vibrometer. Then, a first arriving pulse has a significantly lower frequency (around 75 kHz), and the 150 kHz component starts to manifest around 0.1 ms. Based on the characterization of the 150 kHz transducer (shown in Figure 4-17-a), it is known that the main frequency is excited in the range from 120 to 160 kHz. The non-linear character of the instantaneous frequencies is due to the dispersion of waves in that frequency range (sample phase velocity dispersion curve can be found in Figure 7-19).

7.4.2.2 Mode shape analysis

The analysis of the fundamental understanding of the waves propagating in the bar continues with laser scans of the cross-sectional area performed in the setup presented in Figure 7-1-c. The 13mm bar is analyzed first. Figure 7-7 shows surface displacement observed for both excitation frequencies. During

the whole recorded time, the same plane character is observed, which means that vibration is dominated by the longitudinal vibration.

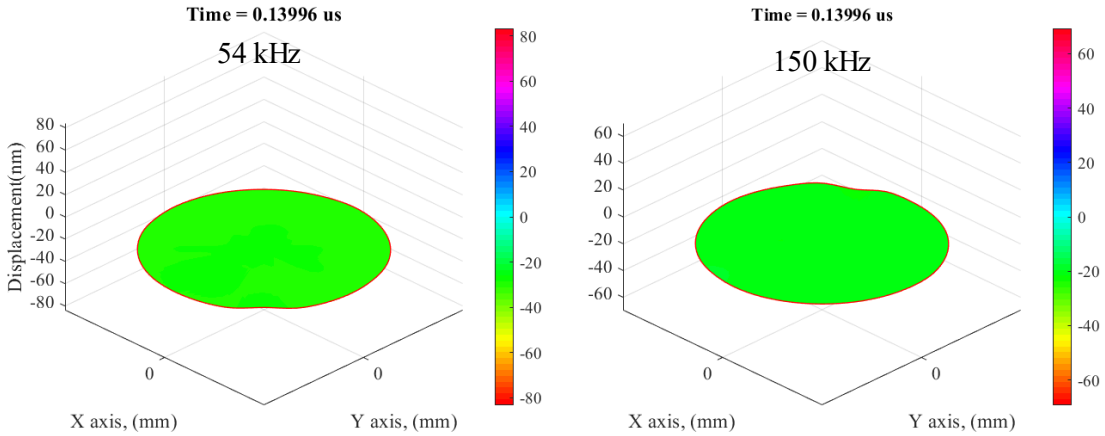

Figure 7-7. Mode shapes observed throughout the laser vibrometer test for the bar 13mm and both 54 and 150 kHz ultrasonic transmitters

The cross-sectional surface vibration of the 25mm bar is presented in Figure 7-8. Different mode shapes are observed during the test. For both excitation frequencies, the first arriving wave manifests with the plane character. When the 54 kHz transducer is used, the surface vibration continues with the plane character, until a bending pattern is seen. Different behaviour is seen with the 150 kHz transducer. After the initial arrival, the surface vibration follows mode shape one observed in the characterization of the 150 kHz transducer (shown in Figure 4-8) and finally reaches mode shape 2 (of thin plates discussed in Chapter 4).

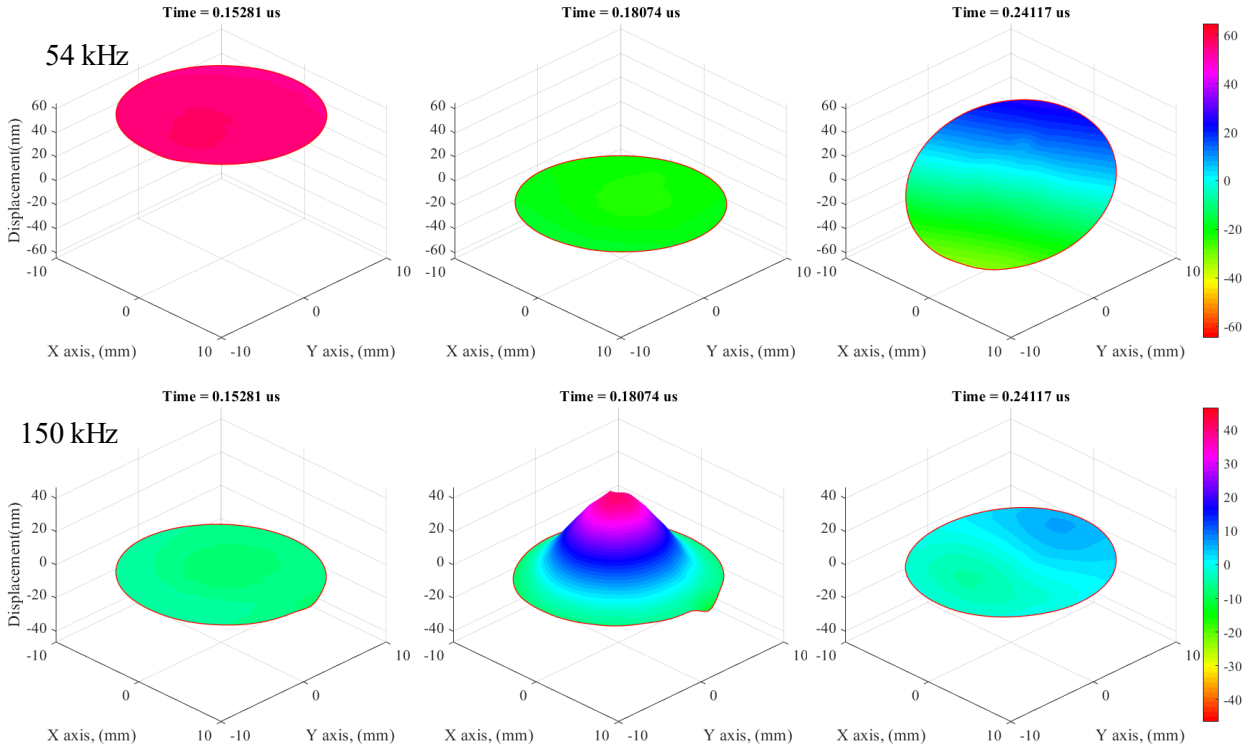

Figure 7-8. Mode shapes observed throughout the laser vibrometer test for the bar 25mm tested under 54 and 150 kHz excitation

In order to keep consistency and enable comparison between different bar diameters, only the first part of the signal will be analyzed in the ultrasonic evaluation section of this study.

7.4.3 Ultrasonic evaluation

The following section presents results for ultrasonic evaluation performed based on wave velocity and attenuation approaches.

7.4.3.1 Wave velocity

Wave velocity analysis is performed based on responses measured in axial and transverse configurations presented in Figure 7-1. Wave velocity is calculated based on the time of the first arriving wave and measured length of each specimen. Six bars are tested for each diameter every month of the test. Finally, mean wave velocity, standard deviation, and coefficient of variation are calculated for each bar diameter.

- Axial test

Ultrasonic pulse velocity results obtained in the axial setup are discussed first. Results of tests performed with 54-kHz transducers are presented in Table 7-2.

Table 7-2. Wave velocity results for all bars (axial setup), tested with 54-kHz ultrasonic transducers.

$D13$	Month	0	1	2	3	4	5	6
	Mean velocity [m/s]	5047	5031	4904	4897	4878	4845	4842
	σ [m/s]	21	22	14	17	19	32	24
	COV [%]	0.42	0.44	0.29	0.35	0.39	0.66	0.42
$D16$	Month	0	1	2	3	4	5	6
	Mean velocity [m/s]	5025	5007	4924	4878	4860	4818	4807
	σ [m/s]	31	33	14	58	19	22	33
	COV [%]	0.62	0.66	0.28	1.19	0.39	0.46	0.62
$D20$	Month	0	1	2	3	4	5	6
	Mean velocity [m/s]	5092	5087	5068	5012	5019	4991	4981
	σ [m/s]	35	22	59	12	17	36	19
	COV [%]	0.69	0.43	1.16	0.24	0.34	0.72	0.69
$D25$	Month	0	1	2	3	4	5	6
	Mean velocity [m/s]	5171	5157	5117	5089	5071	5053	5049
	σ [m/s]	6	29	16	10	14	36	19
	COV [%]	0.12	0.56	0.31	0.2	0.28	0.71	0.12

Results of the UPV test performed with 150-kHz are presented in Table 7-3.

Table 7-3. Wave velocity results for all bars (axial setup), tested with 150-kHz ultrasonic transducers.

$D13$	Month	0	1	2	3	4	5	6
	Mean velocity [m/s]	5388	5365	5329	5325	5298	5280	5274
	σ [m/s]	13	22	24	38	16	22	19
	COV [%]	0.24	0.41	0.45	0.71	0.3	0.42	0.36
$D16$	Month	0	1	2	3	4	5	6
	Mean velocity [m/s]	5356	5335	5309	5272	5269	5262	5197
	σ [m/s]	65	46	51	69	25	30	19
	COV [%]	1.21	0.86	0.96	1.31	0.47	0.57	0.37
$D20$	Month	0	1	2	3	4	5	6
	Mean velocity [m/s]	5402	5397	5365	5362	5351	5299	5283
	σ [m/s]	23	6	47	20	13	11	17
	COV [%]	0.43	0.11	0.88	0.37	0.24	0.21	0.32
$D25$	Month	0	1	2	3	4	5	6
	Mean velocity [m/s]	5477	5435	5417	5387	5362	5341	5330
	σ [m/s]	4	10	10	15	10	12	15
	COV [%]	0.07	0.18	0.18	0.28	0.19	0.22	0.28

Reported values depend highly on the diameter to wavelength ratio (as discussed in Chapter 5.4.6). The lowest velocity is reported for 13mm bars tested with 54 kHz transducers ($D/\lambda = 0.14$), while the highest one is observed in a 25mm bar tested with 150 kHz transducer ($D/\lambda = 0.74$).

Next, the reported mean wave velocities are normalized with the value measured for the unconditioned bar (condition/month 0). The velocity retention plots for both transducers used in the test are shown in Figure 7-9.

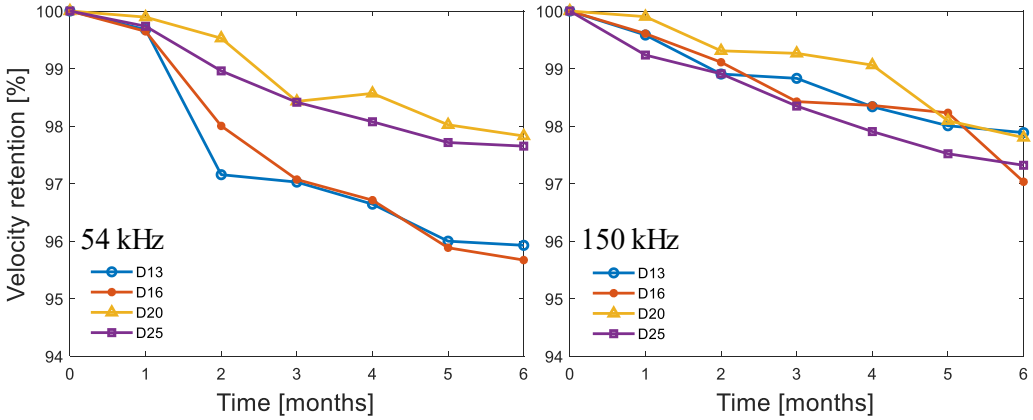

Figure 7-9. Wave velocity trend; axial configuration

For both types of transducers, a reduction of wave velocity is observed with the duration of the conditioning. However, no consistent trend regarding the effect of bar diameter is observed. The reduction is within 5% and does not provide enough sensitivity for field application.

- Transverse test

The results obtained in the transverse configuration are discussed next. Three bars are tested for each diameter, and due to the transducer size, only the 150-kHz transducer is used in the test. The overall results for all bars are presented in Table 7-4.

.

Table 7-4. Wave velocity results for all bars (transverse setup), tested with 150-kHz ultrasonic transducers

$D13$	Month	0	1	2	3	4	5	6
	Mean velocity [m/s]	3088	3084	3078	3074	3069	3067	3056
	σ [m/s]	65	20	32	22	12	15	8
	COV [%]	2.10	0.65	1.04	0.72	0.39	0.49	0.26
$D16$	Month	0	1	2	3	4	5	6
	Mean velocity [m/s]	3073	3064	3058	3053	3040	3026	3020
	σ [m/s]	33	41	25	16	16	17	4
	COV [%]	1.07	1.34	0.82	0.52	0.53	0.56	0.13
$D20$	Month	0	1	2	3	4	5	6
	Mean velocity [m/s]	3077	3073	3063	3059	3051	3037	3036
	σ [m/s]	17	26	61	14	14	13	29
	COV [%]	0.55	0.85	1.99	0.46	0.46	0.43	0.96
$D25$	Month	0	1	2	3	4	5	6
	Mean velocity [m/s]	3067	3064	3058	3054	3048	3037	3036
	σ [m/s]	24	15	37	16	2	5	3
	COV [%]	0.78	0.49	1.21	0.52	0.07	0.16	0.10

Next, the reported mean wave velocities are normalized with the value measured for the unconditioned bar. The velocity retention plot under 150-kHz excitation in the transverse configuration is shown in Figure 7-10.

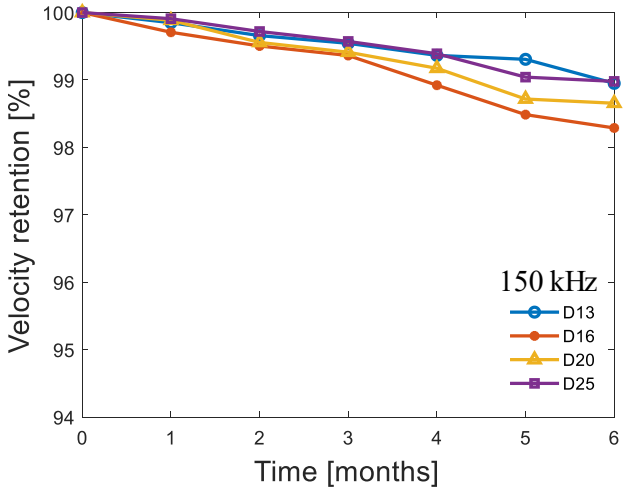

Figure 7-10. Wave velocity trend; transverse configuration

Velocity reduction is observed for all bar diameters. In the transverse configuration, a diameter effect is observed on the reduction rate (beside 13mm bar). The largest diameter is affected the least. This behaviour is expected, as the depth of penetration is the same for all bar diameter. Therefore, the smallest diameter should be affected the most. At the same time, velocity reduction in the transverse configuration is low and reaches 2% after six months of conditioning.

The wave velocity approach is able to catch the deterioration process happening during the conditioning of GFRP bars in an alkaline solution. However, the velocity reduction is not significant and stays within 2-5%. When high precision during the selection of arrival time is not guaranteed, the test might not provide a reliable evaluation. Therefore, an approach based on the change in wave amplitude is investigated next.

7.4.3.2 Wave attenuation analysis

The following sections discuss the wave attenuation analysis based on P-Peak, and discrete frequency bands approach.

- P-Peak amplitude

First, an amplitude change is analyzed based on the amplitude of the first arriving pulse (the maximum value of the first peak), similarly as presented in 5.4.8. Only the axial setup with the 3D-printed holders allows for constant pressure; therefore, only these results are analyzed.

Table 7-5. P-Peak amplitudes for all bars (axial setup), tested with 54-kHz ultrasonic transducers.

$D13$	Month	0	1	2	3	4	5	6
	Mean P-Peak amplitude [mV]	63.08	61.08	52.90	51.01	51.95	51.29	49.56
	σ [m/s]	0.51	0.92	0.75	0.46	3.73	0.96	1.36
	COV [%]	0.81	1.51	1.42	0.90	7.18	1.88	2.75
$D16$	Month	0	1	2	3	4	5	6
	Mean P-Peak amplitude [mV]	83.30	81.26	65.49	57.81	57.82	51.73	44.58
	σ [m/s]	0.29	2.13	0.33	0.68	4.71	2.35	1.05
	COV [%]	0.35	2.62	0.50	1.18	8.15	4.55	2.36
$D20$	Month	0	1	2	3	4	5	6
	Mean P-Peak amplitude [mV]	92.10	87.37	82.54	81.54	78.74	76.64	73.84
	σ [m/s]	1.46	1.42	0.89	0.90	1.02	0.99	1.58
	COV [%]	1.58	1.63	1.07	1.10	1.30	1.29	2.14
$D25$	Month	0	1	2	3	4	5	6
	Mean P-Peak amplitude [mV]	103.89	92.52	85.91	81.97	79.96	79.32	76.76
	σ [m/s]	0.58	2.22	1.07	0.66	1.14	1.18	1.01
	COV [%]	0.56	2.40	1.24	0.80	1.43	1.49	1.32

Two observations can be made based on the data presented in Table 7-5: (i) Higher P-Peak values are observed with an increase of bar diameter, and (b) consistent decrease of the amplitude is observed throughout the whole test for all bar diameters. The first observation is related to the fact that larger bars cover more of the transducer wear surface. Therefore, more energy is sent to the bar. Next, P-Peak amplitudes measured under 150-kHz excitation are presented in Table 7-6.

Table 7-6. P-Peak amplitudes for all bars (axial setup), tested with 150-kHz ultrasonic transducers

$D13$	Month	0	1	2	3	4	5	6
	Mean P-Peak amplitude [mV]	16.99	16.02	15.54	13.45	13.38	12.51	11.25
	σ [m/s]	0.31	0.31	0.11	1.03	0.92	0.24	0.24
	COV [%]	1.85	1.95	0.73	7.69	6.85	1.92	2.13
$D16$	Month	0	1	2	3	4	5	6
	Mean P-Peak amplitude [mV]	9.58	8.81	7.85	7.01	6.35	5.77	5.54
	σ [m/s]	0.19	0.12	0.14	0.14	0.05	0.11	0.10
	COV [%]	1.96	1.34	1.78	2.03	0.79	1.94	1.77
$D20$	Month	0	1	2	3	4	5	6
	Mean P-Peak amplitude [mV]	9.06	8.78	7.56	7.33	7.05	6.85	6.76
	σ [m/s]	0.24	0.13	0.23	0.14	0.10	0.03	0.12
	COV [%]	2.61	1.45	3.07	1.87	1.43	0.46	1.80
$D25$	Month	0	1	2	3	4	5	6
	Mean P-Peak amplitude [mV]	6.93	6.24	5.72	4.70	4.63	4.53	4.38
	σ [m/s]	0.17	0.12	0.46	0.03	0.05	0.15	0.11
	COV [%]	2.46	1.86	8.09	0.67	1.17	3.23	2.52

Again, two observations can be made. Similarly, a consistent decrease of P-Peak amplitudes is observed with the progression of deterioration of the bars. However, an opposite trend of maximum values with respect to the bar diameter is found, and instead of increased participation of bar diameter is wear surface area, the P-peak values decrease for larger bars. This phenomenon can be explained with the frequency analysis shown in Chapter 7.4.2. Based on the data presented in Figure 7-4, the width of first arriving pulses increases with an increase of bar diameter (i.e. first arriving waves have lower frequency). When the characterization information is added (i.e. the lower frequencies are emitted; however, with much lower amplitudes), the observed P-Peak behaviour should be expected.

Finally, the mean P-Peak amplitudes are normalized with the value measured for the unconditioned bar. The P-Peak amplitude retention plots for the bars tested under both 54 and 150-kHz excitation in the axial configuration are shown in Figure 7-11.

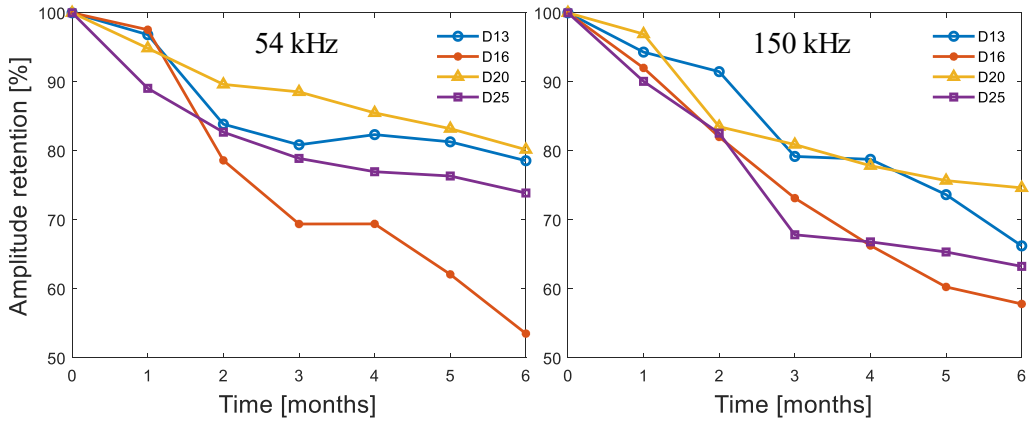

Figure 7-11. P-Peak attenuation trend; axial configuration

The analysis of attenuation trends shown in Figure 7-11 leads to the conclusion that P-Peak amplitude is a more sensitive parameter (a reduction of up to 40% is observed), capable of capturing the deterioration of the GFRP bars. The use of 150-kHz transducers can be recommended as all of the bars reach a maximum reduction of 25-40%, while when the 54 kHz transducer was used, the reduction (after excluding D16 bar) stays within 20-25%.

- Discrete frequency bands

Additionally, an approach based on more than a single point of the dataset is also considered. Attenuation trends are calculated based on energy calculated in discrete frequency bands. Figure 7-12 presents sample time signals measured for D16 bars during the whole duration of the test and their frequency spectra. Signals are windowed with a sharp Tukey window (cosine fraction of 0.1; the window is presented in with red stars) prior to the calculation of the FFTs.

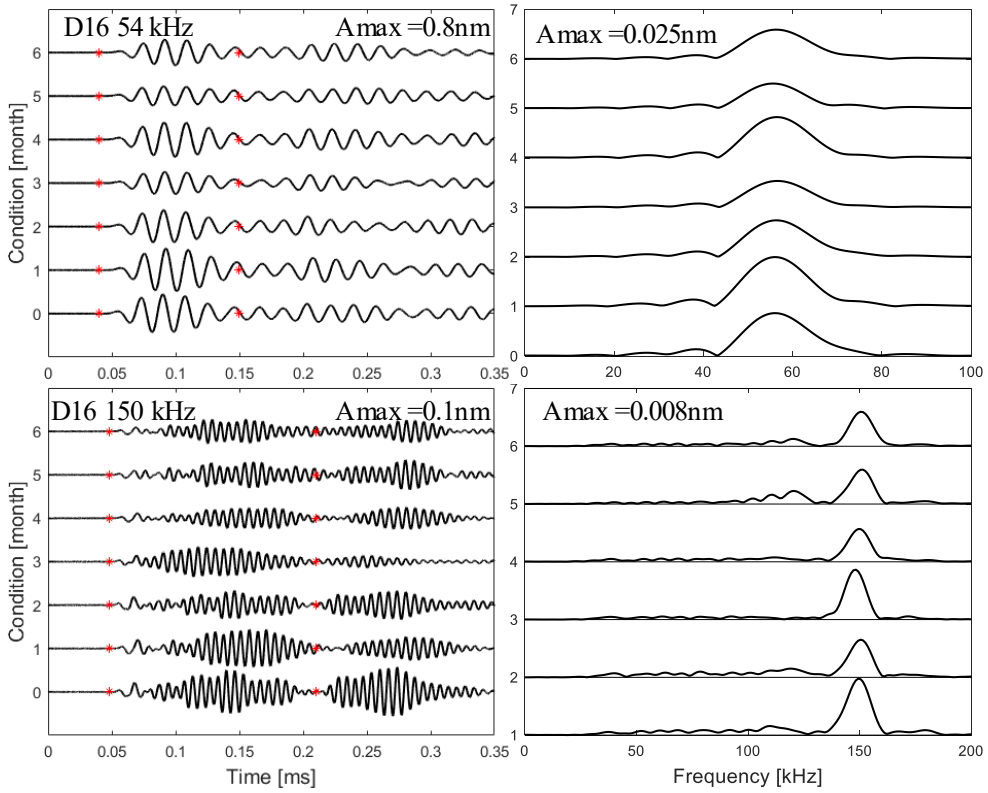

Figure 7-12. Sample time signals and the frequency content measured for D16 bars under both 54 and 150 kHz excitation. Red stars show a window position that is applied before the FFT calculation.

For all bar diameters tested with 54 kHz transducers, a frequency band between 10 and 40 kHz is found more effective, offering consistent results. This might be due to the fact that 54 kHz transducer emits two major frequencies (30 and 50 kHz), and it has previously been shown that the range centred at 30 kHz is more successful. For the D13 to D20 bars tested with 150 kHz probes, a frequency band of 140 to 165 kHz (including the resonant frequency peak) is found the most effective. For bars with a diameter of 25 mm, the arriving pulse has a much-affected character; therefore, a frequency band is applied uniquely and selected as 10 to 120 kHz (which includes all below the resonant frequencies that are found in the characterization). The energy retention plots for the bars tested under both 54 and 150-kHz excitation in the axial configuration are shown in

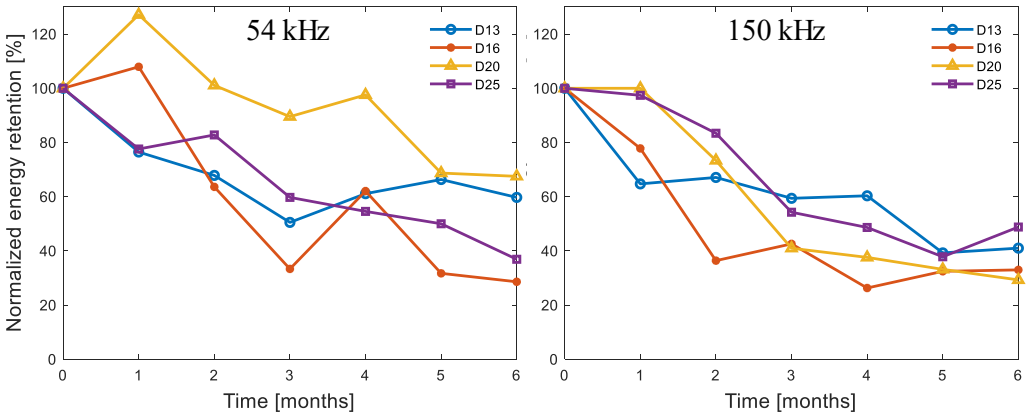

Figure 7-13. Attenuation trends calculated based on discrete frequency bands; axial configuration

The attenuation trend calculated based on energy in the discrete frequency range offers increased sensitivity (reduction up to 80%). However, some parameter fluctuation is observed in the 54 kHz results; however, the overall decreasing trend is preserved.

7.4.4 Numerical simulations

7.4.4.1 Calibration of the model

All activities performed during the calibration are made based on the 300 mm long bar with a diameter of 25 mm.

- Excitation function and damping

In the calibration of the numerical model, equally applied displacement is used as excitation. The Mexican hat wavelet with different central frequencies (matching the frequencies observed in the real ultrasonic tests) is used. The wavelets and their frequency content are presented in Figure 7-14. The wavelet time signals are zero-padded (so the total signal length is the wavelet length multiplied by a ten) prior to the calculation of the FFTs.

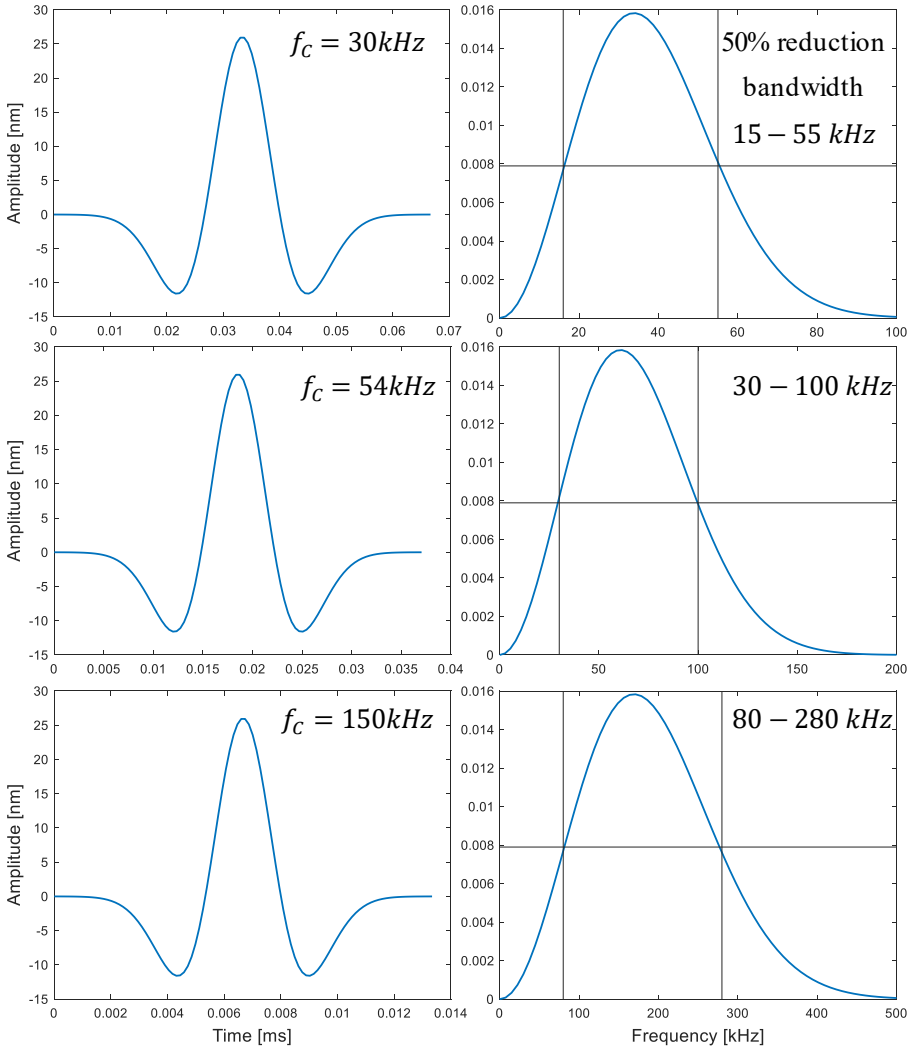

Figure 7-14. Time signals (left column) and frequency content (right column) of the Mexican hat wavelets used as excitation in the calibration of the numerical model. The nominal frequency of wavelets is denoted by f_C and frequency range in the right column describes a bandwidth corresponding to the 50% reduction in the spectral amplitude

For each spectrum, frequency bandwidth corresponding to the 50% reduction of spectral amplitude (6dB reduction) is selected. Next, the total bandwidth is chosen as the addition of the individual frequency ranges. Assuming material damping of 1% and a bandwidth of 16 to 280 kHz, Rayleigh damping constants result in $\alpha = 1902$ and $\beta = 1.0754e - 08$.

• Mesh element size

The study of the element size and final verification of the model is done by comparing the numerical results with theoretical dispersion curves for circular bars. The theoretical solutions come from two sources. First, a solution for the symmetric mode is obtained using the procedure developed by Puckett (2004). Next, the anti-symmetric mode calculated with a commercial software called Disperse (Pavlakovic et al., 2020) is also analyzed. Disperse offers both symmetric and anti-symmetric solutions. Due to the license limitations, a simulation is performed using titanium (Ti6Al4V, grade 5) as bar material. The following material parameters are used: $E = 120\,GPa$, $\rho = 4460\frac{kg}{m^3}$, and $\nu = 0.31$. From the point of view of wavelengths (calculated based on the nominal frequency of 150 kHz transducer), both materials are similar (wavelength in titanium bar is 10% longer), and the calibration can be scaled to the GFRP bar.

Four different mesh element sizes are tested: 3.5 mm (which violates the mesh size requirement shown in section 7.3.4.1, 5160 elements), 2.5 mm (which is smaller than the maximum allowed size of 2.67 mm, 11520 elements), 2 mm (21000 elements), and 1 mm (179400 elements). The simulations are run with MHW with a central frequency of 150 kHz. The displacement is applied in the axial direction (shown in Figure 7-15-b). The responses (displacements) are measured on the side of the bar in the x-axis direction (as presented in Figure 7-15-a).

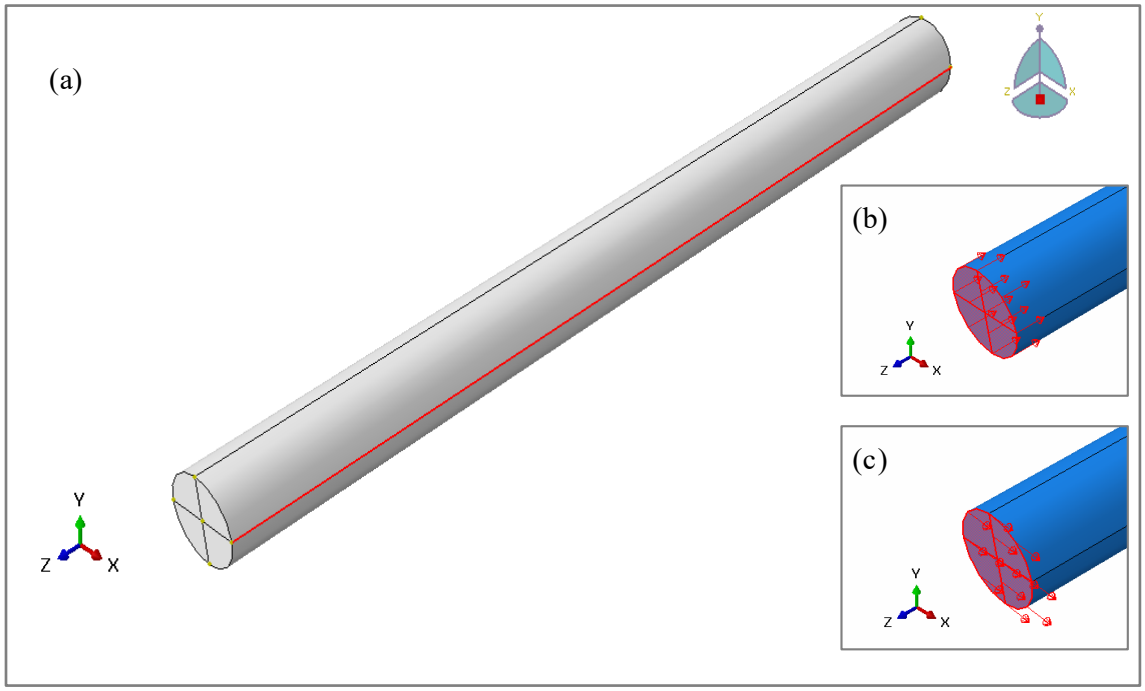

Figure 7-15. Simulated bar: (a) red line highlights the position for the displacement measurements along the bar length and (b) direction of the axial excitation, and (c) direction of the transverse excitation

The comparison between theoretical dispersion curves (obtained using both Puckett's solution and Disperse) and numerical simulations (using different element sizes) are presented in Figure 7-16.

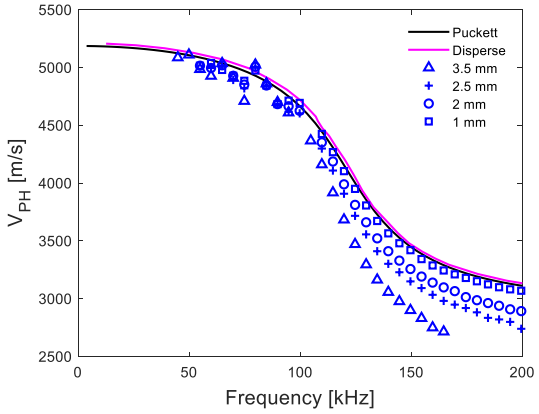

Figure 7-16. Comparison between theoretical and numerical dispersion curves (symmetric mode) calculated for different mesh element sizes.

A negligible effect of element size is observed in the low-frequency range (below 80 kHz), where dispersion does not play a key role. Different behaviour is observed for the frequency range higher than 100 kHz, where only the 1 mm elements guaranteed a good match between the theoretical and numerical dispersion curves. Based on the performed analysis, an element size of 1mm is selected for the remaining simulations.

Next, the simulation with axial excitation is repeated using the MHW with 30 and 54 kHz central frequency. The anti-symmetric vibration mode is obtained by applying the excitation radially (the displacement is prescribed in the x-direction) (shown in Figure 7-15-c). Anti-symmetric simulations are run with the chosen 1 mm elements and for all three wavelets (i.e. f_C = 30, 54, and 150 kHz). Figure 7-17 presents dispersion curves obtained with theoretical solutions and numerical simulations for both symmetric and anti-symmetric modes of vibration.

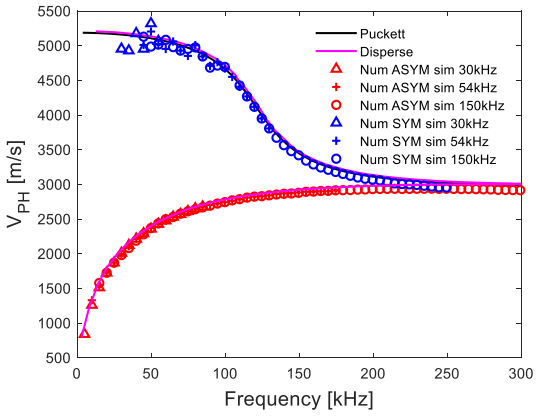

Figure 7-17. Comparison of theoretical and numerical results for the titanium bar. The applied excitation is the simulated MHW (f_C = 30, 54, and 150 kHz)

The numerical model tested under different excitation function (for both axial and transverse direction) shows a close match with the theoretical values. Even in the below 50 kHz range, for the symmetric mode, the numerical data points are within 10% of the theoretical values.

In the next step, the material is changed to GFRP, and the simulation is repeated, using axial excitation and three MHW (30 kHz, 54 kHz, and 150 kHz). The comparison between the theoretical dispersion curves and numerical results is shown in Figure 7-19-a. The close match between the results is observed, with an increased error in the below 50 kHz frequency range. Finally, real displacements are used as excitation (the prescribed surface displacement is taken from the surface laser scans

performed during the characterization of 54 and 150 kHz ultrasonic transducers) and are presented in Figure 7-18.

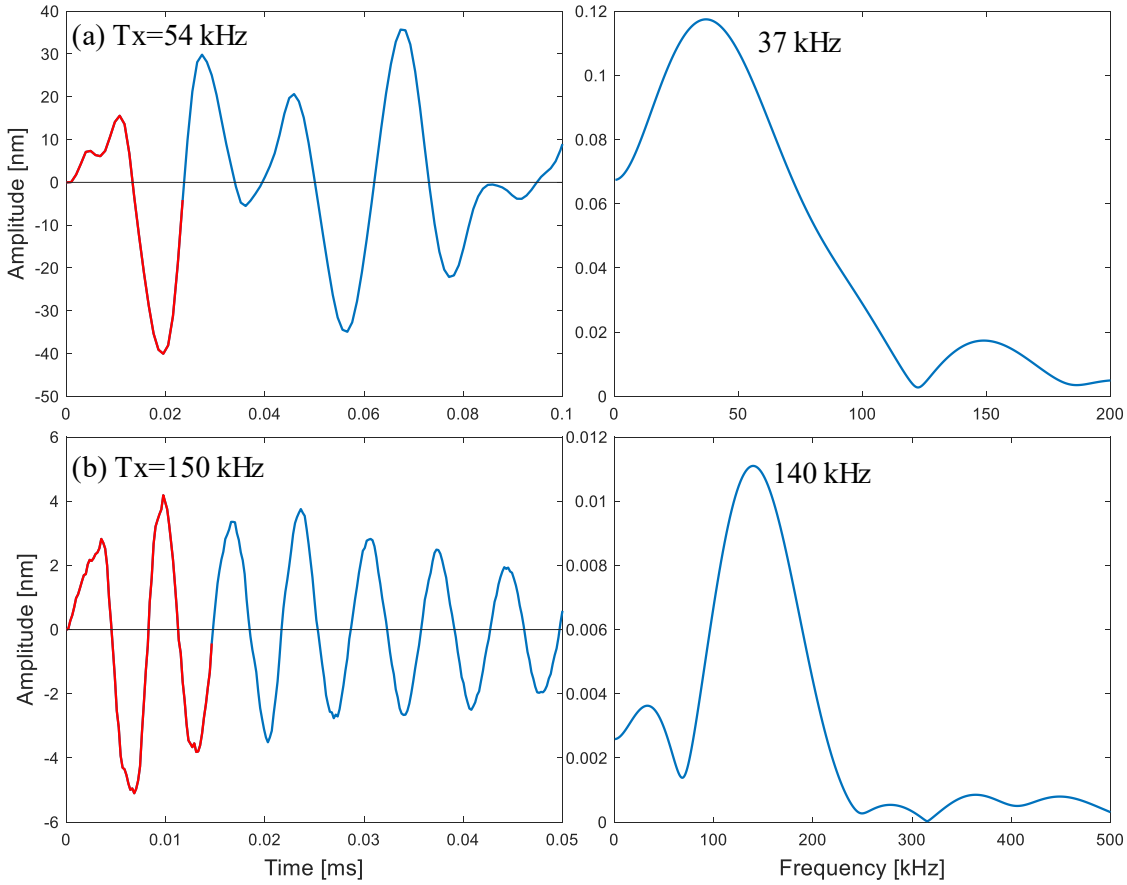

Figure 7-18. Real displacement signals and frequency content used as excitation in simulations: (a) 54 kHz and (b) 150 kHz transducers

Dispersion curves obtained for the numerical simulations of GFRP under real excitation are presented in Figure 7-18-b.

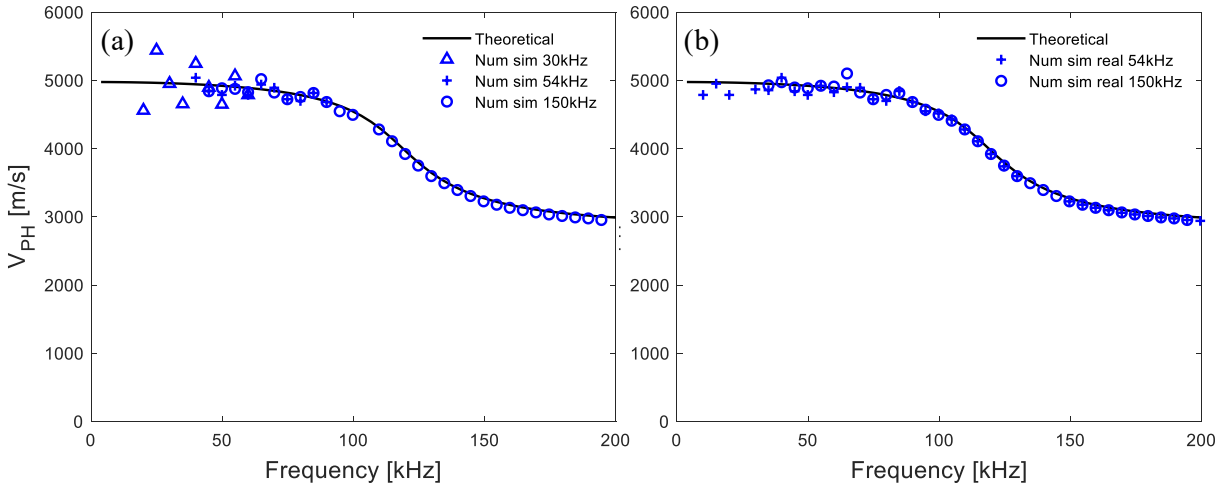

Figure 7-19. Comparison between theoretical dispersion curves and numerical results for the GFRP bar tested under (a) simulated MHW of different central frequency (i.e. 30, 54, and 150 kHz), and (b) real displacement of 54 and 150 kHz transducers, obtained during the characterization.

The phase velocity dispersion curve obtained under real excitation keeps a close agreement with the theoretical dispersion curves. The error in the below 50 kHz frequency range is smaller than when the MHW is used. Sample wave propagation graphs, showing displacements during the wave propagation are showing in Figure 7-20 (symmetric mode) and Figure 7-21 (anti-symmetric mode). The excitation shown in Figure 7-18 is used in the remaining simulations.

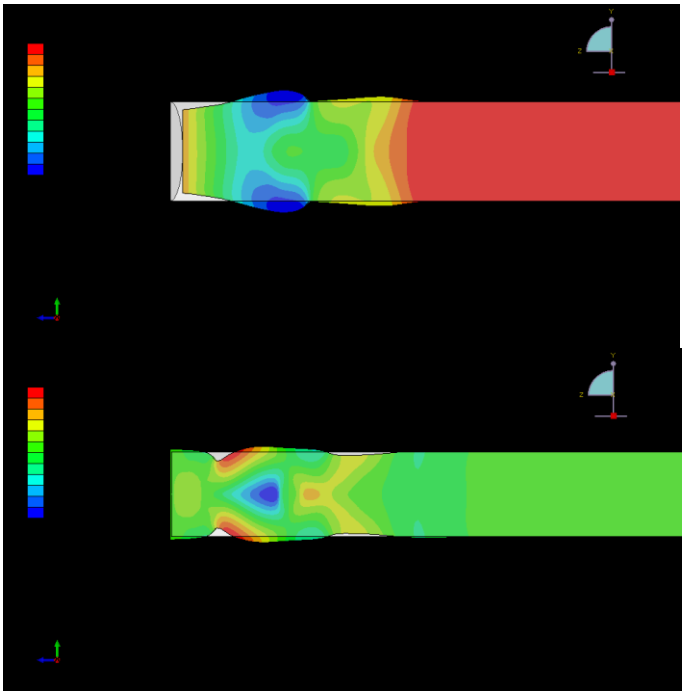

Figure 7-20. Wave propagation, symmetric mode. Colours represent displacement in the z-axis. Excitation used: (a) 54 and (b) 150 kHz.

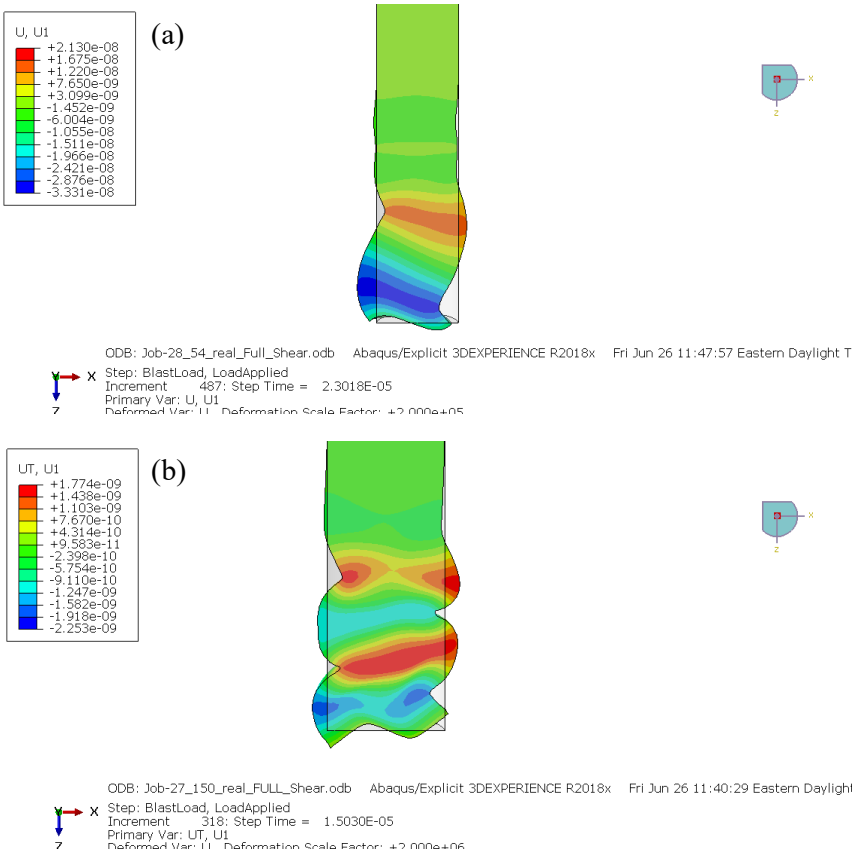

Figure 7-21. Wave propagation, anti-symmetric mode. Colours represent displacement in the x-axis. Excitation used: (a) 54 and (b) 150 kHz

7.4.4.2 Simulation of deterioration

Simulation of deterioration caused by the alkaline ingress into the GFRP bar starts with the analysis of how a reduction in bar radius changes theoretical dispersion curves. Only the symmetric mode is analyzed. The following assumptions are made: (i) the bar is assumed to have a perfect circular cross-section (bar ribs are disregarded, due to the significantly smaller dimension than the wavelength), (ii) the deterioration follows the model proposed by Katsuki and Uomoto (1995), and (iii) the affected outer radial section of the bar has significantly reduced stiffness and can be removed from the model. The effective bar diameters used in simulations, calculated based on the penetration depth rate (Equation 7-4), are shown in Table 7-7.

Table 7-7. Effective bar diameters calculated based on Equation 7-4 for different durations of the accelerated ageing test

Month	0	1	2	3	4	5	6
Bar diameter [mm]	13.00	12.74	12.63	12.55	12.48	12.42	12.37
	16.00	15.74	15.63	15.55	15.48	15.42	15.37
	20.00	19.74	19.63	19.55	19.48	19.42	19.37
	25.00	24.74	24.63	24.55	24.48	24.42	24.37

Next, theoretical dispersion curves for the symmetric mode are calculated for bars in all conditions. The effect of changing the bar diameter on the phase velocity dispersion is shown in Figure 7-22. First, the dispersion curves are compared for initial conditions for all bar diameters. Rayleigh wave velocity is reached faster (i.e. at lower frequencies) for bars with a larger diameter. Reduction of bar diameter results in higher phase velocities in the transition zone between longitudinal and Rayleigh wave velocities. The effects depend on the initial bar diameter. For each bar, the relative difference (*RDiff*) between dispersion curves (at different conditions) with respect to the unconditioned state is calculated as:

$$RDiff_{n-0} = 100\,\frac{V_{PH-Cn} - V_{PH-C0}}{V_{PH-C0}} \tag{7-8}$$

where $RDiff_{n-0}$ is the relative difference calculated between the condition 0 and the n-th condition, V_{PH-C0} is the phase velocity for condition 0 and V_{PH-Cn} is the phase velocity for the deteriorated condition. *RDiff* graphs are presented in Figure 7-22 (second column).

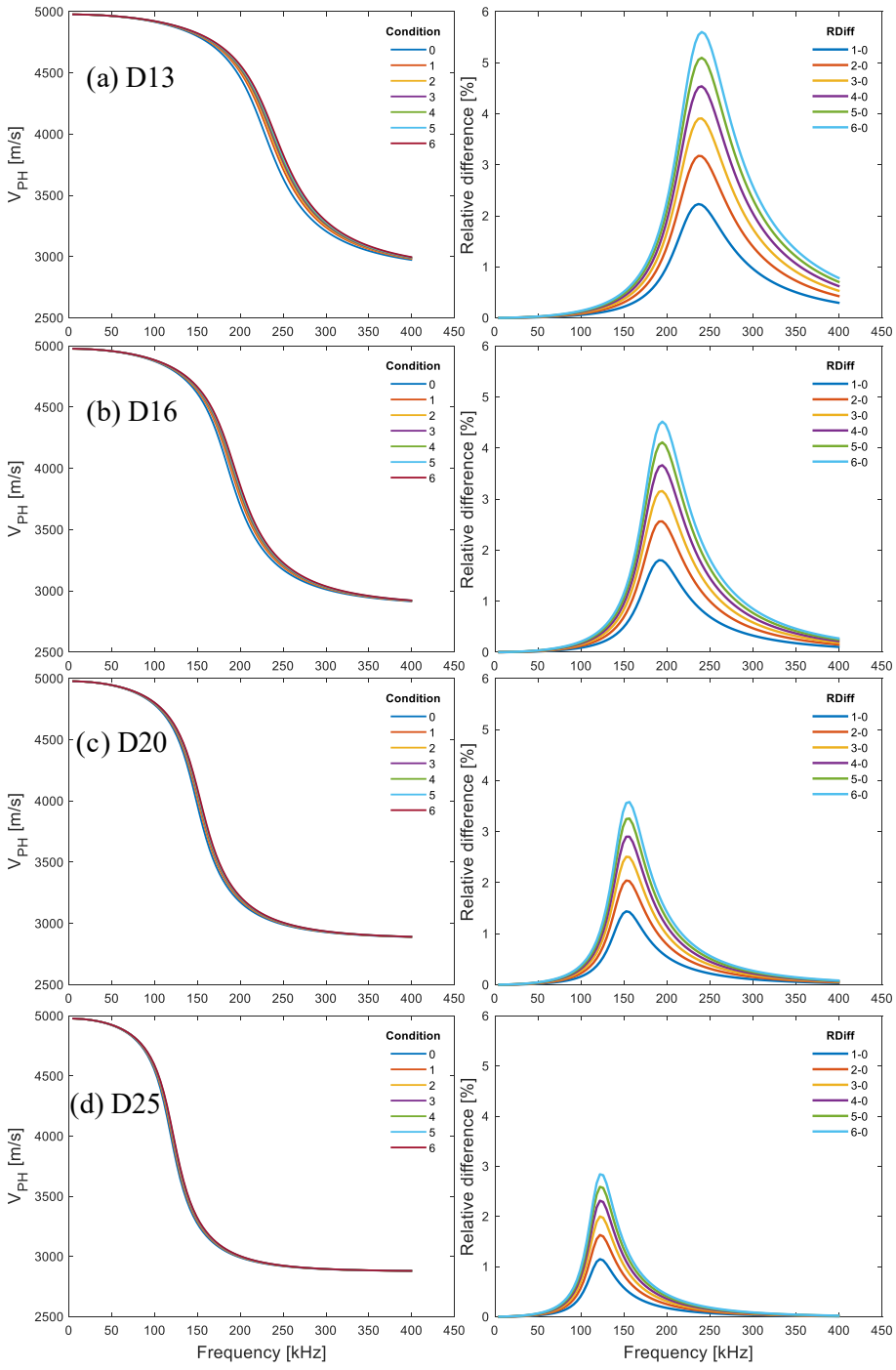

Figure 7-22. Effect of the reduced bar diameter on theoretical dispersion curves. The second column shows how the relative difference (calculated between dispersion curves for the reduced diameters with respect to the unconditioned bar) changes with the progression of diameter reduction.

For each bar diameter and condition, the maximum Rdiff value is selected, and a progression of these values with conditioning time is presented in Figure 7-23.

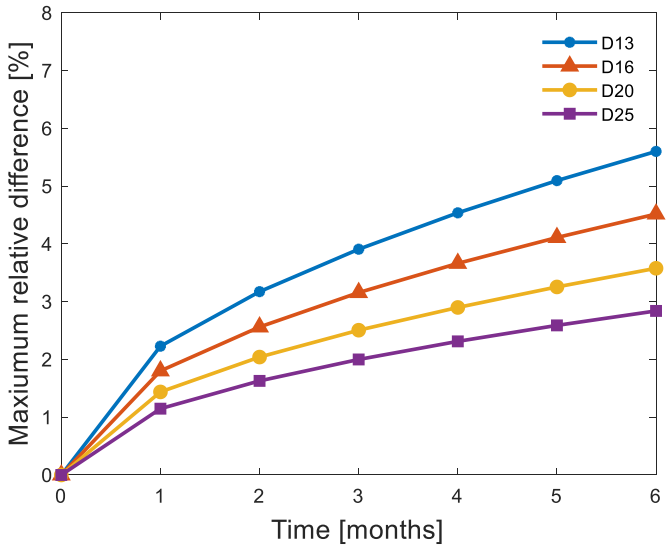

Figure 7-23. Comparison of maximum RDiff values (from Figure 7-22) for all bars at different deterioration stages

The bars with a larger diameter are less affected (for D25 bars, the maximum relative difference is 3%) than the smallest tested bars (for D13, the maxim relative difference is 5.5%), which is anticipated behaviour with the assumed model. The results show good agreement with the shear test trends (presented in Chapter 7.4.5). The detailed comparison of all test results is presented in section 7.4.6.

Next, a series of numerical simulations are run for D13 and D25 (two extreme cases), simulating the degradation of bars with a reduced diameter. The real displacement of the 150 kHz ultrasonic transducer is chosen for excitation as the frequency range between 100 and 350 kHz offers the highest relative difference values. The dispersion curves calculated for the numerical results are presented in Figure 7-24

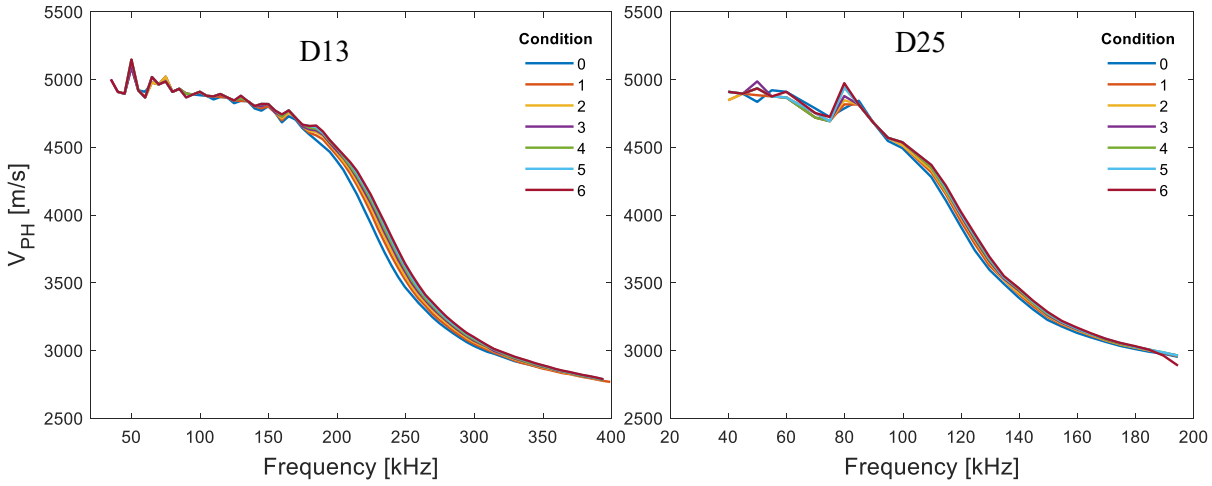

Figure 7-24. Dispersion curves calculated for numerical simulation results for D13 and D25 bars

Similar behaviour is observed as in the case of the theoretical dispersion curves. The comparison between bar condition is made based on the relative difference that is calculated for the most sensitive frequency range (D13: 180-380 kHz, and D25: 90-190 kHz) and presented in Figure 7-25.

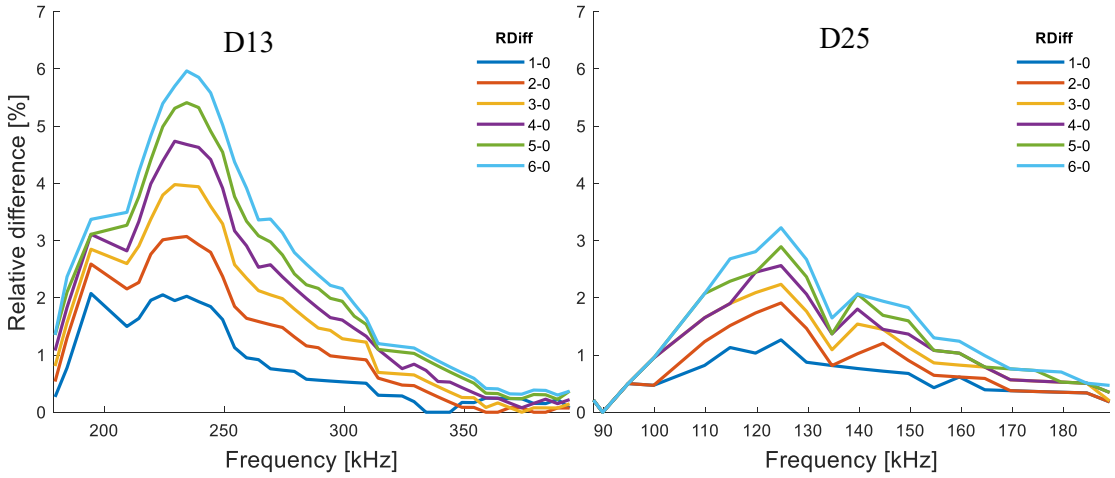

Figure 7-25. The relative difference between dispersion curves (conditions 1-6) and the unconditioned bars for numerical simulation results for bars D13 and D25

The relative difference graphs prove good agreement with the previous findings. Smaller bars are more affected by the change in bar diameter caused by the alkaline solution ingress. Based on all the simulations, an approach based on wave dispersion can be recommended for the monitoring of the

GFRP bar condition. The benefit of this approach is that it considers the whole array of data points, which should minimize the testing errors.

Finally, displacement signals measured at the top of the bar (opposite side of the excitation) are analyzed. No significant difference in the arrival time is observed. However, the time shift between the responses of different conditions arises in the latter part of the signal, which creates an opportunity of applying more sensitive methods like coda wave interferometry. The sample signals extracted from the numerical simulations of unconditioned D13 and D25 bars are compared with the laser vibrometer responses.

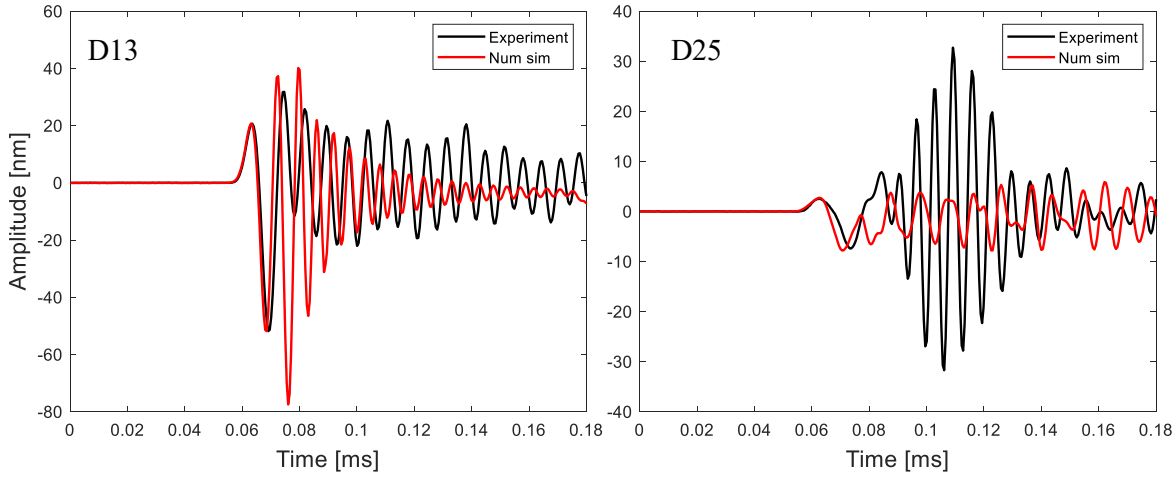

Figure 7-26. Comparison between experimental (laser vibrometer) and numerical result measured at the centre of the bar (opposite to the excitation side)

The numerical model offers good agreement for the first arriving pulse (better match is obtained for D13 bar). However, the model fails to reproduce the later vibrations. This can be related to the definition of excitation in the model. Firstly, the assumed excitation is applied uniformly over the whole cross-sectional area. At the same time, the characterization of the ultrasonic transducer shows that the 150 kHz transducer vibrates in the first mode of vibration (besides the very initial vibration). Secondly, the later vibrations might be related to the constructive and destructive wave interaction, which might not be represented well with the assumed duration of the excitation. Additionally, some errors might be related to the assumed all-free boundary condition. Therefore, the attenuation calculated based on discrete frequency bands is not representative of the real bar condition. On the other hand, the analysis of the first arriving peak (P-Peak) can be performed. P-peak amplitude is calculated based on the

vibration measured at the centre of a bar, similar to the laboratory experiment. The P-Peak retention plot is presented in Figure 7-27.

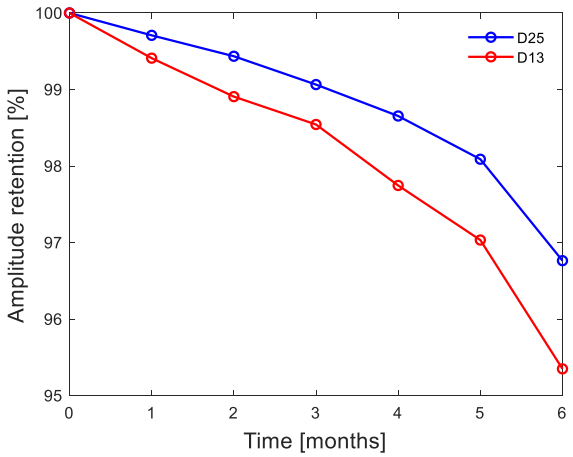

Figure 7-27. P-Peak amplitude retention trend obtained based on numerical simulations for D13 and D25 bars

The decreasing trends are observed for the P-Peak amplitudes for the bars with the simulated deterioration. The loss of signal amplitude is significantly smaller than in the laboratory tests (presented in Figure 7-11). However, in the laboratory test, responses are measured with an ultrasonic receiver, which means that the actual vibration is affected by a frequency response function of the receiver. Therefore, differences between the pure displacement signals and the ultrasonic transducer responses are expected.

7.4.5 Shear test

Next, the shear test results are discussed. During the test, load-displacement curves are recorded. For each bar, failure load is read and used in the calculation of shear strength. Six specimens are used in the calculation of mean ultimate capacity values. The maximum coefficient of variation calculated for all tests is 7%. Table 7-8 presents the failure load recorded for all tests.

Table 7-8. Mean ultimate shear capacity during the six months of testing. The maximum COV calculated for all tests is 7%.

	Mean ultimate capacity [kN]						
Month / Diameter	0	1	2	3	4	5	6
13	52.65	48.13	47.03	46.50	44.27	43.24	42.21
16	95.36	89.33	87.87	85.45	82.33	81.15	78.92
20	125.23	118.50	116.43	114.70	112.85	110.15	107.40
25	203.87	194.00	190.30	187.05	186.25	181.83	178.08

Larger bars are capable of resisting higher cutting force, and the values are consistently decreasing over the duration of the test. Next, the mean failure loads are divided by the nominal cross-sectional area of each bar, according to Equation 7-7. Finally, shear strength is normalized with the value measured for the unconditioned bar. The shear strength retention plots for all of the bars are shown in Figure 7-28.

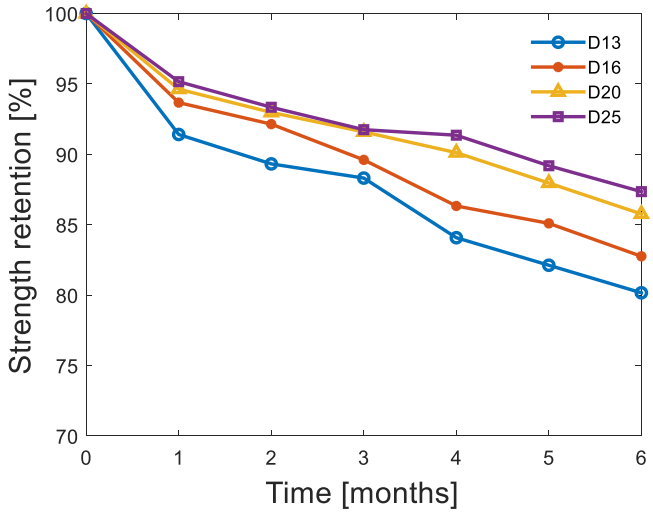

Figure 7-28. Shear strength retention over six months of testing

The deterioration rates and overall bar behaviour follow the findings of Arczewska (2017). Decreasing trends are observed for all bar diameters, and the dependency with bar diameter can be distinguished (i.e. larger bars are affected less). It can be assumed that the depth of penetration of the

alkaline solution is the same for all of the bar diameters; therefore, the cross-sectional area of larger bars is reduced less, which results in a lower reduction of shear strength.

7.4.6 Results comparison

A reliable ultrasonic methodology is needed for in-situ testing, when the non-destructive approach is the only possible solution (the GFRP reinforcing bars show no visual symptoms of deterioration, and cannot be cut out of a structure for the intrusive tests). Therefore, the results of the ultrasonic evaluation are compared with numerical simulations and shear tests. P-Peak amplitudes measured with 150 kHz transducers are selected from the ultrasonic results as the amplitude approach offers increased sensitivity. From the numerical simulation section, maximum *Rdiff* results are chosen; however, the results are rearranged to the retention form (i.e. 100% - maximum *Rdiff*). Finally, strength retention results are selected from the group of shear tests.

Next, logarithmic curves (defined as $y = a + bln(x + 1)$, where y is the estimated retention value, x is the bar condition, and a and b are the coefficients of the fitted line) are fitted to the test results. Figure 7-29 presents retention plots for all tests with fitted logarithmic curves, and

Table 7-9 shows coefficient *b* for each curve (parameter *a* is always equal to 100) and root mean squared error (RMSE) of the fit.

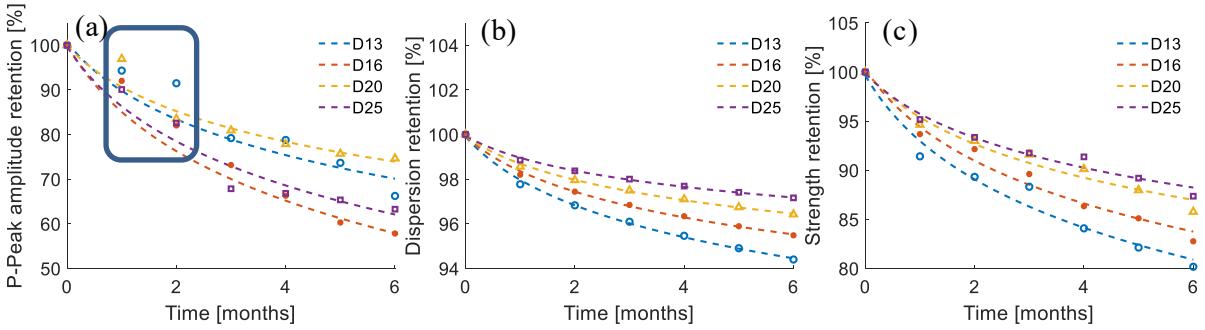

Figure 7-29. Curve fitted test results (dashed lines represent fitted lines, and symbol markers are used for data points): (a) P-Peak amplitudes from ultrasonic evaluation, (b) dispersion retention from numerical simulations, and (c) shear strength retention. The box in figure (a) shows data points that are excluded from the fitting procedure

Table 7-9. Coefficient b and root mean squared error (RMSE) of the curve fitting for different tests and bar diameters

		D13	D16	D20	D25
Ultrasonic evaluation	b	-15.7	-21.7	-13.3	-19.4
	RMSE	3.75	1.03	0.68	1.53
Numerical simulation	b	-2.8	-2.3	-1.8	-1.4
	RMSE	0.11	0.09	0.07	0.05
Shear test	b	-9.6	-8.5	-6.7	-5.9
	RMSE	1.21	0.93	0.86	0.69

Numerical simulations and shear tests show a similar dependence of results with bar diameter. Bars with smaller diameter deteriorate more, which is related to the assumed alkali ingress depth model. Ultrasonic evaluation, however, does not show the same behaviour, and no definite conclusion about the diameter effect can be made. Next, the average value for coefficient b is calculated for each test method, and the ratios between the average parameters for ultrasonic evaluation and shear test and numerical simulation and shear test are calculated. Then, ultrasonic fitted curves and numerical fitted curves are corrected with respect to the appropriate ratio. Figure 7-30-a shows a comparison between the corrected ultrasonic evaluation and shear test fitted curves, and Figure 7-30-b analyzes the corrected numerical simulation and shear test fitted curves.

The comparison of the shear test and corrected ultrasonic evaluation fitted curves shows that ultrasonic evaluation is able to identify the progressive damage. The maximum relative error (calculated as a difference between the two methods normalized with the shear test) between the two test methods is 6.77% (D13), and the smallest relative error is observed for D20 bars (1.15%).

The fitted curves for the shear test and corrected numerical simulation show improved correlation between the curves, and the maximum relative error between the two curves is 1.85%. Numerical simulations confirm that the shear test is correct in capturing deterioration.

Finally, fitted curves for all test methods (i.e. corrected ultrasonic evaluation and numerical simulation and shear test) are compared in Figure 7-30-c.

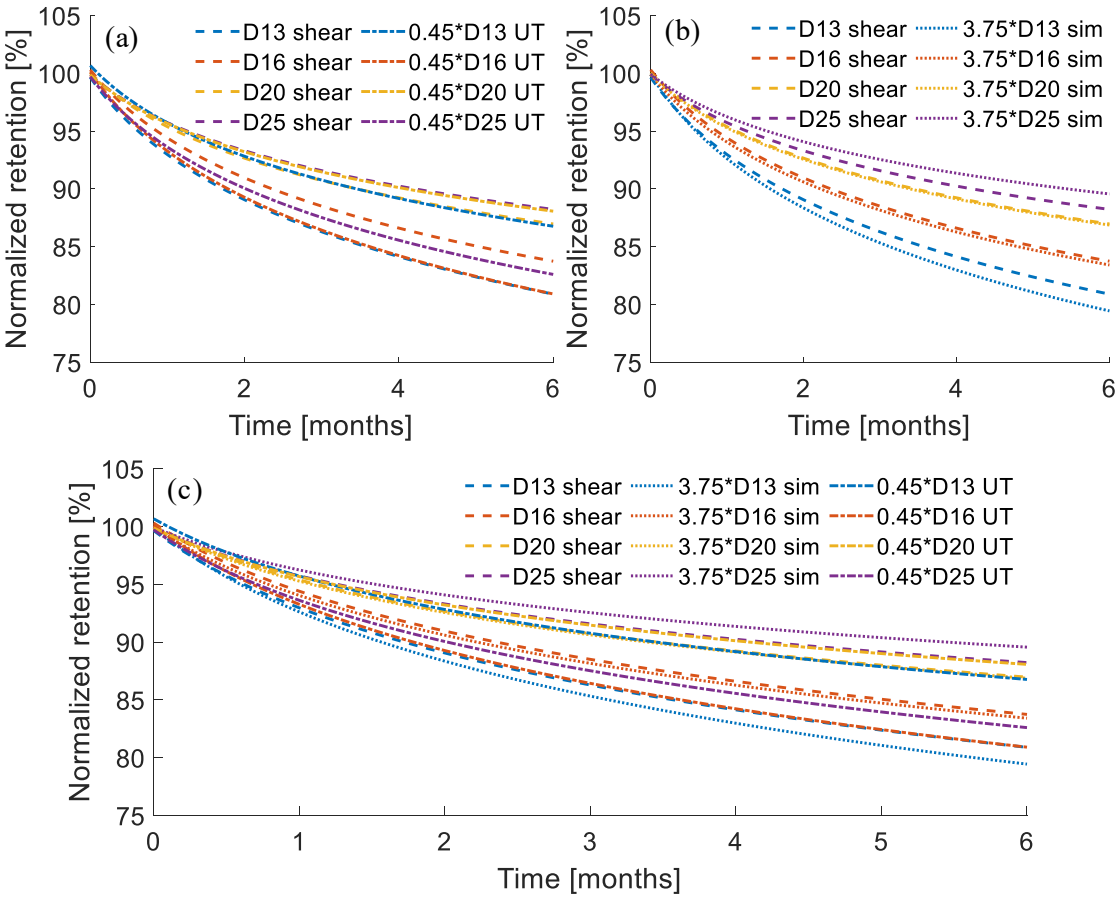

Figure 7-30. Comparison of corrected fitted curves for (a) shear test and ultrasonic evaluation, (b) shear test and numerical simulations, and (c) all test methods (i.e. shear test, numerical simulations, and (c) ultrasonic evaluation)

It can be concluded that ultrasonic evaluation (P-Peak amplitude) can capture deterioration in the GFRP bar and, with proper analysis (the correction factor), can be used to obtained an estimate of the shear strength (and consequently tensile strength) reduction. Ultrasonic evaluation can be improved by addressing the issue of coupling (e.g. decreased coupling area, improve bar surface finish) and using transducers selected based on bar diameter.

7.5 Summary and conclusions

This chapter presents a pilot study of progressive damage of bare GFRP bars, which is a prerequisite step to the evaluation of bars embedded in concrete elements. The bars are subjected to accelerated ageing in alkaline solution and elevated temperature. The study is divided into four sections. Ultrasonic

wave propagation is analyzed first (focusing on frequency content measured with ultrasonic transducers of different resonant frequency and laser vibrometer, and the shape of vibration). Next, ultrasonic evaluation based on wave velocity and amplitude attenuation approaches is performed. The responses are measured with ultrasonic transducers in an axial and transverse direction (with respect to a bar length). The numerical simulations are also considered to add a more comprehensive understanding of wave propagation and investigate other testing methods. Finally, a destructive shear test is carried on the bars. The experiment investigates the level of damage in bars and verifies the ultrasonic evaluation. The following main conclusions can be offered, and detailed conclusions can be found in Chapter 8.

1. The frequency content of responses and cross-sectional displacement patterns change with bar diameter. Therefore, if two bars (of different diameters) are in the same condition, the measured signals will have different ultrasonic features.
2. Wave velocity can successfully identify damage progression, due to alkali ingress, in GFRP bars. However, the selectivity of the method is low (maximum observed reduction is within 5%).
3. The sensitivity of the evaluation can be increased by considering wave attenuation.
4. No consistent conclusion can be made regarding the effect of bar diameter on the wave velocity.
5. The effect of reduced diameter (due to alkali ingress into GFRP bar) studied with the numerical simulation shows that the change in P-wave velocity (axial readings) is insignificant.
6. Analysis of wave dispersion (side of bar measurements) shows promising results and shows good agreement with shear test findings in the literature.
7. The obtained shear strength trends follow results found in the literature and show strength reduction for all bar diameter.
8. Larger bar diameters are affected less because the penetration depth of the alkaline solution is the same for all bar diameters (therefore, the relative effect is smaller for the larger bars). The same bar diameter effect is observed in the numerical simulation results.

It can be concluded that ultrasonic evaluation can capture deterioration in the GFRP bar and, with proper analysis (the correction factor), can be used to obtained an estimate of the shear strength (and

consequently tensile strength) reduction. The maximum error of the ultrasonic evaluation with respect to the shear test is less than 7%. Ultrasonic evaluation can be improved by addressing the issue of coupling (e.g. decreased coupling area, improve bar surface finish) and using transducers selected based on bar diameter.

Chapter 8
Conclusions and further research

The main objective of this research project was to enhance the understanding of the frequency effects on ultrasonic measurements and establish a comprehensive methodology for early damage detection of composite materials (based on wave velocity, attenuation, and dispersion). To achieve the major objective, the following specific objectives were defined and discussed within Chapters 4-7. Firstly, frequency content transmitted by ultrasonic transducer typically used in civil engineering applications was studied with the use of a state-of-the-art laser Doppler vibrometer. The characterization procedure included measurement taken through the air and solid medium (i.e. glass specimen). The second specific objective was to evaluate how the frequency content of the recorded ultrasonic measurements changes with different resonant frequency transducers and how it depends on specimen dimensions. To accomplish this goal, a group of concrete specimens of different diameters and lengths were tested with a traditional ultrasonic pulse velocity method (using ultrasonic transducers with different resonant frequencies) and the laser vibrometer. The third objective was to investigate the applicability of novel signal processing techniques (i.e. wavelet synchrosqueezed transform, WSST) to attenuation based, early damage detection approach for cementitious materials. The objective was accomplished by verifying the WSST method using synthetic signals and two real, lab-scale applications (i.e. concrete beams and cemented sand layer). The final objective was to investigate the functionality of the newly developed ultrasonic procedure (i.e. based on characterized ultrasonic transducers, WSST enhanced velocity and attenuation approach) to progressive damage of glass fibre reinforced polymer specimens (GFRP). The ultrasonic evaluation was verified with the traditional destructive test (i.e. shear test) and numerical simulations. The following sections give conclusions regarding each individual specific objective.

8.1 Characterization of ultrasonic transducers using laser Doppler interferometer in kHz-range for civil engineering applications (Chapter 4)

This study presents the characterization of three P-wave ultrasonic transmitters that are frequently used in the evaluation of civil engineering materials. The wear surface displacement has been measured with the state-of-the-art laser vibrometer. The following conclusions can be given.

1. Firstly, the measured surface displacements are compared with analytical mode shapes obtained from the vibrating plates theory. The analysis of three types of P-wave transducer shows that they do not respond to the excitation in the same way. For all transducers, the surface displacement during the active phase of the excitation pulse consists of resonances of the piezo-crystal and the wearing-surface plate. The contribution of the surface displacement due to the plate vibration is significant. The quarter-wave matching wear plate is designed to increase energy output by constructive wave interference; however, it does so at the expense of frequency bandwidth. This leads to the conclusion that (i) the construction of the 54 kHz should be revisited by the manufacturer and modified, so the resonant frequency of the piezo element matches the resonance of the plate, and (ii) from the point of view of the transducer user, the plate resonant frequency has to be taken into account in the NDT evaluation. The surface behaviour changes during the passive phase of the excitation, when the observed vibration matches single analytical mode shapes. Therefore, it is critical to ensure a constant coupling area and quality throughout the whole evaluation process (an additional coupling plate can be proposed). Any coupling variation will affect the transmitted signal, especially for the 54-kHz transducer, when the response goes through different mode shapes. Moreover, if the maximum transferred amplitude is desired, it is sufficient to couple only a section of the wear face, which can be selected by the smallest area that guarantees a certain amplitude level for all mode shapes. The level can be selected by the transducer user and will be different for all three types for the tested probes.

2. The scans of response along transmitter diameter and global and self normalization of signals revealed sections on the wear surface that contribute differently to the overall response of the transmitter. Based on the analysis of residual signals (with respect to the edge, centre, and the middle point between), three significant regions have been defined. The analysis provides more detailed information about the frequencies sent to a medium. The possible application of the finding includes improved FEA modelling (with detailed and more accurate excitation information). The characterization of the frequency content that is sent to the tested medium is fundamental in the evaluation process of highly attenuative structural materials (e.g. concrete).

3. The contribution of edges has greater importance for higher frequency transducers (150 and 250 kHz). In such transducers, edges do not emit nominal frequencies at all. The results of the wear surface section analysis show that it is extremely important to keep consistency in

coupling throughout the whole testing procedure. If different areas of the transducer are coupled (either during different tests or when the dismounting of transducers is necessary), it will lead to different frequency content being transferred to the tested medium. As a result, waves of different wavelengths will be propagating, and inconsistencies related to wavelength to specimen dimension or defect ratios will skew the evaluation. To limit the frequency content being transferred, it is recommended to provide coupling for just the central section of the transducer.

4. The characterization performed with the glass block offers a more realistic condition (i.e. coupling and the interaction between the transducer and the tested material are included). It can be concluded that the presence of the glass block does not affect the nominal frequency significantly (only the amplitude reduction effect is present). At the same time, the frequency content is modified in the below 100 kHz range. Although the amplitude in that range is low, relative to the nominal frequency, it might play a significant role for the applications in concrete, where the non-homogenous nature of the material significantly attenuates ultrasonic waves.

5. It has been shown that the response measured on the top surface of the glass block is quickly affected by the boundary condition effects (a surface wave excited by the arriving pulse, travelling along the diagonals of the glass block). Therefore, if the receiver characterization is to be performed, a precise windowing (eliminating the boundary conditions effects) is needed.

6. In the first practical application, concrete cylinders of constant diameter and different lengths are tested using standard UPV technique. It has been shown that the traditional analysis that disregards the frequency content of the measured signals may lead to the wrong interpretation of ultrasonic data (regarding the size of the detectable defect). However, if the spectral analysis is included, the proper identification of frequency components is not obvious (presence of additional components different than the nominal frequency). One of the identification methods may require modal analysis performed with FEA software, which is an advanced and time-consuming process. Alternatively, it has been shown that the presence of the low frequencies can be explained through the characterization procedure. Moreover, the measured responses consist only of the frequencies much lower than the nominal, which means that one deals with much longer wavelengths. Therefore, identification of small defects might not be possible. For the longest tested specimen, the arriving wave can have a wavelength of up to 2.3 times longer

than anticipated. Based on the characterization, the experimental setup can be then optimized in the iterative process, so the resonant frequency of the receiver matches the maximum frequency peak observed in the first iteration for the received signals.

7. The second application considers concrete beams in two conditions and deals with a damage detection problem. It is demonstrated that early damage detection is not possible using the traditional wave-velocity techniques (i.e. UPV). The prior knowledge of the frequency content sent to the medium obtained from transducer characterization improves the evaluation process. The approach based on the total spectral energy of signals gives high values for the early damage detection estimators (RAI), which enables the correct condition assessment. The technique can be further improved by applying the WSST method. The presence of the frequency components in measured responses is explained with the matching transducer profile, which provides a strong rationale for applying a mode extraction technique (i.e. WSST). When the reconstructed modes are analyzed separately, each mode represents different frequencies, which can also be seen as different wavelengths. For surface wave analysis, it implies a different penetration depth. It is possible to select the most sensitive one to be used in the damage detection analysis. In the presented analysis, the extracted mode centred on 30 kHz (mode 30, lower frequency of the two available) gave higher damage indicator value (higher value means a larger extent of difference in material condition). Mode 30 is associated with a longer wavelength and deeper penetration depth. Therefore, the wave has a greater chance of being affected by the micro defects that are present after the freeze and thaw conditioning. Finally, the ultrasonic evaluation is verified with a compression test. The analysis based on the prior knowledge of characterized transducers and well-described frequency content can offer up to 24% relative increase in the method effectiveness (higher RAI values, when the WSST approach is compared to the full spectral range approach).

8.2 Frequency and geometry effects on ultrasonic pulse velocity measurements of concrete specimens (Chapter 5)

UPV is a common method for the assessment of a relative concrete condition. In the presented study, several tests and specimen aspects are investigated, and the following conclusions ensuring the increase in the UPV method reliability can be offered.

1. The time delay calibration is performed using different setups (i.e. steel and PVC calibration rods, concrete specimens, and transducer face-to-face configuration). It is shown that the traditionally used calibration rods do not provide reliable UPV results for concrete. Therefore, it is recommended to perform the time delay calibration process directly on test specimens (a couple of different spacing distances between the transmitter and receiver have to be measured) along with the face-to-face calibration (to include the baseline delay of the ultrasonic system).

2. The simple numerical model is used to verify that resonant frequencies of the specimens (i.e. axial, bending, and torsional frequencies) are not masking ultrasonic results (i.e. the specimen resonant frequencies are different than the ones introduced in the ultrasonic evaluation).

3. The presented results show how the electrical pulse sent from the function generator and then amplified can change based on the frequency used in the test. As a result, the amplitude of the UPV response will not only depend on the tested medium condition, but also on the amplitude of the input pulse, which is frequency-dependent. The response of the ultrasonic transducer in terms of the actual displacements, measured with the state-of-the-art laser vibrometer, is also presented. The ultrasonic response has a complex character, instead of the single pulse response typically assumed, and consists not only of the desired resonant frequency of the transducer (when driven at the resonant) but also a series of other, lower frequencies. Therefore, one deals with more complicated waveforms than expected, and the laser-vibrometer-based characterization of ultrasonic transducers used in the test is recommended. It is recommended that the characterization procedure was performed by manufacturers.

4. The minimal specimen length requirement given by the ASTM (ASTM International, 2016a) is verified in the presented study. It is found that the current requirement of specimen length should be extended to 4 effective wavelengths, instead of a single wavelength recommended currently, to ensure a 5% relative error of the UPV test. If the new recommendation is not fulfilled, the error of the UPV method can reach up to 20%.

5. The influence of the increasing specimen length is also studied. It is found that at a certain length level, UPV results change their original frequency content. In practice, the arriving wave has a longer wavelength than the one sent from the transmitter. Therefore, the use of high frequencies (i.e. above 150 kHz) is limited and might be misleading because of the mismatch between the anticipated and arriving wavelengths. In such a situation, an effective wavelength should be used.

6. The effects of the ratio of specimen diameter and wavelength are studied, and it is shown that when the ratio is smaller or close to the unity, the longitudinal velocity is present, which is lower than the P-wave velocity. The effect is observed until $D/\lambda_P \geq 3$, and when is present, the P-wave velocity correction factor, based on the Poisson's ratio, has to be included.

7. Finally, the attenuation of the first arriving peak is studied. A linear dependence between a logarithmic decrement and normalized length has been found. Therefore, the material damping ratio found in this study is frequency independent. The mean damping ratio value of $\zeta = 0.14$ for concrete was measured for the ultrasonic range of 54 to 250 kHz of the excitation signal.

8.3 Novel application of wavelet synchrosqueezed transform (WSST) for condition assessment of cementitious materials (Chapter 6)

In this study, the advantages of applying the WSST to include the wave attenuation approach for condition assessment of cementitious materials is demonstrated. The application of the WSST to ultrasonic signals is first demonstrated based on three numerical models. Next, the characterization of the ultrasonic transducer used in the study is performed. The WSST is used to extract the main modes that are transmitted to the specimens. Finally, two applications are considered: the method is applied to the detection of distributed damage (concrete beams subjected to freeze and thaw cycles) and localized damage (cemented sand specimen with the undersurface void). The following conclusions can be offered for each section.

8.3.1 WSST - numerical example

1. The WSST technique is based on WT; therefore, similar computational issues to WT occur. Firstly, the COI effect is studied (inaccurate reconstruction of amplitude). The effect is not present in cyclic signals. Therefore, the discontinuous sinusoidal signal is considered first. The COI effect exists at the ends of a vector, or the COI effect is shifted to the discontinuities (if the signal includes discontinuities such as commonly used zero-padding).

2. Next, the COI effect is studied with exponentially decaying sinusoidal signals in the ultrasonic frequency range from 5 to 100 kHz. The energy ratio between reconstructed and original time signals is defined for the first two periods of the signals. It has been shown that the ratio decreases with an increase in signal frequency. Similarly, the standard deviation of the residual signal is calculated for the first two periods. An exponential increase is observed, meaning that the amplitude in the first section of the signal will be increasingly affected by the increase of

the signal's frequency. The effect is critical for multi-component signals observed in NDT evaluation.

3. Finally, the separation between components of multi-component signals is studied. Three frequency regions can be defined. The no-error region is defined as long as the energy ratio stays above 0.7, which corresponds to the relative frequency ratio ($|\Delta f|/(f_1 + f_2)$) greater than 0.3. An acceptable reconstruction error zone is defined as $0.2 > |\Delta f|/(f_1 + f_2) > 0.3$. The lower end of that zone corresponds to the energy ratio of 0.48. Finally, when the relative frequency ratio is below 0.2, the reconstruction is not possible. For the practical applications, the frequency content of ultrasonic transducers must be known and verified in order to apply the WSST technique.

8.3.2 Ultrasonic transducer characterization

1. The wear surface of the 54-kHz transducer is scanned with the laser vibrometer. The vibration of the centre of the transducer is analyzed in detail. It shows an additional frequency component other than the nominal resonant frequency. Based on this information, the frequency content of the received signals can be anticipated, and the relevant receivers can be selected. Moreover, the appropriate frequency bands for the spectral analysis can be chosen. Finally, the extracted modes can be further used (the possible applications include using the mode signals for enriching numerical models or for the estimation of the frequency response function for individual modes), and analysis of individual wavelengths is possible.

8.3.3 Distributed damage application

1. The attenuation approach, based on the WSST technique, is successfully presented based on four sensing techniques. The application includes typical contact sensors (i.e. accelerometer and ultrasonic transducer), a novel application of hydrophone for the specimen evaluation from a surface (a semi-contact technique), and the state-of-the-art laser Doppler vibrometer (a fully non-contact device).

2. The selection of the appropriate sensor is performed based on the characterization procedure of the transmitter used in the test. Based on the characterization, an accelerometer with the resonant frequency matching one of the modes of the transmitter and the ultrasonic receiver matching the transmitter are selected.

3. A dense receiver array (used with the laser vibrometer array) helps to identify reflections from boundaries in the signals, which is important for the selection of the window length for the calculations.

4. The relative attenuation index is calculated for the full-time signals and all sensing techniques first. The best results of the full-time signals analysis were obtained for accelerometers (RAI of 87%) due to the matching resonant frequency with the more sensitive frequency range of the responses. The selection of only the frequency ranges associated with the main frequency peaks of the transmitted signal improves the RAI results. The most sensitive frequency range is centred at 30 kHz. Similar RAI values were obtained for the sensor for which that frequency is available (i.e. accelerometers, UTx, and laser vibrometer). The lowest separation was obtained for the hydrophone, which is not sensitive in the low-frequency range. The frequency range centred at 50 kHz, which is related to the frequency of excitation, is less sensitive for the condition assessment of the tested beams. The WSST algorithm offers further improvements, and mode 30 gives the highest RAI values. For all sensing techniques, besides the hydrophone, the RAI is above 90%. Overall, the best evaluation was performed with the matching pair of ultrasonic transducers (RAI = 97%). WSST-based RAI offers a 52% improvement in damage detection when compared with the full-time signal analysis.

8.3.4 Localized damage application

The methodology is also tested in the cemented sand specimen. Two series of measurements are taken. An ultrasonic wave is sent with an ultrasonic transducer, and the responses are measured with a laser vibrometer.

1. Analysis of the original time signals showed no significant wave velocity change with the presence of the void in one of the measuring lines. However, distinct amplitude changes were observed when the measuring point was located on top of the void. The relative energy and relative attenuation index were calculated based on spectral energy. Additionally to the full spectral range, based on the transducer characterization, two frequency bins centred at the resonant frequencies were proposed. It has been shown that the 30-kHz rage is more sensitive to damage detection.

2. Using vibration mode extraction techniques (e.g. the WSST), it is possible to analyze only the precisely filtered signals. The WSST was applied to the measured signals, and the 30 and 50-

kHz modes were extracted. The procedure was repeated as for the group of original time signals. The same amplitude character of void presence was observed. However, due to the filtered nature of signals, it is easier to analyze the changes in the frequency content of the signals due to the void presence. The mode analysis follows the finding that the 30-kHz mode is more sensitive to damage detection.

3. Additionally, the relative dispersion index is calculated based on phase velocity dispersion curves. The presence of the void manifests itself with an additional mode; therefore, the dispersion curves are a useful tool for damage identification. The RDI values calculated for the tests can reach up to 130%.

4. Finally, full-time signals and mode analysis approaches are compared. The basic calculation of the relative attenuation index can be improved by analyzing only the sensitive part of spectra (the assessment can be improved by 17% with respect to the basic calculation). The selection of the frequency ranges can only be performed based on the ultrasonic transmitter characterization procedure. Further improvement was obtained applying the WSST technique, and the WSST-based assessment offered a 21% improvement when compared to the basic evaluation.

8.4 Ultrasonic evaluation and finite element analysis of damage in glass fibre reinforced polymer (GFRP) bars (Chapter 7)

Chapter 7 presents a pilot study of progressive damage of GFRP bars, which is required before the evaluation of concrete elements with GFRP reinforcement can be considered. The bars are subjected to accelerated ageing in alkaline solution and elevated temperature. The study is divided into four sections. Ultrasonic wave propagation is analyzed first (focusing on frequency content measured with ultrasonic transducers of different resonant frequency and laser vibrometer, and the shape of vibration). Next, ultrasonic evaluation based on wave velocity and amplitude attenuation approaches is performed. The responses are measured with ultrasonic transducers in an axial and transverse direction (with respect to a bar length). The numerical simulations are also considered to add a more comprehensive understanding of wave propagation and investigate other testing methods. Finally, a destructive shear test is carried on the bars. The experiment investigates the level of damage in bars and verifies the ultrasonic evaluation. The following detailed conclusions can be offered for each activity of this study.

8.4.1 Understanding of waves in GFRP bars

1. The frequency content of responses varies significantly with bar diameter and time. The first arriving pulse can have a much wider width than anticipated based on the nominal resonant frequency of the ultrasonic transducer. Therefore, if two bars (of different diameters) are in the same condition, they might produce signals having different ultrasonic features.

2. The laser vibrometer surface scans show that the surface vibration depends on the bar diameter. For smaller bar diameters, only the plane vibration is observed. Displacement observed in larger bars is more complicated and more prone to be affected by the frequency of the excitation.

8.4.2 Ultrasonic evaluation

1. A consistent decrease in wave velocity is observed with the progression of damage. However, the velocity reduction is within 5%, which does not offer enough sensitivity for field applications.

2. No consistent conclusion can be made regarding the effect of bar diameter on the wave velocity.

3. The transverse configuration (tested with 150 kHz probes) shows that the velocity in larger bars is less affected (besides D13 bar). The maximum reduction in the transverse configuration is only 2%.

4. Wave amplitude retention analysis (calculated based on the amplitude of the first peak [P-Peak] and energy in a discrete frequency band) offers increased sensitivity. Less variability is obtained with 150 kHz transducers.

8.4.3 Numerical simulation

1. The effect of reduced diameter (due to alkali ingress into GFRP bar) on dispersion curves studied based on the theoretical dispersion curves shows that depending on bar diameter, different frequencies offer increased sensitivity. From a practical standpoint, it should be beneficial to test bars with a smaller diameter with transducers with higher resonant frequency than the larger bar (i.e. the most sensitive frequency for D13 bar is centred around 250 kHz, while for D25 bars, it is centred around 125 kHz).

2. Analysis of dispersion curves obtained with the numerical model shows good agreement with shear test findings in the literature. Based on all the simulations, an approach based on wave

dispersion can be recommended for the monitoring of the GFRP bar condition. The benefit of this approach is that it considers the whole array of data points, which should minimize the testing errors.

3. Finally, displacement signals measured at the top of the bar (opposite side of the excitation) are analyzed. No significant difference in the arrival time is observed. However, the time shift between the responses of different conditions arises in the latter part of the signal, which creates an opportunity of applying more sensitive methods like coda wave interferometry.

4. The numerical model offers good agreement for the first arriving pulse. However, the model fails to reproduce the latter vibration. This can be related to the definition of excitation in the model. Firstly, the assumed excitation is applied uniformly over the whole cross-sectional area. At the same time, the characterization of the ultrasonic transducer shows that the 150 kHz transducer vibrates in the first mode of vibration (besides the very initial vibration). Secondly, the latter vibration might be related to the constructive and destructive wave interaction, which might not be represented well with the assumed duration of the excitation. Additionally, some errors might be related to the assumed all-free boundary condition.

5. The analysis of the first arriving peak (P-Peak) amplitude shows decreasing trends with the simulated deterioration. However, the loss of signal amplitude is significantly smaller than in the laboratory tests. In the laboratory test, responses are measured with an ultrasonic receiver, which means that the actual vibration is affected by a frequency response function of the receiver. Therefore, differences between the pure displacement signals and the ultrasonic transducer responses are expected.

8.4.4 Shear test

The shear test results follow the trends shown by other researchers and show strength reduction for all bar diameter. Larger bar diameters are affected less because the penetration depth of the alkaline solution is the same for all bar diameters (therefore, the relative effect is smaller for the larger bars). The same bar diameter effect is observed in the numerical simulation results. However, it is not reproduced in some ultrasonic laboratory tests.

8.4.5 Overall conclusion

It can be concluded that ultrasonic evaluation can capture deterioration in the GFRP bar and, with proper analysis (the correction factor), can be used to obtained an estimate of the shear strength (and consequently tensile strength) reduction. The maximum error of the ultrasonic evaluation with respect to the shear test is less than 7%. Ultrasonic evaluation can be improved by addressing the issue of coupling (e.g. decreased coupling area, improve bar surface finish) and using transducers selected based on bar diameter.

8.5 Future work

A possible extension of the work presented in this thesis includes:

Characterization of ultrasonic transducers using laser Doppler interferometer in kHz-range for civil engineering applications:

- Use glass block with a diagonal cut (i.e. 45 degrees, a beam splitter) that would allow for simultaneous scanning of ultrasonic transducers and receivers.
- Complete a 3D laser vibrometer scanning of the wear surface ultrasonic transducer. Investigate the in-plane (transverse) movement of the surface and frequency content associated with it.

Frequency and geometry effects on ultrasonic pulse velocity measurements of concrete specimens:

- Include a study of the aggregate size effect. Test specimens can include cylinders made out of the mortar and different concrete mixes.

Novel application of wavelet synchrosqueezed transform (WSST) for condition assessment of cementitious materials:

- Extend the study with the intermediate stages of freeze and thaw damage.

Ultrasonic evaluation and finite element analysis of damage in glass fibre reinforced polymer (GFRP) bars:

- Numerical simulations show promising signal behaviour affecting the latter part of signals (i.e. time shift in the latter part increases with damage progression). Compare numerical results and laboratory experiments and verify the applicability of the coda wave interferometry method.

- Extend the methodology for GFRP bars embedded in concrete elements (this extension will need to address the issue of different wave mechanics of embedded bars) and GFRP profiles (the extension will need to address the issue of more complicated geometry).

8.6 Summary

The numerical and experimental work efforts presented in this study investigate the frequency effects on ultrasonic measurements and establish a comprehensive methodology for early damage detection of composite materials (based on wave velocity, attenuation, and dispersion). The characterization procedure, developed for ultrasonic transducers typically used in civil engineering applications, reveals that frequency content, transmitted by the transducers to the tested medium, consists of more than just transducer resonant frequency. The importance of using well-characterized ultrasonic transducers (i.e. including the full frequency content in the NDT evaluation) is demonstrated on the ultrasonic evaluation of concrete elements, cemented sand specimen, and GFRP reinforcing bars. The study of frequency effects is continued with concrete cylinders of different dimensions. Therefore, practical recommendations regarding the minimum specimen length, effects of increasing length and diameter, and limitations regarding the use of high frequencies in the ultrasonic evaluation of concrete elements are given. Next, a framework based on wave velocity and attenuation (including a demonstration of the advantages of applying the wavelet synchrosqueezed transform [WSST]) is proposed for the evaluation of distributed damage (i.e. early damage induced by freeze and thaw cycles in concrete elements) and localized damage (i.e. cemented sand specimen with an undersurface void). The results indicate that the WSST technique has the potential to improve both the detection of distributed damage by up to 52% and localized damage detection by up to 36%. Finally, a progressive deterioration of GFRP reinforcing bars is studied using the developed ultrasonic procedure. The comparison of ultrasonic evaluation based on wave amplitude, destructive shear test, and numerical simulations shows that ultrasonic techniques can successfully predict the degradation of shear strength (and ultimately tensile strength) of GFRP bars (with the maximum error of 7%). The findings presented in this thesis provide practical recommendations and frameworks that can successfully increase the reliability of non-destructive ultrasonic evaluation of composite materials used in civil engineering applications.

References

Abo-Qudais, S. A. (2005). Effect of concrete mixing parameters on propagation of ultrasonic waves. *Construction and Building Materials, 19*(4), 257-263. 10.1016/j.conbuildmat.2004.07.022

Abraham, O., & Popovics, J. S. (2010). Impact-Echo Techniques for Evaluation of Concrete Structures . In C. Maierhofer, H. -. Reinhardt & G. Dobmann (Eds.), *Non-Destructive Evaluation of Reinforced Concrete Structures, Volume 2 - Non-Destructive Testing Methods* (pp. 466-489). Woodhead Publishing.

Abraham, O., Piwakowski, B., Villain, G., & Durand, O. (2012). Non-contact, automated surface wave measurements for the mechanical characterisation of concrete. *Construction and Building Materials, 37*, 904-915. 10.1016/j.conbuildmat.2012.03.015

ACI Committee 318. (2014). *318-14: Building Code Requirements for Structural Concrete and Commentary.*

Aggelis, D. G., Shiotani, T., & Polyzos, D. (2009). Characterization of surface crack depth and repair evaluation using Rayleigh waves. *Cement & Concrete Composites, 31*(1), 77-83.

Aggelis, D. G., Kordatos, E. Z., Strantza, M., Soulioti, D. V., & Matikas, T. E. (2011). NDT approach for characterization of subsurface cracks in concrete. *Construction and Building Materials, 25*(7), 3089-3097. 10.1016/j.conbuildmat.2010.12.045

Aggelis, D. G., Polyzos, D., & Philippidis, T. P. (2005). Wave dispersion and attenuation in fresh mortar: theoretical predictions vs. experimental results. *Journal of the Mechanics and Physics of Solids, 53*(4), 857-883. 10.1016/j.jmps.2004.11.005

Aggelis, D. G., & Shiotani, T. (2007). Repair evaluation of concrete cracks using surface and through-transmission wave measurements. *Cement and Concrete Composites, 29*(9), 700-711. 10.1016/j.cemconcomp.2007.05.001

American Concrete Institute. (2018). *CT-18: ACI Concrete Terminology.* Farmington Hills: American Concrete Institute.

Arczewska, P. (2017). *Practical Performance Criteria and Durability Prediction Modeling of Glass Fiber Reinforced Polymer (GFRP) Bars.* UWSpace.

Arczewska, P., Polak, M. A., & Penlidis, A. (2017). Deterioration of tensile and shear strength of GFRP bars. *American Concrete Institute, ACI Special Publication, 2017-October* (SP 327), 789-803.

ASTM International. (2008). *ASTM D2845-08 Standard Test Method for Laboratory Determination of Pulse Velocities and Ultrasonic Elastic Constants of Rock (Withdrawn 2017)*. ASTM International.

ASTM International. (2012). *ASTM: 469−12 Standard Test Method for Static Modulus of Elasticity and Poisson's Ratio of Concrete in Compression*. ASTM International.

ASTM International. (2014a). *ASTM C215-14 Standard Test Method for Fundamental Transverse, Longitudinal, and Torsional Resonant Frequencies of Concrete Specimens*. ASTM International.

ASTM International. (2014b). *E1065/E1065M-14 Standard Guide for Evaluating Characteristics of Ultrasonic Search Units*. ASTM International.

ASTM International. (2016a). *C597-16 Standard Test Method for Pulse Velocity Through Concrete*. ASTM International.

ASTM International. (2016b). *D7205/D7205M − 06 Standard Test Method for Tensile Properties of Fiber Reinforced Polymer Matrix Composite Bars*. ASTM International.

ASTM International. (2017a). *ASTM: E122-17 Standard Practice for Calculating Sample Size to Estimate, With Specified Precision, the Average for a Characteristic of a Lot or Process*. ASTM International.

ASTM International. (2017b). *D7617/D7617M − 11 Standard Test Method for Transverse Shear Strength of Fiber-reinforced Polymer Matrix Composite Bars*. ASTM International.

ASTM International. (2018a). *ASTM: C39/C39M−18 Standard Test Method for Compressive Strength of Cylindrical Concrete Specimens*. ASTM International.

ASTM International. (2018b). *C33/C33M-18 Standard Specification for Concrete Aggregates*. ASTM International.

ASTM International. (2019). *D7705/D7705M − 12 Standard Test Method for Alkali Resistance of Fiber Reinforced Polymer (FRP) Matrix Composite Bars used in Concrete Construction*. ASTM International.

ASTM International. (2020). *E1316-20 Standard Terminology for Nondestructive Examinations*. ASTM International.

Bittner, J. A., & Popovics, J. S. (2019). Direct imaging of moisture effects during slow dynamic nonlinearity. *Applied Physics Letters, 114*(2)10.1063/1.5063904

Bouchikhi, E. H., Choqueuse, V., Benbouzid, M. E. H., Charpentier, J. F., & Barakat, G. (2011). (2011). A comparative study of time-frequency representations for fault detection in wind turbine. Paper presented at the 3584-3589. 10.1109/IECON.2011.6119891

Brisken, A. F., & Smith, L. S. (1980). In General Electric Company (Ed.), *Wear plate for piezoelectric ultrasonic transducer arrays.*

Büssow, R. (2007). An algorithm for the continuous Morlet wavelet transform. *Mechanical Systems and Signal Processing, 21*(8), 2970-2979. 10.1016/j.ymssp.2007.06.001

Callister Jr., W. D., & Rethwisch, D. G. (2014). *Materials Science and Engineering: An Introduction*. Wiley.

Canney, M., Bailey, M., Crum, L., Khokhlova, V., & Sapozhnikov, O. (2008). Acoustic characterization of high intensity focused ultrasound fields: A combined measurement and modeling approach. *The Journal of the Acoustical Society of America, 124*(4), 2406-2420. 10.1121/1.2967836

Castro, P. F., & Carino, N. J. (1998). Tensile and nondestructive testing of FRP bars. *Journal of Composites for Construction, 2*(1), 17-26.

Chaix, J., Garnier, V., & Corneloup, G. (2006). Ultrasonic wave propagation in heterogeneous solid media: Theoretical analysis and experimental validation. *Ultrasonics, 44*(2), 200-210. 10.1016/j.ultras.2005.11.002

Chen, Y., Davalos, J. F., Ray, I., & Kim, H. (2007). Accelerated aging tests for evaluations of durability performance of FRP reinforcing bars for concrete structures. *Composite Structures, 78*(1), 101-111. 10.1016/j.compstruct.2005.08.015

Chiachío, J., Bochud, N., Chiachío, M., Cantero, S., & Rus, G. (2017). A multilevel Bayesian method for ultrasound-based damage identification in composite laminates. *Mechanical Systems and Signal Processing, 88*, 462-477. 10.1016/j.ymssp.2016.09.035

Chivers, R. C. (1986). Time-delay spectrometry for ultrasonic transducer characterisation. *Journal of Physics E: Scientific Instruments, 19*(10), 834-843. 10.1088/0022-3735/19/10/015

Choi, H., Palacios, G., Popovics, J. S., & Chao, S. -. (2018). Monitoring damage in concrete columns using ultrasonic tomography. *ACI Structural Journal, 115*(2), 545-558. 10.14359/51701117

Clough, R. W., & Penzien, J. (1993). *Dynamics of Structures*. McGraw-Hill.

Dai, S., Wuttke, F., & Santamarina, J. C. (2013). Coda Wave Analysis to Monitor Processes in Soils. *Journal of Geotechnical and Geoenvironmental Engineering, 139*(9), 1504-1511. 10.1061/(ASCE)GT.1943-5606.0000872

Dassault Systemes Simulia Corp. (2012). *ABAQUS Analysis User's Manual 6.12-3*.

Daubechies, I. (1992). *Ten lectures on wavelets*. Society for Industrial and Applied Mathematics.

Daubechies, I., Lu, J., & Wu, H. (2011). Synchrosqueezed wavelet transforms: An empirical mode decomposition-like tool. *Applied and Computational Harmonic Analysis, 30*(2), 243-261. 10.1016/j.acha.2010.08.002

Daubechies, I., Maes, S., & Maes, S. (2017). A Nonlinear Squeezing of the Continuous Wavelet Transform Based on Auditory Nerve Models. In A. Aldroubi, & M. Unser (Eds.), *Wavelets in Medicine and Biology* (pp. 527-546). Routledge. 10.1201/9780203734032-20

Eiras, J. N., Kundu, T., Popovics, J. S., Monzó, J., Borrachero, M. V., & Payá, J. (2016). Effect of carbonation on the linear and nonlinear dynamic properties of cement-based materials. *Optical Engineering, 55*(1)10.1117/1.OE.55.1.011004

Eiras, J. N., Kundu, T., Popovics, J. S., & Payá, J. (2018). Cement-based material characterization using nonlinear single-impact resonant acoustic spectroscopy (NSIRAS). In T. Kundu (Ed.), *Nonlinear Ultrasonic and Vibro-Acoustical Techniques for Nondestructive Evaluation* (pp. 487-508)

Eiras, J. N., Monzó, J., Payá, J., Kundu, T., & Popovics, J. S. (2014). Non-classical nonlinear feature extraction from standard resonance vibration data for damage detection. *Journal of the Acoustical Society of America, 135*(2), EL82-EL87. 10.1121/1.4862882

Ensminger, D., & Bond, L. J. (2011). *Ultrasonics: Fundamentals, Technologies, and Applications, Third Edition*. CRC Press. 10.1201/b11173

Erikson, K. (1979a). Pulse-Echo Ultrasonic Transducer Characterization. *IEEE Transactions on Sonics and Ultrasonics, 26*(1), 1. 10.1109/T-SU.1979.31056

Erikson, K. (1979b). Tone-Burst Testing of Pulse-Echo Transducers. *IEEE Transactions on Sonics and Ultrasonics, 26*(1), 7-13. 10.1109/T-SU.1979.31058

Eriksson, T. J. R., Ramadas, S. N., & Dixon, S. M. (2015). Ultrasonics. *Ultrasonics, 65*, 242-248.

Erki, M. A., & Rizkalla, S. H. (1993). FRP Reinforcement for Concrete Structures. *Concrete International, 15*(6), 48-53.

Fartosy, S. (2018). *Non-destructive Evaluation of Damage in Concrete with Applications in Shallow Foundations* https://uwspace.uwaterloo.ca/handle/10012/13926

Feeney, A., Kang, L., Rowlands, G., Zhou, L., & Dixon, S. (2019). Dynamic Nonlinearity in Piezoelectric Flexural Ultrasonic Transducers. *IEEE Sensors Journal, 19*(15), 6056-6066. 10.1109/JSEN.2019.2911158

Feeney, A., Kang, L., Somerset, W. E., & Dixon, S. (2019). The Influence of Air Pressure on the Dynamics of Flexural Ultrasonic Transducers. *Sensors (Basel, Switzerland), 19*(21), 4710. 10.3390/s19214710

Fei, C., Lin, P., Li, D., Wu, Y., Wu, R., Chen, J., & Yang, Y. (2019). Fabrication and Characterization of High-Sensitivity Ultrasonic Transducers With Functionally Graded Design. *IEEE Sensors Journal, 19*(16), 6650-6654. 10.1109/JSEN.2019.2905625

Feng, M. Q., De Flaviis, F., & Kim, Y. J. (2002). Use of microwaves for damage detection of fiber reinforced polymer-wrapped concrete structures. *Journal of Engineering Mechanics, 128*(2), 172-183. 10.1061/(ASCE)0733-9399(2002)128:2(172)

Fiberline Composites. (2017). *Fiberline Composites.* https://fiberline.com/. Access date: Jun-10-2017.

Genikomsou, A. S., Balomenos, G. P., Arczewska, P., & Polak, M. A. (2018). Transverse Shear Testing of GFRP Bars with Reduced Cross Sections. *Journal of Composites for Construction, 22*(5)10.1061/(ASCE)CC.1943-5614.0000880

Ghaib, M., Shateri, M., Thomson, D., & Svecova, D. (2018). Study of FRP bars under tension using acoustic emission detection technique. *Journal of Civil Structural Health Monitoring, 8*(2), 285-300. 10.1007/s13349-018-0273-8

Ghofrani, S., & McLernnon, D. C.Comparison of the cross deleted wigner representation and the matching pursuit distribution (via adaptive signal decomposition). Paper presented at the *3rd International Conference on Image and Signal Processing, ICISP 2008,* 516-526.

Gibson, A., & Popovics, J. S. (2005). Lamb wave basis for impact-echo method analysis. *Journal of Engineering Mechanics, 131*(4), 438-443. 10.1061/(ASCE)0733-9399(2005)131:4(438)

Gowayed, Y. (2013). 1 - Types of fiber and fiber arrangement in fiber-reinforced polymer (FRP) composites. In N. Uddin (Ed.), *Developments in Fiber-Reinforced Polymer (FRP) Composites for Civil Engineering* (pp. 3-17). Woodhead Publishing.

Halabe, U. B. (2013). 18 - Non-destructive evaluation (NDE) of composites: techniques for civil structures. In V. M. Karbhari (Ed.), *Non-Destructive Evaluation (NDE) of Polymer Matrix Composites* (pp. 483-517e). Woodhead Publishing.

Ham, S., Song, H., Oelze, M. L., & Popovics, J. S. (2017). A contactless ultrasonic surface wave approach to characterize distributed cracking damage in concrete. *Ultrasonics, 75*, 46-57. 10.1016/j.ultras.2016.11.003

Hazra, B., Sadhu, A., & Narasimhan, S. (2017). Fault detection of gearboxes using synchro-squeezing transform. *Journal of Vibration and Control, 23*(19), 3108-3127. 10.1177/1077546315627242

Herrera, R. H., Han, J., & van der Baan, M. (2013). Applications of the synchrosqueezing transform in seismic time-frequency analysis. *Geophysics, 79*(3), V55-V64. 10.1190/GEO2013-0204.1

Huo, J., Jin, B., Yu, Q., He, Y., & Liu, Y. (2016). Effect of Microstructure Variation on Damage Evolution of Concrete at High Temperatures. *ACI Materials Journal, 113*(5), 547-558. 10.14359/51689102

In, C., Kim, J., Kurtis, K. E., & Jacobs, L. J. (2009). Characterization of ultrasonic Rayleigh surface waves in asphaltic concrete. *NDT and E International, 42*(7), 610-617. 10.1016/j.ndteint.2009.04.007

Jones, R. (1949). The non-destructive testing of concrete. *Magazine of Concrete Research, 1*(2), 67-78. 10.1680/macr.1949.1.2.67

Jones, R. (1957). The effect of frequency on the dynamic modulus and damping coefficient of concrete. *Magazine of Concrete Research, 9*(26), 69-72. 10.1680/macr.1957.9.26.69

Jones, R., & Facaoaru, I. (1968). An analysis of answers to a questionnaire on the ultrasonic pulse technique. *Matériaux Et Constructions, 1*(5), 457-465. 10.1007/BF02473743

Jones, R., & Facaoaru, I. (1969). Recommendations for testing concrete by the ultrasonic pulse method. *Mat. Constr.,* (2), 275–284.

Karbhari, V. M. (2013). 1 - Introduction: the future of non-destructive evaluation (NDE) and structural health monitoring (SHM). In V. M. Karbhari (Ed.), *Non-Destructive Evaluation (NDE) of Polymer Matrix Composites* (pp. 3-11). Woodhead Publishing.

Katsuki, F., & Uomoto, T. (1995). Prediction of deterioration of FRP rods due to alkali attack. In L. Taerwe (Ed.), *Non-Metallic (FRP) Reinforcement for Concrete Structures* (pp. 100-107). CRC Press. 10.1201/9781482271621-19

Kemp, M., & Blowes, D. (2011). *Concrete Reinforcement and Glass Fibre Reinforced Polymer.* Queensland roads edition no ii.

Khan, Z., Majid, A., Cascante, G., Hutchinson, D. J., & Pezeshkpour, P. (2006). Characterization of a cemented sand with the pulse-velocity method. *Canadian Geotechnical Journal, 43*(3), 294-309. 10.1139/t06-008

Khan, Z., Cascante, G., & El Naggar, M. H. (2010). Measurement of dynamic properties of stiff specimens using ultrasonic waves. *Canadian Geotechnical Journal, 48*(1), 1-15. 10.1139/T10-040

Kijewski, T., & Kareem, A. (2003). Wavelet Transforms for System Identification in Civil Engineering. *Computer-Aided Civil and Infrastructure Engineering, 18*(5), 339-355. 10.1111/1467-8667.t01-1-00312

Kim, S. D., Shin, D. H., Lim, L. M., Lee, J., & Kim, S. H. (2005). Designed strength identification of concrete by ultrasonic signal processing based on artificial intelligence techniques. *IEEE Transactions on Ultrasonics, Ferroelectrics, and Frequency Control, 52*(7), 1145-1151.

Kirlangic, A. S. (2013). *Condition Assessment of Concrete Beams Using Ultrasonic Surface Waves.* UWSpace.

Kirlangic, A. S., Cascante, G., & Polak, M. A. (2015). Condition Assessment of Cementitious Materials Using Surface Waves in Ultrasonic Frequency Range. *Geotechnical Testing Journal, 38*(2), 139-149. 10.1520/GTJ20140011

Kirlangic, A. S., Cascante, G., & Polak, M. A. (2016). Assessment of Concrete Beams with Irregular Defects Using Surface Waves. *ACI Materials Journal, 113*(1), 73. 10.14359/5168807

Kirlangic, A. S., Cascante, G., & Polak, M. A. (2017). Characterization of Piezoelectric Accelerometers Beyond the Nominal Frequency Range. *Geotechnical Testing Journal, 40*(1), 37-46. 10.1520/GTJ20150091

Krstulovic-Opara, N., Woods, R. D., & Al-Shayea, N. (1996). Nondestructive Testing of Concrete Structures Using the Rayleigh Wave Dispersion Method. *ACI Materials Journal, 93*(1), 75-86. 10.14359/9799

Kuhl, W., & Kaiser, H. (1952). Absorption of structure-borne sound in building materials without and with sand-filled cavities. *Acta Acustica United with Acustica, 2*(4), 179-188.

Leissa, A. W. (1969). *Vibration of plates.* NASA Report No. SP-160.

MacGregor, J. G., & Wight, J. K. (2005). *Reinforced Concrete. Mechanics and Design*. Pearson Education Inc.

Mahajan, G. V., & Aher, V. S. (2012). Composite Material: A Review over Current Development and Automotive Application. *International Journal of Scientific and Research Publications, 2*(11)

Mahbaz, S., Cascante, G., & Dusseault, M. B. (2019). Calibration of a Piezoelectric Transducer through Laser Measurements and Numerical Simulation. *Journal of Environmental and Engineering Geophysics, 24*(1), 39-48. 10.2113/JEEG24.1.39

Mahmoud, A. M., Ammar, H. H., Mukdadi, O. M., Ray, I., Imani, F., Chen, A., & Davalos, J. F. (2011). Ultrasonic evaluation of CFRP-concrete interface for specimens under temperature and water-immersion aging effects. *Advances in FRP Composites in Civil Engineering - Proceedings of the 5th International Conference on FRP Composites in Civil Engineering,* , 562-566.

Maierhofer, C., Reinhardt, W. -., & Dobmann, G. (2010). *Non-Destructive Evaluation of Reinforced Concrete Structures, Volume 1 - Deterioration Processes and Standard Test Methods*. Woodhead Publishing.

Marzouk, H., & Jiang, K. (1995). Effects of Freezing and Thawing on the Tension Properties of High-Strength Concrete. *ACI Materials Journal, 91*(6), 577-586. 10.14359/1378

McCann, D. M., & Forde, M. C. (2001). Review of NDT methods in the assessment of concrete and masonry structures. *NDT & E International, 34*(2), 71-84. 10.1016/S0963-8695(00)00032-3

Mehta, K. P. (2001). Reducing the Environmental Impact of Concrete. *Concrete International, 23*(10), 61-66.

Mihalec, M., Slavič, J., & Boltežar, M. (2016). Synchrosqueezed wavelet transform for damping identification. *Mechanical Systems and Signal Processing, 80*, 324-334. 10.1016/j.ymssp.2016.05.005

Miklowitz, J. (1978). CHAPTER 4 - Time Harmonic Waves in Elastic Waveguides. In J. Miklowitz (Ed.), *North-Holland Series in Applied Mathematics and Mechanics* (pp. 178-230). North-Holland.

Miller, E. B., & Eitzen, D. G. (1979). Ultrasonic Transducer Characterization at the NBS. *IEEE Transactions on Sonics and Ultrasonics, 26*(1), 28-36. 10.1109/T-SU.1979.31060

Mori, K., Spagnoli, A., Murakami, Y., Kondo, G., & Torigoe, I. (2002). A new non-contacting non-destructive testing method for defect detection in concrete. *NDT and E International, 35*(6), 399-406. 10.1016/S0963-8695(02)00009-9

Moss, B. C., & Scruby, C. B. (1988). Investigation of ultrasonic transducers using optical techniques. *Ultrasonics, 26*, 179-188.

Mouritz, A. P. (2000). Ultrasonic and interlaminar properties of highly porous composites. *Journal of Composite Materials, 34*(3), 218-239. 10.1106/WL60-VFNN-7WEU-4DAV

Mukherjee, A., & Arwikar, S. J. (2005a). Performance of glass fiber-reinforced polymer reinforcing bars in tropical environments - Part I: Structural scale tests. *ACI Structural Journal, 102*(5), 745-753.

Mukherjee, A., & Arwikar, S. J. (2005b). Performance of glass fiber-reinforced polymer reinforcing bars in tropical environments - Part II: Microstructural tests. *ACI Structural Journal, 102*(6), 816-822.

Nkurunziza, G., Debaiky, A., Cousin, P., & Benmokrane, B. (2005). Durability of GFRP bars: A critical review of the literature. *Progress in Structural Engineering and Materials, 7*(4), 194-209. 10.1002/pse.205

Nobach, H., Tropea, C., Cordier, L., Bonnet, J., Delville, J., Lewalle, J., Farge, M., Schneider, K., & Adrian, R. (2007). Review of Some Fundamentals of Data Processing. In C. Tropea, A. L. Yarin & J. F. Foss (Eds.), *Springer Handbook of Experimental Fluid Mechanics* (). Springer Handbooks.

Obaidat, M. S., & Abu-Saymeh, D. S. (1992). Methodologies for characterizing ultrasonic transducers using neural network and pattern recognition techniques. *IEEE Transactions on Industrial Electronics, 39*(6), 529-536. 10.1109/41.170972

Obaidat, M. S., Khalid, H., & Sadoun, B. (1998). Ultrasonic transducer characterization by neural networks. *Information Sciences, 107*(1), 195-215. 10.1016/S0020-0255(97)10048-2

Ohdaira, E., & Masuzawa, N. (2000). Water content and its effect on ultrasound propagation in concrete — the possibility of NDE. *Ultrasonics, 38*(1), 546-552. 10.1016/S0041-624X(99)00158-4

Owino, J. O., & Jacobs, L. J. (1999). Attenuation measurements in cement-based materials using laser ultrasonics. *Journal of Engineering Mechanics, 125*(6), 637-647. 10.1061/(ASCE)0733-9399(1999)125:6(637)

Pachori, R. B., & Nishad, A. (2016). Cross-terms reduction in the Wigner–Ville distribution using tunable-Q wavelet transform. *Signal Processing, 120*, 288-304. 10.1016/j.sigpro.2015.07.026

Papadakis, E. P. (1979). Theoretical and Experimental Methods to Evaluate Ultrasonic Transducers for Inspection and Diagnostic Applications. *IEEE Transactions on Sonics and Ultrasonics, 26*(1), 14-27. 10.1109/T-SU.1979.31059

Park, Y., Ramirez, G., Abolmaali, A., & Kim, Y. H. (2015). Acoustic emission performances of stressed-gfrp bars embedded in concrete under accelerated aging conditions. *AEI 2015: Birth and Life of the Integrated Building - Proceedings of the AEI Conference 2015,* 248-258. 10.1061/9780784479070.023

Pavlakovic, B., Lowe, M., Alleyne, D. & Cawley, P. (2020). *Disperse.* http://www.disperse.software/. Access date: Aug-10-2020.

Philippidis, T. P., & Aggelis, D. G. (2005). Experimental study of wave dispersion and attenuation in concrete. *Ultrasonics, 43*(7), 584-595. 10.1016/j.ultras.2004.12.001

Planès, T., & Larose, E. (2013). A review of ultrasonic Coda Wave Interferometry in concrete. *Cement and Concrete Research, 53*, 248-255. 10.1016/j.cemconres.2013.07.009

Popovics, J. S. (2003). NDE techniques for concrete and masonry structures. *Progress in Structural Engineering and Materials, 5*(2), 49-59. 10.1002/pse.146

Popovics, J. S., & Abraham, O. (2010). Surface wave techniques for evaluation of concrete structures . In C. Maierhofer, H. -. Reinhardt & G. Dobmann (Eds.), *Non-Destructive Evaluation of Reinforced Concrete Structures, Volume 2 - Non-Destructive Testing Methods* (pp. 441-465). Woodhead Publishing

Popovics, S. (2005). Effects of uneven moisture distribution on the strength of and wave velocity in concrete. *Ultrasonics, 43*(6), 429-434. 10.1016/j.ultras.2004.09.007

Puckett, A. (2004). *An Experimental and Theoretical Investigation of Axially Symmetric Wave Propagation In Thick Cylindrical Waveguides*

Rigby, S. E., Barr, A. D., & Clayton, M. (2018). A review of Pochhammer-Chree dispersion in the Hopkinson bar. *Proceedings of the Institution of Civil Engineers: Engineering and Computational Mechanics, 171*(1), 3-13. 10.1680/jencm.16.00027

Rose, J. L. (1999). *Ultrasonic Waves in Solid Media Joseph L. Rose*. Cambridge University Press.

Sanjurjo, A., Hettiarachchi, S., Lau, K., Wood, B., & Cox, P. (1993). *Development of Metallic Coatings for Corrosion Protection of Steel Rebars.* Washington, DC: National Academy of Sdences.

Schmerr, L. W., Lopez-Sanchez, A., & Huang, R. (2006). Complete ultrasonic transducer characterization and its use for models and measurements. *Ultrasonics, 44*, e753-e757. 10.1016/j.ultras.2006.05.088

Schmerr, L. W., & Song, S. (2007). *Ultrasonic nondestructive evaluation systems.* https://doi.org/10.1007/978-0-387-49063-2

Snieder, R. (2006). The Theory of Coda Wave Interferometry. *Pure and Applied Geophysics, 163*(2), 455-473. 10.1007/s00024-005-0026-6

Son, L. H., & Yuen, G. C. S. (1993). Concrete Defects Son L.H., Yuen G.C.S. In L. H. Son, & G. C. S. Yuen (Eds.), *Building Maintenance Technology* (pp. 74-99). Palgrave.

Song, H., & Popovics, J. S. (2019a). Contactless ultrasonic wavefield imaging to visualize near-surface damage in concrete elements. *Applied Sciences (Switzerland), 9*(15)10.3390/app9153005

Song, H., & Popovics, J. S. (2019b). Extracting non-propagating oscillatory fields in concrete to detect distributed cracking. *Journal of the Acoustical Society of America, 146*(4), 2655-2670. 10.1121/1.5130568

Stauffer, J. D., Woodward, C. B., & White, K. R. (2005). Nonlinear Ultrasonic Testing with Resonant and Pulse Velocity Parameters for Early Damage in Concrete. *ACI Materials Journal, 102*(2), 118-121. 10.14359/14305

Tallavo, F., Cascante, G., & Pandey, M. D. (2011). Ultrasonic transducers characterisation for evaluation of stiff geomaterials. *Geotechnique, 61*(6), 501-510. 10.1680/geot.9.P.087

Tesfamariam, S., & Martin-Perez, B. (2010). Stress wave propagation for evaluation of reinforced concrete structures. In C. Maierhofer, H. -. Reinhardt & G. Dobmann (Eds.), *Non-Destructive Evaluation of*

Reinforced Concrete Structures, Volume 2 - Non-Destructive Testing Methods (pp. 417-440). Woodhead Publishing.

Thakur, G., Brevdo, E., Fučkar, N. S., & Wu, H. (2013). The Synchrosqueezing algorithm for time-varying spectral analysis: Robustness properties and new paleoclimate applications. *Signal Processing, 93*(5), 1079-1094. 10.1016/j.sigpro.2012.11.029

Thakur, G., & Wu, H. (2011). Synchrosqueezing-Based Recovery of Instantaneous Frequency from Nonuniform Samples. *SIAM Journal on Mathematical Analysis, 43*(5), 2078-2095. 10.1137/100798818

Torrence, C., & Campo, G. P. (1998). A Practical Guide to Wavelet Analysis. *Bulletin of the American Meteorological Society, 79*(1), 61-78. 10.1175/1520-0477(1998)0792.0.CO;2

Vary, A. (1979). Correlations between ultrasonic and fracture toughness factors in metallic materials. *ASTM Special Technical Publication,* (677), 563-578.

Vary, A. (1980). Concepts and techniques for ultrasonic evaluation of material mechanical properties. *Proceedings of the Symposium on Waste Management,* , 123-141.

Verástegui-Flores, R. D., Di Emidio, G., Bezuijen, A., Vanwalleghem, J., & Kersemans, M. (2015). Evaluation of the free–free resonant frequency method to determine stiffness moduli of cement-treated soil. *Soils and Foundations, 55*(5), 943-950. 10.1016/j.sandf.2015.09.001

Vinh, P. C., & Malischewsky, P. G. (2006). Explanation for Malischewsky's approximate expression for the Rayleigh wave velocity. *Ultrasonics, 45*(1-4), 77-81. 10.1016/j.ultras.2006.07.001

Wang, P., Gao, J., & Wang, Z. (2014). Time-Frequency Analysis of Seismic Data Using Synchrosqueezing Transform. *IEEE Geoscience and Remote Sensing Letters, 11*(12), 2042-2044. 10.1109/LGRS.2014.2317578

Wang, S., & Adler, L. (1984). Ultrasonic studies of strength-related properties of graphite. *Review of Progress in Quantitative Nondestructive Evaluation, 3 B*, 1211-1219.

Wang, T., Cheung, F., & Butera, M. (1992). An automated digital beam profile system for ultrasonic transducer characterization. *NDT and E International, 25*(4), 171-176. 10.1016/0963-8695(92)90157-C

Wiciak, P., Cascante, G., & Polak, M. A. (2020). Frequency and Geometry Effects on Ultrasonic Pulse Velocity Measurements of Concrete Specimens. *ACI Materials Journal, 117*(2), 205-216. 10.14359/51722399

Wolf, F., Lahmer, T., Bahr, L., Hauck, A., Sutor, A., Lerch, R., & Kaltenbacher, M. (2008). Finite element modeling of ultrasonic transducer by utilizing an inverse scheme for the determination of its material parameters. *2008 IEEE Ultrasonics Symposium,* , 784-787. 10.1109/ULTSYM.2008.0188

Wootton, I. A., Spainhour, L. K., & Yazdani, N. (2003). Corrosion of steel reinforcement in carbon fiber-reinforced polymer wrapped concrete cylinders. *Journal of Composites for Construction, 7*(4), 339-347. 10.1061/(ASCE)1090-0268(2003)7:4(339)

Xiang, J., & Liang, M. (2012). Wavelet-Based Detection of Beam Cracks Using Modal Shape and Frequency Measurements. *Computer-Aided Civil and Infrastructure Engineering, 27*(6), 439-454. 10.1111/j.1467-8667.2012.00760.x

Xu, K., Ren, C., Deng, Q., Jin, Q., & Chen, X. (2018). Real-time monitoring of bond slip between GFRP bar and concrete structure using piezoceramic transducer-enabled active sensing. *Sensors (Switzerland), 18*(8)10.3390/s18082653

Yaman, I. O., Inci, G., Yesiller, N., & Aktan, H. M. (2001). Ultrasonic Pulse Velocity in Concrete Using Direct and Indirect Transmission. *Materials Journal, 98*(6), 450-457. 10.14359/10843

Yang, Y., Cascante, G., & Polak, M. A. (2011). New Method for the Evaluation of Material Damping Using the Wavelet Transform. *Journal of Geotechnical and Geoenvironmental Engineering, 137*(8), 798-808. 10.1061/(ASCE)GT.1943-5606.0000485

Zerwer, A., Cascante, G., & Hutchinson, J. (2002). Parameter estimation in finite element simulations of Rayleigh waves. *Journal of Geotechnical and Geoenvironmental Engineering, 128*(3), 250-261. 10.1061/(ASCE)1090-0241(2002)128:3(250)

Zerwer, A., Polak, M. A., & Santamarina, J. C. (2003). Rayleigh wave propagation for the detection of near surface discontinuities: Finite element modeling. *Journal of Nondestructive Evaluation, 22*(2), 39-52. 10.1023/A:1026307909788

Zhu, J., & Popovics, J. (2005). Non-contact imaging for surface-opening cracks in concrete with air-coupled sensors. *Materials and Structures, 38*(9), 801-806. 10.1007/BF02481652